PROBING THE EARLY UNIVERSE AND DARK ENERGY WITH MULTI-EPOCH COSMOLOGICAL DATA

Renée Hlozek

Christ Church
Astrophysics
Department of Physics

A thesis submitted in candidature for the degree of Doctor of Philosophy

Trinity Term 2011

PROBING THE EARLY UNIVERSE AND DARK ENERGY WITH MULTI-EPOCH COSMOLOGICAL DATA

Renée Hlozek
Christ Church
Astrophysics
Department of Physics

ABSTRACT

Contemporary cosmology is a vibrant field, with data and observations increasing rapidly. This allows for accurate estimation of the parameters describing our cosmological model. In this thesis we present new research based on two different types of cosmological observations, which probe the universe at multiple epochs. We begin by reviewing the current concordance cosmological paradigm, and the statistical tools used to perform parameter estimation from cosmological data. We highlight the initial conditions in the universe and how they are detectable using the Cosmic Microwave Background radiation. We present the angular power spectrum data from temperature observations made with the Atacama Cosmology Telescope (ACT) and the methods used to estimate the power spectrum from temperature maps of the sky. We then present a cosmological analysis using the ACT data in combination with observations from the Wilkinson Microwave Anisotropy Probe to constrain parameters such as the effective number of relativistic species and the spectral index of the primordial power spectrum, which we constrain to deviate from scale invariance at the 99% confidence limit. We then use this combined dataset to constrain the primordial power spectrum in a minimally parametric framework, finding no evidence for deviation from a power-law spectrum. Finally we present Bayesian Estimation Applied to Multiple Species, a parameter estimation technique using photometric Type Ia Supernova data to estimate cosmological parameters in the presence of contaminated data. We apply this algorithm to the full season of the Sloan Digital Sky Survey II Supernova Search, and find that the constraints are improved by a factor of three relative to the case where one uses a smaller, spectroscopically confirmed subset of supernovae.

A thesis submitted in candidature for the degree of Doctor of Philosophy
University of Oxford

Trinity Term 2011

ACKNOWLEDGMENTS

This thesis would not have been possible without the support and encouragement of my friends, family and colleagues.

I would like to thank Joanna Dunkley, who has been a wonderful and supportive DPhil supervisor, who always made me feel like my contribution was valid and who put up with my strange (and verbose) ways in a calm, encouraging manner. It is a pleasure working with and learning from you.

I would like to thank Bruce Bassett, who gave me my first lessons in the joys of research and is an inspiration to me. I would also like to thank Marina Cortês, Martin Kunz, Jacques Kotze, Yabebal Tadesse, Melvin Varughese, Mat Smith and James Newling. Thanks to Chris Lintott for friendship, support and inspiration to get the science message out there; Joe Zuntz for handy coding tips and for being a loyal friend; Sarah for her constant belief in me; for Olaf who is a never-ending source of interest and debate; my former office mates Seba, Paul, Cristina, Sam and David for many laughs (and macarons with Maayane!). Thanks to Pedro and the other members of the cosmology group: Tim, Chris, Graeme, Charmaine, Tessa, Phil and Thibaut for interesting Monday lunches. Thanks to the ACT team for support and especially Sudeep for teaching me many great Python tips, to David Spergel for excellent ideas and advice and Jon for his calming voice on telecons. Finally thanks those in the Astrophysics group that made this DPhil such an enriching experience.

I thank Nick for his brotherly support and helping me not to take myself too seriously, and thank my mom, Glenda, who is always 'in my corner', cheering me on as part of the R'nM team. I would also like to thank Marli for listening to me rant about physics and for a friendship that has stood the test of time and distance, and Nicole for her lasting friendship across the seas.

I would like to thank the Marsh and Billinge families for welcoming me into your lives so graciously. Finally, I would like to thank Doddy for helping me enjoy my final year in Oxford and for providing me with countless hours of support, encouragement and love. My life and work are richer for knowing you.

CONTENTS

1

INTRODUCTION

1.1 THE COSMOLOGICAL MODEL

Cosmology has undergone a data revolution in the past 20 years. Once a data-starved field where one had only intuition to guide new models and theories, it is now rich in data from observations made at many wavelengths; from measurements of the light coming from the birth of the universe to late-time measurements of exploding stars. These data help us test and refine our cosmological model, and open up new areas of research and study. In the current concordance cosmological model, the universe began 13.7 billion years ago in a hot dense state known as the big bang. Small fluctuations in the density of the early universe seeded the structures we see today. A period of rapid expansion, known generically as inflation, increased the size of the universe by many orders of magnitude in a short time, resulting in the very nearly flat universe we observe. The universe is well described by relatively few cosmological parameters, and yet our cosmological model is far from complete, and there are outstanding questions that have yet to be answered. Dark matter, while being evident through its gravitational effects, still needs to be classified. Dark energy, believed to be responsible for the apparent acceleration of the universe, remains an enigma and understanding its origin and nature is one of the great unsolved mysteries of contemporary cosmology. In addition, while inflation predicts many features observed in the cosmic microwave background (CMB), the details of which inflationary scenario is correct (and indeed whether or not the inflationary picture is an accurate description of early universe physics) remains unknown. In this chapter we will describe the cosmological model and the current observational status of the field.

1.1.1 Friedmann-Lemaître-Robertson-Walker Cosmology

Modern cosmological observations are generally presented in the context of the homogeneous and isotropic Friedmann-Lemaître-Robertson-Walker (FLRW) solution [1–4] of Einstein's equations in General Relativity[1] [6]. The metric in this solution is represented by the line element

$$ds^2 = -c^2 dt^2 + a^2(t)\gamma_{ij} dx^i dx^j, \tag{1.1}$$

where γ_{ij} is the metric with constant curvature k, or

$$\gamma_{ij} dx^i dx^j = \frac{dr^2}{1-kr^2} + r^2(d\theta^2 + \sin^2\theta d\phi^2). \tag{1.2}$$

The parameter t is proper time and $a(t)$. Alternatively it can be expressed in terms of the comoving distance

$$\chi = \int_{t_e}^{t} c \frac{dt'}{a(t')} \tag{1.3}$$

where the relationship between the comoving distance χ and the coordinate distance r is

$$r = \frac{1}{\sqrt{k}} \sin(\sqrt{k}\chi). \tag{1.4}$$

The spatial part of the line element Eq. (1.1) is then expressed as

$$\gamma_{ij} dx^i dx^j = d\chi^2 + \sin^2\chi(d\theta^2 + \sin^2\theta d\phi^2). \tag{1.5}$$

Note that from here on we work in natural units in which the speed of light $c = 1$. Also, in this notation $a(t_0) = a_0 = 1$ today when the radius of curvature was $R = \sqrt{k}^{-1}$; at other times the radius of curvature of the universe is given by $a(t)R$. In addition $\sin(ix) = i\sinh(x)$; hence the Eq. (1.4) is valid for all values of curvature. In such a negatively curved universe (which would resemble a saddle), objects appear further

---

[1] The study of inhomogeneous cosmologies is a large and growing field (see Clifton et al. [5] for a recent review), but we shall not discuss it in any detail in this work.

away than they really are. In a positively curved universe (such as a sphere) the opposite is true. Figure 1.1 illustrates universes with different values of curvature. General relativity allows us to connect the curvature of the universe to its energy

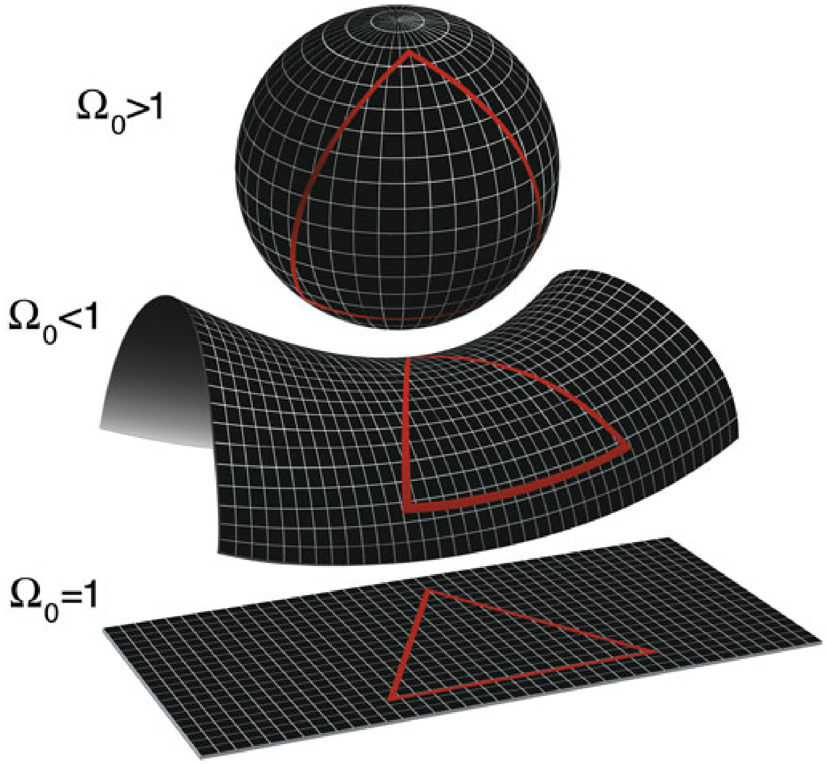

Figure 1.1 The geometry of a two-dimensional universe: a closed, positively curved universe (top, $k = 1$) is of finite size and angles in a triangle drawn on this surface add up to more than 180 degrees - travelling far enough in one direction would lead one back to one's starting point. Also illustrated in the middle panel is the saddle, or negatively curved ($k = -1$) universe, and the flat universe (bottom). Image credit: NASA / WMAP Science Team.

content. The Einstein equations:

$$G_{\mu\nu} \equiv R_{\mu\nu} - \frac{1}{2} g_{\mu\nu} R = 8\pi G T_{\mu\nu} + g_{\mu\nu}\Lambda \tag{1.6}$$

relate the Einstein tensor, $G_{\mu\nu}$, to the Ricci tensor, $R_{\mu\nu}$ (itself a function of the metric $g_{\mu\nu}$ and its derivatives); its contraction, the Ricci scalar $R = g^{\mu\nu} R_{\mu\nu}$; and the energy-momentum tensor $T_{\mu\nu}$, where $G = 6.673 \times 10^{-11}$ m^3 kg^{-1} s^{-2} is Newton's gravitational constant, and Λ is the cosmological constant. This relationship is often summarised in the saying "Matter tells space how to curve, space tells matter how to move". In the case of a perfect fluid, the energy-momentum tensor is expressed in terms of its pressure P and density ρ as

$$T^{\mu}_{\nu} = diag(-\rho, P, P, P). \tag{1.7}$$

The time-only (00) part of the Einstein equations yields the Friedmann equation,

$$\left(\frac{\dot{a}}{a}\right)^2 = \frac{8\pi G\rho}{3} - \frac{k}{a^2} + \frac{\Lambda}{3}. \tag{1.8}$$

The spatial component leads to the Raychaudhuri equation:

$$\frac{\ddot{a}}{a} = -\frac{4\pi G}{3}(\rho + 3p) + \frac{\Lambda}{3}, \tag{1.9}$$

where the term $3p$ comes from the trace of the spatial components of the energy-momentum tensor given in Eq. (1.7).

We can express Eq. (1.8) instead in terms of the Hubble parameter $H(a) = \dot{a}/a$, as

$$H^2(a) = \frac{8\pi G}{3}\left(\rho_m + \rho_\gamma + \rho_K + \rho_\Lambda\right), \tag{1.10}$$

where the energy density of curvature is $\rho_K = -3k^2/8\pi G a^2$, the energy density of the vacuum energy is $\rho_\Lambda = \Lambda/8\pi G$, and we have expressed the energy density ρ of Equation (1.10) explicitly as a sum of the energy components in matter (m) and radiation (γ). It is useful to define the critical density $\rho_c(a) = 3H^2(a)/8\pi G$ as the energy density of a flat universe, which today has a value around 10^{-29} g cm^{-3}. The energy densities of the other components can then be expressed in terms of this critical density as the *density parameter* $\Omega_i(a) = \rho_i(a)/\rho_c$. Note that while in general the density parameter is a function of the scale factor (and therefore time), if this dependence is not made explicit, then the value Ω_i is taken as the value today, at $a = 1$.

Finally, the continuity equation is given as

$$\frac{\dot{\rho}}{\rho} = -3H(1 + w) \tag{1.11}$$

where the equation of state of the fluid is $w = p/\rho$. For constant values of w we can integrate the equation to get the evolution of the fluid density as a function of time. In the multi-component universe described above, the equation of state of each fluid component is distinct, with $w = 0$ for the dust (matter) component, $w = 1/3$ for radiation, $w = -1/3$ for curvature and $w = -1$ for a cosmological constant. The fact that the various components vary differently with scale factor means that they will dominate the total energy budget of the universe at different times. It is worth noting that curvature influences the background equations in more ways that the other components - as it directed affects the geodesics, and therefore the distance measures defined in a FLRW universe, whereas the other components only enter the background equations through the Friedmann equation, Eq. 1.10.

The *redshift* of an object can be determined observationally by measuring the difference between the observed wavelength λ_o of a photon relative to its emitted wavelength λ_e,

$$z = \frac{\lambda_o - \lambda_e}{\lambda_e}. \tag{1.12}$$

We can relate the change in wavelength of an object due to the expansion of space through

$$\lambda_o = \frac{a(t_o)}{a(t_e)}\lambda_e \tag{1.13}$$

and hence obtain the redshift of an object observed today (i.e. $t_o = t_0$) in terms of the scale factor:

$$\frac{a_e}{a_0} = \frac{1}{(1+z)} \tag{1.14}$$

where $a_0 = a(t_0)$ is the radius of curvature of the universe today, and again we see that the model is scaled so that $a_0 = 1$ in a flat universe. We also define conformal time

$$\eta(t) = \int \frac{dt}{a} \tag{1.15}$$

which is a co-ordinate independent measure of time as it contains the scale factor, which defines the rate of expansion of space.

1.1.2 Cosmic Components

The universe consists of multiple components, each of which behave differently with redshift, as we can see from Eq. (1.11). A schematic plot of the densities of the principal components are shown in Figure 1.2. The early universe was dominated by radiation, with the relative amounts of the two quantities scaling as

$\rho_\gamma/\rho_m = \Omega_\gamma/\Omega_m a^{-1} \simeq \Omega_\gamma/\Omega_m(1+z)$. Given the critical densities of matter and radiation today, the redshift at which the two quantities are equal is $z \simeq 3200$ [7]. This occurs before the decoupling of photons and electrons, which happens at a redshift of around $z \simeq 1100$. In the standard picture, the universe remains in an epoch of matter domination until late times $z \simeq 0.7$, after which time the vacuum energy dominates over the matter density. The total matter component can be broken down further

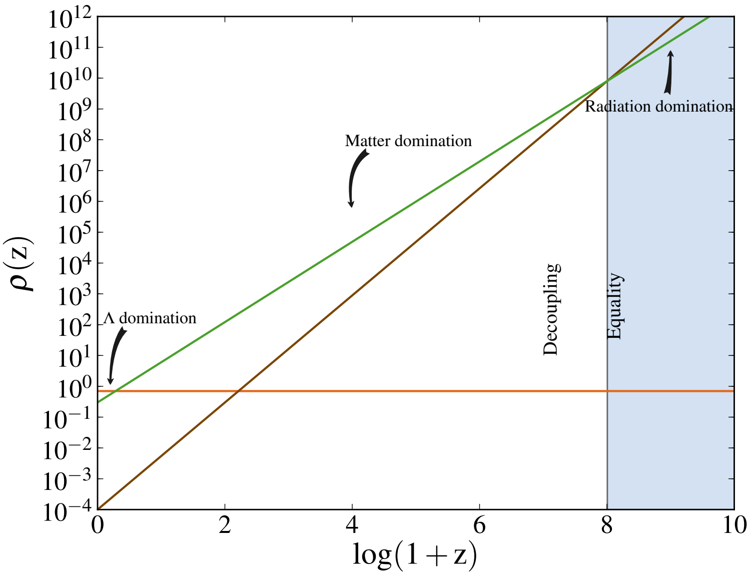

Figure 1.2 The densities of the components of the universe are shown as a function of redshift for matter, radiation and a cosmological constant. The energy densities of these three components scale differently with redshift, resulting in epochs when the various components dominate the energy budget of the universe, indicated by arrows.

into a baryonic contribution, expressed as Ω_b, and a non-baryonic component, *dark matter*, characterised by its density Ω_c. While they make up all the visible matter we see today, baryons make up only a small fraction of the total energy budget of the universe, around 5%, with the largest component of the matter content described as this dark matter.

In addition to a cold dark matter component, we include neutrinos in the cosmic components. In the standard scenario, there are three species[2] of these weakly

---

[2] As we shall see later, the effective number of species is slightly larger than three even in the standard scenario due to heating caused by the fact that neutrinos are slightly coupled in the early universe.

interacting particles, all of which have negligible mass and contribute to the relativistic energy density in the early universe. While precision electroweak measurements place tight constraints on the number of neutrino species [8], neutrinos change the expansion rate of the universe through their energy density (see Tegmark [9], Lesgourgues and Pastor [10] and Hannestad [11] for reviews of neutrinos in cosmology), and affect the perturbations in the early universe [12]. The energy density of neutrinos is lower than that of photons by a factor $\rho_\nu = N_{eff} 7/8(4/11)^{4/3}\rho_\gamma$, where N_{eff} is a parameter constrained by observations and is 3.04 in the standard concordance model. The neutrino temperature is also lower by a factor of $(4/11)^{4/3}$ relative to photons. This will have implications for how they affect the expansion rate in the early universe; in the following sections we will discuss the impact of this on the CMB at small scales (see Hou et al. [13] for a concise recent review, and the more complete discussions in Bashinsky and Seljak [12], Hu and Dodelson [14], Hu et al. [15]).

Finally, *dark energy* (a phrase first coined by Michael Turner in 1998 [16]), in its simplest form is parameterised by the cosmological constant, Λ, with constant equation of state $w = -1$. Independent measurements of the CMB, Type Ia supernovae, galaxy clusters and baryon acoustic oscillations (BAO) constrain the amount of the total energy contained in this dark component to be $\Omega_\Lambda = 0.734 \pm 0.029$ [7].

1.1.3 *The Cosmology of the Early Universe*

The concordance model is that the universe started 13.7 billion years ago in a hot dense state, with quantum fluctuations in the early universe seeding the large-scale structures that we see today. We will not focus much attention on the very first moments in the lifetime of the universe, other than to discuss ways in which the initial conditions are imprinted in the early universe shortly after the big bang.

In the hot, dense, plasma phase of the early universe the photons and electrons interacted via Thomson scattering, resulting in a small mean-free path of the photons. The optical depth in conformal time is

$$\tau(\eta) = \int_{\eta}^{\eta_0} a n_e \sigma_T d\eta', \tag{1.16}$$

where n_e is the electron density and σ_T is the Thomson scattering cross-section. During this time, the photon mean-free path is short compared to the expansion of the universe, and hence the universe is opaque. Once the universe cools to below a few MeV, the protons and neutrons can no longer remain in chemical equilibrium, they decouple and their ratios 'freeze out'. Before freeze-out, the protons and neutrons were kept in equilibrium by the weak interactions:

$$n + \nu \leftrightarrow p + e^-, n + e^+ \leftrightarrow p + \bar{\nu}. \tag{1.17}$$

After the process of $e^\pm$ annihilation, electrons recombine with protons to form hydrogen, and then the other light elements. Big bang nucleosynthesis (BBN) is extremely sensitive to the expansion rate of the universe at early times, since the temperature and expansion rate are closely linked. This could be modified from the standard case by having 'extra' relativistic species which can be thought of as effectively adding in more radiation to the early universe. Just before $e^\pm$ annihilation, the energy density was given by

$$\rho_R = \rho_\gamma + N_{eff}\rho_\nu + \rho_e, \tag{1.18}$$

where $N_{eff} = 3$ indicates three species of neutrinos. In actual fact, while there are three species of neutrinos, the *effective* number of species is modified by heating of the neutrinos, since they are not exactly decoupled at early times, changing the value of N_{eff} to 3.046 even in the standard BBN scenario [17–24]. If one expresses the change in energy density from standard concordance as $\rho'_R = \rho_R + \Delta N_{eff}\rho_\nu; \;\; \Delta N_{eff} = N_{eff} - 3$, then the change to the expansion rate can be expressed as [25]

$$\left(\frac{H'}{H}\right)^2 = \frac{\rho'_R}{\rho_R} = 1 + \frac{7\Delta N_{eff}}{43}. \tag{1.19}$$

Alternatively, one could modify nucleosynthesis by changing the baryon to photon ratio, $\eta_B = (n_B/n_\gamma) = 10^{-10}\eta_{10}$, which in turn affects Y_P, the amount of primordial helium in the universe, a relationship which has been fitted with a simple linear mapping [26],

$$Y_P = 0.2384 + \eta_{10}/625. \tag{1.20}$$

An increase in the amount of helium atoms in the early universe will effectively remove electrons from the plasma, and hence increase the mean free path of the photons, damping oscillations in the fluid. A non-negligible component of dark energy in the early universe would also alter the expansion rate at early times, changing the abundances of primordial elements and affecting the CMB.

After decoupling, the photons that were once bound to the electrons through Thomson scattering free-stream away rapidly. These are the photons we detect today as the CMB, their wavelengths stretched as they travel towards us. The CMB is extremely well described by a thermal blackbody as a function of frequency, and is uniquely defined by its temperature. This has been measured as $T_{CMB} = 2.72548 \ \pm 0.00057$K (95% CL) [27]. This implies that the universe must have been in causal contact at the time the photons left the surface of last scattering, when the universe was at a temperature of roughly 3000K. The CMB is remarkably uniform on the sky, with fluctuations in temperature of only 1 part in 100 000. In terms of scales more common to everyday life, this ratio is roughly the same as the ratio between the height of a wave and the diameter of the earth. The particle horizon at the time of last scattering was around one degree, which leads to a problem known as the horizon problem: assuming only FLRW expansion, the universe could not have been causally connected at the time the CMB photons were emitted. This problem can be overcome if the universe was in fact much smaller at early times. In addition to the uniformity of the CMB, measurements of the statistics of the CMB (which will be derived in the following section) imply that the universe is approximately flat. Again, in the FLRW context, there is no reason *a priori* why we expect the universe to be flat. In fact, given that the curvature of the universe scales as $(1+z)^{-2}$, if the constraint today is that the amount of curvature is around 1%, this would have to be less than 10^{-8} at the time of recombination or 10^{-15} at BBN, an idea first discussed by Dicke and Peebles [28].

1.1.4 *Inflation*

The so-called *horizon* and *flatness* problems can be solved if the universe underwent a period of rapid expansion. This term is generically known as *inflation*, and was first proposed by Alan Guth [29] and Alexei Starobinsky [30]. A simple calculation illustrates how inflation solves the flatness problem [31]. Given that the curvature of the universe scales as $\Omega_k = k/a^2H^2$, Ω_k will tend to zero as aH grows. In order for this to happen, we need to have an accelerating universe, or $d/dt(1/aH) < 0$. Given the definition for H, this occurs for $w < -1/3$. In the case of a scalar field, $w \simeq -1$, and $a \propto \exp Ht$, which is exponential growth in the scale factor of the universe.

A period of rapid inflation solves not only the flatness problem as described above, it also addresses the horizon problem. In the inflationary context, the uniformity of the universe is created initially thermally on microscopic scales, with the subsequent inflationary phase stretching those scales to roughly the size of the universe today. The same mechanism inflationary scenario also seeds the quantum mechanical *anisotropies* present in the early universe that eventually give rise to the structures we see today. Let us consider inflation occurring due to a canonical single scalar field $\phi(\boldsymbol{x}, t)$, fully specifiied by its potential $V(\phi)$ with a Lagrangian $\mathcal{L} = \frac{1}{2}(\partial\phi)^2 - V(\phi)$. The ratio of the pressure to the density of this field is

$$\frac{p}{\rho} = \frac{\dot{\phi}^2/2 - V(\phi)}{\dot{\phi}^2/2 + V(\phi)} \tag{1.21}$$

which is negative if the field is potential dominated, or $\dot{\phi} \ll V(\phi)$.

In an expanding universe, the equations of motion for the scalar field are given by:

$$\ddot{\phi} + 3H\dot{\phi} + \partial_\phi V = 0 \tag{1.22}$$

assuming for the time being that the field is only very slowly varying as a function of space, and hence is homogeneous. In the case of *slow-roll*, the field (and hence the Hubble rate) vary slowly, and so the second derivative of the field ϕ can be ignored. The slow-roll conditions are expressed in terms of the potential of the field as:

$$\epsilon_{sr} = \frac{M_{pl}^2}{2}\left(\frac{\partial_\phi V}{V}\right)^2; \qquad \eta_{sr} = M_{pl}^2 \frac{\partial_{\phi\phi} V}{V}, \tag{1.23}$$

where $M_{pl} = m_{pl}/\sqrt{8\pi}$ is the reduced Planck mass and the subscript is to distinguish the slow-roll parameter η_{sr} from the conformal time η. Slow-roll inflation occurs only if both parameters are typically very small, of order 10^{-2}. If these conditions are satisfied, the background evolution is then given by $H^2 \approx V(\phi)/3M_{pl}^2$, which is constant, and $\dot{\phi} = -\partial_\phi V/3H$.

While the field ϕ is smooth on average (and hence we can solve Eq. (1.22) for the motion of the field), we need to consider the perturbations in the field, or $\phi(\boldsymbol{x}, t) = \phi^0(t) + \delta\phi(\boldsymbol{x}, t)$. We restrict ourselves to the case of scalar perturbations.

1.1.5 *Primordial Power Spectra*

Continuing to work under slow-roll, we take a Fourier transform of the perturbations in ϕ:

$$\delta\phi(\boldsymbol{k}, t) = \int d\boldsymbol{k} e^{i\boldsymbol{k}\boldsymbol{x}} \delta\phi(\boldsymbol{x}, t). \tag{1.24}$$

The evolution equation for the perturbations then becomes

$$\ddot{\delta\phi} + 3H\dot{\delta\phi} + \delta\phi \frac{k^2}{a^2H^2} = 0. \tag{1.25}$$

A crucial statistical measure of the primordial scalar fluctuations is the power spectrum of the comoving curvature perturbation, $\mathcal{R}$, defined as

$$\langle \mathcal{R}_{\boldsymbol{k}} \mathcal{R}^*_{\boldsymbol{k}'} \rangle = (2\pi)^3 \delta(\boldsymbol{k} - \boldsymbol{k}') \mathcal{P}_{\mathcal{R}}(k) \tag{1.26}$$

Geometrically, one can think of $\mathcal{R}$ as measuring the spatial curvature of comoving hypersurfaces. We then define the primordial power spectrum as [32]:

$$\mathcal{P}(k) \equiv \Delta^2_{\mathcal{R}}(k) = \frac{k^3}{2\pi^2} \mathcal{P}_{\mathcal{R}}(k) \tag{1.27}$$

The spectrum is often approximated by a power law (around some pivot scale k_0), with an amplitude $A_s \simeq 2.4 \times 10^{-9}$ [33] and a spectral index (or tilt) of the power spectrum, n_s as:

$$\mathcal{P}(k) = A_s(k_0) \left(\frac{k}{k_0}\right)^{n_s - 1}. \tag{1.28}$$

Hence we have the relation

$$n_s - 1 = \frac{d \ln \mathcal{P}(k)}{d \ln k}. \tag{1.29}$$

A *scale invariant* spectrum is one for which the derivative is zero and hence for which $n_s = 1$. One can also parameterise deviation from a power-law spectrum in terms of an index that depends on scale k, the so-called running of the spectral index, $dn_s/d\ln k$, modifying Equation (1.28) as

$$\mathcal{P}(k) = A_s(k_0) \left(\frac{k}{k_0}\right)^{n_s - 1 + \frac{1}{2}(dn_s/d\ln k)\ln(k/k_0)} \tag{1.30}$$

Perturbations in the curvature $\mathcal{R}$ are related to perturbations in the inflaton field ϕ through

$$\langle \mathcal{R}_{\boldsymbol{k}} \mathcal{R}^*_{\boldsymbol{k}'} \rangle = \left(\frac{H}{\dot{\phi}} \right)^2 \langle \delta\phi(\boldsymbol{k}, t) \delta\phi^*(\boldsymbol{k}', t) \rangle. \tag{1.31}$$

Under slow-roll the Gaussian fluctuations in the inflaton scale with the Hubble parameter:

$$\langle \delta\phi(\boldsymbol{k}, t) \delta\phi^*(\boldsymbol{k}', t) \rangle = (2\pi)^3 \delta(\boldsymbol{k} - \boldsymbol{k}') \frac{(2\pi)^2}{k^3} \Delta^2_\phi(k)\,; \;\; \Delta^2_\phi(k) = \left(\frac{H}{2\pi} \right)^2. \tag{1.32}$$

We can relate the spectrum of scalar perturbations $\mathcal{P}(k)$ to the spectrum of perturbations in ϕ through $\mathcal{R}_k = (H/\dot{\phi})\delta\phi_k$ (assuming the de Sitter solution on superhozion scales), where we evaluate the power spectrum at horizon crossing, where $k = a(t_*)H(t_*)$:

$$\mathcal{P}(k) = \Delta^2_{\mathcal{R}}(k) = \left(\frac{H}{\dot{\phi}} \right)^2 \Delta^2_\phi(k) = \frac{H^2(t_*)}{(2\pi)^2} \frac{H^2(t_*)}{\dot{\phi}}. \tag{1.33}$$

Given that the curvature perturbation $\mathcal{R}$ approaches a constant on super-horizon scales, the spectrum at horizon crossing specifies the power spectrum fully until a given fluctuation mode re-enters the horizon. In addition, in quasi de Sitter space (where the potential is slowly varying and $H \simeq$ const.) this solution is still valid, as different k modes will enter the horizon at different times when $a(t_*)H(t_*)$ has a slightly different value - which is the case for slow-roll inflation.

1.1.6 Dark Energy

The cosmological constant introduced in Equation (1.6) is the simplest way to parameterise a fluid driving the observed late-time acceleration of the universe. The defining property of the cosmological constant is that its density remains constant even as the universe expands. This strange property is the reason why the cosmological constant cannot be anything currently known (assuming again that it is not an artifact of an incorrect description of gravity, such as those suggested in models where Einstein gravity is modified on large scales; see Clifton et al. [5] for a recent review). The simplest suggestion for dark energy is an energy density inherent in the vacuum, the aptly named vacuum energy, which is an idea which is by no means 'new' [34–37] (see Ishak [38], Frieman [39], Carroll [40] for pedagogical reviews on dark energy, vacuum energy and the accelerating universe). However, this simple solution fails to correctly explain the size of the observed energy density of the cosmological constant. Combined measurements from different independent observations constrain the value of the cosmological constant to be around $\rho_{\rm vac} \simeq 2 \times 10^{-10}$ erg cm^{-3} [7, 41–45], which is between 60 to 120 orders of magnitude smaller than the expected contribution (the values vary depending on the cut-off scale of the particular quantum field theory underlying the vacuum energy).

Perhaps even more strangely, it seems that the universe has only started accelerating relatively recently, on timescales similar to the timescale of the formation of the solar system. Given that the attractor solution to a set of dynamical equations with an accelerating phase would be a dark energy dominated universe, one might ask why we appear to live at a special time when there was enough dark energy to have observational consequences, but not too much so as to make structure formation impossible. This interesting problem is not one addressed in this thesis, but remains one of the unsolved challenges in dark energy studies. A plethora of theories other than the cosmological constant have been suggested to describe dark energy, including modelling the component as a scalar field. Without any clear theoretical favourite, general phenomenology is used observationally to try and distinguish between models using the equation of state w, and in particular to look for dynamical behaviour of the equation of state with redshift, or $w = w(z)$. This is often tested within a few different empirical frameworks (e.g. Chevallier and Polarski [46], Linder [47], Weller and Albrecht [48], Bassett et al. [49], Corasaniti et al. [50]). While theoretical completeness and motivation are required for any viable alternative to the cosmological constant, a significant detection of dark energy dynamics would narrow the allowed region of models significantly, making the estimation of the value of $w(z)$ a key research area in contemporary cosmology.

1.2 COSMIC MICROWAVE BACKGROUND

1.2.1 *Density Perturbations and CMB anisotropies*

While the CMB sky is a remarkably uniform blackbody (with a temperature of 2.72548K as mentioned in the previous section), measuring the anisotropies in the CMB gives us valuable insight into early universe physics. In this section we will use the notation of Wayne Hu's excellent pedagogical review [51], which has provided many a grad student with the insight to understand the physics of the CMB. We now review the phenomenology of the cosmic microwave background.

The temperature anisotropies are described in terms of temperature perturbations around a mean on the sky, $\Theta(\hat{\mathbf{n}}) = \Delta T/T(\hat{\mathrm{n}})$. The temperature fluctuations we observe on the sky result from spatial fluctuations on the surface of last scattering and so we can decompose the temperature field into spherical harmonics,

$$\Theta(\hat{\mathbf{n}}) = \sum_{\ell=0}^{\infty} \sum_{m=-\ell}^{\ell} a_{\ell m} Y_{\ell m}(\hat{\mathbf{n}}), \tag{1.34}$$

where the complex function $Y_{\ell m}(\hat{\mathbf{n}}) = Y_{\ell m}(\theta, \varphi) = \sqrt{\frac{2\ell_1(\ell-m)!}{4\pi(\ell+m)!}} e^{im\varphi} P_m^\ell(\cos\theta)$ is related to the Legendre polynomial $P_m^\ell(\cos\theta)$. This decomposition into spherical harmonic waves is complete (because the $Y_{\ell m}$ form an orthogonal basis set) and so this decomposition accurately describes the fluctuations on the sky. The expansion coefficients are then given by

$$a_{\ell m} = \int_{4\pi} \Theta(\hat{\mathbf{n}}) Y^*_{\ell m}(\hat{\mathbf{n}}) d\Omega, \tag{1.35}$$

where the $d\Omega$ is the spherical volume element of the sphere. This can be related to the real space correlation of the temperature between two regions on the sky as:

$$\langle \Theta(\hat{\mathbf{n}}) \Theta(\hat{\mathbf{n}}') \rangle = \frac{1}{4\pi} \sum_{\ell=0}^{\infty} (2\ell+1) C_\ell P_\ell(\cos\theta), \tag{1.36}$$

where $\hat{\mathbf{n}} \cdot \hat{\mathbf{n}}' = \cos\theta$. The relationship between the angle θ on the sky and the Fourier mode, ℓ, is $\theta \simeq 200^\circ/\ell$. Assuming that the fluctuations are Gaussian[3], all the information about the field is described by the two point statistic of the field or power

---

[3] This assumption is currently being tested by a large number of groups as any primordial non-Gaussianity will be a powerful test of inflationary theory, however we assume Gaussian fluctuations here.

spectrum, C_ℓ given by the coefficients

$$C_\ell = \frac{1}{(2\ell+1)} \sum_{m=-\ell}^{\ell} \langle |a_{\ell m}|^2 \rangle. \tag{1.37}$$

The number of measurements possible in the sum of Eq. (1.37) is a function of the scale considered. Each mode ℓ there are $2\ell+1$ parts in the sum over m above, and therefore there is a *cosmic variance* error associated with each C_ℓ, which quantifies the observational limit in even perfect observing conditions. This is given by

$$\Delta C_\ell = \sqrt{\frac{2}{f_{sky}(2\ell+1)}} C_\ell, \tag{1.38}$$

where the fraction f_{sky} parameterises the amount of sky available to make the measurements - the more area on the sky one can observe, the smaller the errorbar on the measurement of the C_ℓ.

An observer today sees the anisotropies as they appeared on a shell at the last scattering surface: $\boldsymbol{x} = D_{lss}\hat{\mathbf{n}}$, where D_{lss} is the comoving distance to recombination. The observed anisotropy is expressed in Fourier space as [14]:

$$\Theta(\hat{\mathbf{n}}, \eta_0) = 4\pi \sum_{\ell m} Y_{\ell m}(\hat{\mathbf{n}}) \left[(-i)^\ell \int \frac{d^3k}{(2\pi)^3} \Theta_\ell(k, \eta_0) Y^*_{\ell m}(\hat{\boldsymbol{k}}) \right], \tag{1.39}$$

where $\Theta_\ell(k, \eta_0) = \int_0^{\eta_0} d\eta S(k, \eta) j_\ell(kD_{\mathrm{lss}})$ is transfer function, $S(k, \eta)$ is the source term and $j_\ell(kD_{\mathrm{lss}})$ is the spherical Bessel function which projects three-dimensional Fourier $(\mathbf{k})$ space into two-dimensional spherical Fourier (ℓ) space. The transfer function therefore maps an initial perturbation of a mode k to the angular power at a spherical scale ℓ at recombination. The key idea behind this integral approach is that the source term $S(k, \eta)$ does not depend on the spherical decomposition, while the Bessel function does not depend on cosmology. Finally then, the power spectrum can be expressed in spherical harmonics over the full sky as

$$C_\ell = \frac{2}{\pi} \int \frac{dk}{k} \mathcal{P}(k) |\Theta_\ell(k, \eta_0)|^2. \tag{1.40}$$

This clearly shows how the power spectrum of fluctuations on the sky is related to the primordial power spectrum of fluctuations given in Equation (1.27). We also note that the fluctuations in the angular power spectrum are driven by what affects the transfer function, or $|\Theta_\ell(k, \eta_0)|^2$, term. Under the assumptions that $\mathcal{P}(k)$ is scale invariant, the power spectrum would also be scale invariant if the $|\Theta_\ell(k,\eta_0)|^2$ had no structure to it. Thus the 'wiggles' we see in the CMB are purely due to the effects of the photon-baryon fluid and its interactions, and are not from primordial fluctuations. The types of scale-dependent effects we see in the CMB are related to what contributes to the $|\Theta_\ell(k,\eta_0)|^2$ term.

The contributions to the total temperature anisotropies are chiefly from density fluctuations in the photons, the gravitational potential and the Doppler shift due to the bulk velocity $\mathbf{v_b}$ of the photon-baryon fluid. In this case (and assuming for the moment tight coupling which means that there is no Silk damping) [52–54]:

$$\Theta \propto \frac{\delta_\gamma}{4} + \Phi + \hat{\mathrm{n}} \cdot \mathbf{v_b} \bigg|_{\eta_{rec}} \tag{1.41}$$

where we solve for the power spectrum at recombination. Given that the density of photons goes like $\rho_\gamma \propto T^4$, we see that the photon perturbations scale as $\delta_\gamma/4$. The cancellation of the first two terms leads to the so called Sachs-Wolfe term of $\Theta = \Phi/3$, which dominates the power of the CMB on large angular scales.

In Fourier space, temperature perturbations obey $\dot{\Theta} = 1/3kv_\gamma$, where the photon velocity v_γ is written as the projection of the velocity along the line of sight (a scalar), as this projection is the component which acts against gravity in the coupled system. The factor of a third is due to conservation of photon number, where $n_\gamma \propto T^3$. The Euler equation for the fluid conserves photon momentum, and is

$$\dot{v}_\gamma = k\Theta. \tag{1.42}$$

Combining the two leads to a second-order differential equation for Θ:

$$\ddot{\Theta} + c_s^2 k^2 \Theta = 0, \tag{1.43}$$

where we have defined $c_s \equiv \sqrt{\dot{p}/\dot{\rho}} = 1\sqrt{3}$ as the sound speed of the fluid.

Ignoring for simplicity the velocity terms in Eq. (1.41) leads to an oscillating solution $\Theta \propto A\cos(k\eta_{rec}c_s) + B$, where A and $B \neq 0$ are numerical coefficients, and $\eta_{rec}c_s$ is the distance sound can travel by recombination, usually referred to as the sound horizon.

There is a balance between photon radiation pressure and gravitational driving - the photons balance out the drag of gravity with radiation. This leads to the 'bumps' in the temperature power spectrum, as $C_\ell \propto \Theta_\ell^2$. The height difference between the odd and even peaks is due to the fact that the solution does not oscillate around zero but around a constant B, and this value is controlled by the baryon density $\Omega_b h^2$. This simple solution does not of course reflect all the different effects on the CMB, but gives an understanding of the underlying structure of the anisotropy spectrum. The additional effects can be included by modifying the contributions to the differential equation for Θ.

One such effect is the tight coupling approximation. Until now we have also assumed tight coupling; that the mean free path of the photons was small relative to the physical scale of the fluctuations in temperature. For small scales this is no longer the case, and the temperature power spectrum is damped. During photon-baryon coupling the photons travel according to a 'random walk' of distance determined by the Thomson scattering cross-section, the number of electrons (which is proportional to the baryon number density) and the ionisation fraction through

$$\mu(\eta) = \int_{\eta_0}^{\eta} a(\eta') x_e n_e \sigma_T d\eta', \tag{1.44}$$

where the scale factor a and the conformal time are related by $\eta(t) = \int dt/a$. The Silk damping scale [55] is the scale corresponding to this mean free path, which for a random walk (and assuming only standard processes in the early universe) is given as [53]:

$$x_s = 0.6\Omega_m^{1/4}\Omega_b^{-1/2}a_{rec}^{3/4}h^{-1/2}. \tag{1.45}$$

The primordial parameters that affect the damping tail are ones also constrained by the other peaks, and so the damping tail provides a consistency check of the physics at recombination. Anything that changes the amount of relativistic energy density at early times will change the amount of damping present on small scales (in addition to affecting the perturbations in the early universe, which we will discuss in the next section). One way to modify the amount of relativistic energy density is by changing the effective number of neutrino species, N_{eff}. As discussed above, this changes the relativistic energy density as $\rho_\nu = N_{eff} 7/8(4/11)^{4/3}\rho_\gamma$, 'adding more' energy for increasing N_{eff}, which will lead to a higher level of damping on small scales. It is on precisely these scales where the Atacama Cosmology Telescope (ACT) has great statistical power, and we shall see in Chapter 3 how these parameters are constrained using ACT data.

We now discuss further the influence of cosmological parameters on the form of the power spectrum.

1.2.2 *Influence of Ccosmological Parameters*

The very simple form presented in the previous section does not include all contributions to the temperature fluctuations, but shows how the oscillations are set up in the fluid. As we already mentioned, the baryon density changes the height difference between the odd and even peaks, in that if there are more baryons, the 'load' is deeper, and so the compressions in the fluid are stronger. This increases the odd (first, third etc.) peaks relative to the even peaks.

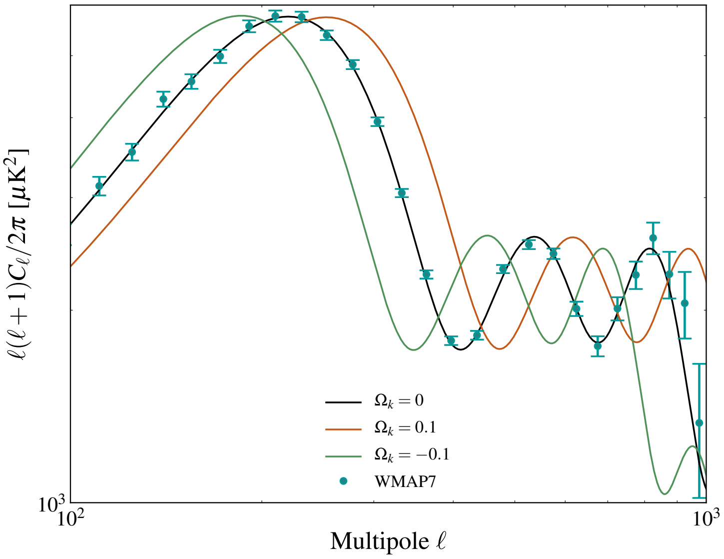

Figure 1.3 The geometry of the universe affects the cosmic microwave background: the first peak shifts to the right in an open universe, and to the left in a closed universe. Data from the WMAP satellite [7, 33, 56, 57] are plotted to illustrate how current data favour a flat geometry of the universe.

The geometry of the universe is measured by the position of the first peak, under the assumption of a power-law power spectrum. In a negatively curved universe (i.e. $\Omega_k > 0$ since the sum of the density parameters of the other components is less than unity) the peaks are shifted to the right, while the opposite is true for a closed universe ($\Omega_k < 0$), as is shown in Figure 1.3. This shift is because for an open universe, an object of the same intrinsic physical size (the CMB fluctuation) appears smaller, and vice versa for a closed universe.

There is a degeneracy between the curvature of the universe and the value of the Hubble constant [7, 33, 56]. While the CMB is almost 'blind' to this degeneracy, it is resolved when considering independent priors on the value of the Hubble constant [58]. As we will discuss in Chapter 4, this is also an important consideration when allowing for a general primordial power spectrum. In addition to its position, the height of the first peak is also controlled by the dark matter content, $\Omega_c h^2$, in that increasing the dark matter content (relative to a fixed baryon content) decreases the height of the first peak. This can be understood in terms of the radiation driving the oscillations. Changing the amount of matter changes when recombination happens, and thus changes the amount of radiation pressure (or rather the length of time that radiation was driving the oscillations). The larger the matter content, the earlier equality happens and hence less radiation driving occurs; thereby decreasing the peak height.

The small-scale CMB power spectrum is particularly sensitive to things which alter the amount of relativistic energy density at early times, as this will affect the Silk damping scale, as introduced earlier. In addition to changing the expansion rate, 'extra' effective relativistic species change not only the background expansion, but also affect the perturbations in the early universe. As suggested by the name 'relativistic', the neutrinos are almost entirely decoupled in the early universe and begin to free-stream at much higher redshifts than the redshift of photon-baryon decoupling. Neutrinos can stream out of overdensities in all directions and hence neutrino perturbations are damped on subhorizon scales. Moreover they introduce anisotropic stress (off-diagonal components in the stress-energy tensor), sourcing metric perturbations - a

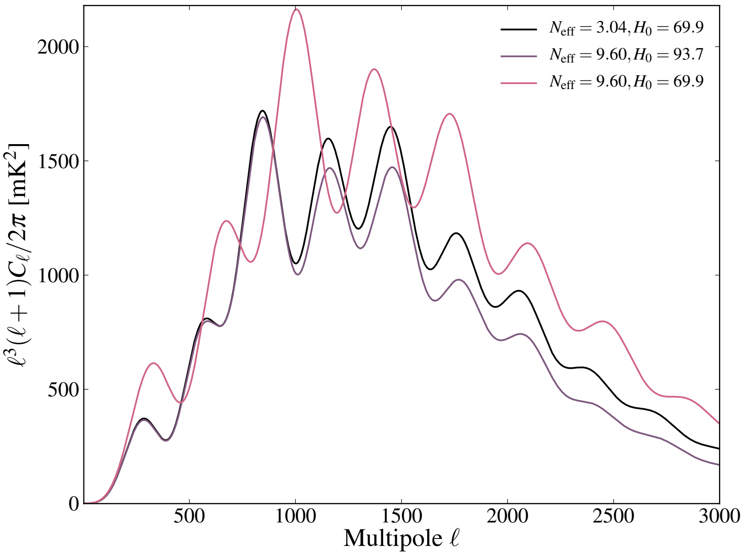

Figure 1.4 Extra energy density at early times damps small-scale power: this figure shows the effect of adding extra energy density at early times. The black model is a ΛCDM model with standard parameter values, while the purple and pink curves both correspond to a universe with a large amount of extra relativistic energy density at early times, parameterised through the number of relativistic degrees of freedom, $N_{eff} = 9.6$.

feature which can not simply be 'imitated' by an isotropic fluid, as the change in expansion rate can. Lastly, because neutrino perturbations travel at the speed of light, they move faster than the acoustic oscillations (recall that the acoustic oscillations travel at the speed of sound in the photon-baryon fluid), inducing a phase shift in the peaks of the small-scale CMB. Figure 1.4 illustrates the effect of increasing the effective number of massless neutrino species, N_{eff} on the CMB temperature power spectrum. In the pink case we have kept all the other values of the parameters the same. In this model the redshift of equality is decreased (equality happens later as there is more radiation present at early times). In addition, it moves the first peak due to the extra energy density in the universe. If one instead changes the other parameters accordingly, to leave the first peaks unchanged (by increasing the matter density and the Hubble constant, see the purple curve) the effect of the extra neutrino species is to *dampen* the power in the higher order peaks, corresponding to small-scale fluctuations. The primordial power spectrum feeds through to the temperature power spectrum

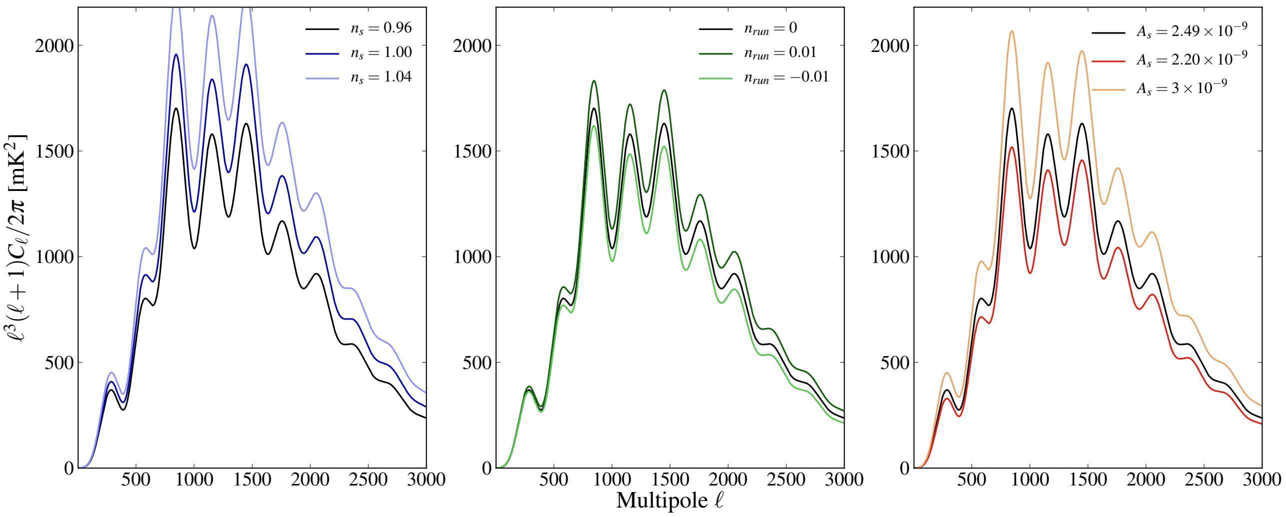

Figure 1.5 The primordial power spectrum changes the temperature anisotropies: the power law spectrum with $(n_s, A_s, dn_s/d\ln k) = (0.96, 2.49 \times 10^{-9}, 0)$ is shown in black for all three panels, where two of the three parameters are held fixed while the other is varied. In the left panel, we change the value of the spectral index n_s, changing the power law. The dark blue shows the spectrum for a scale-invariant power law. The middle panel shows the effect of changing the running of the spectral index with scale, while the right panel shows the effect of the amplitude of the primordial fluctuations on the CMB.

via Eq. (1.40). The parameters describing the primordial power will thus change the observed temperature spectrum, a feature which will be exploited in Chapter 4. Figure 1.5 shows how the primordial power changes the temperature power spectrum. We are considering only scalar perturbations in all cases. The value of the power-law index, n_s changes the power on all scales (see the left panel), however the dominant effects occur on small scales for this choice of pivot scale. All models cross at a pivot point in ℓ (which is not visible here due to the large range in ℓ plotted) corresponding to $\ell * \simeq \chi_{\mathrm{rec}}\mathrm{k}_0$, where $\chi_{\mathrm{rec}} = 14000$ Mpc is the comoving distance to the last scattering surface. The running of the spectral index determines if the power law varies with scale, or rather, it determines whether the power at large values of k is up- (or down-) weighted. Negative running damps the spectrum on small scales, while positive running increases the power at large values of of the high-k modes. Note that the running leaves the temperature spectrum unchanged at low multipoles due to the choice of pivot scale as $k_0 = 0.002$ Mpc^{-1}. Finally the overall amplitude of the power law (shown in the right hand panel) changes the amount of power on all scales by a fixed amount and therefore the ratio between the spectrum with high A_s to the spectrum with standard values will be constant.

1.2.3 Secondary Anisotropies and Foregrounds

The primordial temperature power spectrum is heavily damped on small scales due to Silk damping [55]. It is on these scales, however, that emission from *secondary effects* starts to dominate. An important source of secondary anisotropy is the Sunyaev-Zel'dovich (SZ, Sunyaev and Zel'dovich [59]) emission from galaxy clusters. As CMB photons travel towards us, they interact with the hot gas in the center of galaxy clusters.

We discuss the effect qualitatively here; an excellent review of the SZ effect is found in Carlstrom et al. [60]. The high-energy electrons in the cluster inverse-Compton scatter the incident CMB photons to higher frequencies, increasing the intensity of the photons at higher frequencies. Because of the shape with frequency of the photon spectrum, the spectral distortion of the photons has a 'null' around 220 GHz, and is expressed as a temperature change in the photons as:

$$\frac{\Delta T_{\rm SZ}}{T_{\rm CMB}} = f(x) \int n_e \frac{k_B T_e}{m_e c^2} \sigma_T d\ell, \tag{1.46}$$

where $k_B = 1.38 \times 10^{-23}$ m^2 kg s^{-2} K^{-1} is the Boltzmann constant, c is the speed of light, n_e, T_e, m_e are the number density, temperature and mass of the electron respectively; $x = h\nu / k_B T_{\rm CMB}$ and

$$f(x) = \left(x \frac{e^x + 1}{e^x - 1} - 4 \right) (1 + \delta_{SZ}(x, T_e),) \tag{1.47}$$

where $\delta_{SZ}(x, T_e)$ is the relativistic correction to the frequency dependence. This results in a temperature anisotropy decrement at low frequencies, a null at 220 GHz and an increment at higher frequencies (illustrated through the simulations in Figure 1.6) and makes it possible to detect galaxy clusters through their SZ signature in CMB maps, which has proved successful for both the Atacama Cosmology Telescope and South Pole Telescope groups [61, 62].

The emission in the small-scale CMB temperature is dominated by unresolved clusters. Uncertainties in the gas physics within the cluster lead to uncertainties in the functional

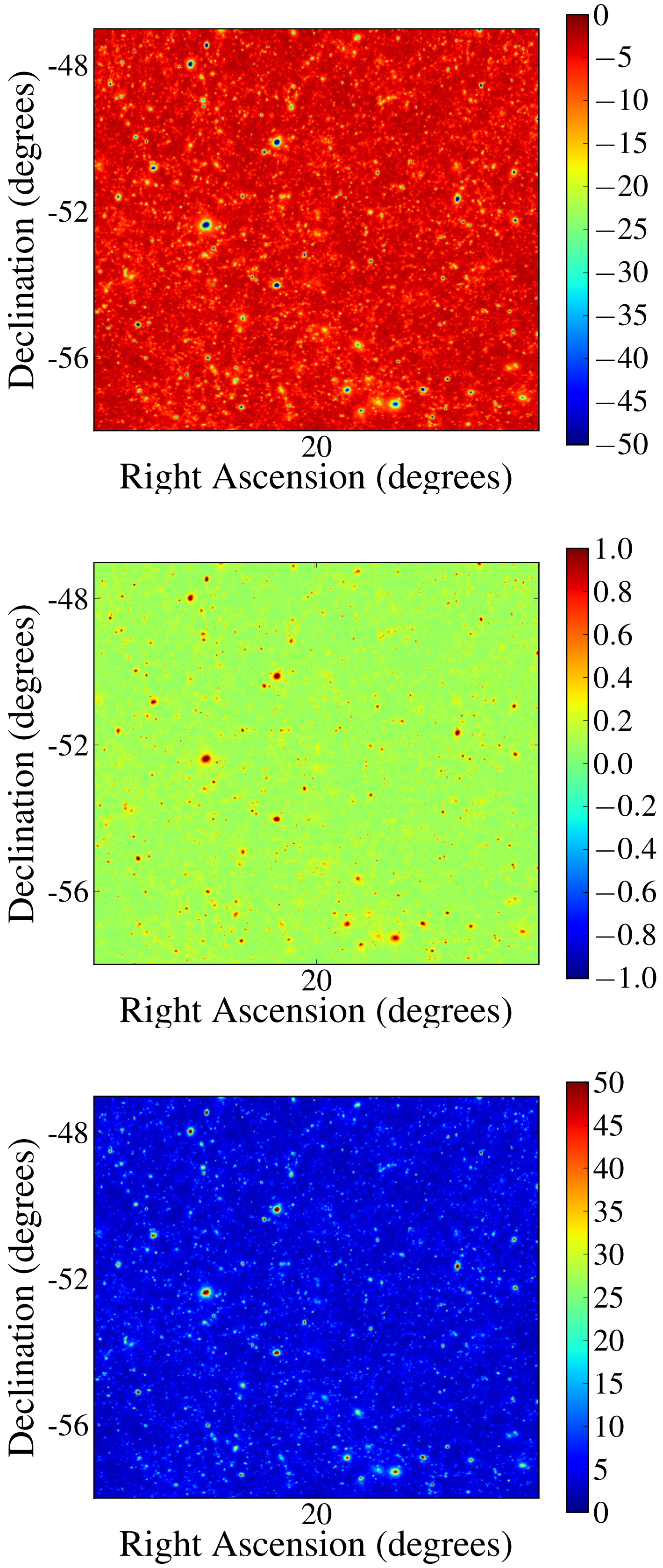

Figure 1.6 The Sunyaev-Zel'dovich effect: the SZ effect changes the frequency distribution of the CMB photons passing through a cluster, resulting in a temperature decrement at frequencies lower than the SZ null (left panel) and an incremement at frequencies higher than the null frequency of 220 GHz (right panel). The scale of the middle panel has been reduced to allow for any discernable temperature difference. These figures were made using the simulations of Sehgal et al. [63] projected onto a patch of the ACT-observed sky.

form of the power of this unresolved emission as a function of multipole, and hence a popular method of including this component in the total temperature power spectrum is through a template and an amplitude, as will be discussed in Chapter 2.

In addition to the thermal SZ effect described above, there is an additional contribution from the motion of the galaxy cluster itself relative to the rest frame of the CMB, known as the kinetic SZ effect. This motion will induce an additional Doppler boost proportional to the peculiar velocity of the cluster along the line of sight. This emission does not have the additional frequency dependence, however, and is generally a subdominant component of the total emission from galaxy clusters.

In addition to secondary effects, small-scale temperature measurements are also sensitive to emission from foreground galaxies. Not only do the CMB photons interact with matter along the line of sight between us and the surface of last scattering (we will discuss the effect of weak gravitational lensing on the CMB in the next section), but we also see light from galaxies at intermediate redshifts projected onto the sky. We see infrared emission from distant galaxies with a distribution in redshift space that peaks at around $z \simeq 1 - 4$. The emission from these star-forming galaxies is mainly thermal re-emission from dust grains surrounding young, hot stars. While some galaxies are resolved and appear as point sources in the CMB map (which can be removed), there is a residual diffuse component that cannot be removed; it is this component that adds to the power of the microwave sky on small scales. A simple model for the diffuse emission of dusty galaxies is with two terms, one resulting from the Poisson distribution of sources (which yields a flat C_ℓ spectrum), and a term describing the clustering of these sources, which we discuss in more detail in Chapters 2 and 3.

Unresolved radio sources provide another source of foreground emission in the small-scale sky. These are generally radio-loud active galactic nuclei which emit synchrotron emission with a frequency dependence of $S(\nu) \propto \nu^{-0.5}$ in flux units. These sources are also distributed according to a Poisson distribution, and so in $\ell(\ell+1)C_\ell/2\pi$ they have a multipole dependence of ℓ^2.

1.2.4 *Weak Lensing of the CMB*

The photons we observe today at a temperature of 2.72548 K have been travelling towards us for most of the lifetime of the universe. The dominant change the photons have undergone is redshifting due to the expansion of space. As they pass through the universe, they interact not only with galaxies and clusters through the SZ effect introduced earlier, but also interact with large scale structure in the form of the dark matter potentials. These potentials distort spacetime around them, and lens the CMB photons, effectively 'moving' temperature around on the sky. Figure 1.7 illustrates how such a potential distorts the path of a CMB photon. The quantity that we are concerned with is the deflection of a photon from its original path as it moves past a potential. A single photon will interact with many structures between the CMB and us, and hence we observe the sum of the small deflections from all structures integrated along the line of sight. Given that the depth of a potential along the line of sight is

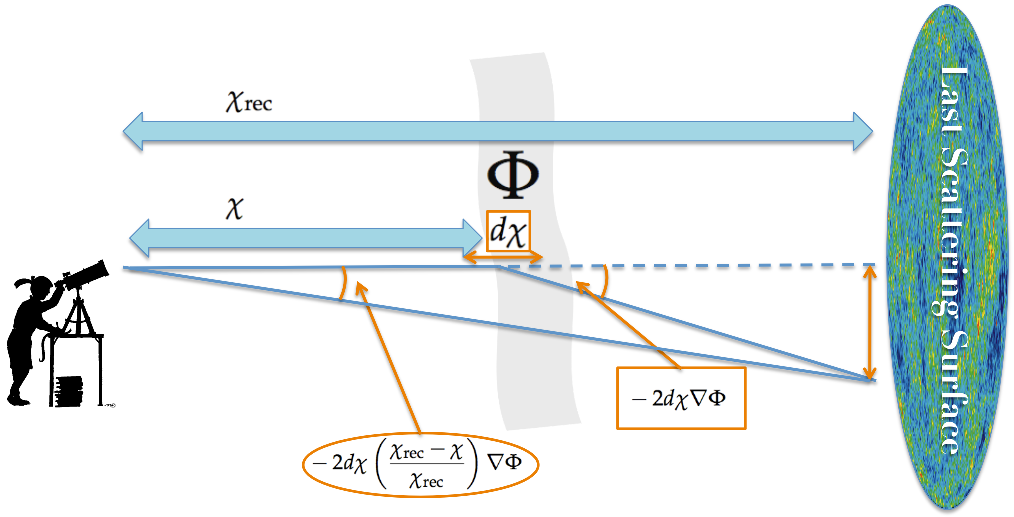

Figure 1.7 Lensing perturbs photons: CMB photons coming from the last scattering surface, at a comoving distance $\chi_{\rm rec}$, are perturbed by a gravitational potential Φ at a distance χ. The deflection angle at the source is obtained by integrating an angle related to the infinitesimal comoving distance $d\chi$, $\delta\alpha = -2d\chi\nabla_\perp\Phi$, and the total deflection $\boldsymbol{d}(\hat{\mathbf{n}})$ is then given by Equation (1.49).

of order 2×10^{-5} radians, the typical deflection from a potential is $\simeq 10^{-4}$ rad. The typical comoving size of the potential with the most power (and therefore contributing the most to the deflection) is around 450 Mpc (see Figure 4.5 in Chapter 4 for the comoving power spectrum), and so it will pass through roughly 14000/450 potentials between us and the CMB, which is 14000 Mpc away in comoving coordinates. Hence the total deflection should be $\sqrt{30} \times 10^{-4} = 0.000547$ rad $\simeq 2$ arcminutes [64]. This corresponds to multipoles of around $\ell > 100^\circ\ [17 \times 10^{-3}\ \mathrm{rad}/^\circ]/0.000547\ \mathrm{rad} \simeq 3000$. This is of course the same regime where Silk damping is prevalent, and so the lensing signal is the strongest signal in those ranges. Figure 1.8 illustrates the small fluctuations in the temperature from lensing deflection, and highlights the need for small-scale experiments to probe the ranges where lensing is important. While these small deflections of the CMB by potentials are on very small scales, these deflections are *correlated* on the sky on angular scales related to the size of the potential. The maximum lensing effect is from a potential (or 'lens') half way between the observer and the background image (in our case the CMB). Hence, the angular scale on which the deflections are correlated is 450/7000Mpc, which corresponds to a few degrees. This means that as well as affecting the small-scale CMB, they will have an effect on the peaks at larger multipoles, changing the statistics of the primordial peaks at the percent level.

Another key idea to remember is that lensing does not change the overall brightness of the CMB, it only moves photons around on the sky. If the CMB were truly isotropic we would not be able to observe any lensing signal whatsoever. Linked to this, we are only concerned with the relative deflection of neighbouring light rays - we cannot tell the value of the absolute deflection due to lensing. This is another way of stating that lensing introduces a temperature gradient on the sky.

We now describe the effect of lensing on the temperature spectrum, following closely the excellent review of Lewis and Challinor [64]; an updated review is provided by Hanson et al. [66]. The effect of lensing is to map the temperature anisotropy $\Theta(\hat{\mathbf{n}})$ at

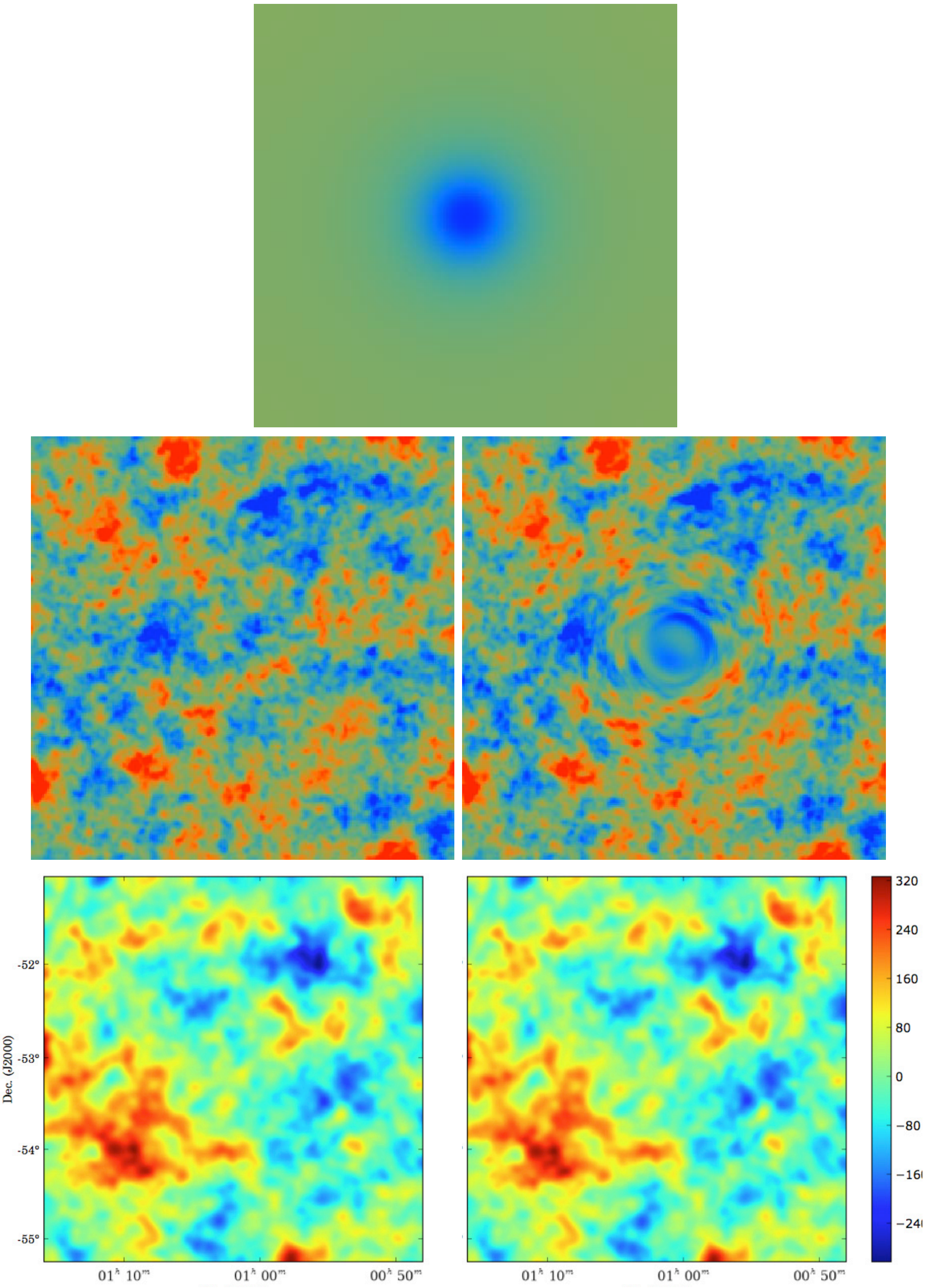

Figure 1.8 Small-scale deflections from lensing: the top row shows a spherically symmetric deflection field $d(\hat{\mathbf{n}})$, on a $10^\circ \times 10^\circ$ field. The left and right panel of the middle row show the unlensed and lensed temperature fields from such a deflection. The top two rows are taken from Hu and Okamoto [65]. Typically the amount of deflection by large scale structure is much smaller, however, as can be seen from a simulated map of the CMB without lensing (left panel, bottom row) and after lensing (right panel, bottom row). The shift in power is on scales of order 1 arcminute, making them virtually impossible to note with the naked eye.

position $\hat{\mathbf{n}}$ according to the lensing potential as:

$$\begin{aligned}\widetilde{\Theta}(\hat{\mathbf{n}}) &= \Theta(\hat{\mathbf{n}} + \boldsymbol{\nabla}\phi(\hat{\mathbf{n}})) \\ &\simeq \Theta(\hat{\mathbf{n}}) + \nabla^i\Theta(\hat{\mathbf{n}})\nabla_i\phi(\hat{\mathbf{n}}) + \frac{1}{2}\nabla^i\phi(\hat{\mathbf{n}})\nabla^j\phi(\hat{\mathbf{n}})\nabla_i\nabla_j\Theta(\hat{\mathbf{n}}) + \ldots, \end{aligned} \quad (1.48)$$

where $\widetilde{\Theta}(\hat{\mathbf{n}})$ is the lensed temperature and $\Theta(\hat{\mathbf{n}})$ is the unlensed temperature field. This series expansion is not a good approximation on all scales, but we can use it to see how the potential results in lensed temperature anisotropies.

From Figure 1.7, we see that the deflection $\boldsymbol{d}(\hat{\mathbf{n}})$ is given by:

$$\begin{aligned}\boldsymbol{d}(\hat{\mathbf{n}}) &= -2\int_0^{\chi_{\rm rec}} d\chi \left(\frac{\chi_{\rm rec}-\chi}{\chi_{\rm rec}}\right)\nabla_\perp\Phi(\chi\hat{\mathbf{n}},\chi) \\ &= \nabla\left[-2\int_0^{\chi_{\rm rec}} d\chi \left(\frac{\chi_{\rm rec}-\chi}{\chi\chi_{\rm rec}}\right)\Phi(\chi\hat{\mathbf{n}},\chi)\right]\end{aligned} \quad (1.49)$$

From this we can redefine the deflection as

$$\boldsymbol{d}(\hat{\mathbf{n}}) = \nabla\phi(\hat{\mathbf{n}}). \quad (1.50)$$

Hence the lensing potential is in turn given by the line-of-sight integral in terms of the comoving distance to the source (the last scattering surface), $\chi_{\rm rec}$ and the 3-dimensional *gravitational* potential Φ as

$$\phi(\hat{\mathbf{n}}) = -2\int_0^{\chi_{\rm rec}} d\chi \left(\frac{\chi_{\rm rec}-\chi}{\chi\chi_{\rm rec}}\right)\Phi(\chi\hat{\mathbf{n}},\chi). \quad (1.51)$$

In this thesis we will use the flat-sky approximation [67, 68], which transforms

$$\sum_{\ell,m} a_{\ell m}Y_{\ell m}(\hat{\mathbf{n}}) \to \int \frac{d^2\boldsymbol{l}}{(2\pi)^2}\Theta\left(\boldsymbol{l}\right)e^{i\boldsymbol{l}\cdot\hat{\mathbf{n}}} \quad (1.52)$$

and hence the Fourier transforms of the temperature and the lensing potential (and their gradients) are:

$$\Theta(\hat{\mathbf{n}}) = \int \frac{d^2\boldsymbol{l}}{(2\pi)^2}\Theta\left(\boldsymbol{l}\right)e^{i\boldsymbol{l}\cdot\hat{\mathbf{n}}}; \qquad \boldsymbol{\nabla}\Theta(\hat{\mathbf{n}}) = i\int \frac{d^2\boldsymbol{l}}{(2\pi)^2}\boldsymbol{l}\Theta(\boldsymbol{l})e^{i\boldsymbol{l}\cdot\hat{\mathbf{n}}} \quad (1.53)$$

$$\phi(\hat{\mathbf{n}}) = \int \frac{d^2\boldsymbol{l}}{(2\pi)^2}\phi(\boldsymbol{l})e^{i\boldsymbol{l}\cdot\hat{\mathbf{n}}}; \qquad \boldsymbol{\nabla}\phi(\hat{\mathbf{n}}) = i\int \frac{d^2\boldsymbol{l}}{(2\pi)^2}\boldsymbol{l}\phi(\boldsymbol{l})e^{i\boldsymbol{l}\cdot\hat{\mathbf{n}}} \quad (1.54)$$

We can then express Eq. (1.51) in Fourier space to second order in the lensing potential ϕ as:

$$\begin{aligned}\widetilde{\Theta}(\boldsymbol{l}) &\simeq \Theta(\boldsymbol{l}) - \int \frac{d^2\boldsymbol{l}'}{(2\pi)^2}\boldsymbol{l}'\cdot(\boldsymbol{l}-\boldsymbol{l}')\phi(\boldsymbol{l}-\boldsymbol{l}')\,\Theta(\boldsymbol{l}') + \\ &-\frac{1}{2}\int \frac{d^2\boldsymbol{l}'}{(2\pi)^2}\int \frac{d^2\boldsymbol{l}''}{(2\pi)^2}\boldsymbol{l}'\cdot(\boldsymbol{l}'+\boldsymbol{l}''-\boldsymbol{l})\boldsymbol{l}'\cdot\boldsymbol{l}''\Theta(\boldsymbol{l}')\phi(\boldsymbol{l}'')\phi^*(\boldsymbol{l}'+\boldsymbol{l}''-\boldsymbol{l})\end{aligned} \tag{1.55}$$

The second term in Eq. (1.55) shows how lensing causes a 'mixing' of ℓ modes through the convolution of the lensing potential with the temperature field. It therefore correlates modes across a band which is characterised by the power at the scale corresponding to a given deflection angle [68].

We can then express the power spectrum of the lensed temperature field,

$$\langle\widetilde{\Theta}(\boldsymbol{l})\widetilde{\Theta}^*(\boldsymbol{l}')\rangle = \delta(\boldsymbol{l}-\boldsymbol{l}')\widetilde{C}_\ell^{TT} \tag{1.56}$$

using the relation $\phi(\boldsymbol{l}) = \phi^*(-\boldsymbol{l})$ in terms of the unlensed temperature power spectrum:

$$\widetilde{C}_\ell^{TT} = C_\ell^{TT} + \int \frac{d^2\boldsymbol{l}'}{(2\pi)^2}[\boldsymbol{l}'\cdot(\boldsymbol{l}-\boldsymbol{l}')]^2 C^{\phi\phi}_{|\boldsymbol{l}-\boldsymbol{l}'|}C^{TT}_{\ell'} - C_\ell^{TT}\int \frac{d^2\boldsymbol{l}'}{(2\pi)^2}(\boldsymbol{l}\cdot\boldsymbol{l}')^2 C^{\phi\phi}_{\ell'} \tag{1.57}$$

where $C_\ell^{\phi\phi}$ is the power spectrum of the lensing potential. This simplifies to

$$\widetilde{C}_\ell^{TT} = (1 - l^2 R^\phi)C_\ell^{TT} + \int \frac{d^2\boldsymbol{l}}{(2\pi)^2}[\boldsymbol{l}'\cdot(\boldsymbol{l}-\boldsymbol{l}')]^2 C^{\phi\phi}_{|\boldsymbol{l}-\boldsymbol{l}'|}C^{TT}_{l'} \tag{1.58}$$

where the *total mean-squared deflection* is defined as

$$R^\phi \equiv \frac{1}{2}\langle|\nabla\phi|^2\rangle = \frac{1}{4\pi}\int \frac{dl}{l} l^4 C_\ell^{\phi\phi}. \tag{1.59}$$

Again, the second term in Equation (1.58) is a convolution of the unlensed power spectrum with the lensing deflection field and is what causes the blurring and smoothing of the power spectrum peaks through lensing. This 'Robin Hood' effect decreases power in the peaks and increases power in the troughs of the spectrum. In addition to the smoothing of the peaks from lensing, the lensing potential has another effect on the total CMB. As mentioned above, the unlensed CMB power spectrum loses power at high ℓ due to Silk damping. While there is still a contribution from the unlensed power, the lensed power spectrum at high-ℓ (where $\ell \gg \ell'$) is mainly probing the deflection power, or

$$\widetilde{C}_\ell^{TT} \propto \ell^2 C_\ell^{\phi\phi} R^T. \tag{1.60}$$

It is the combination of these effects (the smoothing of the peaks and the increase in power at high multipoles) that allows one to test directly for the presence of lensing in the high-ℓ CMB temperature spectrum, without directly reconstructing the lensing potential. As we will show in Chapter 3, we can replace $C_\ell^{\phi\phi}$ with $A_L C_\ell^{\phi\phi}$, where we take the deflection power as directly predicted by ΛCDM. In the case of no lensing, this parameter would be consistent with zero, whereas standard lensing would yield $A_L = 1$. In this straightforward way we see that small-scale temperature data allow one to probe potentially new physics.

The power spectrum for the deflection field (defined in Eqs. (1.49,1.50)) is related to the power spectrum of the lensing potential via $C_\ell^{dd} = \ell(\ell+1)C_\ell^{\phi\phi}$. In addition to testing for the effect of lensing on the temperature spectrum, one can reconstruct the lensing field directly using an estimator which is quadratic in the temperature field. The reconstruction and detection of the deflection field has been successfully achieved directly [69] or through cross correlations of temperature maps with large scale structure [70, 71].

1.2.5 *Observational Context*

The observational community has been heavily invested in measuring the properties of the temperature (and polarisation) of the CMB for many years, through many different experiments. Early observations from the Cosmic Background Explorer [72–83] confirmed the presence of anisotropies in the temperature of the radiation at the level of one part in 100000. In the years following the COBE satellite, experiments were made from the ground from the TOCO experiment and others in the Chilean Andes [84–87], at the South Pole [88–91], the Canary Islands and Tenerife [92–95], the United

Kingdom [96, 97], the United States [98, 99] and Canada [100]. These were combined with measurements from balloon-borne experiments [101–105] to measure the first peak in the anisotropy power spectrum of the temperature field. The BOOMERANG

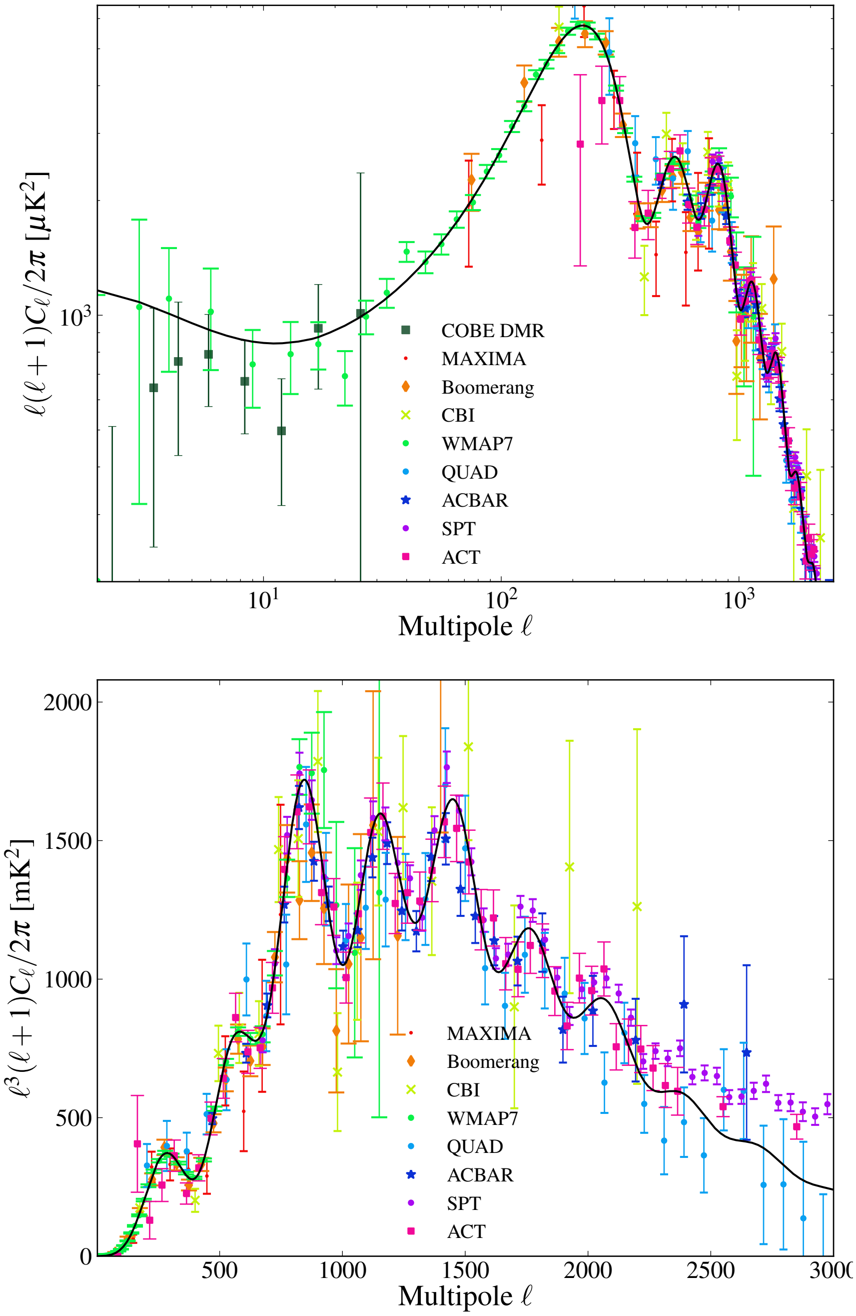

Figure 1.9 Observations of the CMB: a sample of CMB experiments are shown in approximately chronological order [72, 104, 106–108] from COBE to the latest data release from the WMAP satellite. The top panel is shown as $\ell(\ell+1)C_\ell$ to emphasise the Sachs-Wolfe plateau on large scales, while the bottom panel is presented as $\ell^3(\ell+1)C_\ell$ and highlights small-scale measurements of the temperature anisotropy.

[106] and Maxima [104] experiments crucially measured not only the first peak but the trough thereafter (and in so doing concluded that there was an oscillatory spectrum). Since then, the WMAP satellite mission [7, 33, 56, 57] has pinned down the spectrum to unprecendented accuracy, confirming that a simple cosmological model is in excellent agreement with cosmological data out to multipoles of $\ell = 1000$. In addition, ground-based experiments such as ACBAR [108, 109], the Very Small Array (VSA, Grainge et al. [110]), Archeops [111] and the Cosmic Background Imager (CBI, Sievers et al. [107]) have provided confirmation of the standard cosmological picture and have probed the temperature spectrum out to smaller scales.

An up-to-date list of all CMB experiments, including the timeline of operation for each experiment, is provided at the NASA LAMBDA[4] website. Figure 1.9 shows the power spectrum from past and current CMB experiments, illustrating that the measurement and classification of the CMB anisotropies are astounding accomplishments by a diverse group of researchers.

This thesis is concerned with recent small-scale measurements of the CMB provided by the Atacama Cosmology Telescope (ACT). It is one of two international experiments aimed at probing the microwave sky on small scales. While we will not discuss the results from the other experiment, the South Pole Telescope (SPT, [112–114]), it is worth noting that they are complementary experiments.

1.3 SMALL-SCALE POWER SPECTRUM OBSERVATIONS

1.3.1 *The Atacama Cosmology Telescope*

Figure 1.9 not only illustrates CMB data from the Cosmic Background Explorer [72] to the recent WMAP 7 measurements [7, 115], but highlights the science driver of small-scale temperature measurements. Before the measurements from the ACT and SPT groups, the high-ℓ spectrum had been probed by a few experiments, but the errorbars were large at high multipoles.

---

[4] http://lambda.gsfc.nasa.gov/product/expt/

This points to the fact that a very sensitive instrument capable of high resolution observations is required to make quality measurements up to multipoles of $\ell \simeq 10000$. In order to probe and characterise the secondary effect of SZ emission which will be important at large multipoles, a small-scale telescope of this sort would have to have multiple detectors operating in frequency bands around the SZ null frequency.

The Atacama Cosmology Telescope (ACT) is one such telescope capable of sensitive observations with roughly arcminute resolution. It is a 6-meter, off-axis Gregorian telescope located on Cerro Toco in the Atacama desert of Northern Chile, at 22.9586° south latitude, 67.7875° west longitude. The altitude (5190 m), stable atmosphere and arid conditions make the site ideal for observations of the CMB, with a median precipitable water vapor (PWV) of 0.49 mm during the observing run.

ACT has been operating since late 2007, and in its current incarnation (without polarisation sensitivity) ceased observations in January 2011. ACT observations are focused on two regions: a 5°-wide strip centered along the celestial equator (leading to an area of 324 square degrees used in current publications) and a 9° strip centered on declination $-53.^\circ3$. This latter Southern Strip has an area of 296 square degrees, including the data from the 2007 to 2010 seasons.

In this thesis we will discuss observations of the Southern sky in the 2008 season using 148 GHz only (Chapter 2) and a combination of 148 GHz and 218 GHz data in Chapter 3. Observations made using the highest frequency band were not used in the analysis presented in this work.

The key science capability of ACT is that it has an angular resolution of $1.4'$ over a few hundred square degrees of the sky. The angular resolution translates into the small scales of the power spectrum that ACT is sensitive to - the analysis we will discuss probes the power spectrum to multipoles of $\ell = 10000$.

1.3.2 *Map-making*

The first publically released data product of most CMB experiments is the map of temperature anisotropies of the sky. However, these maps represent much of the data analysis procedure, and in general there is much processing required to turn the actual measurements made by a telescope such as ACT, which are typically fifteen-minute sections of time ordered data (TOD), into a map of the microwave sky. The data are calibrated both by using measurements of the response of the bolometer to an object of known temperature and by cross-calibrating with the WMAP temperature maps. This is also used to understand and correct for any drifts in the pointing of the telescope. These TODs contain all the information of the sky, however, and including the atmosphere, point sources, diffuse emission from secondaries and the CMB. The map-making yields a maximum likelihood estimate for the power on the sky from the TODs. This maximum likelihood estimate is found by solving the mapping equation [116]:

$$\boldsymbol{P}^{\mathrm{T}}\boldsymbol{N}^{-1}\boldsymbol{P}\widetilde{\boldsymbol{m}} = \boldsymbol{P}^{\mathrm{T}}\boldsymbol{N}^{-1}\boldsymbol{d} \tag{1.61}$$

where the map is represented by a vector $\boldsymbol{m}$ of length given by the number of pixels (typically 10^7), $\boldsymbol{d} = \boldsymbol{P}\boldsymbol{m} + \boldsymbol{n}$ is the data, with $\boldsymbol{P}$ a matrix projecting the map into the timestream (the TODs) and $\boldsymbol{n}$ is the noise.

The map $\widetilde{\boldsymbol{m}}$ is solved for iteratively using a preconditioned conjugate gradient method [117, 118]. One of the main reasons that solving for the maps is a difficult procedure is that the atmospheric signal is correlated across detectors and is much stronger than the signal we are trying to estimate. In addition the noise from the telescope is not isotropic. For this reason angle-averaged spectra are used in the final cosmological analysis. The map-making procedure will be outlined in more detail in Chapter 2.

1.3.3 *Power Spectrum Estimation*

Large-scale CMB experiments (such as WMAP) have mapped out the entire sky and, with the exception of masking out regions of strong foreground emission and point sources, have been able to use all the possible ℓ modes to determine the power spectrum. With small-scale measurements this is not possible. ACT measures the microwave sky to high levels of precision, but only on a small (of order hundreds of degrees) patch of the sky. This has both advantages and disadvantages. On the one hand, the small patch means that one can use two-dimensional Fourier transforms on the flat patch without needing to do spherical harmonic decomposition. On the other hand, however, the small patch leads to edge effects and mode-mode coupling. This is understood because the power spectrum on a small patch is a convolution of the full-sky power spectrum with the power spectrum of the mask - which in the case of a small patch is most of the sky.

In the ACT analysis we use the formalism of Das et al. [119] and use the Adaptive Multi-Taper-Method (AMTM, Oh et al. [120]). The two main elements of the MTM approach is to use tapers that effectively remove the edges of the patches, but that are designed to be concentrated in the frequency domain. This stops the aliasing of power that occurs when the map has hard edges, a fact which is only necessary when not computing a full sky spectrum. The fact that experiments like ACT observe small patches is due to the compromise between resolution and survey area; in order to scan an area of the sky deeply with high resolution, ACT cannot cover the entire sky as is the case for satellites like WMAP and Planck. In addition, its location in the southern hemisphere means that it cannot access all of the sky, whereas satellites do not suffer from the same issues of sky coverage.

In ACT observations, masks are also used to remove the emission from bright point sources. The edges in the mask leak power leaking from small scales into large scales. This effect is due to the large range in power of the CMB spectrum from $500 < \ell < 10000$ - the maps have a large effective ‘dynamic range’ in power spectrum space. In order to remove the dynamic range before computing the power spectrum, the maps are ‘prewhitened’ in real space, corresponding to a multiplication by roughly an ℓ^4 spectrum, because the CMB power spectrum scales as ℓ^{-4} for multipoles $\ell \geq 1000$. This reduces further the leaking of power from higher modes to lower ℓ modes.

Another consequence of having a long strip, as is the case for ACT, is that the two-dimensional Fourier transform would have very elongated modes in one direction. Rather than computing the spectrum in one long strip, one can break up the patch of sky into smaller (roughly square) patches. The spectrum is then computed in each patch, and a weighted average based on the noise in the patch is used to obtain a final spectrum.

In general in the ACT analysis we split the time ordered data into four parts, and then make one map per part, yielding four maps per section of the sky. We then compute weighted average of the six independent cross spectra, i.e. if we label the spectra from 1 to 4, we have six - $1 \times 2, 1 \times 3, 1 \times 4, 2 \times 3, 2 \times 4, 3 \times 4$ - independent cross-spectra. Creating a spectrum from many different sub-maps removes noise bias. The noise in each sub-map is uncorrelated, hence the cross-spectrum between maps cancels the noise contribution, reducing the errors on the final spectrum. In addition, this prescription allows one to test for inconsistencies in the map-making and power spectrum estimation pipeline. The intrinsic signal in each patch of the sky is identical (it is coming from the same region of the CMB on the sky), and so any differences would be due to the map-maker or the power spectrum pipeline. We will discuss these tests in Chapter 2.

1.4 SUPERNOVA COSMOLOGY

While the cosmic microwave background probes the universe at early times, observations of Type Ia supernovae (SNe Ia) were first used in the late 1990's to probe the expansion of the universe at late times. We will briefly introduce supernova cosmology, and focus on next generation photometric supernova surveys, which will generate orders of magnitude more candidates than current data.

1.4.1 *Type Ia Supernovae*

A Type Ia supernova is believed to be a hydrogen deficient white dwarf star existing in a binary pair, that has accreted matter off the other star in its pair. The accretion from the companion star feeds the white dwarf until it can no longer support itself from degenerate gravitational collapse, as it nears the Chandrasekhar mass limit [121]. Once this happens the star explodes violently, often outshining its host galaxy by several magnitudes. We will not go into the details of the thermonuclear processes involved

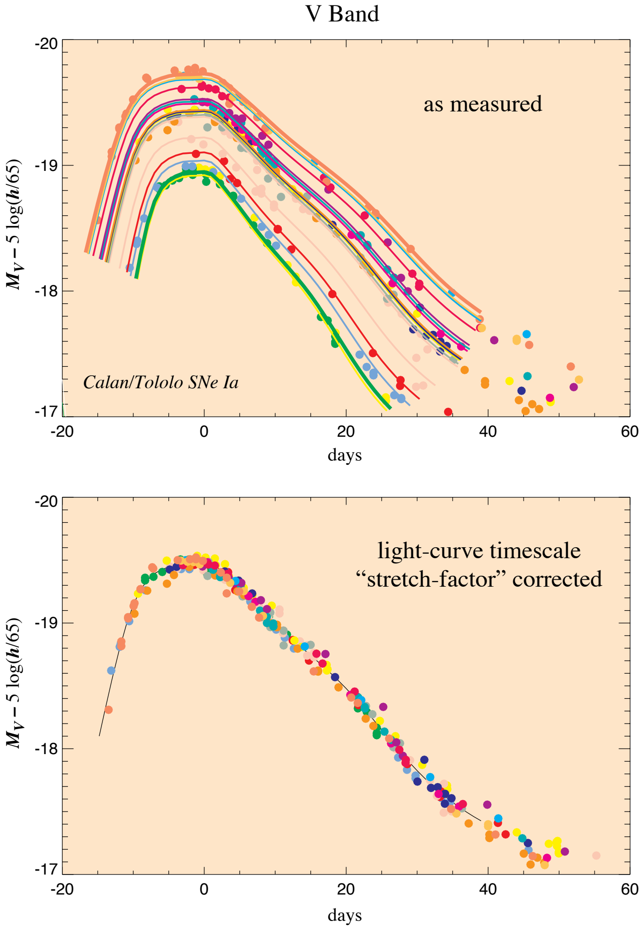

Figure 1.10 The brightness-stretch relation: the brightest SNe fade the fastest. This empirical observation [122] is critical in 'standardising' SN, in that by observing the time taken for the SN to fade, one can calibrate for its absolute brightness, and hence its distance modulus. Figure from Perlmutter et al. [123].

in a SN explosion, however, the key process for SN cosmology is the radioactive decay of the products ^{56}Ni and ^{56}Co produced in the explosion. Observationally, the light-curve of the supernova consists of measurements taken of the light of the star in different filters, over a certain time frame as the star burns, brightens and then fades. The peak luminosity is determined by the mass of ^{56}Ni available for burning [124], in that for a fully burned white dwarf the amount of Ni available is linked to the mass of the star itself. This provides the first motivation for SNe Ia as 'standard candles' with the same intrinsic brightness. There is, however, significant scatter in the brightness of SNe, as can be seen in the top panel of Figure 1.10. Luckily, there is an empirically observed relation between the brightness of a SN and the time it takes to fade from maximum light [122]. This allows one to measure the time taken for a SN to fade by a given number of magnitudes, and then *infer* the absolute magnitude of the SN, without necessarily having observed it exactly at or before maximum light. Hence SNe Ia are 'standardisable' candles and are used as a distance indicator through their luminosity distance.

The luminosity distance, $d_L(z)$ relates the intrinsic flux of an object to its apparent brightness, providing a measure of the distance to the object:

$$d_L(z) = \frac{c(1+z)}{H_0\sqrt{\Omega_k}} \sinh\left(\sqrt{\Omega_k}\chi(z)\right) \tag{1.62}$$

where $\chi(z)$ is the comoving distance. Assuming photon conservation, the luminosity distance is related to the angular diameter distance (see Eq. (1.62)) via $d_L(z) = (1+z)^2 d_A(z)$.

The distance modulus relates this luminosity distance to the difference between the absolute (intrinsic) magnitude M and apparent magnitude m of the object:

$$\mu \equiv m - M = 5\log d_L + 5\log\left(\frac{c}{H_0}\right) + 25 \tag{1.63}$$

where d_L is measured in Mpc, H_0 is the value of the Hubble parameter today in km s^{-1} Mpc^{-1} and $c = 3 \times 10^5$ km s^{-1} is the speed of light.

1.4.2 *Observational Status*

Since the confirmation of the accelerated expansion of the universe using SNe Ia, many different surveys have taken data of SNe [125–130], with a high-z sample from the Hubble Space Telescope [131], and anchored with a low redshift sample [132–138], over many different ranges of redshift. Figure 1.11 shows the Union2 compilation of SN data, which illustrate the different redshift ranges and errors of the different measurements on the Hubble diagram. In addition the recently released Supernova Legacy Survey (SNLS, Sullivan et al. [130]) data add to the data from intermediate to high redshifts. Supernovae directly probe the expansion (and acceleration) of the universe, and the data are used to constrain the energy densities of matter and dark energy (under the assumption of a flat universe) and to measure not only the value of the equation of state of dark energy, w, but to probes its evolution with redshift $w(z)$. The Hubble diagram of current SN data is shown in Figure 1.11. The differences in distance modulus for models with very different cosmologies are subtle, and going to high redshift will increase the lever arm of these measurements, and allow one to probe the possible dynamics of dark energy. Traditionally once Type Ia supernova candidates are selected according to the quality of the light curve fit to a template, they are followed up by large 8m-class telescopes to obtain spectra of the candidates. These spectra provide *confirmation* that the data are in fact Type Ia, through the appearance of the characteristic SiII absorption line in the spectrum of

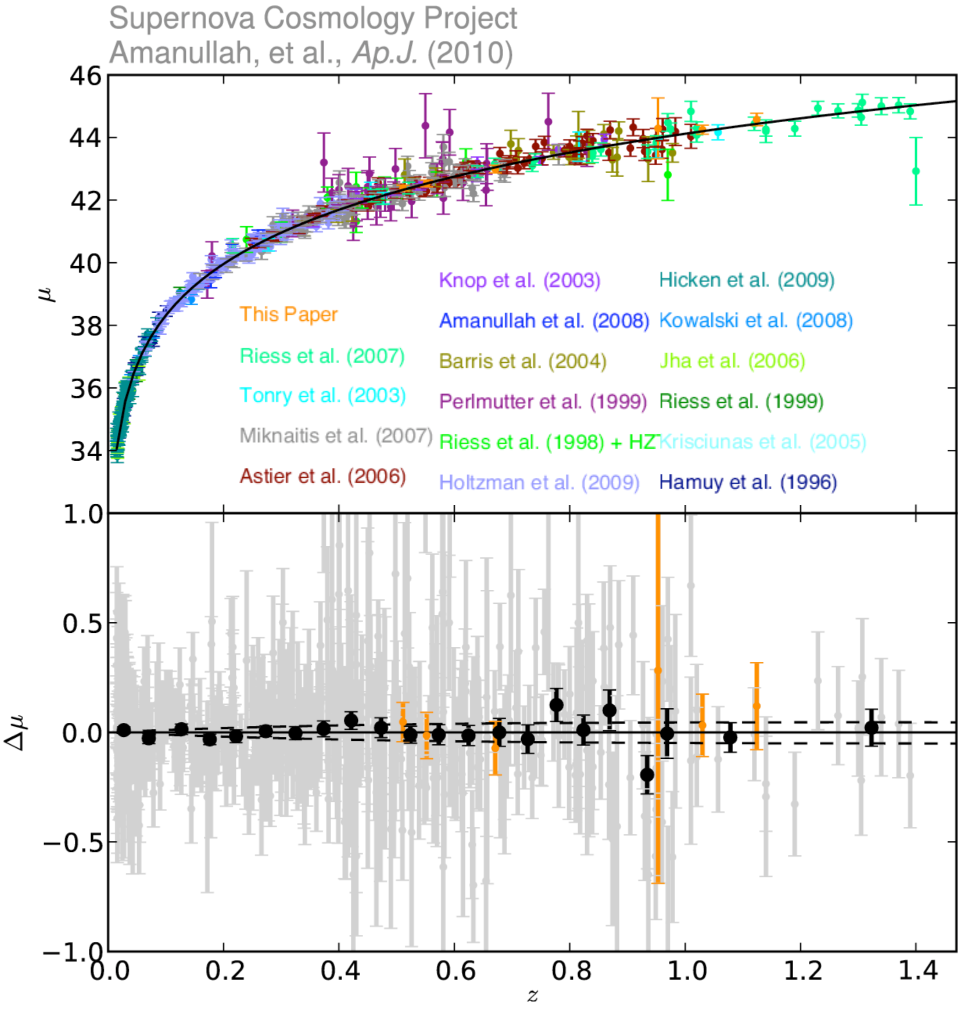

Figure 1.11 The current SN sample: as compiled in the Union2 dataset (Figure taken from Amanullah et al. [139]). Not shown here are the updated sample from the Supernova Legacy Survey [130], these data supplement the data with 242 SNe with redshifts between $0.08 < z < 1.06$.

the SN. The current state-of-the-art is that no supernova data are used unless it is confirmed that the supernovae in fact belong to the Type Ia class.

Taking spectra is not a simple operation however. Typically the integration time required to obtain a high signal-to-noise spectrum of the SN scales with redshift as $t_{spec} \simeq (1+z)^{4-6}$ and hence there is a limit to how many spectra can be obtained for candidate SNe and on how deep in redshift one can probe with spectroscopically confirmed data. Current surveys such as the Dark Energy Survey (DES, The Dark Energy Survey Collaboration [141]) and future surveys such as the Large Synoptic Survey Telescope (LSST, Wang et al. [142]) will yield orders of magnitude more SNe than are currently known. Despite the systematic errors in supernova data, this vast increase in the sample size available will allow one to beat down the errorbars on measurements of cosmic parameters. Figure 1.12 shows the expected increase in the number of SNe as a function of time for the next decade. All of these data are from

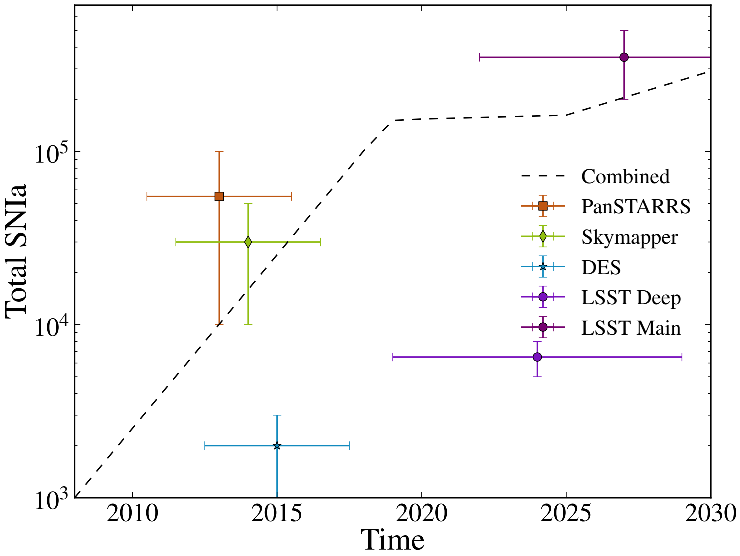

Figure 1.12 The expected increase in number of SN candidates: from near-future surveys which have recently started taking data (such as the SkyMapper and PanSTARRS surveys) to the expected numbers from conservative estimates for the Large Synoptic Survey Telescope, taken from the most conservative case present in Figure 11.2 of the LSST science specifications [140]. The dashed line shows the cumulative number of SNe (added at the end of each of the surveys for visual purposes). The rapid increase in the number of SN Ia candidates detected will revolutionise photometric supernova cosmology.

photometric surveys, and hence only a small fraction of these data will be followed up using spectroscopic techniques.

1.4.3 *Contaminants*

Given that the future SN candidates will not all be followed up, one might expect contamination from other SN types. While Type Ia supernovae are created from thermonuclear burning and accretion of one star onto the surface of a white dwarf, these are not the only bright objects in the sky resulting from explosions. Massive stars (above around 10 solar masses) will undergo *core collapse* as they run out of fuel to sustain them from gravitational collapse.

These exploding stars are also bright and occur frequently in the universe (at rates comparable to the SN Ia rate), however the same evidence for them being 'standardisable candles' is not available. These stars all start out with different masses, and hence will explode with different masses, approaching the Chandrasekhar mass limit from above and not below. They thus form a contaminant population, and many of the photometric SN Ia candidates will actually be core-collapse SNe.

Core-collapse SNe are however believed to be dimmer than their SN Ia counterparts [143]. The amount of data available from core-collapse SNe is much less than the sample of Type Ia Supernovae, and hence the absolute distribution properties of the core-collapse remain an uncertainty in any cosmological analysis. As an example, Falck et al. [144] investigate different possible forms for the deviation in distance modulus from the standard Ia relationship.

Removing the contaminant distribution is a statistical problem, and one for which Bayesian Estimation Applied to Multiple Species (BEAMS) was designed. We will see in Chapter 5 how the BEAMS is applied in the context of photometric SN data, and how it provides an avenue to perform statistical inference in the presence of contaminated data.

1.5 STATISTICAL TECHNIQUES

1.5.1 *Bayesian Statistics*

Throughout this thesis, we will employ Bayesian statistical methods. While Bayesian theory is an extremely mature field (the name of the theory itself comes from the Reverend Bayes who formulated the methods in the 18^{th} century), it has only been applied to the field of cosmology in the last few decades. While the debate between frequentist and Bayesian approaches is by no means the theme of this thesis, it is worth briefly outlining the difference between frequentist and Bayesian methods. According to the frequentist definition, the probability of throwing a 'Heads' from a two-sided coin is

$$P(H) = \lim_{x \to \infty} \frac{\text{Number of heads}}{\text{Number of tails}} = 0.5. \tag{1.64}$$

Hence if a frequentist was engaged in a game of coin-toss, threw a coin ten times and got the result HHHHHHHHHH; if asked what the probability was of throwing heads again, he might reply that the probability was still $P(H) = 0.5$, since the events are independent of one another. However, if a Bayesian was asked what the probability of throwing a heads on the next turn was, she would build into her reply her *prior* knowledge of the throws that went before, and would calculate the probability of P(H) assuming this prior knowledge. Given that she has seen the coin tossed as heads ten times, her posterior probability for the coin coming up as heads again will be pushed towards unity given this prior knowledge. This simple example illustrates the difference between the two schools of thought - Bayesian theorists include prior information on the parameters to calculate the *posterior* probability, while frequentists include no such prior. In the context of Bayesian parameter estimation, we construct these prior and posterior probabilities in the sections that follow.

1.5.2 *Priors and Likelihoods*

Key to the idea of parameter fitting is the concept of the posterior and likelihood. The posterior $P(\boldsymbol{\theta}|\boldsymbol{d})$, describes how likely the theoretical model $\boldsymbol{\theta}$ is given the data $\boldsymbol{d}$. The posterior is in general difficult to determine, and is instead related to the likelihood

$P(\boldsymbol{d}|\boldsymbol{\theta})$ (which simply put is how likely the observed data are assuming a specific model $\boldsymbol{\theta}$) through Bayes' Theorem:

$$P(\boldsymbol{\theta}|\boldsymbol{d}) = P(\boldsymbol{d}|\boldsymbol{\theta})\frac{P(\boldsymbol{\theta})}{P(\boldsymbol{d})} \tag{1.65}$$

where $P(\boldsymbol{\theta})$ is the prior on the model $\boldsymbol{\theta}$, which is derived from prior experiments or physical intuition (e.g., the prior could force the Hubble parameter $H_0 > 0$) and $P(\boldsymbol{d})$ is the evidence, which in most cases is an arbitrary normalisation factor. In general, the least informative (and most conservative prior) is the Jeffreys' prior, which is uniform in log space.

One example of a likelihood function is the Gaussian likelihood

$$P(\boldsymbol{d}|\boldsymbol{\theta}) = \frac{1}{\sqrt{2\pi|C|}}e^{-\chi^2/2} \tag{1.66}$$

where $\chi^2 = (\boldsymbol{d}-\boldsymbol{t})^{\mathrm{T}}C^{-1}(\boldsymbol{d}-\boldsymbol{t})$ relates the data $\boldsymbol{d}$ to the theoretical prediction $\boldsymbol{t}$ and the error covariance C^{-1}.

Consider an additional constraint on the posterior denoted by $\boldsymbol{\tau}$. The marginalised posterior can be expressed $P(\boldsymbol{\theta}|\boldsymbol{d})$ as a sum over all possible realisations of $\boldsymbol{\tau}$:

$$P(\boldsymbol{\theta}|\boldsymbol{d}) = \sum_{\tau} P(\boldsymbol{\theta},\boldsymbol{\tau}|\boldsymbol{d}). \tag{1.67}$$

Conversely, in order to obtain the one-dimensional posterior of a parameter i, one marginalises the posterior over all the parameters in a parameter set that do not include that parameter, which (assuming that the parameters $\boldsymbol{\theta}$ are continuous):

$$P(\theta_i|\boldsymbol{d}) = \int_{j\neq i} P(\boldsymbol{\theta}|\boldsymbol{d})d\theta_j. \tag{1.68}$$

1.5.3 *Parameter Estimation*

In our analysis we will use Monte Carlo Markov Chain (MCMC) methods and in particular the Metroplis-Hastings (MH) acceptance criterion [145]. The name *Monte Carlo* comes from the fact that the algorithm uses probabilistic sampling to map out the posterior of a given problem. MCMC is particularly suited to problems where there are a large number of parameters p describing a particular model, as the time needed for the sampling method to converge scales approximately with the number of dimensions of the parameter space. This is not the case in a grid-based approach, where a finite grid is constructed with intervals $\delta\theta$ (we assume here that the step size is the same for all parameters, but that will not necessarily be true in general) in each dimension. The scale of the problem then increases as $\delta\theta^p$.

The MH algorithm can be summarised as follows:

1. Start with an initial parameter vector $\boldsymbol{\theta_0}$ (where the 0 indexes the step number), and compute the likelihood of this parameter vector, $P(\boldsymbol{d}|\boldsymbol{\theta_0})$ and the prior $P(\boldsymbol{\theta_0})$, combining to give the posterior (ignoring the evidence as it does not depend on parameters and will divide out when taking the ratio of posteriors).
2. Take a trial step in the parameter space, defined by the vector $\boldsymbol{\delta\theta}$ drawn randomly from a Gaussian distribution and add this to the initial vector $\boldsymbol{\theta_1} = \boldsymbol{\theta_0} + \boldsymbol{\delta\theta}$.
3. Compute the posterior for the new point as in the first step.
4. Compute the ratio of the posteriors of the two parameter vectors,
$$\frac{P(d|\boldsymbol{\theta_0})P(\boldsymbol{\theta_0})}{P(d|\boldsymbol{\theta_1})P(\boldsymbol{\theta_1})}.$$
5. Accept this point $\boldsymbol{\theta_1}$ if the ratio of posteriors greater than a uniformly generated random number $0 < q < 1$.
6. If the point is accepted, $\boldsymbol{\theta_1}$ is recorded, and if not, the vector $\boldsymbol{\theta_0}$ is recorded in the chain instead.

The final two points are the fundamental characteristic about the Metropolis-Hastings method. Any step $\boldsymbol{\theta_*}$ is accepted with a probability that depends on the posterior, and *not only* if the new point leads explicitly to a higher value of the posterior. This allows the sampling chain to avoid local minima and to sample the parameter space efficiently. In addition, because the distribution is sampled according to the ratio of posteriors, you can reconstruct the parameters statistics directly from the chain that results, as the number density of a given parameter value in the chain depends on the probability of that value, $n(x) \propto p(x)$. In the case of an MCMC chain, the marginalisation in Eq. (1.68) reduces to considering only an ordered chain for the parameter θ_i, since you are then effectively summing over the other dimensions in the parameter space. The statistics of an individual chain are reconstructed from the number density in that 50% of a given chain will lie below the marginalised median of that parameter, with 68% of the chain lying in the 68% confidence interval of the marginalised chain.

In general one needs to be specific about the priors used and whether the final posterior is determined mainly by the data or by the prior. It is key to make sure when running MCMC that the chains are converged (i.e. that the parameter space is well sampled and that the mean value of the chain does not drift as a function of step number), we test for this when running our MCMC analysis using the methods of Dunkley et al. [146].

2

FIRST DATA RELEASE OF THE ATACAMA COSMOLOGY TELESCOPE: POWER SPECTRA AND PARAMETERS FROM 148GHZ DATA.

2.1 INTRODUCTION

The cosmic microwave background (CMB) radiation captures a view of the universe at only $\sim 400,000$ years after the big bang. Measuring the angular power spectrum of temperature anisotropies in the CMB has been crucial in developing the current standard cosmological model, in which the universe today contains some 5% baryonic matter, 23% dark matter and 72% dark energy, which we refer to as the ΛCDM model. The temperature power spectrum has been measured to good precision for multipole moments $\ell \lesssim 3000$. At angular scales with $\ell \lesssim 2000$, the power spectrum matches the predictions of ΛCDM, and it can be used to constrain multiple parameters of the cosmological model (e.g Sievers et al. [107], Reichardt et al. [108], Brown et al. [149], Dunkley et al. [156]).

At $\ell \gtrsim 3000$, the signal from the primary CMB anisotropy becomes dominated mainly by two populations. The first consists of point source emission from both radio and dusty infrared-emitting galaxies. The second is the population of massive galaxy clusters that give rise to the Sunyaev-Zel'dovich (SZ) effect [59], in which CMB photons scatter off the electrons of the hot intra-cluster medium. Removal of the brightest

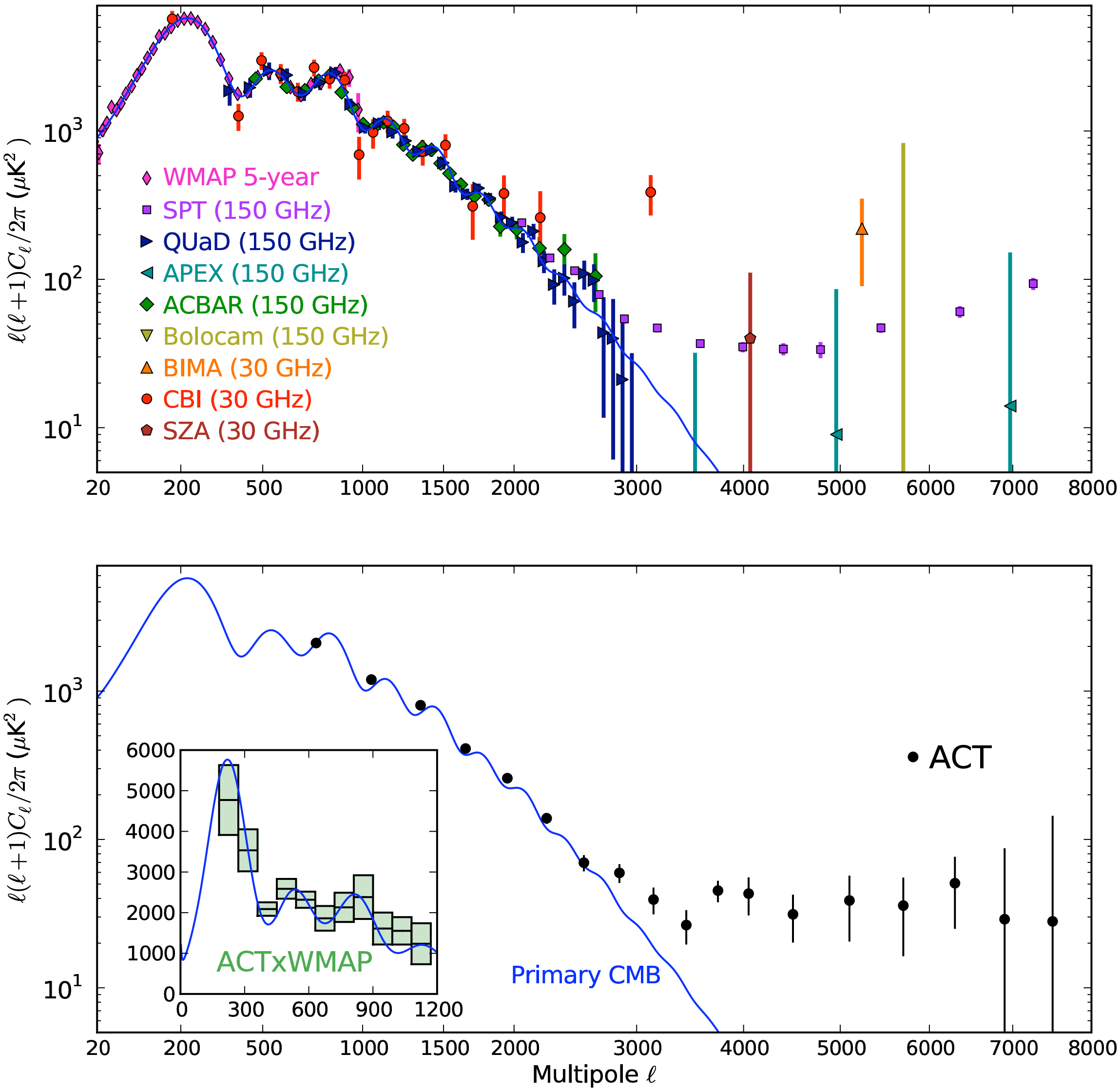

Figure 2.1 Recent measurements of the CMB power spectrum, including this work. *Top:* the measurements of WMAP [147], Bolocam [148], QUaD [149, 150], APEX-SZ [151], ACBAR [108], SZA [152], BIMA [153], CBI [107], and SPT [154]. For all the results, a radio point source contribution has been removed either by masking before computing the power spectrum (at 150 GHz), or by masking and modelling the residual (at 30 GHz and for WMAP). APEX-SZ additionally masks clusters and potential IR sources. *Bottom:* The ACT power spectrum from this work. The inset shows the cross-power spectrum between ACT and WMAP maps in the ACT southern field, which is discussed in Fowler et al. [155]. Only the analysis of the ACT power spectrum is presented in this chapter. In both panels and the inset, the solid curve (blue) is the ΛCDM model of Dunkley et al. [156] (including lensing). The SZ effect and foreground sources are expected to contribute additional power, as shown in Figure 2.2. For display purposes—and only in this figure—we scale our result by 0.96 in temperature relative to the Uranus calibration of the ACT maps.

foreground galaxies and SZ clusters can reduce their contributions to the power spectrum, but the net anisotropy power due to unidentified sources still dominates the exponentially falling primary anisotropy spectrum at small scales.

The top panel of Figure 2.1 shows recent measurements of the anisotropy at $\ell > 2000$. In analyses of 30 GHz data, radio point sources are masked out and a residual component is modelled and subtracted. For 150 GHz analyses, radio sources are masked and the residual radio and dusty galaxy contribution is estimated.

The SZ effect has a unique frequency signature. In CMB temperature units (the units of Figure 2.1) the amplitude at 150 GHz is roughly half that at 30 GHz. The amount of SZ power is governed by σ_8, which measures the amplitude of the cosmic matter power spectrum on $8h^{-1}$ Mpc scales; the SZ power scales approximately as $\sigma_8^7(\Omega_b h)^2$ [157, 158]. At 30 GHz, CBI reports [107] excess emission above the ΛCDM model at $\ell \approx 3000$ after accounting for all known radio sources [159]. A possible source of the "CBI excess" is the SZ effect. The SZA data [152], also at 30 GHz and also after accounting for point sources, are consistent with the ΛCDM model at $\ell = 4000$. The ACBAR results [108] at 150 GHz are consistent with the CBI excess and ΛCDM. Sievers et al. [107] show that all the above data in the top panel of Figure 2.1 are consistent, within 95% CL, with ΛCDM plus a SZ contribution of $\sigma_8 = 0.922 \pm 0.047$ (1σ error bars). Recently, the South Pole Telescope (SPT) group reported $\sigma_8 = 0.773 \pm 0.025$ based on the power spectrum at 150 and 220 GHz [154].

In this chapter, we present a first measurement of the CMB anisotropy power spectrum in the range $600 < \ell < 8000$ (corresponding to angular scales of approximately 1.4′ to 18′). The observations were made at 148 GHz in 2008 with the Atacama Cosmology Telescope. Figure 2.1 (bottom panel) shows the results, which are discussed in Section 2.5. The dynamic range of the power spectrum is large enough that we employ new techniques in spectral estimation. We confirm that difference maps of the data give power spectra consistent with no signal and that the power spectrum is insensitive to several details of our analysis. We use the shape of the power spectrum to bound the dusty galaxy contribution and the power from SZ clusters. In Chapter 3 we will discuss improvements on the cosmological parameter estimation through improved power spectrum measurements and noise treatment.

2.2 INSTRUMENT AND OBSERVATIONS

The Atacama Cosmology Telescope (ACT) is a telescope optimised for arcminute-scale CMB anisotropy measurements [160, 161]. The Millimeter Bolometer Array Camera (MBAC), the current focal-plane instrument for ACT, uses high-purity silicon lenses to reimage sections of the Gregorian focal plane onto three rectangular arrays of detectors. The arrays each contain 1000 transition edge sensor (TES) bolometers. Their spectral coverage is determined by metal-mesh filters [162] having measured band centers of 148 GHz, 218 GHz, and 277 GHz. The bolometers are cooled to 300 mK by a two-stage helium sorption fridge backed by commercial pulse-tube cryocoolers. For more details see Swetz et al. [163] and Fowler et al. [155].

2.3 POWER SPECTRUM METHOD

We estimate the CMB power spectrum using the adaptive multi-taper method (AMTM) with prewhitening, described in Das et al. [119]. We make independent maps from subsets of the data and use only cross-spectra between maps to estimate the final power spectrum. All operations are performed using the flat-sky approximation. We summarise the method in this section.

2.3.1 *Fields Used for Power Spectrum Analysis*

We find the power spectrum of our map by separate analysis of each of the 13 patches used in the ACT analysis. Each patch is $4^\circ.2 \times 4^\circ.2$ in size, and together they cover a rectangular area of the map from $\alpha = 0^{\rm h}48^{\rm m}$ to $6^{\rm h}52^{\rm m}$ (12° to 103°) in right ascension and from $\delta = -55^\circ 16'$ to $-51^\circ 05'$ in declination. This area is the region of a larger survey having the lowest noise. We also split the raw data into four subsets of roughly equal size, with the data distributed so that any four successive nights go into different subsets. The four independent maps generated from these subsets cover the same area and have approximately the same depth. All maps are fully cross-linked. That is, they all contain data taken with the sky both rising and setting.

2.3.2 *Spectrum of a Single Patch*

We estimate the spectra of the 13 patches independently, before taking a weighted average to find the final spectrum. There are four independent sky maps, from which six cross-spectra and four auto-spectra are evaluated on each patch. We use a weighted mean of only the cross-spectra for the final spectral estimate. The weights depend on both the cross- and auto-spectra, as discussed below. Before separating the four maps into 13 patches, each beam-convolved map, $T_b(\boldsymbol{\theta})$, is initially filtered in Fourier space with a high-pass function $F_c(\ell)$. This filter suppresses modes at large scales that are largely unconstrained. These modes arise from a combination of instrument properties, scan strategy, and atmospheric contamination. We choose a squared sine filter, given in Fourier space by the smooth function

$$F_c(\ell) = \begin{cases} 0 & : \quad \ell < \ell_{\rm min} \\ \sin^2 x(\ell) & : \quad \ell_{\rm min} < \ell < \ell_{\rm max} \\ 1 & : \quad \ell < \ell_{\rm max} \end{cases}$$

where $x(\ell) \equiv (\pi/2)(\ell - \ell_{\rm min})/(\ell_{\rm max} - \ell_{\rm min})$. We choose $\ell_{\rm min} = 100$ and $\ell_{\rm max} = 500$. The 13 patches of the map are treated separately from this point. The map of each patch is prewhitened using a local, real-space operation to reduce the dynamic range of its Fourier components [119]. The prewhitening operation involves adding a fraction (2%) of the map to an approximation of its Laplacian. The Laplacian is computed in real space by taking the difference between the map convolved with disks of radius one and three arcminutes respectively. Then the maps are multiplied by the point source mask. The prewhitening step greatly reduces the leakage of power from low to high multipoles caused by the action of the point source mask on the highly coloured CMB power spectrum. The explicit details of the pre whitening method are outlined in Section IV of Das et al. [119].

For each patch, we compute the six 2D cross-spectra and four 2D auto-spectra. The axes correspond to right ascension and declination. Each spectrum is computed using the adaptively weighted multi-taper method, using $N_{\text{tap}} = 5^2$ tapers having resolution parameter $N_{\text{res}} = 3$ (see Das et al. [119]). Windowing the maps with 25 orthogonal taper functions allows us to extract most of the statistical power available in the maps, at the expense of broadening the resolution in angular frequency by a factor of approximately N_{res}. At this stage, each 2D cross-spectrum, $\tilde{C}_\ell^{i\alpha\beta}$, between submaps α and β on patch i incorporates the effects of the filter, prewhitening, tapering, the point source mask, and the beam; they are analogous to a "pseudo power spectrum" of an apodised map (e.g., Hivon et al. [164]). Each 2D spectrum is then averaged in annuli with a narrow range of $|\ell|$ to give the binned pseudo-spectrum $\tilde{\mathcal{B}}_b$, with

$$\tilde{\mathcal{B}}_b^{i\alpha\beta} = P_{b\ell}\tilde{\mathcal{B}}_\ell^{i\alpha\beta}. \tag{2.1}$$

Throughout this thesis we define $\mathcal{B}_\ell \equiv \ell(\ell+1)C_\ell/2\pi$. The binning function $P_{b\ell}$ is set to one for pixels lying in an annular bin (indexed by b) of width $\Delta\ell = 300$ centered on $|\ell| = \ell_b$, and zero elsewhere. The size of the patches and the resolution of the tapers dictates the width of the bins. For our square patches of side $s = 4^\circ.2$, the fundamental frequency resolution in Fourier space is $\Delta\ell = 2\pi/s \approx 90$. The application of the tapers with a resolution parameter $N_{\text{res}} = 3$ further degrades the resolution to $N_{res}\Delta\ell$, so bins chosen to be smaller than $\Delta\ell \sim 270$ would be unavoidably correlated. The binning function is also set to zero where $|\ell_x| < 270$. This region of Fourier space is particularly sensitive to scan-synchronous effects, either fixed to the ground or in phase with the azimuth scan.

The binned pseudo spectrum $\tilde{\mathcal{B}}_b^{i\alpha\beta}$ is then deconvolved with the mode-mode coupling matrix, which takes into account the combined effects of tapering and masking and can be computed exactly. Lastly, we divide by the ℓ-space representations of the prewhitening filter, of the high-pass filter $F_c(\ell_b)$, and of the beam to obtain an unbiased estimate of the true underlying spectrum $\mathcal{B}_b^{i\alpha\beta}$.

This procedure has been tested with simulations. The number and resolution of the tapers are chosen as the optimal balance between maximising information and minimising bias caused by leakage of power. The simulations confirm that increasing the number of tapers beyond 5^2 has a negligible effect on the spectrum errors.

2.3.3 *Combining Patches*

The final power spectrum estimator is given by a weighted mean over $N = 13$ patches,

$$\hat{\mathcal{B}}_b = \frac{\sum_{i=1}^{N} w_b^i \hat{\mathcal{B}}_b^i}{\sum_{i=1}^{N} w_b^i}, \tag{2.2}$$

where[1] $\hat{\mathcal{B}}_b^i \equiv \sum_{\alpha,\beta;\alpha<\beta} \mathcal{B}_b^{i\alpha\beta}/6$ is the mean of the six deconvolved cross-power spectra in patch i (assuming equal weights), and α and β index the four independent maps of that patch. The weights are chosen as the inverse of the variance of this estimator in each patch, i.e. $w_b^i = 1/\sigma^2(\hat{\mathcal{B}}_b^i)$, where

$$\sigma^2(\hat{\mathcal{B}}_b^i) \equiv \left\langle (\hat{\mathcal{B}}_b^i)^2 \right\rangle - \left\langle \hat{\mathcal{B}}_b^i \right\rangle^2 \tag{2.3}$$

and the average is taken over the several cross-spectra computed for patch i. The first term contains the 4-point function of the temperature field and is approximated as,

$$\left\langle (\hat{\mathcal{B}}_b^i)^2 \right\rangle \simeq \frac{2}{M(M-1)} \times \sum_{\substack{\alpha,\beta,\gamma,\delta \\ \alpha<\beta;\gamma<\delta}} (\mathcal{B}_b^{\alpha\beta}\mathcal{B}_b^{\gamma\delta} + \mathcal{B}_b^{\alpha\delta}\mathcal{B}_b^{\beta\gamma} + \mathcal{B}_b^{\alpha\gamma}\mathcal{B}_b^{\beta\delta}), \tag{2.4}$$

where $M = 4$ is the number of submaps per patch. We have neglected any connected (non-Gaussian) part of the 4-point function due to components such as point sources. This is a reasonable approximation when choosing the 13 weights, because the expression (Eq. (2.4)) is dominated by the auto-spectrum terms, which in turn are noise-dominated.

2.4 POWER SPECTRUM RESULTS

The binned estimate of the power spectrum $\hat{\mathcal{B}}_b$ is shown in Figures 2.2 and 2.1. With our method the bandpowers are estimated to have less than 1% correlation with neighboring bins, but the window functions have a small overlap, which we account for in the analysis. At $\ell \lesssim 2500$, the estimated power is consistent with previous observations by ground and balloon-based experiments. The features of the acoustic peaks are not distinguished with the coarse binning, but with the fluctuation band-power measured to 5%, this spectrum offers a powerful probe of cosmological

---

[1] Here we introduce the notation $\hat{X}$ as an unbiased estimator of the quantity X, in the sense $\langle \hat{X} \rangle = X$.

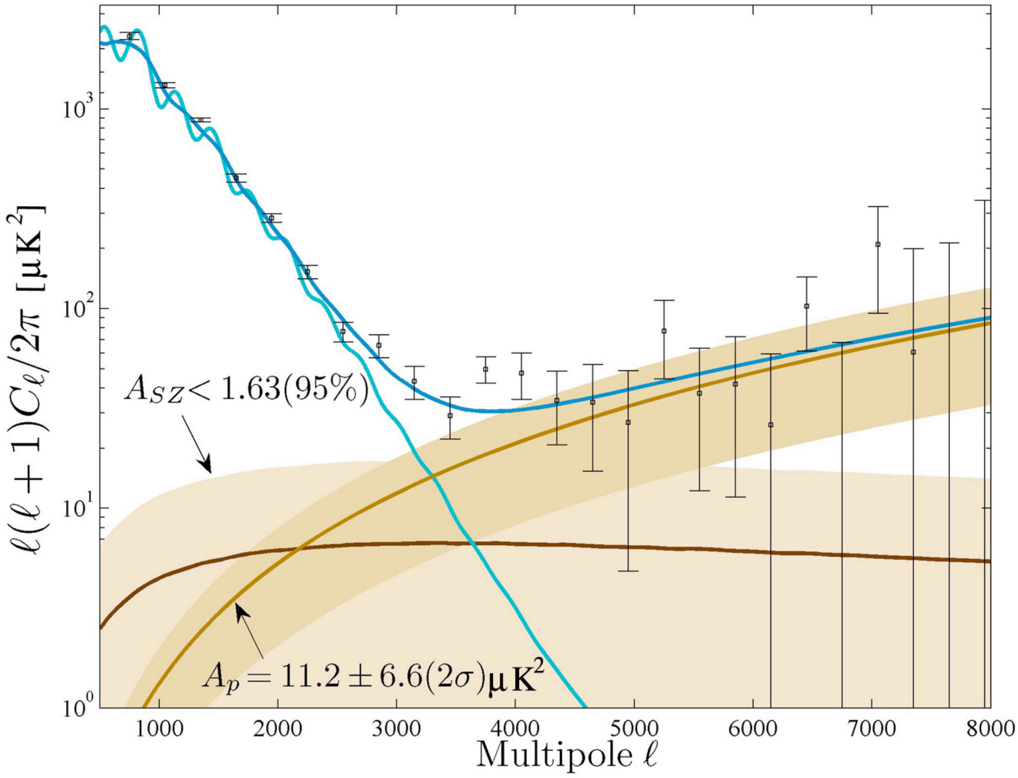

Figure 2.2 The observed power spectrum in bandpowers at 148 GHz from ACT observations (points with error bars). At large angular scales there is good agreement with the lensed ΛCDM model of the primary CMB (light blue curve shown for $\ell < 4700$). The χ^2 of the model is 7.1 for 4 ACT data points in the range $600 < \ell < 1800$. The best-fitting model to the full dataset is shown (dark blue, the highest curve for all $\ell > 2500$). The complete model includes the primary CMB model plus both a Poisson power from point sources and SZ power from clusters; both additional components have been allowed to vary. The complete model has been smoothed by convolution with a boxcar window function of width $\Delta\ell = 300$; the primary CMB model has not been smoothed. The narrower, gold band shows the marginalised 95% CL limits on the Poisson amplitude, while the curve indicates the best-fit amplitude $A_p = 11.9\,\mu\mathrm{K}^2$. The wider pink band shows the 95% CL upper bound on the SZ amplitude, $A_{\rm SZ} < 1.63$; the dark curve inside it shows the best-fit value of $A_{\rm SZ} = 0.63$. The Poisson and SZ power are consistent with higher frequency observations and with ΛCDM predictions. The fitting procedure is described in Section 2.5.

fluctuations on small scales. A clear excess of power is seen at $\ell \gtrsim 2500$ which can be attributed to point sources and, to a lesser extent, to the SZ effect. The large-scale modes are recovered only after iterating the maps. To test for convergence of noiseless maps, we compute the spectra $\hat{C}_b^i$ of difference maps, between the processed simulation map and input simulated sky, at successive iteration numbers i. To account

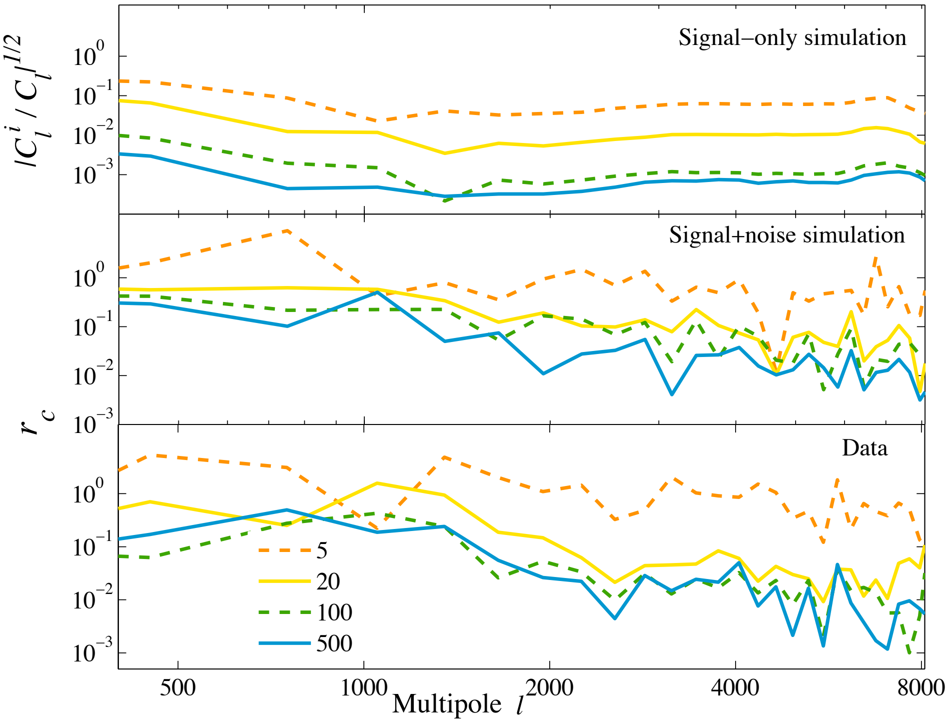

Figure 2.3 Convergence of the maps as a function of iteration. The mapmaking algorithm converges well by iteration 500. For signal-only simulations (*top*), the amplitude of fluctuations in the difference between the processed output map at iteration i and the input map (denoted $\sqrt{C_b^i}$), is less than 1% of the amplitude of fluctuations in the input map ($\sqrt{C_b}$) at all scales by $i = 500$. Iterations $i = 5, 20, 100$, and 500 are shown. For simulations with noise and for the data (*middle and bottom*, respectively), convergence is tested by estimating the maximum change in power between the processed map at iteration i and iteration 1000, as a fraction of the uncertainty in the power in the final map. For iteration 500 this fraction r_c (described in Section 2.4) is sufficiently small, less than 0.5 at all scales.

for differences that are non-uniform between data subsets, we use the auto-spectra. We show that the amplitude of fluctuations in the difference map ($\sqrt{\hat{C}_b^i}$) is small, less than 1% of the amplitude of fluctuations in the input map ($\sqrt{\hat{C}_b}$) at all scales by iteration 500, as shown in Figure 2.3. To test for convergence in the data, where we do not know the input map, we estimate the maximum change in power between the processed map at iteration i and the final iteration, estimated as $\sqrt{2\hat{C}_b^i\hat{C}_b}$ using auto-spectra. Here $\hat{C}_b^i$ is the spectrum of the difference map between iteration i and the final iteration, number 1000. We define the convergence ratio r_c as this change in power given as a fraction of the uncertainty in the power, $\sigma(\hat{C}_b)$, and find it to be sufficiently small (less than 0.5) by iteration 500 at all scales. The cross-correlation

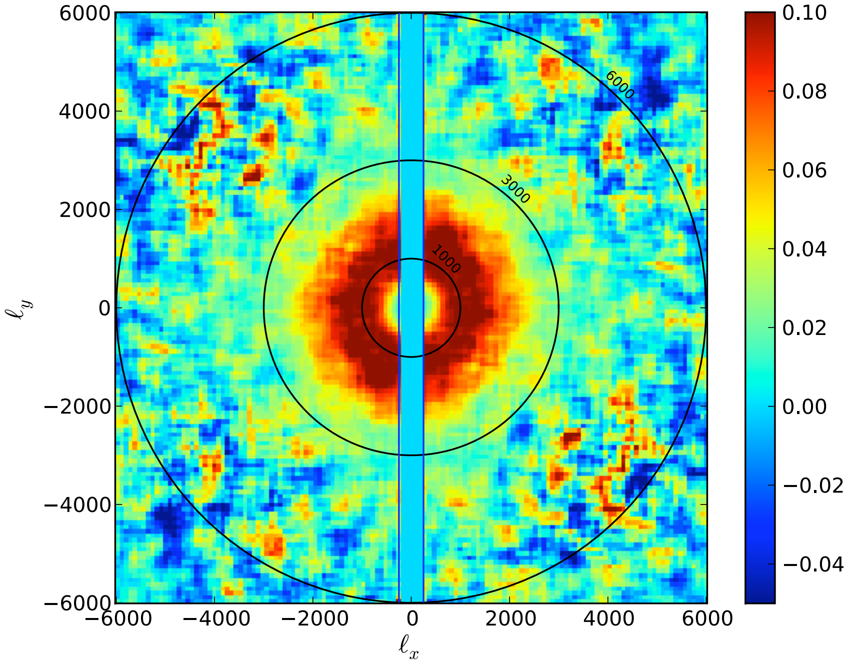

Figure 2.4 The estimated two-dimensional power spectrum C_ℓ, multiplied by a factor of ℓ to emphasise the angular, rather than the radial, variation. The power is consistent with being isotropic, when divided into wedges of $\Delta\theta = 20°$. The vertical lines indicate the narrow region $|\ell_x| < 270$, where excess power from scan-synchronous signals contaminates the power spectrum. This region is not used for the power spectrum analysis. The regions near $(|\ell_x|, |\ell_y|) \approx (4000, 4000)$ are more noisy but not biased. A power spectrum computed without these regions is consistent with the one we present.

with WMAP suggests that the maps are well converged down to $\ell \sim 200$. We do not divide the angular power spectrum by a transfer function at any value of ℓ.

We test the isotropy of the power spectrum by estimating the power as a function of phase $\theta = \tan^{-1}(\ell_y/\ell_x)$. We compute the inverse-noise-weighted two-dimensional pseudo spectrum coadded over map subsets and patches. The mean cross-power pseudo spectrum is shown in Figure 2.4, indicating the region masked at $|\ell_x| < 270$. The spectrum is symmetric for ℓ to $-\ell$, as it is for any real-valued maps. To quantify any anisotropy, the power averaged over all multipoles in the range $500 < \ell < 8000$ is computed in wedges of $\Delta\theta = 20°$. It is found to be consistent with an isotropic 2D spectrum. We test that the signals in separate data subsets are consistent by taking the cross-spectrum of two difference maps formed from the temperature maps, T^i, of

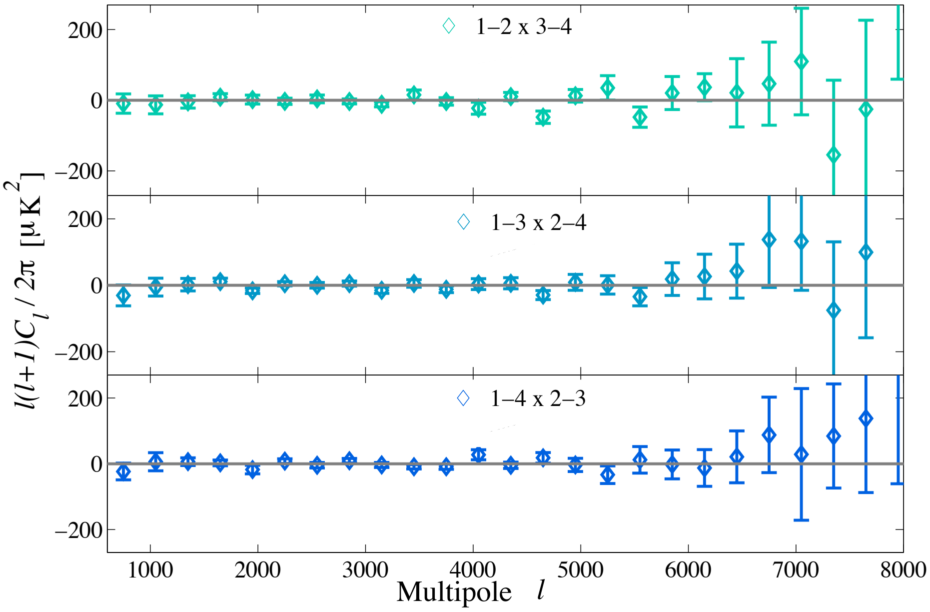

Figure 2.5 Cross-spectra of difference maps formed from four data subsets. In the top panel, two maps $T^{12} \equiv T^1 - T^2$ and $T^{34} \equiv T^3 - T^4$ are formed; both are expected not to contain signal. The cross-spectrum is consistent with no signal. The lower two panels show the same cross-spectra for the other two permutations of the four data subsets and are also consistent with no signal (χ^2 is 25.2, 27.1, and 28.4 in the three panels with 25 degrees of freedom).

the four data subsets via:

$$T^{12}(\hat{n}) \equiv [T^1(\hat{n}) - T^2(\hat{n})]/2 \tag{2.5}$$

$$T^{34}(\hat{n}) \equiv [T^3(\hat{n}) - T^4(\hat{n})]/2. \tag{2.6}$$

The data subsets are described in Section 2.3.1. The difference maps are expected to contain noise but no residual signal. We estimate the cross-spectrum of the difference maps, $\hat{C}_b = \langle \tilde{T}^{12}\tilde{T}^{34} \rangle$ using the methods described in Section 2.3 for $M = 2$ data segments. The two other permutations of the data, $\hat{C}_b = \langle \tilde{T}^{13}\tilde{T}^{24} \rangle$, and $\langle \tilde{T}^{14}\tilde{T}^{23} \rangle$ are also tested. The three difference spectra, shown in Figure 2.5, are consistent with no signal.

2.5 CONSTRAINTS ON SZ AND IR EMISSION

We perform a simple analysis of the power spectrum to quantify the combined contribution from dusty galaxies and radio sources, and the level of SZ emission.

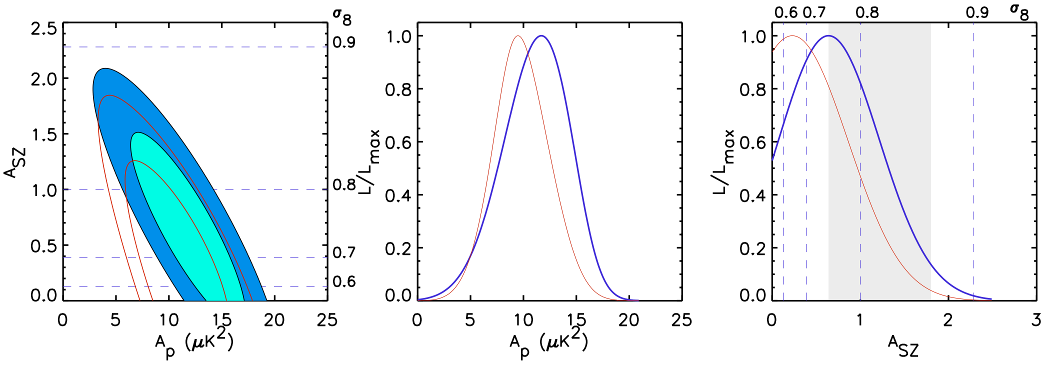

Figure 2.6 Probability distributions for the amplitude A_p of an IR Poisson point source contribution of the form $\mathcal{B}_\ell \equiv \ell(\ell+1)C_\ell/2\pi = A_p(\ell/3000)^2$, and of $A_{\rm SZ}$, the amplitude of the SZ effect relative to that of a model with $\sigma_8 = 0.80$. Each panel shows two models for the point source power spectrum. In one case, we assume the point sources are uncorrelated Poisson-distributed sources. In the second case, we marginalise over the amplitude of a clustered term scaling as $\mathcal{B}_\ell \propto \ell$. *Left:* The two-dimensional distribution of A_p and $A_{\rm SZ}$. The filled (blue) regions assume unclustered sources; the unfilled (red) regions allow for clustered sources. *Center:* The distribution of A_p marginalised over $A_{\rm SZ}$. In the center and right panels, the curve peaking at higher amplitude (blue) assumes uncorrelated sources. The point source power is consistent with SCUBA and BLAST data at higher frequencies. *Right:* The distribution of $A_{\rm SZ}$ marginalised over A_p. The shaded region shows the 95% CL limits on σ_8 inferred from WMAP data combined with distance priors.

We assume a ΛCDM cosmology with lensing of the CMB and parameters from the five-year WMAP analysis combined with BAO and supernovae measurements [165]. A full investigation of cosmological parameter constraints will be given in Chapter 3, which was made possible from improved absolute calibration and a more thorough treatment of astrophysical foregrounds. Our model for the power at 148 GHz is

$$\mathcal{B}_\ell^{\rm th} = \mathcal{B}_\ell^{\rm CMB} + A_{\rm SZ}\mathcal{B}_\ell^{\rm SZ} + A_p\left(\frac{\ell}{3000}\right)^2 + \mathcal{B}_\ell^{corr} \tag{2.7}$$

where $\mathcal{B}_\ell^{\rm CMB}$ is the lensed primary CMB power spectrum; $\mathcal{B}_\ell^{\rm SZ}$ is a template spectrum corresponding to a prediction for the SZ emission in a model with $\sigma_8 = 0.8$ at 148 GHz; A_p quantifies the Poisson point source power, required to be positive; and $\mathcal{B}_\ell^{corr}$ corresponds to clustered point source power from clustered galaxies. The SZ template we use includes the correlated thermal and kinetic SZ (kSZ) effect derived from numerical simulations and is described in detail in Sehgal et al. [63]. Its amplitude is assumed to scale with σ_8 as the seventh power, such that $A_{\rm SZ} = (\sigma_8^{\rm SZ}/0.8)^7$ for fixed baryon density. This accounts approximately for the frequency-dependent combination of the thermal SZ component scaling as the 7.5 to 8th power of σ_8 and the sub-dominant kSZ scaling as the fifth power. The expected point source power C_p is given by

$$C_p = g(\nu)^2 \int_0^{S_{\mathrm{cut}}} S^2 \frac{\mathrm{d}N}{\mathrm{d}S}\,\mathrm{d}S \quad (\mu\mathrm{K}^2\ \mathrm{sr}) \tag{2.8}$$

an integral over all sources with flux S up to some maximum flux S_{cut}, where $g(\nu) \equiv (c^2/2k\nu^2) \times [(\mathrm{e}^x - 1)^2/x^2\mathrm{e}^x]$ converts flux density to thermodynamic temperature, and $x \equiv h\nu/kT_{\mathrm{CMB}}$. Then A_p is the binned $\ell(\ell+1)C_p/2\pi$ Poisson power at pivot $\ell_0 = 3000$. In thermodynamic $\mu\mathrm{K}^2$, $C_p = 0.698 \times 10^{-6} A_p$. The conversion to $\mathrm{Jy}^2\ \mathrm{sr}^{-1}$ at 148 GHz is $C_p\ [\mathrm{Jy}^2\ \mathrm{sr}^{-1}] = 1.55\ C_p\ [10^{-5}\ \mu\mathrm{K}^2\ \mathrm{sr}]$.

The infrared sources are expected to be clustered. At small angles galaxies cluster with typical correlation function $C(\theta) \propto \theta^{-0.8}$ (e.g., Peebles [166]), which would give $C_\ell \propto \ell^{-1.2}$ on non-linear scales. Motivated by this, we first adopt a simple template for the correlated power,

$$\mathcal{B}_\ell^{corr} = A_c \left(\frac{\ell}{3000}\right) \tag{2.9}$$

and fit for the amplitude A_c. Note that on larger scales, $\ell < 300$, $\mathcal{B}_\ell^{corr}$ is expected to flatten and gradually turn over (e.g., Scott and White [167]), but at these scales at 148 GHz the CMB dominates. Models suggest that the power from source clustering is less than the Poisson component at scales smaller than $\ell = 2000$ [167–169]. This is consistent with observations at 600 GHz by BLAST [170, 171]. We therefore impose a prior that the correlated power be less than the Poisson power at $\ell = 3000$, i.e., $0 < A_c < A_p$. This model is likely too simplistic, and the correlated power may have an alternative shape (e.g., Sehgal et al. [63], or the halo model considered in Viero et al. [171]). If the power from dusty galaxies is instead better described by a linear matter power spectrum scaled by a bias factor, $\mathcal{B}_\ell^{corr}$ becomes almost degenerate with the SZ component $\mathcal{B}_\ell^{\mathrm{SZ}}$ (see, e.g., Hall et al. [113]). Since it is not possible to separate these components with data at a single frequency, our limit on the SZ contribution at 148 GHz should be considered as the upper limit on the sum of the SZ power and a degenerate correlated source power. Multi-frequency data will enable us to investigate the shape and amplitude of the correlated component more fully. Given this model, the likelihood of the data is given by

$$-2\ln\mathcal{L} = (\mathcal{B}_b^{th} - \mathcal{B}_b)^{\mathrm{T}}\boldsymbol{\Sigma}^{-1}(\mathcal{B}_b^{th} - \mathcal{B}_b) + \ln\det\boldsymbol{\Sigma}, \tag{2.10}$$

with covariance matrix $\boldsymbol{\Sigma}$ defined from the scatter between 13 patches. The theoretical spectrum B_b^{th} is computed from the model using $\mathcal{B}_b^{th} = w_{b\ell}\mathcal{B}_\ell^{th}$, where $w_{b\ell}$ is an approximate form of the bandpower window function in band b. We marginalise over the calibration uncertainty analytically [172, 173].

The uncertainty on the shape of the window function is small, of order 1.5% for the 148 GHz band, compared to 12% overall calibration uncertainty in power. The window uncertainty is therefore neglected throughout this analysis. We verify that this approximation is valid by including the window function uncertainty in the likelihood calculation. The beam Legendre transform is first expanded in orthogonal basis functions, and the uncertainties on the basis function coefficients are used to derive the window function covariance matrix. The covariance is dominated by a small number of modes, so a singular value decomposition is taken. The ten largest modes are included in the likelihood, following the method described in Appendix A of Hinshaw et al. [118]. We find that including the window function uncertainty has only a negligible effect on parameter estimates ($< 0.05\sigma$). The ACT/MBAC beam measurements and the orthogonal function expansion are described in detail in Hincks et al. [161].

We confirm that the expected values of parameters A_{SZ}, A_p, and A_c are recovered from maps of the ACT simulated sky. We tested simulations with and without noise in the map, and simulations with realistic timestream noise run through the mapper.

Table 2.1 Amplitudes of power from secondary sources

	A_{SZ}	σ_8^{SZ}	$A_p(\ell = 3000)$ [μK^2]	C_p [$10^{-5}\mu$K^2]	C_p [Jy^2 sr^{-1}]	χ^2/dof
Poisson sources	< 1.63	< 0.86	11.2 ± 3.3	0.78 ± 0.23	1.22 ± 0.36	27.0/23
Poisson + correlated sources	< 1.36	< 0.84	9.7 ± 2.8	0.68 ± 0.20	1.05 ± 0.30	26.7/22

In the range $600 < \ell < 1800$, where foreground emission and secondary effects are sub-dominant, the data are consistent with the lensed ΛCDM model alone, with χ^2

= 7.1 for four degrees of freedom (dof). If we rescale the maps to check consistency with the model (multiplying temperatures by 0.96, a 0.7σ change in the calibration), then the χ^2 value becomes 3.0 with 3 dof. We do not rescale the maps in the analysis that follows, though the scale factor is allowed to vary when we marginalised over uncertainties.

Using the full range $600 < \ell < 8100$, we find marginalised constraints on $A_p = 11.2 \pm 3.3\ \mu\mathrm{K}^2$ (thus, $C_p = (0.78 \pm 0.23)\ \times 10^{-5}\ \mu\mathrm{K}^2$) and $A_{\mathrm{SZ}} < 1.63$ (95% CL). The minimum $\chi^2 = 27.0$ for 23 dof. Assuming the scaling of A_{SZ} as $(\sigma_8^{SZ})^7$, this implies an upper limit of $\sigma_8^{\mathrm{SZ}} < 0.86$ (95% CL). The one- and two-dimensional distributions are shown in Figure 2.6, with limits given in Table 2.1. Marginalising over the possible SZ power, ACT detects a residual point source component at 3σ ($\delta\chi^2 = 10$). Marginalising over a correlated term with $A_c < A_p$ gives $A_p = 9.7 \pm 2.8\ \mu\mathrm{K}^2$, and $\sigma_8^{\mathrm{SZ}} < 0.84$ with $\chi^2 = 26.7$ for 22 dof. Because A_c is forced to be positive, its inclusion has the effect of lowering the limits on A_p and A_{SZ}. Nevertheless, we do not find evidence for a correlated component with current sensitivity levels. The estimated parameters vary by less than 0.6σ when the minimum angular scale is varied in the range $5000 < \ell_{max} < 8000$, or the SZ template is replaced by the spectrum of Komatsu and Seljak [158], which is approximately 15% lower than our template in the relevant range of ℓ from 1000–5000. We note that there are multiple models for predicting A_{SZ} (e.g., Bond et al. [174], Kravtsov et al. [175]) and that the relation between A_{SZ} and σ_8 is an active area of research.

We also combine the ACT spectrum with the WMAP 5-year data [156] to constrain the six-parameter ΛCDM model (defined by the baryon density, cold dark matter density, cosmological constant, optical depth to reionization, and the amplitude and scale dependence of primordial fluctuations at $k = 0.002$ Mpc^{-1}). We model the SZ and point source contribution using Equation 3.12, neglecting a correlated component. We find similar results for the point source and SZ amplitude in this extended model, with $A_p = 11.5 \pm 3.2$, and $A_{\mathrm{SZ}} < 1.66$ (95% CL). The ΛCDM parameters are consistent with WMAP alone, with $100\Omega_b h^2 = 2.27 \pm 0.06$, $\Omega_c h^2 = 0.111 \pm 0.006$, $\Omega_\Lambda = 0.738 \pm 0.030$, $n_s = 0.964 \pm 0.014$, $\tau = 0.086 \pm 0.017$, and $10^9 A_s = 2.4 \pm 0.1$.

2.5.1 *Comparison to Other Point Source Observations*

The residual source level, $C_p = (0.78 \pm 0.23)\ \times 10^{-5}\,\mu\mathrm{K}^2$, combines power from radio sources and dusty galaxies that were not removed by the mask. We consider three radio source models, namely Toffolatti et al. [176], de Zotti et al. [177] and Sehgal et al. [63], details are given in Fowler et al. [155]. We expect residual power of $A_p = 6.4\,\mu\mathrm{K}^2$ ([176], after rescaling by 0.4), $A_p = 4.1\,\mu\mathrm{K}^2$ de Zotti et al. [177], and $A_p = 7\,\mu\mathrm{K}^2$ [63]. These models' amplitudes correspond to $C_p^{\mathrm{Radio}} = 0.43, 0.29,$ and $0.49 \times 10^{-5}\,\mu\mathrm{K}^2$ respectively. The correction for those few sources below 20 mJy that we mask can be neglected; it is smaller than the spread among the models. Given the uncertainties in the models, we subtract the typical model from the total source level and infer that the component from residual IR sources lies in the approximate range $0.2\ \mu\mathrm{K}^2 \lesssim C_p^{\mathrm{IR}} \times 10^5 \lesssim 1\,\mu\mathrm{K}^2$.

The ACT result on total point source power is similar to those of APEX at 150 GHz, which finds $C_p = 1.1^{+0.9}_{-0.8}\ \times 10^{-5}\,\mu\mathrm{K}^2$ [151], of ACBAR ($C_p = 2.7^{+1.1}_{-2.6}\ \times 10^{-5}\,\mu\mathrm{K}^2$, Reichardt et al. [108]), and SPT ($C_p = (0.74 \pm 0.06) \times 10^{-5}\,\mu\mathrm{K}^2$, Hall et al. [113]). This last measurement employs a lower flux level for removing discrete sources: 6.4 mJy versus our cut at 20 mJy. While this difference means that the C_p presented will contain roughly three times as much power from radio sources as the SPT measurement, we nevertheless find that the total residual power due to point sources is consistent between the two results, given the conservative assumption that at least one-quarter of the point source power observed by ACT is due to dusty galaxies rather than to radio sources.

The IR source models in the literature for 148 GHz make a range of predictions. For example, for sources less than 20 mJy the Lagache et al. [178] model gives $C_p = 40 \times 10^{-5}\,\mu\mathrm{K}^2$, the Negrello et al. [168] model gives $C_p = 1.2\ \times 10^{-5}\,\mu\mathrm{K}^2$, and the Sehgal et al. [63] model gives $C_p = 17.5\ \times 10^{-5}\,\mu\mathrm{K}^2$. The best agreement comes with the Negrello et al. [168] model.

The emission from dusty galaxies in the rest frame can be modelled as $S_0(\nu) \propto \nu^{\beta} B_\nu(T)$, with emissivity index $\beta \sim 1.5$ and Planck function $B_\nu(T)$. The effective index α, where

$S(\nu) \propto \nu^{\alpha}$ ($C_\ell \propto \nu^{2\alpha}$), accounts for the redshift of the sources, the intrinsic temperature variation T, and the index β. SCUBA has observed emission at 850 μm (353 GHz), where we expect a similar population of galaxies to contribute (e.g., Greve et al. [179, 180]). Using SCUBA galaxy number counts and a model for dN/dS, Scott and White [167] estimate the Poisson power to be $C_p = 730\times10^{-5}\,\mu\mathrm{K}^2$ (190 $\mathrm{Jy}^2\ \mathrm{sr}^{-1}$) for $S_{\mathrm{cut}} = 50\,\mathrm{mJy}$. Combined with residual IR source level observed by ACT, this implies an effective spectral index of $\alpha_{150-350}$ between 2.6–3.3. This is consistent with emission from dusty star-burst galaxies at high redshift and in line with predictions by White and Majumdar [181] and Negrello et al. [168]. It also agrees with the $\alpha = 2.6 \pm 0.6$ index inferred from source fluxes measured with MAMBO (1.2 mm) and SCUBA (850 μm) [179], and with $\alpha = 2.3$ measured from AZTEC (1.1 mm) and SCUBA [182]. Observations by BLAST at 500 μm (600 GHz) have Poisson power $(2.7 \pm 0.2) \times 10^3\ \mathrm{Jy}^2\ \mathrm{sr}^{-1}$ [171]. Combining this with the ACT data leads to an estimate of the effective index $2.7 \lesssim \alpha_{150-600} \lesssim 3.6$, consistent with findings by APEX. The consistency with $\alpha_{150-350}$ suggests that similar populations are being probed at these frequencies, although BLAST is sensitive to a lower redshift range than ACT.

2.5.2 *Comparison to other SZ observations*

The ACT constraints on the SZ power indicate an amplitude of fluctuations $\sigma_8^{\mathrm{SZ}} < 0.86$ (95% CL). This result is consistent with estimates that combine the primordial CMB anisotropy with distance measures, $\sigma_8 = 0.81 \pm 0.03$ [165], and improves on SZ-inferred limits at 150 GHz from Bolocam ($\sigma_8^{\mathrm{SZ}} < 1.57$) [148], Boomerang ($\sigma_8^{\mathrm{SZ}} < 1.14$ at 95% CL) [183], and APEX ($\sigma_8^{\mathrm{SZ}} < 1.18$) [151]. We do not see evidence for an excess of SZ power, in contrast to lower frequency observations by CBI at 30 GHz which prefer a value 2.5σ higher than the concordance value ($\sigma_8^{\mathrm{SZ}} = 0.922 \pm 0.047$, [107]).

The ACT result is also consistent with the recently reported $\sigma_8^{\mathrm{SZ}} = 0.773 \pm 0.025$ ($A_{\mathrm{SZ}} = 0.42 \pm 0.21$) from the South Pole Telescope [184]. The SPT team prefers a form for the correlated point sources that is covariant with the SZ template in the $\ell = 3000$ range [113]. If such a form is correct, then the A_{SZ} we report should be interpreted as an upper limit on correlated point sources plus the SZ effect. Analysis of the ACT's 218 and 277 GHz data will shed light on possible forms of the correlated component.

The ACT results on σ_8 are also consisent with several recent studies based on the analysis of ROSAT X-ray flux-selected clusters. We note that these X-ray cluster studies themselves are consistent with measures of σ_8 from richness or weak-lensing selected cluster samples. There is slight tension between the results of Henry et al. [185], who find $\sigma_8(\Omega_m/0.32)^{0.30} = 0.86 \pm 0.04$ (for $\Omega_m < 0.32$) using cluster gas temperatures measured with the ASCA satellite. Vikhlinin et al. [186] however, obtain $\sigma_8(\Omega_m/0.25)^{0.47} = 0.813 \pm 0.013\,(stat) \pm 0.024\,(sys)$ using temperatures derived from Chandra observations, which is In better agreement with our findings. Similarly, Mantz et al. [187] find that in spatially flat models with a constant dark energy equation of state, ROSAT X-ray flux-selected clusters yield $\Omega_m = 0.23 \pm 0.04$, $\sigma_8 = 0.82 \pm 0.05$.

2.6 DISCUSSION

We have presented an initial power spectrum C_ℓ, of the CMB sky made using data from the Atacama Cosmology Telescope at 148 GHz over a range of power exceeding 10^4.

We interpreted the spectrum with a simple model composed of the primary CMB, a possible SZ contribution, and uncorrelated point sources. This analysis provides a new upper bound on the SZ signal from clusters ($\sigma_8^{SZ} < 0.86$ at 95% CL, though this is subject to uncertainty in the SZ models).

These high angular resolution measurements probe the microwave power spectrum out to arcminute scales. Above $\ell \sim 2500$, the spectrum is sensitive to non-linear processes such as the formation of galaxy clusters and dusty galaxies. On the low-ℓ end, the spectrum measures the Silk damping tail of the CMB which can be computed using linear perturbation theory as applied to the primordial plasma. It is clear that to understand the $\ell \gtrsim 1000$ end of the primary CMB, and thus to improve significantly on measurements of the scalar spectral index and its running, source modelling will be required. We present such improved constraints in Chapter 3.

3

COSMOLOGICAL PARAMETERS FROM THE POWER SPECTRUM OF THE 2008 SOUTHERN SURVEY

3.1 INTRODUCTION

In this chapter we present cosmological parameter constraints from improved power spectra estimated from the ACT 2008 observing season of the southern sky. This builds on the initial results presented in Chapter 2 in that we use the ACT data to constrain cosmological parameters using the power spectrum up to $\ell \simeq 2500$, and in addition tighten constraints on the parameters which describe the model for secondary anisotropies, relative to previous work. Improved map-making and power spectrum estimates, with use of a larger area of sky, now allow us to place new constraints on cosmological models. We combine the ACT 148 GHz data with WMAP observations, and additional cosmological distance measures, to constrain the ΛCDM model and a set of extensions that have particular effects at small scales.

This work in this chapter was published in Dunkley et al. [33] as one of a set of papers on the ACT 2008 data in the southern sky: Swetz et al. [188] describes the ACT experiment; Dünner [189] describes the observing strategy and the data; Hajian et al. [190] describes the calibration to WMAP; Das et al. [69] presents the power spectra measured at 148 GHz and 218 GHz, and this chapter estimates parameters from the power spectrum results. A high-significance SZ galaxy cluster catalog is presented in Marriage et al. [191], with multi-wavelength observations described in Menanteau et al.

[192] and their cosmological interpretation in Sehgal et al. [193]. Marriage et al. [194] presents the 148 GHz point source catalog. The chapter is structured as follows: in Section 3.2 we describe the ACT likelihood and parameter estimation methodology. In Section 3.3 we present results on SZ and point source parameters from the small-scale power spectra. In Section 3.4 we present constraints on a set of cosmological models in combination with other cosmological data, and conclude in Section 3.6.

3.2 METHODOLOGY

This section describes the methods used to estimate parameters from the ACT power spectra. We will estimate two sets of parameters: 'primary' and 'secondary'. Primary parameters describe the cosmological model from which a theoretical primary CMB power spectrum can be computed. Secondary parameters describe the additional power from SZ fluctuations and foregrounds. We construct an ACT likelihood function that returns the probability of the ACT data given some theoretical CMB power spectrum and a set of secondary parameters. Primary and secondary parameters are then estimated from ACT and additional datasets using Markov Chain Monte Carlo (MCMC) methods. The ACT likelihood function is described in Section 3.2.1, and the MCMC methods in 3.2.2.

3.2.1 *ACT Likelihood*

For maps of temperature fluctuations at 148 GHz and 218 GHz, three cross-spectra are estimated in bands in the range $500 < \ell < 10000$ for 148 GHz, and $1500 < \ell < 10000$ for both the 218 GHz and the 148×218 GHz cross-spectrum (see Das et al. [69]). A likelihood function is constructed to estimate parameters from these spectra. The function returns the likelihood of the data, $p(d|C_\ell^{\mathrm{CMB}}, \Theta)$, given a theoretical lensed CMB spectrum, C_ℓ^{CMB}, and a set of secondary parameters describing the additional small-scale power, Θ. In this analysis we consider two likelihoods: the '148+218' likelihood, which returns the likelihood of all three spectra given a model, and the '148-only' likelihood, which returns the likelihood of just the 148 GHz spectrum given a model.

The temperature fluctuations in the ACT maps are expected to be the sum of fluctuations from lensed CMB, thermal and kinetic SZ, radio point sources, infrared point sources, and thermal dust emission from the Galaxy (see e.g., Sehgal et al. [63]). These vary as functions of frequency. The lensed CMB and the kinetic SZ are blackbody emission, and so are constant as a function of frequency in thermodynamic units. The thermal SZ emission has a known frequency dependence [59] and has negligible contribution at 218 GHz. The radio point sources emit synchrotron, and the IR sources emit thermally, so both can be modelled as following power law emission in flux given a narrow enough frequency range. For frequency ν and direction $\hat{\mathbf{n}}$ the signal in the maps can be modelled in thermal units as

$$\Delta T(\nu, \hat{\mathbf{n}}) = \Delta T^{\mathrm{CMB}}(\hat{\mathbf{n}}) + \Delta T^{\mathrm{SZ}}(\nu, \hat{\mathbf{n}}) + \Delta T^{\mathrm{fg}}(\nu, \hat{\mathbf{n}}) \tag{3.1}$$

with lensed CMB fluctuations $\Delta T^{\mathrm{CMB}}(\hat{\mathbf{n}})$. The SZ signal is the sum of thermal and kinetic components

$$\Delta T^{\mathrm{SZ}}(\nu, \hat{\mathbf{n}}) = \frac{f(\nu)}{f(\nu_0)} \Delta T_0^{\mathrm{tSZ}}(\hat{\mathbf{n}}) + \Delta T^{\mathrm{kSZ}}(\hat{\mathbf{n}}), \tag{3.2}$$

where the factor $f(\nu) = 2 - (x/2)/\tanh(x/2)$, for $x = h\nu/k_B T_{\mathrm{CMB}}$, converts the expected SZ emission from the Rayleigh-Jeans (RJ) limit to thermodynamic units, and $\Delta T_0^{\mathrm{tSZ}}$ is the expected signal at frequency ν_0. At 218 GHz there is negligible thermal SZ signal, with $f(218) = 0$. The point source and Galactic components are modelled as

$$\Delta T^{\mathrm{fg}}(\nu, \hat{\mathbf{n}}) = \frac{g(\nu)}{g(\nu_0)} \left\{ \Delta T_0^{\mathrm{IR}} \left(\frac{\nu}{\nu_0}\right)^{\alpha_d - 2} + \Delta T_0^{\mathrm{rad}} \left(\frac{\nu}{\nu_0}\right)^{\alpha_s - 2} + \Delta T_0^{\mathrm{Gal}} \left(\frac{\nu}{\nu_0}\right)^{\alpha_g - 2} \right\} \tag{3.3}$$

assuming that the IR and radio source emission in antenna temperature, $\Delta T_0^{\mathrm{IR,rad}}$, scale with global power laws $\alpha_d - 2$ and $\alpha_s - 2$, respectively, where α is the index in flux units. The factor $g(\nu) = (e^x - 1)^2/x^2 e^x$ converts from antenna to CMB thermodynamic temperature at frequency ν. The factors are $g = (1.71, 3.02)$ for 148 GHz and 218 GHz. Power law behavior is also assumed for the Galactic dust emission $\Delta T_0^{\mathrm{Gal}}$. This behavior is expected to be a good approximation between 148 GHz and 218 GHz, but breaks down over larger frequency ranges.

To compute the likelihood one could first estimate the CMB map, by subtracting off the foreground and SZ components. This is commonly done in CMB analyses for subtracting Galactic components (e.g., Bennett et al. [195]), and has also been used for subtracting the IR point sources [113, 154]. However, for the ACT frequencies and noise levels the radio sources cannot be neglected, so a linear combination of the 148 GHz and 218 GHz maps will not remove all the source contamination. Instead, we choose to construct a model for the cross power spectra between frequency ν_i and ν_j,

$$C_\ell^{ij} = \left\langle \widetilde{T}_\ell^*(\nu_i)\widetilde{T}_\ell(\nu_j) \right\rangle \tag{3.4}$$

where $\widetilde{T}_\ell$ is the Fourier transform of $\Delta T(\hat{\mathbf{n}})$. For ACT analysis we use a flat-sky approximation, described in Das et al. [69]. The individual components are assumed to be uncorrelated, so the theoretical cross-spectrum $\mathcal{B}_\ell^{\mathrm{th},ij}$ is modelled from Eq. (3.1) as

$$\mathcal{B}_\ell^{\mathrm{th},ij} = \mathcal{B}_\ell^{\mathrm{CMB}} + \mathcal{B}_\ell^{\mathrm{tSZ},ij} + \mathcal{B}_\ell^{\mathrm{kSZ},ij} + \mathcal{B}_\ell^{\mathrm{IR},ij} + \mathcal{B}_\ell^{\mathrm{rad},ij} + \mathcal{B}_\ell^{\mathrm{Gal},ij} \tag{3.5}$$

where $\mathcal{B}_\ell \equiv \ell(\ell+1)C_\ell/2\pi$ is defined as in Chapter 2. The first term, $\mathcal{B}_\ell^{\mathrm{CMB}}$, is the lensed primary CMB power spectrum and is the same at all frequencies. The thermal SZ (tSZ) power is modelled as

$$\mathcal{B}_\ell^{\mathrm{tSZ},ij} = A_{\mathrm{tSZ}} \frac{f(\nu_i)}{f(\nu_0)} \frac{f(\nu_j)}{f(\nu_0)} \mathcal{B}_{0,\ell}^{\mathrm{tSZ}} \tag{3.6}$$

where $\mathcal{B}_{0,\ell}^{\mathrm{tSZ}}$ is a template power spectrum corresponding to the predicted tSZ emission at ν_0 =148 GHz for a model with $\sigma_8 = 0.8$, to be described in Section 3.2.1.2, and A_{tSZ} is an amplitude parameter. The kinetic SZ (kSZ) power is modelled as

$$\mathcal{B}_\ell^{\mathrm{kSZ},ij} = A_{\mathrm{kSZ}} \mathcal{B}_{0,\ell}^{\mathrm{kSZ}} \tag{3.7}$$

where $\mathcal{B}_{0,\ell}^{\mathrm{kSZ}}$ is a template spectrum for the predicted blackbody kSZ emission for a model with $\sigma_8 = 0.8$, also described in Section 3.2.1.2. The total SZ power is then given by

$$\mathcal{B}_\ell^{\mathrm{SZ},ij} = A_{\mathrm{tSZ}} \frac{f(\nu_i)}{f(\nu_0)} \frac{f(\nu_j)}{f(\nu_0)} \mathcal{B}_{0,\ell}^{\mathrm{tSZ}} + A_{\mathrm{kSZ}} \mathcal{B}_{0,\ell}^{\mathrm{kSZ}}. \tag{3.8}$$

The infrared point sources are expected to be clustered, and their power is modelled as

$$\mathcal{B}_\ell^{\mathrm{IR},ij} = \left[A_d \left(\frac{\ell}{3000} \right)^2 + A_c \mathcal{B}_{0,\ell}^{\mathrm{clust}} \right] \frac{g(\nu_i)}{g(\nu_0)} \frac{g(\nu_j)}{g(\nu_0)} \left(\frac{\nu_i}{\nu_0} \frac{\nu_j}{\nu_0} \right)^{\alpha_d - 2} \tag{3.9}$$

where A_d and A_c are the values of $\mathcal{B}_{3000}^{\mathrm{IR}}$ at 148 GHz for Poisson and clustered dust terms respectively, assuming a normalised template spectrum $\mathcal{B}_{0,\ell}^{\mathrm{clust}}$. This will be described in Section 3.2.1.3. This model assumes the same spectral index for the clustered and Poisson IR power. The radio sources are not expected to be significantly clustered (see, e.g., Hall et al. [113], Sharp et al. [196]), and so can be described by Poisson scale-free power, with

$$\mathcal{B}_{\ell}^{\mathrm{rad},ij} = A_s \left(\frac{\ell}{3000}\right)^2 \frac{g(\nu_i)}{g(\nu_0)} \frac{g(\nu_j)}{g(\nu_0)} \left(\frac{\nu_i}{\nu_0} \frac{\nu_j}{\nu_0}\right)^{\alpha_s - 2} \tag{3.10}$$

with amplitude A_s normalised at ν_0 =148 GHz and $\ell = 3000$.

Though we have described the pivot frequency as ν_0 =148 GHz for all components in Equations (3.6-3.10), in practice we use the band-centers for SZ, radio and dusty sources given in Table 4 of Swetz et al. [188]. The Galactic emission, $\mathcal{B}_{\ell}^{\mathrm{Gal},ij}$, is expected to be sub-dominant on ACT scales, as demonstrated in Das et al. [69] using the FDS dust map [197] as a Galactic dust template. A correlation between the ACT and FDS maps is observed, but implies a Galactic dust contribution of $\mathcal{B}_{3000} < 0.5\ \mu K^2$ at 148 GHz, at least an order of magnitude smaller than the expected SZ signal. It is therefore neglected in this analysis.

Given SZ and clustered source templates, aside from parameters constrained by $\mathcal{B}_{\ell}^{\mathrm{CMB}}$, this model has 7 free parameters: five amplitudes A_{tSZ}, A_{kSZ}, A_d, A_c, A_s, and two spectral indices, α_d, α_s. As we will describe in Sec 2.2.1, we impose priors on some of these and constrain others. We refer to these parameters as 'secondary' parameters, to distinguish them from 'primary' cosmological parameters describing the primordial fluctuations. In part of the analysis we will estimate parameters from the 148 GHz spectrum alone. In this case $i = j$ and $\nu_i = \nu_0$. The model in Eq. (3.5) then simplifies to

$$\mathcal{B}_{\ell}^{\mathrm{th}} = \mathcal{B}_{\ell}^{\mathrm{CMB}} + A_{\mathrm{tSZ}}\mathcal{B}_{0,\ell}^{\mathrm{tSZ}} + A_{\mathrm{kSZ}}\mathcal{B}_{0,\ell}^{\mathrm{kSZ}} + (A_s + A_d)\left(\frac{\ell}{3000}\right)^2 + A_c\mathcal{B}_{0,\ell}^{\mathrm{clust}}. \tag{3.11}$$

This can be further simplified to

$$\mathcal{B}_{\ell}^{\mathrm{th}} = \mathcal{B}_{\ell}^{\mathrm{CMB}} + A_{\mathrm{SZ}}\mathcal{B}_{0,\ell}^{\mathrm{SZ}} + A_p\left(\frac{\ell}{3000}\right)^2 + A_c\mathcal{B}_{0,\ell}^{\mathrm{clust}} \tag{3.12}$$

where $A_p = A_s + A_d$ is the total Poisson power at $\ell = 3000$, and $A_{\mathrm{SZ}} = A_{\mathrm{kSZ}} = A_{\mathrm{tSZ}}$ measures the total SZ power, $\mathcal{B}_{0,\ell}^{\mathrm{SZ}} = \mathcal{B}_{0,\ell}^{\mathrm{tSZ}} + \mathcal{B}_{0,\ell}^{\mathrm{kSZ}}$. The assumption underlying the simplification of the SZ treatment is that the thermal and kinetic SZ spectra have the same dependence on cosmology, and so the relative amplitude between the two contributions is fixed - hence one can simplify the analysis and measure the total SZ power from the sum of the templates. This is the same parameterisation considered in Chapter 2, and has just three secondary parameters: $A_{\rm SZ}$, A_p and A_c.

Using this model, we can compute the theoretical spectra for a given set of secondary parameters Θ, and for a given theoretical CMB temperature power spectrum. The data power spectra are not measured at every multipole, so bandpower theoretical spectra are computed using $C_b^{{\rm th},ij} = w_{b\ell}^{ij} C_\ell^{{\rm th},ij}$, where $w_{b\ell}^{ij}$ is the bandpower window function in band b for cross-spectrum ij, described in Das et al. [69][1]. The data power spectra have calibration uncertainties (to be described in Sec 3.2.1.1). To account for these uncertainties we include two calibration parameters $y(\nu_i)$, for each map i, that scale the estimated data power spectra, $\hat{C}_b^{ij}$, and their uncertainties, as

$$C_b^{ij} = y(\nu_i) y(\nu_j) \hat{C}_b^{ij}. \tag{3.13}$$

The likelihood of the calibrated data is then given by

$$-2\ln\mathscr{L} = (C_b^{\rm th} - C_b)^{\rm T} \mathbf{\Sigma}^{-1} (C_b^{\rm th} - C_b) + \ln\det\mathbf{\Sigma} \tag{3.14}$$

assuming Gaussian uncertainties on the measured bandpowers with covariance matrix $\mathbf{\Sigma}$. For the 148+218 likelihood the model and data vectors $C_b^{\rm th}$ and C_b contain three spectra, $C_b = [C_b^{148,148}, C_b^{148,218}, C_b^{218,218}]$. For the 148-only likelihood, $C_b = C_b^{148,148}$. We use the data between $500 < \ell < 10000$ for the 148 × 148 GHz auto-spectrum, but restrict the range to $1500 < \ell < 10000$ for the 218 × 218 GHz and the 148 × 218 GHz spectra. This range is chosen since for 148 GHz at scales larger than $\ell = 500$ the signal cannot be accurately separated from atmospheric noise, and for 218 GHz the maps do not converge below $\ell = 1500$, described in Das et al. [69]. The bandpower covariance matrix $\mathbf{\Sigma}$ is described in the Appendix of Das et al. [69], and includes correlations between the three spectra. Das et al. [69] demonstrates with Monte-Carlo simulations that the covariance is well modelled by a Gaussian distribution with negligible correlation between bands.

---

[1] Here we use the notation $w_{b\ell}$ for the bandpower window functions; Das et al. [69] uses $B_{b\ell}$.

3.2.1.1 Calibration and Beam Uncertainty

The ACT calibration is described in Hajian et al. [190]. The 148 GHz maps are calibrated using WMAP, resulting in a 2% map calibration error in temperature units, at effective $\ell = 700$. The 218 GHz maps are calibrated using observations of Uranus, with a 7% calibration error at $\ell = 1500$. The two calibration errors have negligible covariance, and are treated as independent errors. For analyses using 148 GHz data alone we marginalise over the calibration uncertainty analytically following Ganga et al. [172] and Bridle et al. [173]. For joint analyses with the 148 GHz and 218 GHz data we explicitly sample the calibration parameters $y(\nu_i)$ with Gaussian priors of $y(148) = 1.00 \pm 0.02$ and $y(218) = 1.00 \pm 0.07$. We check that the analytic and numerical marginalisation methods give the same results for 148 GHz.

The beam window functions are described in Das et al. [69], and are estimated using maps of Saturn. The maps are made with an independent pipeline to the initial ACT beam estimates made in Hincks et al. [161], but produce consistent results. The uncertainties on the beam window functions are of order 0.7% for the 148 GHz band and 1.5% at 218 GHz. Uncertainties in the measured beams are incorporated using a likelihood approximation described in Appendix A of Dunkley et al. [33]. The magnitude of the derived uncertainties is consistent with Hincks et al. [161] and the uncertainties used in the parameter estimation in Chapter 2.

3.2.1.2 SZ Templates

The thermal SZ template $\mathcal{B}^{\rm tSZ}_{0,\ell}$ describes the power from tSZ temperature fluctuations from all clusters, normalised for a universe with amplitude of matter fluctuations $\sigma_8 = 0.8$. There is uncertainty in the expected shape and amplitude of this signal, arising due to incomplete knowledge of the detailed gas physics that affects the integrated pressure of the clusters. Previous cosmological studies, e.g., the ACBAR and CBI experiments, have used templates derived from hydrodynamical simulations [174]. The analysis for WMAP used the analytic Komatsu-Seljak (K-S) spectrum derived from a halo model [198]. Recent studies for SPT have considered simulations and analytic templates from Sehgal et al. [63] and Shaw et al. [199].

In this analysis we use the thermal SZ templates from Sehgal et al. [63][2]. Trac, Bode, and Ostriker [200] constructed several templates by processing a dark matter simulation to include gas in dark matter halos and in the filamentary intergalactic medium. Their 'standard' model, which was first described in Sehgal et al. [63], is referred to here as 'TBO-1'. It is based on the gas model in Bode, Ostriker, and Vikhlinin [201], with the hot gas modelled with a polytropic equation of state and in hydrostatic equilibrium, with star formation and feedback calibrated against observations of local clusters. This is the template considered in the ACT analysis presented in Chapter 2, and has a similar amplitude and shape to the K-S spectrum.

In addition to uncertainties in the shape and amplitude of the thermal SZ power, the shape and amplitude of the expected kinetic SZ power spectrum is highly uncertain. We use the kSZ template described in Sehgal et al. [63], also shown in Figure 3.1. The corresponding template for the 'nonthermal20' model in Trac, Bode, and Ostriker [200] has a similar amplitude. It is also consistent with predictions from second order perturbation theory [202]. In this analysis the contamination of the SZ signal by point sources is neglected, which is shown in Lin et al. [203] to be a good approximation for radio galaxies. Lueker et al. [154] show it is also a good assumption for IR sources for the current levels of sensitivity.

3.2.1.3 Clustered Source Template

The shape and amplitude of the power spectrum of clustered dusty galaxies are not yet well characterised [113, 204–206], although there have been measurements made by Viero et al. [206] from the BLAST experiment. In Chapter 2 we adopted a simple power law model, with $\mathcal{B}_\ell \propto \ell$. In this analysis we move beyond this simple parameterisation by using model templates[3]. The 'Src-1' template is obtained from the infrared source

---

[2] In this thesis we will only discuss one source and one SZ model, further models are tested in Dunkley et al. [33].

[3] For this thesis we will only discuss one source model and one SZ model, further models are tested in Dunkley et al. [33].

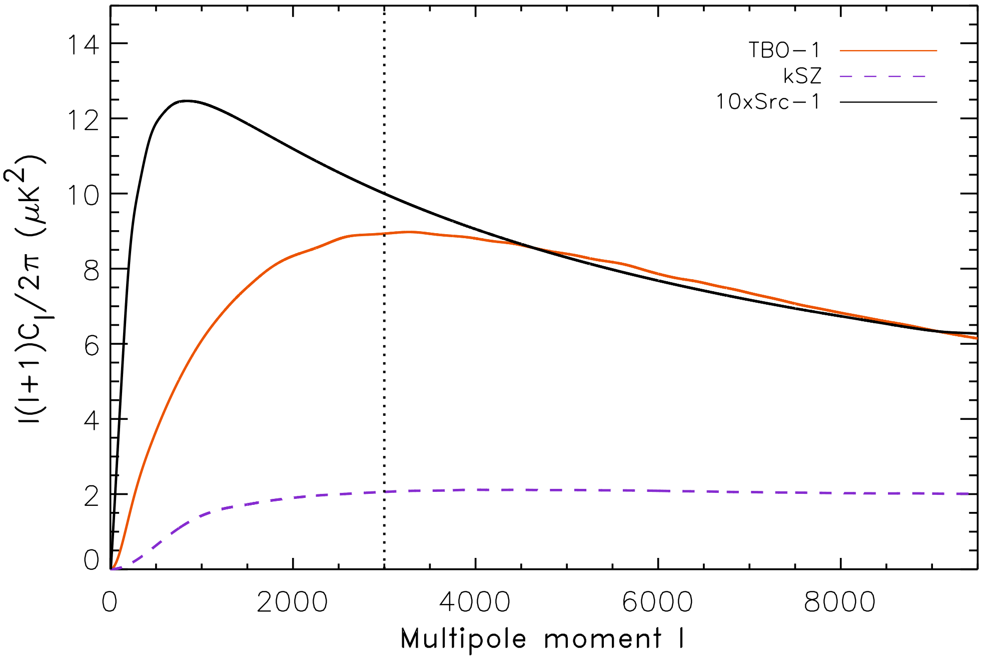

Figure 3.1 Thermal SZ and kSZ templates, normalised at 148 GHz for cosmologies with $\sigma_8 = 0.8$. The 'TBO-1' template is from Sehgal et al. [63], described further in Trac, Bode, and Ostriker [200]. Also shown is the 'Src-1' template for clustered point source emission.

model described in Section 2.5.2 of Sehgal et al. [63]. This model assumes that the IR emission traces star formation in halos at $z < 3$, and that the number of IR galaxies in a given halo is proportional to its mass. For the spectral energy distribution (SED) of the galaxies, the model uses an effective greybody law in which the dust temperature is a function of the CMB temperature, but its value at $z = 0$ is a free parameter. The dust emissivity spectral index and the typical IR luminosity and characteristic masses of the halos hosting IR galaxies are free parameters of the model. The model includes only the two-halo power spectrum given in Eq. (24) of Sehgal et al. [63], with contributions from pairs of galaxies in different halos. The parameters of the model have been updated from Sehgal et al. [63] to better fit the observed BLAST power spectra at 250–500μm[4]. This updated template is shown in Figure 3.1, normalised to unity at $\ell = 3000$. The shape is similar to the clustered model used in the SPT analysis

---

[4] The updated parameters are $\beta = 1.4$, $T_0 = 25.5$, $M_1 = 4 \times 10^{11}$, $M_2 = 2.5 \times 10^{12}$, $M_{\rm cool} = 5 \times 10^{14}$, $L_\star = 2.3 \times 10^{11}$, with definitions in Sehgal et al. [63].

by Hall et al. [113], peaking at $\ell \simeq 1000$.

3.2.1.4 *Likelihood Prescription*

To summarise the methods, an analysis with the '148+218' likelihood follows these steps to return the ACT likelihood for a given model:

- Select primary cosmological parameters, and compute a theoretical lensed CMB power spectrum $\mathcal{B}_\ell^{\rm CMB}$ using the CAMB numerical Boltzmann code [207].
- Select values for secondary parameters $\Theta = \{A_{\rm tSZ}, A_{\rm kSZ}, A_d, A_c, A_s, \alpha_d, \alpha_s\}$, and compute the total theoretical power spectra $\mathcal{B}_\ell^{{\rm th},ij}$ for 148×148, 148×218 and 218×218 using Eq. (3.5).
- Compute the bandpower theoretical power spectra $C_b^{{\rm th},ij} = w_{b\ell}^{ij} C_\ell^{{\rm th},ij}$.
- Select values for the calibration factors for 148 GHz and 218 GHz, and compute the likelihood using Eq. (3.14) for $500 < \ell < 10000$ for 148×148 and $1500 < \ell < 10000$ for 148×218 and 218×218.
- Add the likelihood term due to beam uncertainty, described in Appendix A of Dunkley et al. [33].

A large part of our analysis uses only the 148 GHz spectrum. An analysis done with this '148-only' likelihood follows these steps:

- Select primary cosmological parameters, and compute a theoretical lensed CMB power spectrum $\mathcal{B}_\ell^{\rm CMB}$ using CAMB.
- Select values for secondary parameters $\Theta = \{A_{\rm SZ}, A_p, A_c\}$ and compute the total theoretical power spectrum $\mathcal{B}_\ell^{\rm th}$ at 148 GHz using Eq. (3.12).
- Compute the bandpower theoretical power spectrum $C_b^{\rm th} = w_{b\ell} C_\ell^{\rm th}$.
- Compute the likelihood using Eq. (3.14) for $500 < \ell < 10000$ for 148 GHz.

- Add the likelihood term due to beam uncertainty, described in Appendix A of Dunkley et al. [33], and analytically marginalise over the calibration uncertainty.

3.2.2 *Parameter Estimation Methods*

We use the ACT likelihood for two separate parameter investigations. The first uses the 148+218 likelihood to constrain the secondary parameters, as our initial goal is to characterise the small-scale behavior, and investigate whether this simple model sufficiently describes the observed emission. The second uses the 148-only likelihood to constrain primary and secondary parameters.

3.2.2.1 *Secondary Parameters from 148 and 218 GHz*

For most of the investigation with the 148+218 likelihood we fix the primary cosmological parameters to the best-fit ΛCDM parameters estimated from WMAP, as our goal is to characterise the small-scale power observed by ACT, and check the goodness of fit of this simple model. To map out the probability distribution for these parameters we use an MCMC method. This uses the Metropolis algorithm to sample parameters [208], following the methodology described in Dunkley et al. [146].

There are seven possible secondary parameters, but we do not allow them all to vary freely. The radio sources detected at 148 GHz, described in Marriage et al. [194], are observed to have typical spectral index $S(\nu) \propto \nu^{-0.5}$ in flux units. By fitting a scaled source model from Toffolatti et al. [176] to the detected sources, and using it to extrapolate to fainter sources, Marriage et al. [194] predict a residual radio source power of $C_\ell = 2.8 \pm 0.3$ nK^2. Converting units, we use these measurements to impose a Gaussian prior of $A_s = 4.0 \pm 0.4\ \mu\mathrm{K}^2$, and we fix $\alpha_s = -0.5$. We also fix $A_{\mathrm{kSZ}} = A_{\mathrm{tSZ}}$, as the kSZ component is subdominant at 148 GHz and the SZ models predict them to be the same for a given cosmology. The other parameters (A_{tSZ}, A_d, A_c, and α_d) have uniform priors with positivity imposed on the amplitudes. Parameter results are quoted using the means and 68% confidence limits of the marginalised distributions, with 95% upper or lower limits given when the distribution is one-tailed. We also quote derived parameters to indicate the power in different components at 148 GHz and 218 GHz, for example the total power in SZ at $\ell = 3000$, $\mathcal{B}^{\rm SZ}_{3000} \equiv (\mathcal{B}^{\rm kSZ} + \mathcal{B}^{\rm tSZ})_{3000}$.

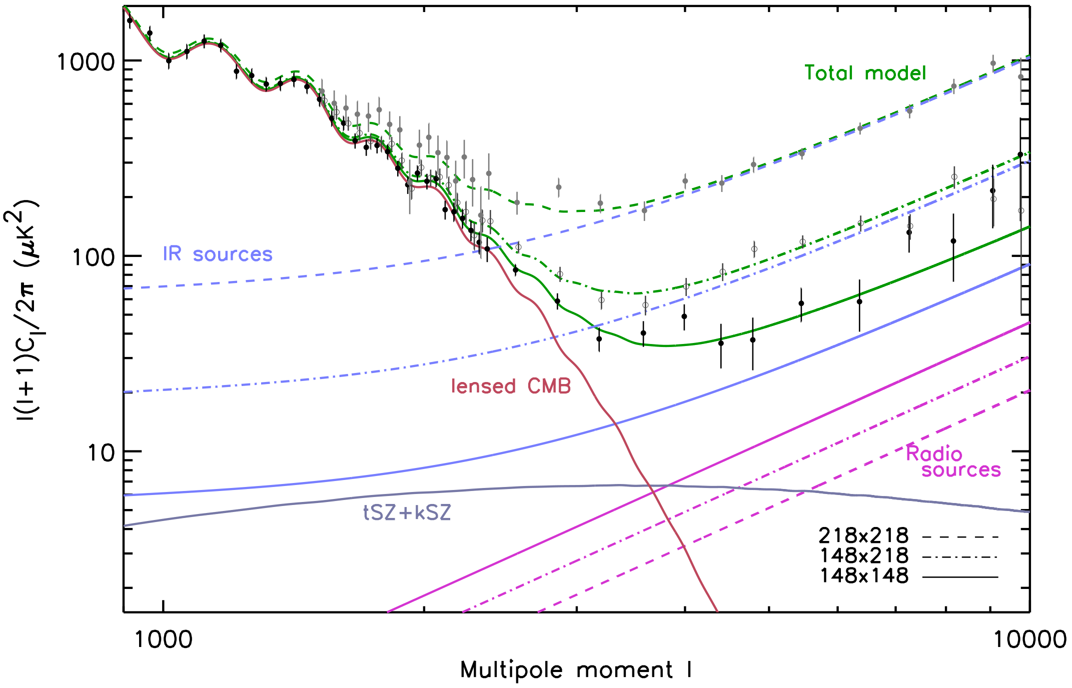

Figure 3.2 The angular power spectrum measured by ACT at 148 GHz and 218 GHz [69], with the theoretical model for CMB, SZ, and point sources best-fit to the three spectra. The lensed CMB corresponds to the ΛCDM model with parameters derived from WMAP [7]. It dominates at large scales, but falls exponentially due to Silk damping. The majority of power at $\ell > 3000$ comes from extragalactic point sources below a ≈20 mJy flux cut after masking. The radio sources are sub-dominant, and are constrained by a source model fit to detected sources at 148 GHz [194]. The infrared source emission, assumed to follow a power law, is dominated by Poisson power at small scale, but about 1/3 of the IR power at $\ell = 3000$ is attributed to clustered source emission, assuming a template described in the text. The best-fit SZ (thermal and kinetic) contribution at 148 GHz (assuming the TBO-1 template, Sehgal et al. [63]) is 7 μK^2 at $\ell = 3000$; the subdominant kinetic SZ also contributes at 218 GHz. The data spectra and errors have been scaled by best-fit calibration factors of 1.02^2, 1.02×1.09 and 1.09^2 for the 148×148, 148×218 and 218×218 spectra respectively.

3.2.2.2 *Parameters from 148 GHz*

In order to explore the probability distributions for a set of cosmological models, we use the 148-only likelihood for parameter estimation. The focus is on using the $1000 < \ell < 3000$ spectrum to improve constraints on primary cosmological parameters. It is important that the SZ and foregound contribution be marginalised over, but we exclude the more contaminated 218 GHz data given the current uncertainties in the foreground model. To map out the distribution for cosmological parameters we use MCMC methods to explore the probability distributions for various cosmological models.

We parameterise cosmological models using

$$\{\Omega_b h^2, \Omega_c h^2, \Omega_\Lambda, \Delta^2_{\mathcal{R}}, n_s, \tau\}. \tag{3.15}$$

These are the basic ΛCDM parameters, describing a flat universe with baryon density $\Omega_b h^2$, cold dark matter (CDM) density $\Omega_c h^2$, and a cosmological constant Ω_Λ. Primordial perturbations are assumed to be scalar, adiabatic, and Gaussian, described by a power law with spectral tilt n_s, and amplitude $\Delta^2_{\mathcal{R}}$, defined at pivot scale $k_0 = 0.002$ Mpc^{-1}. We assume 'instantaneous' reionisation, where the universe transitions from neutral to ionised over a redshift range $\Delta z = 0.5$, with optical depth τ. Reionisation likely takes place more slowly (e.g. Gnedin [209], Trac et al. [210]), but current CMB measurements are insensitive to this choice [115]. We also consider an additional set of primary parameters

$$\{dn_s/d\ln k, r, N_{eff}\}, \tag{3.16}$$

that describe primordial perturbations with a running scalar spectral index $dn_s/d\ln k$, a tensor contribution with tensor-to-scalar ratio r and a varying number of relativistic species N_{eff}. These parameters are added individually to the ΛCDM model in order to look for possible deviations from the concordance cosmology. These parameters all take uniform priors, with positivity priors on r and N_{eff}. The tensor spectral index is fixed at $n_t = -r/8$, and both the index and ratio are defined as in e.g., Komatsu et al. [165]. We generate the lensed theoretical CMB spectra using CAMB[5], and for computational efficiency set the CMB to zero above $\ell = 4000$ where the contribution is subdominant, less than 5% of the total power. To use the 148-only ACT likelihood there are three secondary parameters, $A_{\rm SZ}$, A_p, and A_c. We use the TBO-1 and Src-1 SZ and clustered source templates, and impose positivity priors on these parameters.

---

[5] Version Feb 2010, with Recfast 1.5.

We do not use any information explicitly from the 218 GHz spectrum in this part of the analysis, using just the 148-only likelihood, although results are checked using the 148+218 likelihood. The ACT likelihood is combined with the seven-year WMAP data and other cosmological data sets. We use the MCMC code and methodology described in Appendix C of Dunkley et al. [156], with the convergence test described in Dunkley et al. [146]. A subset of results are cross-checked against the publicly available CosmoMC code.

To place constraints on cosmological parameters we use the 7-year WMAP data in combination with ACT, using the WMAP likelihood package v4.1 described in Larson et al. [115]. WMAP measures the CMB over the full sky to 0.2° scales. All WMAP-only results shown for comparison use MCMC chains from LAMBDA[6], again described in Larson et al. [115]. While small-scale CMB data from ACBAR and QUAD provide higher signal-to-noise on $\ell < 1600$ scales [108, 149], we do not include them in this analysis, to avoid combining data from multiple experiments and to better interpret results derived from ACT. We follow the methodology described in Komatsu et al. [7] to consider the addition of distance measurements from astrophysical observations, on the angular diameter distances measured from Baryon Acoustic Oscillations (BAO) at $z = 0.2$ and 0.35, and on the Hubble constant. The Gaussian priors on the distance ratios, $r_s/D_V(z = 0.2) = 0.1905 \pm 0.0061$ and $r_s/D_V(z = 0.35) = 0.1097 \pm 0.0036$, are derived from measurements from the Two-Degree Field Galaxy Redshift Survey (2dFGRS) and the Sloan Digital Sky Survey Data Release 7 (SDSS DR7), using a combined analysis of the two data-sets by Percival et al. [211]. The parameter r_s is the comoving sound horizon size at the baryon drag epoch, and $D_V(z) \equiv [(1+z)^2 D_A^2(z) cz/H(z)]^{1/3}$ is the effective distance measure for angular diameter distance D_A, and Hubble parameter $H(z)$. The inverse covariance matrix is given by Eq. 5 of Percival et al. [211]. The Gaussian prior on the Hubble constant, $H_0 = 74.2 \pm 3.6$ km s^{-1} Mpc^{-1}, comes from the magnitude-redshift relation from HST observations of 240 low-z Type Ia supernovae at $z < 0.1$ by Riess et al. [212]. The error includes both statistical and systematic errors.

---

[6] `http://lambda.gsfc.nasa.gov/`

3.3 HIGH-ELL SZ AND POINT SOURCE MODEL

In this section we determine the goodness of fit of the SZ and point source model described in Section 3.2.1 to the ACT 148 GHz and 218 GHz power spectra, and estimate its parameters. This uses the 148+218 likelihood summarised in Sec 3.2.1.4, initially holding the ΛCDM model fixed to the primary CMB with parameters given in Komatsu et al. [7]. The best-fit model is a good fit to the three ACT power spectra over the full angular range $500 < \ell < 10000$ ($\chi^2 = 78$ for 106 degrees of freedom), with constraints on parameters given in Table 3.3 for the TBO-1 SZ template and Src-1 source template. The spectra are shown in Figure 3.2, with the estimated components indicated at each frequency. The mean calibration factors, defined in Eq. (3.13), are 1.02 and 1.09 for 148 GHz and 218 GHz respectively. These are consistent with the expected values at the 1-1.2σ level. The best-fitting 1.09 factor is driven by the $\ell < 2500$ part of the 148×218 cross-spectrum, where the primary CMB dominates. At $\ell = 3000$, about half the power at 148 GHz is from the primary CMB (27 out of 50 μK^2), with the remainder divided among SZ, IR Poisson and clustered power, and radio Poisson power (4-8 μK^2 in each component). At 218 GHz, only about 15% of the power comes from the primary CMB at $\ell = 3000$ (27 out of 170 μK^2). Half of the power is attributed to Poisson IR sources, the remaining approximately 35% to power from clustered IR sources. The model fits the cross-spectrum, indicating that a similar population of galaxies is contributing at both frequencies.

Table 3.1 Parameters describing SZ and extragalactic source model at 148 GHz

Parameter[a]	148 GHz -only
$A_{\rm tSZ}$	< 0.77 (95%CL)
A_d (μK^2)	12.0 ± 1.9
A_c (μK^2)	< 7.4 (95%CL)
A_s (μK^2)[b]	4.0 ± 0.4
χ^2/dof	29/46

---

[a] The kSZ and tSZ coefficients are set equal, $A_{\rm kSZ} = A_{\rm tSZ}$. A_d, A_c and A_s are the $\mathcal{B}_{3000}$ power for Poisson infrared galaxies, clustered infrared galaxies, and Poisson radio galaxies at 148 GHz respectively. The ΛCDM parameters are not varied here.

[b] A Gaussian prior $A_s = 4.0 \pm 0.4$ is imposed, and index $\alpha_s = -0.5$ assumed.

Table 3.2 Constraints on SZ emission

Template[a]	A_{tSZ}[b]	$\mathcal{B}^{\mathrm{SZ}}_{3000}$[c] ($\mu$K^2)	$\sigma_8^{\mathrm{SZ},7}$ $0.8\times(A_{\mathrm{tSZ}}^{1/7})$	$\sigma_8^{\mathrm{SZ},9}$ $0.8\times(A_{\mathrm{tSZ}}^{1/9})$
TBO-1	0.62 ± 0.26	6.8 ± 2.9	0.74 ± 0.05	0.75 ± 0.04

---

[a] Template is from Sehgal et al. [63]

[b] We required $A_{\mathrm{kSZ}} = A_{\mathrm{tSZ}}$, as defined in Eqs. (3.6-3.7).

[c] Total tSZ and kSZ power at 148 GHz, as defined in Eq. (3.8).

3.3.1 Constraints on SZ power

The estimated template amplitude, $A_{\mathrm{tSZ}} = 0.62 \pm 0.26$ for the TBO-1 template. Note that A_{kSZ} is fixed equal to A_{tSZ} in this case, with amplitudes defined in Eqs. (3.6-3.7). For the TBO-1 template, the mean amplitude is lower than expected for a universe with $\sigma_8 = 0.8$ $(A_{\mathrm{tSZ}} = 1)$, but not significantly. Using the multi-frequency spectra, power from SZ fluctuations is detected at more than 95% CL, with estimated A_{tSZ} given in Table 3.3.1 and shown in Figure 3.3, marginalised over point source parameters. The

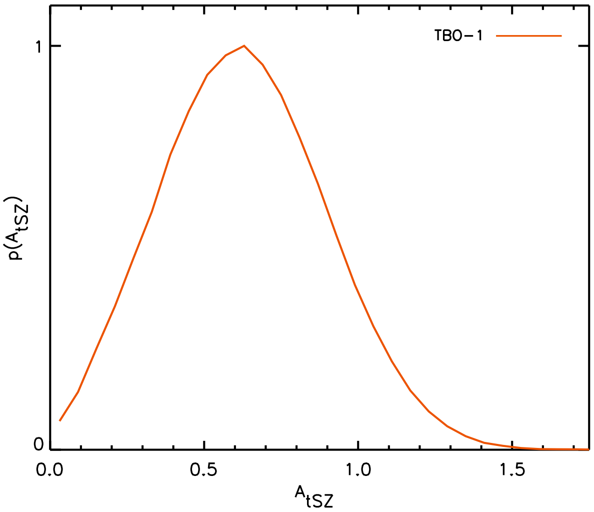

Figure 3.3 One-dimensional marginalised distributions for the estimated thermal SZ power in the ACT power spectra. There is evidence at the 95% CL level for non-zero SZ power. The value $A_{\mathrm{tSZ}} = 1$ corresponds to the predicted thermal SZ amplitude in a universe with $\sigma_8 = 0.8$. The TBO-1 SZ template is shown in Figure 1. The total SZ power (including kSZ) at 148 GHz and $\ell = 3000$ is $\ell(\ell+1)C_\ell^{\mathrm{SZ}}/2\pi = 7 \pm 3$ μK^2.

total SZ power at $\ell = 3000$ (tSZ plus kSZ) is estimated to be

$$\mathcal{B}_{3000}^{\mathrm{SZ}} = 6.8 \pm 2.9\ \mu\mathrm{K}^2. \tag{3.17}$$

This is consistent with observations by SPT [154], and is an improvement over the initial estimate of $A_{\mathrm{tSZ}} < 1.6$ at 95% CL from the ACT power spectrum presented in Chapter 2. In this case we have held the primary CMB parameters fixed. For a single test case we marginalise over the 6 primary ΛCDM parameters in addition to the secondary parameters. This marginalisation results in an increase in the mean value of $\mathcal{B}_{3000}^{\mathrm{SZ}}$ of 0.5 $\mu\mathrm{K}^2$ (a 0.2σ change), but a negligible increase in the uncertainty.

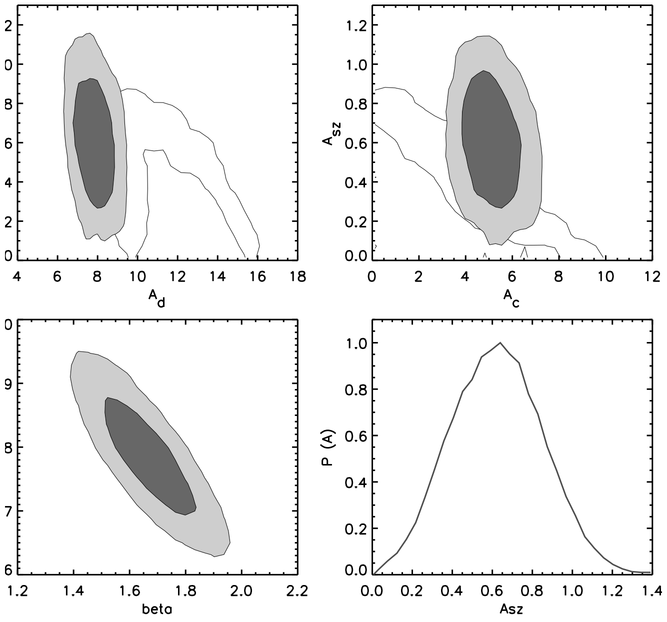

Figure 3.4 Marginalised distributions (68% and 95% CL) for parameters describing the SZ and point source emission in the ACT power spectra. *Left and center*: The degeneracies between the total SZ power, $\mathcal{B}_\ell^{\mathrm{SZ}} \equiv \ell(\ell+1)C_\ell^{\mathrm{SZ}}$, and the infrared point source power, $\mathcal{B}_\ell^{\mathrm{IR}}$, at 148 GHz and $\ell = 3000$ (solid unfilled contours), are broken with the addition of 218 GHz data (solid filled contours). Both the Poisson and clustered IR power are shown, for two different clustered source templates (solid and dashed contours). A clustered source component is required to fit the multi-frequency data at 5σ significance. *Right*: The Poisson dust power and the index $\alpha_d = 3.69 \pm 0.14$ (power law in flux between 148 GHz and 218 GHz, and unconstrained from 148 GHz alone) are anti-correlated; the index indicates a dust emissivity of $\beta \approx 1.7$.

The number of clusters, and therefore the expected SZ power, is a strong function of the amplitude of matter fluctuations, quantified by σ_8 [213]. In our model we scale the SZ templates by an overall amplitude, and would like to infer an estimate for σ_8 from $A_{\rm tSZ}$. In Chapter 2 we assumed a seventh power scaling, with $A_{\rm tSZ} \propto \sigma_8^7$ [158], giving an upper limit of $\sigma_8^{\rm SZ} < 0.84$ at 95% CL, for $A_{\rm tSZ} < 1.6$. However, the exact scaling of the shape and amplitude with cosmology, and in particular with σ_8, is model dependent and not precisely known [154, 200, 214]. For the TBO-1 template the combined tSZ and kSZ signal scales close to the 7th power, with the tSZ varying approximately as the 8th power [200]. To bound the possible range we compute two limits, assuming the tSZ part of the template varies as either σ_8^7 or σ_8^9. The estimated values for $\sigma_8^{\rm SZ}$ in these cases are given in Table 3.3.1.

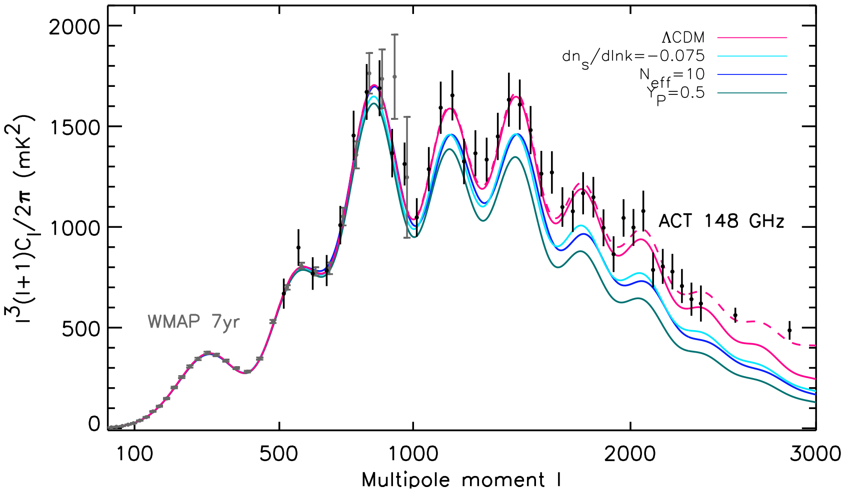

Figure 3.5 The power spectrum measured by ACT at 148 GHz, scaled by ℓ^4, over the range dominated by primordial CMB ($\ell < 3000$). The spectrum is consistent with the WMAP power spectrum over the scales $500 < \ell < 1000$, and gives a measure of the third to seventh acoustic peaks. The best-fit ΛCDM cosmological model is shown, and is a good fit to the two datasets. At $\ell > 2000$ the contribution from point soures and SZ becomes significant (dashed shows the total best-fit theoretical spectrum; solid is lensed CMB). Three additional theoretical models for the primordial CMB are shown with N_{eff}=10 relativistic species, ^{4}He fraction $Y_p = 0.5$, and running of the spectral index $dn_s/d\ln k = -0.075$. They are consistent with WMAP but are excluded at least at the 95% level by the ACT data.

3.3.2 Unresolved Point Source Emission

The power spectrum measures fluctuations due to point sources below a flux cut of approximately 20 mJy. This is not an exact limit since the point source mask is

Table 3.3 Derived constraints on unresolved IR source emission[a]

		148 GHz	218 GHz
Poisson	$\mathcal{B}_{3000}$ (μK^2)[b]	$7.8 \pm 0.7 \pm 0.7$	$90 \pm 5 \pm 10$
	C_ℓ (nK^2)	$5.5 \pm 0.5 \pm 0.6$	$63 \pm 3 \pm 6$
	C_ℓ (Jy^2 sr^{-1})	$0.85 \pm 0.08 \pm 0.09$	$14.7 \pm 0.7 \pm 1.8$
Clustered	$\mathcal{B}_{3000}$ (μK^2)[c]	$4.6 \pm 0.9 \pm 0.6$	$54 \pm 12 \pm 5$
Total IR	$\mathcal{B}_{3000}$ (μK^2)	12.5 ± 1.2	144 ± 13

---

[a] The two errors indicate statistical uncertainty and a systematic error due to clustered template uncertainty.

[b] Equivalent to the parameter A_d for 148 GHz.

[c] Equivalent to the parameter A_c for 148 GHz.

constructed from sources with signal-to-noise ratio greater than 5 [194]. The point source power observed at 148 GHz and 218 GHz has both synchrotron emission from radio galaxies, and IR emission from dusty galaxies. At 148 GHz the point source power, after removal of 5σ sources, is inferred to be split in ratio roughly 1:2 between radio and IR galaxies. Since we impose a prior on the residual radio power from Marriage et al. [194], we do not learn new information about this component from the power spectrum. At 218 GHz the point source power is dominated by IR dust emission. The IR Poisson power is estimated to be $A_d = 7.8 \pm 0.7\ \mu\text{K}^2$, with derived Poisson IR power at 148 GHz and 218 GHz given in Table 3.3.2. A clustered component is required to fit the data, with $A_c = 4.6 \pm 0.9\ \mu\text{K}^2$, corresponding to power at 218 GHz of $\mathcal{B}^{218}_{3000} = 54 \pm 12\ \mu\text{K}^2$. A model with no clustered component has a poorer fit to the data by $\Delta\chi^2 = 28$, indicating a detection of clustering at the 5σ level. It is the 218 GHz power spectrum that provides this detection; the 148 GHz spectrum is consistent with no clustered component.

In flux units, the effective index of unresolved IR emission is

$$\alpha_d = 3.69 \pm 0.14 \tag{3.18}$$

between 148 GHz and 218 GHz, where $S(\nu) \propto \nu^\alpha$. The dust index and Poisson amplitude are anti-correlated, shown in Figure 3.4. This index estimate agrees with observations by SPT, who find $\alpha = 3.9 \pm 0.3$ for the Poisson component, and 3.8 ± 1.2

for the clustered component over the same frequency range [113]. A property that can be derived from the effective index, α, is the dust emissivity index, β. For galaxies at redshift $z = 0$ the dust emission can be described by a modified blackbody, $S(\nu) \propto \nu^{\beta} B_{\nu}(T_d)$, for dust temperature T_d. In the Rayleigh-Jeans (RJ) limit the flux then approximates to $S(\nu) \propto \nu^{\beta+2} T_d$, with $\beta = \alpha - 2$. Using this relation gives a dust emissivity index measured by ACT of $\beta = 1.7 \pm 0.14$, consistent with models (e.g. Draine [215]). However, the RJ limit is not expected to be as good an approximation for redshifted greybodies (e.g. Hall et al. [113]), adding an uncertainty to β of up to $\simeq 0.5$. This should also be considered an effective index, given the likely temperature variation within each galaxy.

3.4 COSMOLOGICAL PARAMETER CONSTRAINTS

In this section we use the 148-only ACT likelihood to estimate primary cosmological parameters, in combination with WMAP and cosmological distance priors. Following the prescription in Section 3.2.1.4 we marginalise over three secondary parameters to account for SZ and point source contamination. We conservatively exclude the 218 GHz data from this part of the analysis, to avoid drawing conclusions that could depend on the choice of model for the point source power.

3.4.1 *The ΛCDM Model*

The best-fit ΛCDM model is shown in Figure 3.5, using the combination $\ell^4 C_\ell$ to highlight the acoustic peaks in the Silk damping regime. The estimated parameters for the ACT+WMAP combination, given in Table 3.4 and shown in Figure 3.6, agree to within 0.5σ with the WMAP best-fit. The spectral index continues to lie below the scale invariant $n_s = 1$, now at the 3σ level from the CMB alone, with $n_s = 0.962 \pm 0.013$. This supports the inflationary scenario for the generation of primordial fluctuations [216–221] and is possible due to the longer lever arm from the extended angular range probed by ACT. With the addition of BAO and H_0 data, the significance of $n_s < 1$ is increased to 3.3σ, with statistics given in Table 3.5.

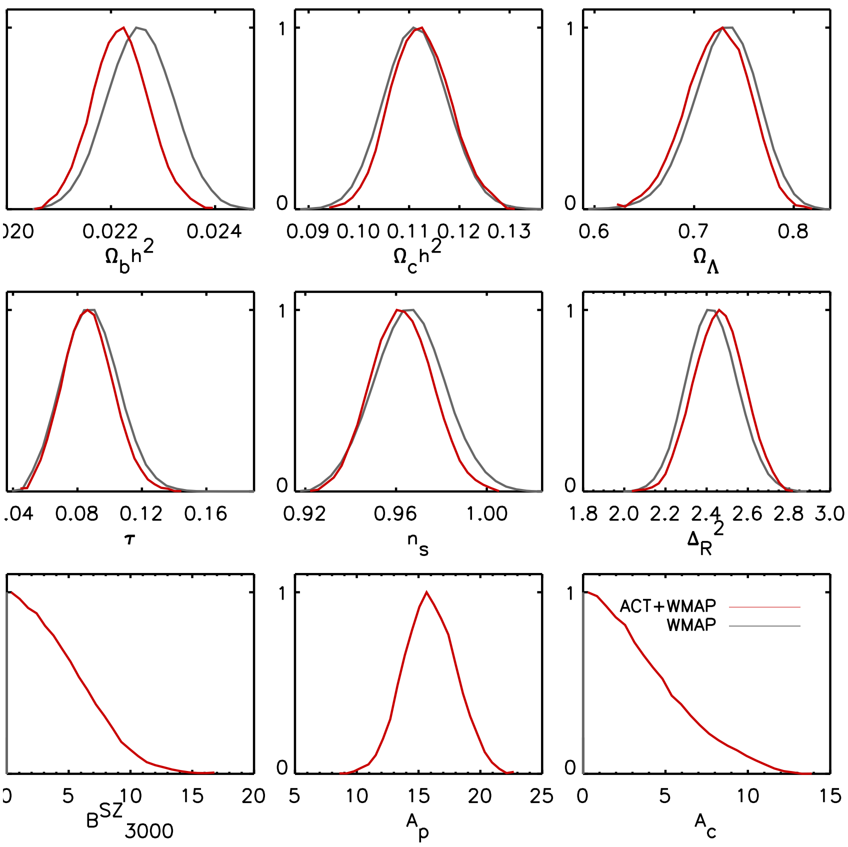

Figure 3.6 One-dimensional marginalised distributions for the 6 ΛCDM parameters (top two rows) derived from the ACT+WMAP combination, compared to WMAP alone. The bottom row shows 3 secondary parameters from the ACT+WMAP data. With the addition of ACT data a model with $n_s = 1$ is disfavoured at the 3σ level.

The ΛCDM parameters are not strongly correlated with the three secondary parameters (A_c, A_p, $A_{\rm SZ}$), as there is limited freedom within the model to adjust the small-scale spectrum while still fitting the WMAP data. We also find consistent results for the ΛCDM parameters if the 148+218 ACT likelihood is used in place of the 148-only likelihood.

3.4.2 *Lensing of the CMB*

The CMB photons are deflected by large-scale structure potentials along their path from the last scattering surface at $z \simeq 1100$ to us (see Lewis and Challinor [64] for a review). The typical (rms) deflection in the ΛCDM model is about $2'.7$ and the deflection pattern is coherent over degree scales, comparable to the size of the acoustic features on the primary CMB. These coherent deflections produce distortions of the hot and cold spots on the CMB, leading to a broadening of their size distribution. In the power spectrum, this effect manifests itself as the smoothing of the acoustic peaks, which can be used as a signal to look for lensing. The first attempt at a detection of lensing in the power spectrum was made in Reichardt et al. [108] using the data from the ACBAR experiment. They quantified the effect of including lensing in their analysis through the log-ratio of the lensed to unlensed Bayesian evidence ($\Delta \ln \mathcal{E}$), and by combining WMAP5 and ACBAR datasets found $\Delta \ln \mathcal{E} = 2.63$. Calabrese et al. [222] analysed the ACBAR data with a different approach, where they introduced a scaling of the power spectrum of the lensing potential ($C_\ell^{\phi\phi} \to A_L C_\ell^{\phi\phi}$, with $A_L = 0$ corresponding to no lensing and $A_L = 1$ to the standard ΛCDM expectation). With WMAP5+ACBAR they found $A_L = 3.0 \pm 0.9$ (68% confidence level). According to footnote 17 of Reichardt et al. [108], a re-analysis of the ACBAR data using this parameterisation yields $A_L = 1.60^{+0.55}_{-0.26}$. Our 148 GHz power spectrum is shown against lensed and unlensed models in Fig. 3.7. We use the parameterisation of Calabrese et al. [222], and constrain the lensing parameter A_L based on WMAP 7-year and ACT power spectra. Fig. 3.8 shows the marginalised 1D likelihood for A_L using WMAP+ACT. We find $A_L = 1.3^{+0.5\ (+1.2)}_{-0.5\ (-1.0)}$ at 68% (95%) confidence, with the best-fit lensed CMB spectrum with $A_L = 1$ having an improved goodness-of-fit to the WMAP+ACT data of $\Delta\chi^2 = 8$ less than the unlensed model. We check for systematics that might have given rise to a spurious lensing signal. The projection scheme (cylindrical-equal-area) used for the ACT maps is not particularly optimised for lensing studies — so we test whether this projection could introduce a lensing-like signal. We simulate a low-noise unlensed CMB signal and run it through the map-making pipeline, and try to reconstruct a "lensing convergence" in the resulting map using standard quadratic estimator techniques [65]. We find the reconstructed convergence power spectrum to be consistent with null (there is a small known bias at high multipoles that we have entirely traced to mode-coupling due to the finiteness of the patch), showing that the projection does not introduce any significant lensing-like signal in our patches. To

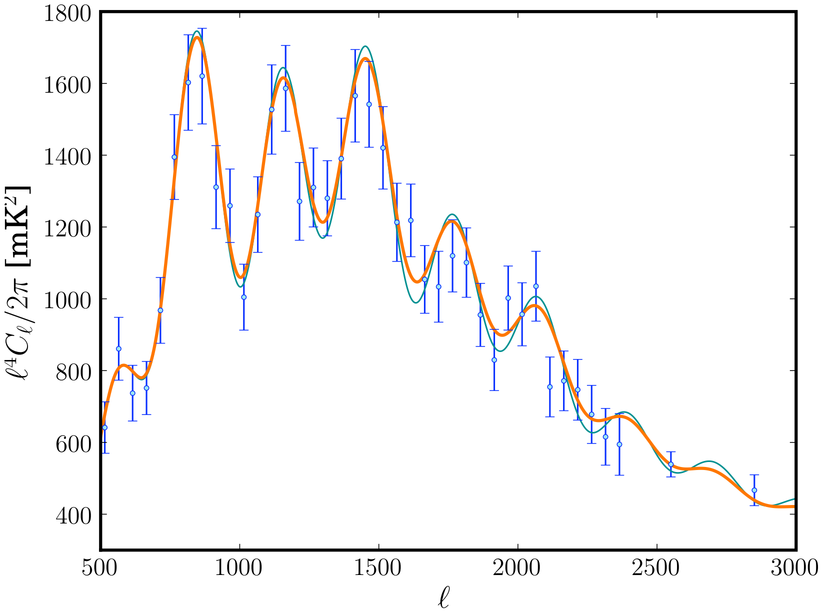

Figure 3.7 Lensing of the CMB smooths out the acoustic peaks in the CMB power spectrum. The best fit model with lensed CMB, secondaries, and point sources is shown as the thick orange curve, while the same with no lensing is shown with the thin green curve.

further test if any other step in our pipeline could produce spurious peak smearing in the power spectrum, we generate an end-to-end simulation of a noisy map exactly as described in Section 2 of Das et al. [69], only this time replacing the lensed CMB signal time-stream with its unlensed version. The resulting maps are then processed through the power spectrum pipeline. We find the lensing amplitude parameter, A_L, described above to be consistent with zero (see Fig. 3.8).

3.4.3 *Inflationary Parameters*

3.4.3.1 *Running of the Spectral Index*

We constrain a possible deviation from power-law primordial fluctuations using the running of the index, $dn_s/d\ln k$, with curvature perturbations described by

$$\Delta^2_{\mathcal{R}}(k) = \Delta^2_{\mathcal{R}}(k_0)\left(\frac{k}{k_0}\right)^{n_s(k_0)-1+\frac{1}{2}\ln(k/k_0)dn_s/d\ln k} . \tag{3.19}$$

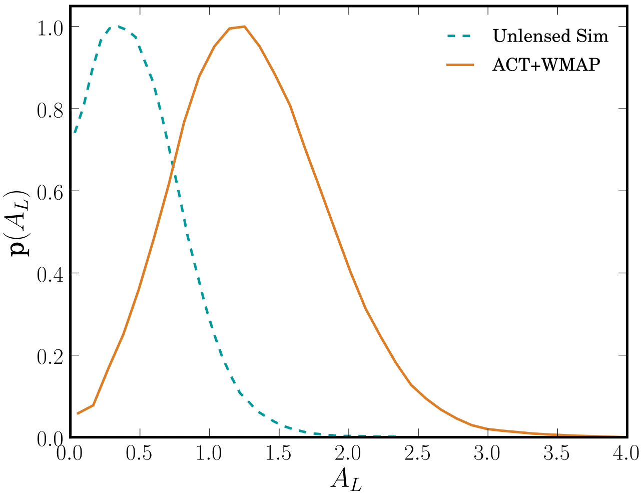

Figure 3.8 One dimensional marginalised distribution (solid line) for the lensing parameter A_L, that scales the expected lensing potential such that $C_\phi \to A_L\, C_\phi$ [222]. An unlensed CMB spectrum would have $A_L = 0$, and the standard lensing case has $A_L = 1$. With ACT+WMAP we find $A_L = 1.3^{+0.5\ (+1.2)}_{-0.5\ (-1.0)}$ (68% (and 95%) limits), a 2.8σ detection of lensing. The dashed line shows the marginalised distribution for A_L, obtained from an unlensed simulation.

The spectral index at scale k is related to the index at pivot point k_0 by

$$n_s(k) = n_s(k_0) + \frac{dn_s}{d\ln k} \ln\left(\frac{k}{k_0}\right). \tag{3.20}$$

The simplest inflationary models predict that the running of the spectral index with scale should be small (see e.g., Kosowsky and Turner [223], Baumann et al. [224]), and the detection of a scale dependence would provide evidence for alternative models for the early universe. Cosmological constraints on deviations from scale invariance have been considered recently (by e.g., Reichardt et al. [108], Easther and Peiris [225], Kinney et al. [226], Shafieloo and Souradeep [227], Verde and Peiris [228]), using various parameterisations. With CMB data alone, the seven-year WMAP data show no evidence for significant running, with $dn_s/d\ln k = -0.034 \pm 0.026$, and -0.041 ± 0.023 when combined with ACBAR and QUAD data [7]. With the measurement of the power spectrum at small scales by ACT, we find

$$dn_s/d\ln k = -0.034 \pm 0.018 \text{ (68\% CL)} \tag{3.21}$$

Table 3.4 ΛCDM and extended model parameters and 68% confidence intervals from the ACT 2008 data combined with seven-year WMAP data.

	Parameter[a]	ΛCDM	ΛCDM $+ dn_s/d\ln k$	ΛCDM $+ r$	ΛCDM $+ N_{eff}$
Primary ΛCDM	$100\Omega_b h^2$	2.214 ± 0.050	2.167 ± 0.054	2.246 ± 0.057	2.252 ± 0.055
	$\Omega_c h^2$	0.1127 ± 0.0054	0.1214 ± 0.0074	0.1099 ± 0.0058	0.152 ± 0.025
	Ω_Λ	0.721 ± 0.030	0.670 ± 0.046	0.738 ± 0.030	0.720 ± 0.030
	n_s	0.962 ± 0.013	1.032 ± 0.039	0.974 ± 0.016	0.993 ± 0.021
	τ	0.087 ± 0.014	0.092 ± 0.016	0.087 ± 0.015	0.089 ± 0.015
	$10^9\Delta^2_{\mathcal{R}}$	2.47 ± 0.11	2.44 ± 0.11	2.37 ± 0.13	2.40 ± 0.12
Extended	$dn_s/d\ln k$		-0.034 ± 0.018		
	r			< 0.25	
	N_{eff}				5.3 ± 1.3
Derived	σ_8	0.813 ± 0.028	0.841 ± 0.032	0.803 ± 0.030	0.906 ± 0.059
	Ω_m	0.279 ± 0.030	0.330 ± 0.046	0.262 ± 0.030	0.280 ± 0.030
	H_0	69.7 ± 2.5	66.1 ± 3.0	71.4 ± 2.8	78.9 ± 5.9
Secondary	B^{SZ}_{3000} (μK^2)	< 10.2	< 12.3	< 10.0	< 12.1
	A_p (μK^2)	16.0 ± 2.0	14.9 ± 2.2	16.0 ± 2.0	15.1 ± 2.1
	A_c (μK^2)	< 8.7	< 10.4	< 8.0	< 11.1
	$-2\ln\mathscr{L}$	7500.0	7498.1	7500.1	7498.7

---

[a] For one-tailed distributions, the upper 95% CL is given. For two-tailed distributions the 68% CL are shown.

and $dn_s/d\ln k = -0.024 \pm 0.015$ including BAO+H_0. The estimated parameters are given in Tables 3.4 and 3.5. Parameters are sampled using a pivot point $k_0 = 0.002$ Mpc^{-1} for the spectral index, and are reported in the Tables using this pivot, to allow easy comparison with previous analyses including Komatsu et al. [7]. This choice of pivot point results in the index being strongly anti-correlated with the running, with $n_s(0.002) = 1.032 \pm 0.039$. In Figure 3.9 we show the index and its running at a decorrelated pivot point $k_0 = 0.015$ Mpc^{-1}, chosen to minimize the correlation between the two parameters [229]. This illustrates the strength of the ACT data to constrain the primordial spectral index independently of its scale dependence. To allow conversion between pivot points, the relation between the index at these two scales is

$$n_s(k_0 = 0.015/\mathrm{Mpc}) = n_s(k_0 = 0.002/\mathrm{Mpc}) + \ln(0.015/0.002)\frac{dn_s}{d\ln k} \tag{3.22}$$

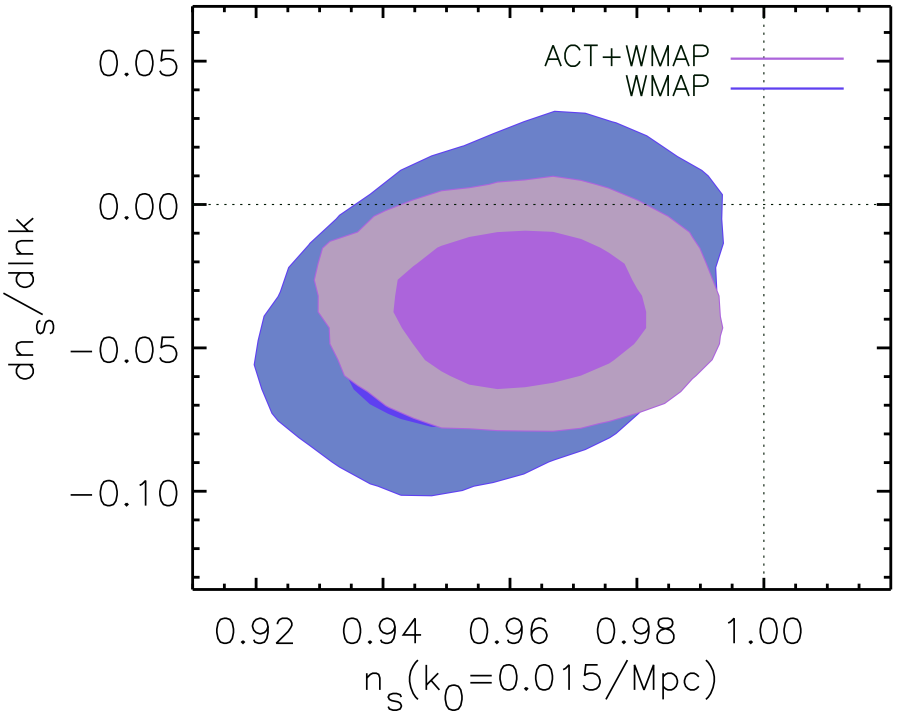

Figure 3.9 Two-dimensional marginalised limits (68% and 95%) for the running of the index $dn_s/d\ln k$, and the spectral index, n_s, plotted at the pivot point that minimizes their correlation, $k_0 = 0.015/\mathrm{M}pc$, for ACT+WMAP compared to WMAP. This model has no tensor fluctuations. A negative running is preferred, but the data are consistent with a power-law spectral index, with $dn_s/d\ln k = 0$.

with other cosmological parameters unchanged. The running prefers a negative value at 1.8σ, indicating enhanced damping at small scales, but there is no statistically significant deviation from a power law spectral index. The running is weakly anti-correlated with the SZ and clustered source amplitudes, since a more negative running decreases the power at small scales. Marginalising over the running leads to a $\sim 25\%$ increase in the upper limit on the SZ and clustered source power for this model compared to ΛCDM, as shown in Table 3.4. This is compensated at small scales by a $\sim 0.5\sigma$ decrease in the Poisson source power.

Given that $dn_s/d\ln k$ is more sensitive to the small-scale spectrum, and may be affected by the modelling of the point source and SZ contributions, we choose this model to investigate the sensitivity of the constraints to choices made in the likelihood. We

Table 3.5 ΛCDM and extended model parameters and 68% confidence intervals from the ACT 2008 data combined with seven-year WMAP data, and measurements of H_0 and BAO

	Parameter[a]	ΛCDM	ΛCDM $+\, dn_s/d\ln k$	ΛCDM $+\, r$	ΛCDM $+\, N_{eff}$
Primary ΛCDM	$100\Omega_b h^2$	2.222 ± 0.047	2.206 ± 0.047	2.237 ± 0.048	2.238 ± 0.046
	$\Omega_c h^2$	0.113 ± 0.0034	0.1148 ± 0.0039	0.1117 ± 0.0033	0.140 ± 0.015
	Ω_Λ	0.724 ± 0.016	0.713 ± 0.019	0.729 ± 0.017	0.715 ± 0.017
	n_s	0.963 ± 0.011	1.017 ± 0.036	0.970 ± 0.012	0.983 ± 0.014
	τ	0.086 ± 0.013	0.095 ± 0.016	0.086 ± 0.015	0.086 ± 0.014
	$10^9\Delta^2_{\mathcal{R}}$	2.46 ± 0.09	2.39 ± 0.10	2.40 ± 0.10	2.44 ± 0.09
Extended	$dn_s/d\ln k$		-0.024 ± 0.015		
	r			< 0.19	
	N_{eff}				4.56 ± 0.75
Derived	σ_8	0.813 ± 0.022	0.820 ± 0.023	0.811 ± 0.022	0.885 ± 0.039
	Ω_m	0.276 ± 0.016	0.287 ± 0.019	0.271 ± 0.017	0.285 ± 0.017
	H_0	69.9 ± 1.4	69.1 ± 1.5	70.4 ± 1.5	75.5 ± 3.0
Secondary	B^{SZ}_{3000} (μK^2)	< 9.7	< 11.4	< 10.2	< 12.1
	A_p (μK^2)	16.1 ± 2.0	15.2 ± 2.0	16.1 ± 2.0	15.3 ± 2.1
	A_c (μK^2)	< 8.4	< 10.3	< 8.4	< 10.2

---

[a] For one-tailed distributions, the upper 95% CL is given. For two-tailed distributions the 68% CL are shown.

find less than 0.1σ variation in primordial parameters if we limit the analysis to the $\ell < 5000$ data. The beam is measured sufficently well over the angular range of interest that results are not changed if the beam uncertainty is neglected. These tests are described further in Section 3.5, and give us confidence that the errors are not dominated by systematic effects.

3.4.3.2 *Gravitational Waves*

The concordance ΛCDM model assumes purely scalar fluctuations. Tensor fluctuations can also be seeded at early times, propagating as gravitational waves. They contribute to the CMB temperature and polarisation anisotropy, polarising the CMB with both an E-mode and B-mode pattern (e.g. Zaldarriaga and Seljak [67], Kamionkowski et al. [230]). The tensor fluctuation power is quantified using the tensor-to-scalar ratio $r = \Delta^2_h(k_0)/\Delta^2_{\mathcal{R}}(k_0)$, where Δ^2_h is the amplitude of primordial gravitational waves, with pivot scale $k_0 = 0.002/\mathrm{Mpc}$. Inflationary models predict tensor fluctuations, with

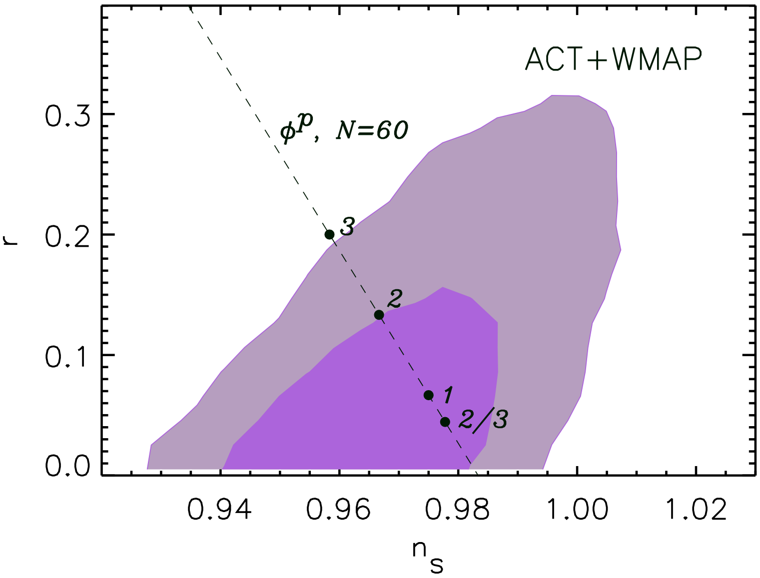

Figure 3.10 Two-dimensional marginalised distribution (68% and 95% CL) for the tensor-to-scalar ratio r, and the scalar spectral index n_s, for ACT+WMAP data. By measuring the $\ell > 1000$ spectrum, the longer lever arm from ACT data further breaks the $n_s - r$ degeneracy, giving a marginalised limit $r < 0.25$ (95% CL) from the CMB alone. The predicted values for a chaotic inflationary model with inflaton potential $V(\phi) \propto \phi^p$ with 60 e-folds are shown for $p = 3, 2, 1, 2/3$; $p > 3$ is disfavoured at $>$ 95% CL.

amplitude related to the potential of the inflaton field (see e.g., Baumann et al. [224] for a recent review and the seminal work on the subject, Liddle and Lyth [231])

Direct B-mode polarisation measurements from the BICEP experiment provide limits of $r < 0.7$ (95% CL, Chiang et al. [232]). Temperature and E-mode fluctuations over a range of scales currently provide a stronger indirect constraint on r, with $r < 0.36$ (95% CL) from the WMAP data [7]. Models with a large value for r have increased power at large scales, which can be partly compensated by increasing the spectral index of scalar fluctuations and reducing the scalar amplitude. This '$n_s - r$' degeneracy can be partly broken with lower-redshift observations that limit $r < 0.24$ (95% CL) from WMAP+BAO+H_0 [7]. It can also be broken by measuring temperature fluctuations at $\ell > 1000$. The tightest CMB-only constraints so far have come from WMAP CMB data combined with ACBAR and QUAD small-scale CMB data [149], with $r < 0.33$ (95% CL). With ACT combined with WMAP, the improved

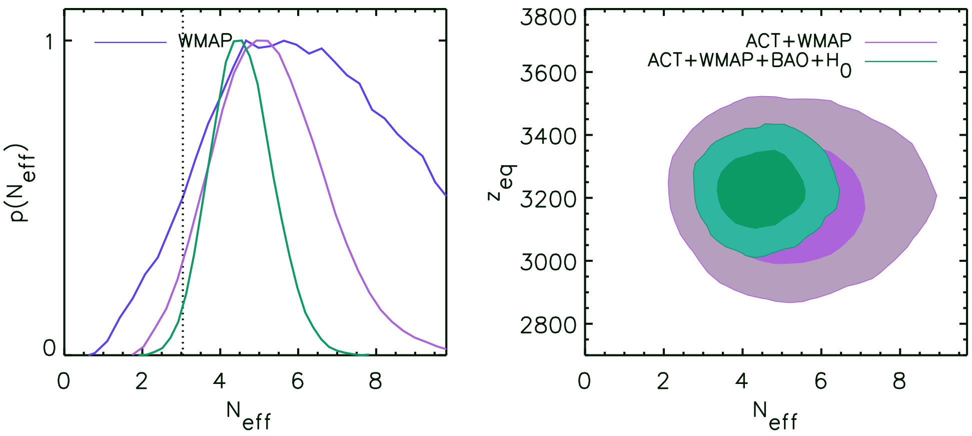

Figure 3.11 Constraints on the effective number of relativistic species, N_{eff}. *Left*: One-dimensional marginalised distribution for N_{eff}, for data combinations indicated in the right panel. The standard model assumes three light neutrino species (N_{eff}=3.04, dotted line); the mean value is higher, but 3.04 is within the 95% CL. *Right:* Two-dimensional marginalised distribution for N_{eff} and equality redshift $z_{\rm eq}$, showing that N_{eff} can be measured separately from $z_{\rm eq}$. N_{eff} is bounded from above and below by combining the small-scale ACT measurements of the acoustic peaks with WMAP measurements. The limit is further tightened by adding BAO and H_0 constraints, breaking the degeneracy between N_{eff} and the matter density by measuring the expansion rate at late times.

measurement of the primordial power at $1500 < \ell < 2500$ scales gives

$$r < 0.25 \ (95\% \ \mathrm{CL}) \tag{3.23}$$

for the CMB temperature anisotropy power spectrum alone, comparable to constraints from combined cosmological datasets ($r < 0.19$ at 95% CL for ACT+WMAP+BAO+H_0). The parameter estimates are given in Tables 3.4 and 3.5, and the dependence of the tensor amplitude on the spectral index is shown in Figure 3.10. For this model the secondary parameters are not strongly correlated with the tensor amplitude. For chaotic inflationary models with inflaton potential $V(\phi) \propto \phi^p$ and N e-folds of inflation, the predicted tensor-to-scalar ratio is $r = 4p/N$, with $n_s = 1 - (p+2)/2N$. The CMB data exclude $p \geq 3$ at more than 95% confidence for $N = 60$ e-folds.

3.4.4 *Non-standard Models*

In addition to specifying the primordial perturbations, the concordance model assumes that there are three light neutrino species, that standard BBN took place with specific predictions for primordial element abundances, and that there are no additional particles or fluctuations from components such as cosmic defects. The damping tail measured by ACT offers a probe of possible deviations from this standard model.

3.4.4.1 *Number of Relativistic Species*

The CMB is sensitive to the number of relativistic species at decoupling. Changing the effective number of species affects the evolution of perturbations by altering the expansion rate of the universe. Neutrinos also stream relativistically out of density fluctuations, with additional species suppressing the CMB peak heights and shifting the acoustic peak positions [12, 54].

The standard model of particle physics has three light neutrino species, consistent with measurements of the width of the Z boson, giving $N_\nu = 2.984 \pm 0.008$ (Particle Data Book). Three neutrino species contribute about 11% of the energy density of the universe at $z \approx 1100$, with $\rho_{rel} = (7/8(4/11)^{4/3} N_{eff})\rho_\gamma$. Cosmological datasets are sensitive to ρ_{rel}, which can be composed of any light particles produced during the Big Bang that do not couple to electrons, ions, or photons; or any additional contribution to the energy density of the universe such as gravitational waves. Three light neutrino species correspond to N_{eff}=3.04. Any deviation would indicate either additional relativistic species, or evidence for non-standard interactions or non-thermal decoupling [12].

Recent constraints on the number of relativistic species have been explored with CMB data from WMAP combined with low redshift probes by e.g., Komatsu et al. [7], Spergel et al. [57], Dunkley et al. [156], Ichikawa et al. [233], Mangano et al. [234], Hamann et al. [235], Reid et al. [236]. With WMAP data a detection was made of relativistic species with $N_{eff}> 2.7$ (95% CL), but the upper level was unconstrained. By combining with distance measures, Komatsu et al. [7] limit the number of species to $N_{eff}= 4.34 \pm 0.88$, and Reid et al. [236] added optical cluster limits and LRG power spectrum measures to find $N_{eff}= 3.77 \pm 0.67$. Mantz, Allen, and Rapetti [237] include X-ray cluster gas fraction and cluster luminosity measurements from ROSAT and

Chandra to estimate N_{eff}= $3.4^{+0.6}_{-0.5}$, improving limits by constraining the matter power spectrum at low redshift. BBN observations limit N_{eff} to 3.24 ± 0.6 [238].

By combining the ACT power spectrum measurement with WMAP, the effective number of species is estimated from the CMB to be

$$N_{eff} = 5.3 \pm 1.3 \text{ (68\% CL)}. \tag{3.24}$$

A universe with no neutrinos is excluded at 4σ from the CMB alone, with the marginalised distribution shown in Figure 3.11. We can now put an upper bound on N_{eff} from the CMB alone using ACT. This improved measurement comes from the third to seventh peak positions and heights. The right panel of Figure 3.11 shows the redshift of equality, $z_{\rm eq}$, as a function of the number of species. The relation of $z_{\rm eq}$ to the number of species is given in Eq. 53 of Komatsu et al. [7]. With large scale measurements the observable quantity from the third peak height is just $z_{\rm eq}$, leading to a strong degeneracy between N_{eff} and $\Omega_c h^2$. With small-scale information the CMB data allow a meassure of N_{eff} in addition to $z_{\rm eq}$ due to the additional effects of anisotropic stress on the perturbations. As an example, a model with N_{eff}= 10 that fits the WMAP data is shown in Figure 3.5. With a large N_{eff} the higher peaks are damped, and slightly shifted to larger multipoles. The model is excluded by the ACT spectrum in the $1000 < \ell < 2500$ regime.

The central value for N_{eff} preferred by the ACT+WMAP data is 1.7σ above the concordance value, with increased damping over the ΛCDM model; improved measurements of the spectrum will help refine this measurement. This is not interpreted as a statistically significant departure from the concordance value; the best-fit χ^2 is only 1.3 less than for N_{eff}=3.04. The degeneracy between N_{eff} and $\Omega_c h^2$ results in a higher mean value for σ_8, 0.906 ± 0.059, with all estimated parameters given in Table 3.4. As with the running of the spectral index, an increase in neutrino species, leading to enhanced damping, is weakly correlated with an increase in the upper limits on SZ and clustered source power, and corresponding decrease in the Poisson power, at the $\sim 1\mu$K level. By adding the BAO and H_0 data the $N_{eff}-\Omega_c h^2$ degeneracy is further broken, with $N_{eff} = 4.56 \pm 0.75$ (68% CL). This central value is higher than from joint constraints including X-ray and optical cluster measurements [236, 237]; improved CMB and low redshift measurements will allow further constraints and consistency checks.

3.5 SENSITIVITY TO LIKELIHOOD ASSUMPTIONS

A set of assumptions are made in the ACT likelihood. We choose the ΛCDM+running model to check their effect on cosmological parameters, as subtleties in the small-scale treatment can be probed more thoroughly with this model than with the 6-parameter ΛCDM. The fiducial constraints on the ΛCDM+running model use data between $500 < \ell < 10000$, including beam error and a 2% calibration error in temperature, and use the Src-1 clustered source template and the TBO-1 SZ template. We test the sensitivity to the calibration and beam uncertainty. Removing the 2% calibration error in the maps decreases the errors on the primary parameters by up to 0.2σ. When the beam error is neglected, the constraints are tightened by about 0.1σ, but this is not a significant effect, consistent with the measurement of the beam. If instead the angular range is restricted to $\ell < 5000$, the primary cosmological parameters are unaffected, but the SZ and point source amplitudes are more poorly determined. Further tests on different model templates for the SZ and clustering amplitude of point sources are tested in Dunkley et al. [33].

3.6 DISCUSSION

The power spectra measured at 148 GHz and 218 GHz by ACT, using observations made in the southern sky in 2008, have provided a new probe of the physics affecting microwave fluctuations at small scales. The concordance ΛCDM cosmological model continues to be favoured, and possible deviations from this model are more tightly constrained. At 148 GHz and 218 GHz, the CMB is dominant at scales larger than $\ell \simeq 3000$ and 2000 respectively, after bright sources have been removed. At smaller scales, a simple model for SZ and point source emission is a good fit to the ACT power spectra. By using multi-frequency information we see a preference for non-

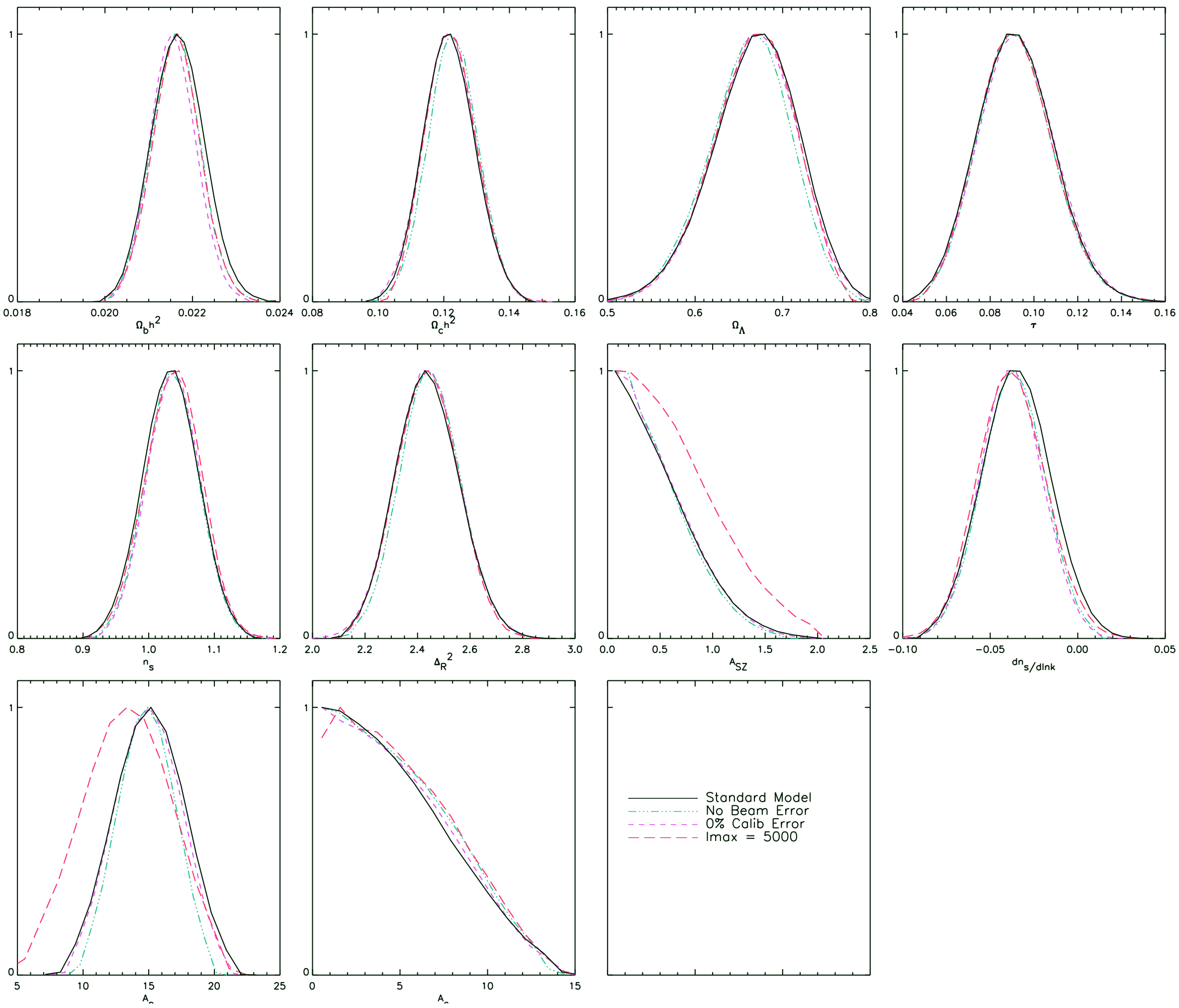

Figure 3.12 Tests of the 148 GHz likelihood for the ΛCDM model with a running spectral index. The 'standard' model uses the likelihood settings described in Sec 3.2.1. Changing the angular range used from $\ell_{max} = 10000$ to 5000 only alters the distribution of the secondary parameters, but leaves the primary model parameters unchanged. Parameters are tightened by about 0.1σ if the beam error is set to zero ('No beam error'), and by up to 0.2σ is the calibration error is removed ('0% Calib error').

zero thermal Sunyaev-Zel'dovich fluctuations in the 148 GHz power spectrum at 2σ, with an amplitude consistent with observations by the South Pole Telescope. The mean amplitude is lower than the simplest cluster models predict for a universe with $\sigma_8 = 0.8$, but at less than 2σ significance. The level is consistent with expectations from recent models that include more complex gas physics; continued comparisons of observations and theory will allow progress to be made on cluster modelling. The frequency dependence of the infrared emission has the expected behavior of greybody emissivity from dusty star-forming galaxies at redshifts $1 < z < 4$, and a clustered infrared point source component is detected in the ACT data at 5σ significance.

The $1000 < \ell < 3000$ spectrum provides a measure of the third to seventh acoustic peaks in the CMB, and the Silk damping tail from the recombination process at $z = 1100$. Using this measurement we place tighter constraints on deviations from the ΛCDM model. Given the uncertainty on the expected power spectrum from infrared point sources, we have limited this part of the analysis to the power spectrum from 148 GHz. The data are found to be consistent with no deviations from ΛCDM, and the gravitational lensing of the temperature power spectrum is at the expected level, with an unlensed signal disfavoured at 2.8σ. We have detected relativistic species at 4σ from the CMB alone, consistent with the expected levels. The best-fit models prefer increased damping beyond the ΛCDM expectation, but at less than the 2σ level. The cosmological parameters considered have distinct effects on the power spectrum, but there is some degeneracy between N_{eff} and $dn/d\ln k$. This means that an enhanced damping leads to higher mean values for N_{eff}, or to more negative $dn/d\ln k$. These are seen at 1.4-1.8σ from the concordance value when considered individually as extensions to ΛCDM, but there is no evidence that these deviations are statistically preferred.

4

THE ATACAMA COSMOLOGY TELESCOPE: A MEASUREMENT OF THE PRIMORDIAL POWER SPECTRUM

4.1 INTRODUCTION

The CMB constrains the power spectra of scalar and tensor perturbations, the relic observables associated with a period of inflation in the early universe [57, 108, 225–228, 239–248]. The standard models of inflation predict a power spectrum of adiabatic scalar perturbations close to scale-invariant. Such models are often described in terms of a spectral index n_s and an amplitude of perturbations $A_s(k_0)$ as $\mathcal{P}(k) = A_s(k_0)\left(\frac{k}{k_0}\right)^{n_s-1}$, where k_0 is a pivot scale. A wide variety of models, however, predict features in the primordial spectrum of perturbations, which alter the fluctuations in the CMB [239, 245, 249–261], which can be constrained using reconstruction of the primordial power.

Primordial fluctuations evolve over cosmic time to form the large scale structures that we see today. Therefore, a precision measurement of the power spectrum of these fluctuations, imprinted on the CMB, impacts all aspects of cosmology. Recent measurements of the CMB temperature and polarisation spectra have put limits on the deviation from scale invariance including a variation in power-law with scale (e.g., a running of the spectral index, Kosowsky and Turner [223]); in particular data from the Atacama Cosmology Telescope (ACT) [33, 69] combined with WMAP satellite data [115] find no evidence for running of the spectral index with scale and disfavour a scale-invariant spectrum with $n_s = 1$ at 3σ, as discussed in Chapter 3.

In this Chapter we probe a possible deviation from power-law fluctuations by considering the general case where the power spectrum is parameterised as bandpowers within bins in wavenumber (or k) space. This 'agnostic' approach allows for a general form of the primordial power spectrum without imposing any specific model of inflation on the power spectrum, and facilitates direct comparison with a wide range of models. Such tests of the primordial power have been considered by various groups [57, 228, 239–241, 247, 248, 262–265]. We revisit the calculation because of ACT high sensitivity over a broad range in angular scale.

This chapter is based on data from 296 square degrees of the ACT 2008 survey in the southern sky, at a central frequency of 148 GHz. The resulting maps have an angular resolution of 1.4′ and a noise level of between 25 and 40 μK per arcmin^2.

4.2 METHODOLOGY

4.2.1 *Angular Power spectrum*

Following the work of Wang et al. [239], Tegmark and Zaldarriaga [240], Bridle et al. [241], Mukherjee and Wang [242] and Spergel et al. [57], we parameterise the primordial power spectrum $\mathcal{P}(k)$ using bandpowers in 20 bins, logarithmically spaced in mode k from $k_1 = 0.001$ to $k_{20} = 0.35$ Mpc^{-1} , with $k_{i+1} = 1.36k_i$ for $1 < i < 19$. To ensure the power spectrum is smooth within bins, we perform a cubic spline such that:

$$\mathcal{P}(k) = A_s(k_0)\times = \begin{cases} 1 & \text{for} \quad k < k_1 \\ A_iP_i + B_iP_{i+1} & \\ + \quad \left((A_i^3 - A_i)C_i + (B_i^3 - B_i)C_{i+1}\right)\frac{h_i^2}{6} & \\ & \text{for} \quad k_i < k < k_{i+1} \\ P_{20} & \text{for} \quad k > k_{20} \\ & (1) \end{cases}$$

where the P_i are the power spectrum amplitudes within bin i, normalised so that $P_i = 1$ corresponds to scale invariance. The $A_s(k_0)$ is a normalised amplitude of scalar density fluctuations, which we take to be 2.36×10^{-9} [115], and is the amplitude for a power-law spectrum around a pivot scale of $k_0 = 0.002$ Mpc^{-1}. We do not vary the amplitude in our analysis as the power in the individual bands is degenerate with the overall amplitude; if a higher value was used, the estimated bandpowers would be lower by the corresponding amount, as we are measuring the total primordial power within a bin. The coefficients C_i are the second derivatives of the input binned power spectrum data [266], $h_i = k_{i+1} - k_i$ is the width of the step and $A_i = (k_{i+1} - k)/h_i$ and $B_i = (k - k_i)/h_i$. We do not impose a 'smoothness penalty' as discussed in Verde and Peiris [228] and in Peiris and Verde [247]. These models are unnecessarily complicated for the type of features one might search for in the data. Adding more parameters to the parameter set makes it easier for the model to fit bumps and wiggles in the spectrum, hence as the number of bins increases, this parameterisation will fit the noise in the data, particularly on large scales (small values of k). This in turn is expected to increase the goodness-of-fit of the model by approximately one per additional parameter. Hence, a model that fits the data significantly better than the standard ΛCDM power law would yield an increase in the likelihood of more than one per additional parameter in the model. The logarithmic spacing in k means that this is less of a problem at high multipoles, as many measurements are used to estimate the power in each band. The primordial power spectrum is related to the CMB power spectra through the radiation transfer functions $T_T(k)$, $T_E(k)$ and $T_B(k)$ (defined as in Komatsu and Spergel [267]) as:

$$C_\ell^{\alpha\beta} \propto \int k^2 dk \mathcal{P}(k) T_\alpha(k) T_\beta(k) \tag{4.2}$$

where α and β index T, E or B, corresponding to temperature or the two modes of polarisation. The correspondence between multipole ℓ and mode k (in Mpc^{-1}) is roughly $\ell \simeq kd$, where $d \simeq 14000$ Mpc is the comoving distance to the last scattering surface. Figure 4.1 shows schematically how the primordial power spectrum translates to the temperature angular power spectrum. In each case, a single step function is used for the primordial power spectrum in Eq. (4.2). Previous analyses have only constrained the primordial power out to $k \lesssim 0.15$ Mpc^{-1} [57, 241, 247]. The arcminute resolution of ACT means that one can constrain the primordial power out

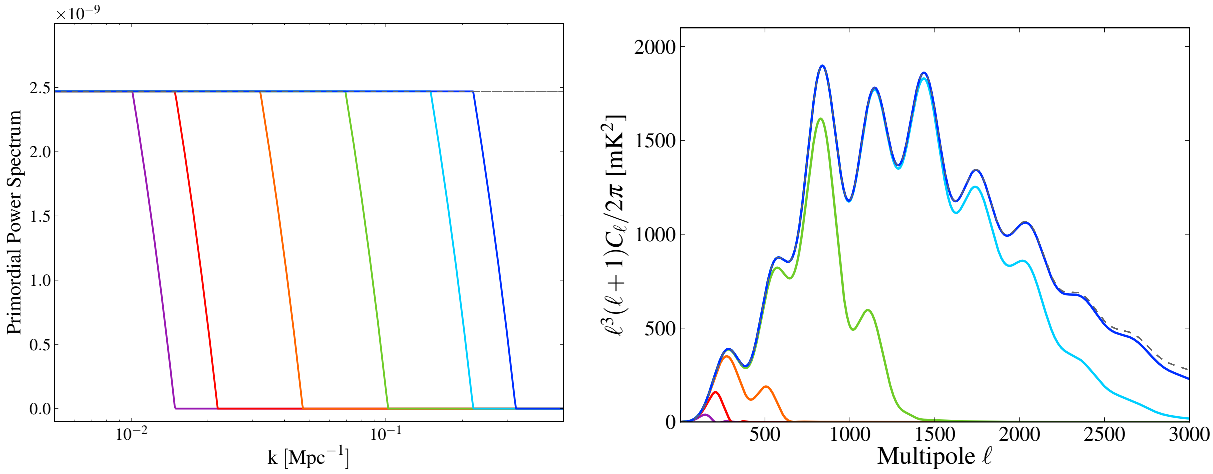

Figure 4.1 Stepping up in power: we show schematically the angular power spectrum (right panel) resulting from building up the primordial power spectrum $\mathcal{P}(k)$ in bins (left panel), from $k = 0.007$ Mpc^{-1} (left-most curve in the top panel) to $k = 0.22$ Mpc^{-1} (right-most curve). The power in each case is normalised to a single amplitude before the step function, and set to zero afterwards, so that as more bins are added to the primordial spectrum, it tends towards a scale-invariant spectrum (shown as the dashed line). Correspondingly, the C_ℓ spectrum (plotted as $\ell^3(\ell+1)C_\ell^{TT}/2\pi$ mK^2 in the right panel) also tends to a spectrum characterized by $n_s = 1$, also shown as the grey dashed curve.

to larger values of k ($\simeq 0.19$ Mpc^{-1}). The primary CMB power spectrum decreases exponentially due to Silk damping [55] at multipoles greater than $\ell \simeq 2000$, while the power spectrum from diffuse emission of secondary sources begins to rise from $\ell \simeq 2000$. The ACT measurement window between $1000 < \ell < 3000$ provides a new window with which to constrain any deviation from a standard power-law spectrum, as this is in the range of scales before the power from secondary sources dominates. We use the 148 GHz measurements from the 2008 ACT Southern Survey, and include polarisation and temperature measurements from the WMAP satellite with a relative normalisation determined by Hajian et al. [190]. We use the ACT likelihood described in Chapter 3 and the WMAP likelihood found in Larson et al. [115].

4.2.2 *Parameter Estimation*

Our cosmological models are parameterised using:

$$\{\Omega_c h^2, \Omega_b h^2, \theta_A, \tau, \mathbf{P}\}, \tag{4.3}$$

where $\Omega_c h^2$ is the cold dark matter density; $\Omega_b h^2$ is the baryon density; h is the dimensionless Hubble parameter such that $H_0 = 100h$ km s^{-1}Mpc^{-1}; θ_A is the ratio of the sound horizon to the angular diameter distance at last scattering, and is a measure of the angular scale of the first acoustic peak in the CMB temperature fluctuations; τ is the optical depth at reionisation, which we consider to be 'instantaneous' (equivalent to assuming a redshift range of $\Delta z = 0.5$ for CMB fluctuations) and $\mathbf{P} = \{P_i\},\ \ i = 1, .., 20$, is the vector of bandpowers where $P_i = 1 \ \forall \ i$ describes a scale-invariant power spectrum. We assume a flat universe in this analysis. In addition, we add three parameters, $A_{\rm SZ}, A_p, A_c$, to model the secondary emission from the Sunyaev-Zel'dovich effect from clusters, Poisson-distributed and clustered point sources respectively, marginalising over templates as described in Chapters 2 and 3. We impose positivity priors on the amplitudes of these secondary parameters. We modify the standard Boltzmann code CAMB[1] [268] to include a general form for the primordial power spectrum, and generate lensed theoretical CMB spectra to $\ell = 4000$, above which we set the spectra to zero for computational efficiency, as the signal is less than 5% of the total power.

The likelihood space is sampled using Markov Chain Monte Carlo methods (MCMC). The analysis is performed on chains of length $N = 200000$. We sample the chains and test for convergence following the prescription in Dunkley et al. [146], using a covariance matrix determined from initial runs.

We impose limiting values on the power spectrum bands $0 < P_i < 10$ for all i. To avoid exploring regions of parameter space inconsistent with current astronomical measurements, we impose a Gaussian prior on the Hubble parameter today of $H_0 = 74.2 \pm 3.6$ km s^{-1} Mpc^{-1} from Riess et al. [269].

---

[1] http://cosmologist.info/camb

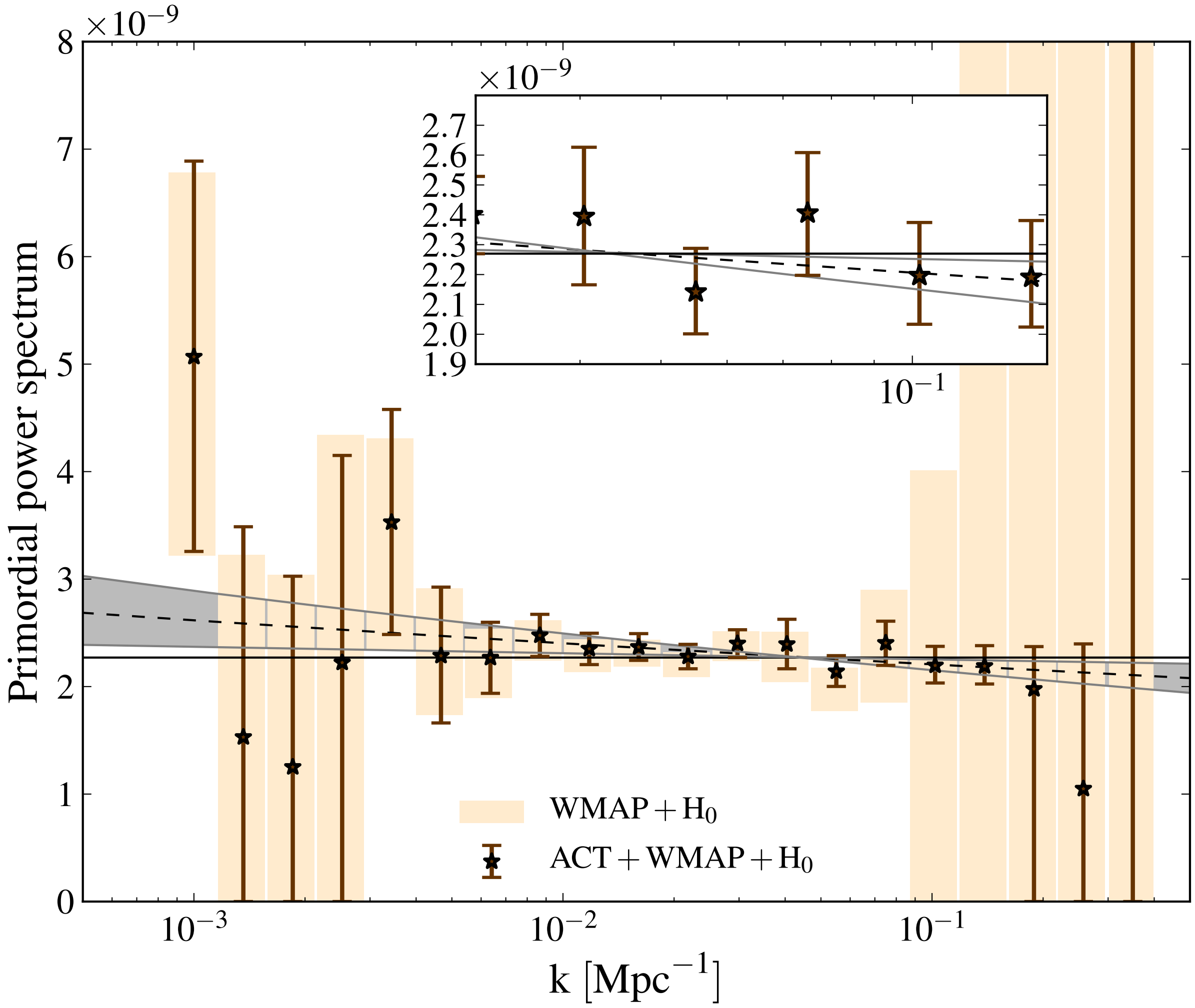

Figure 4.2 Primordial power constraints: the constraints on the primordial power spectrum from the ACT data in addition to WMAP data compared to the WMAP constraints alone. In both cases, a prior on the Hubble parameter from Riess et al. [269] was included. Where the marginalised distributions are one-tailed, the upper errorbars show the 95% confidence upper limits. On large scales the power spectrum is constrained by the WMAP data, while at smaller scales the ACT data yield tight constraints up to $k = 0.19$ Mpc^{-1}. The horizontal solid line shows a scale-invariant spectrum, while the dashed black line shows the best-fit ΛCDM power-law with $n_s = 0.963$ from the results in Chapter 3, with the spectra corresponding to the 2σ variation in spectral index indicated by solid band. The constraints are summarised in Table 4.1.

Table 4.1 Estimated power spectrum bands in units of 10^{-9}.

Wavenumber k (Mpc^{-1})	Power spectrum band^{a,b}	WMAP only binned $\mathcal{P}(k)$	ACT+WMAP binned $P(k)$
0.0010	P_1	$4.99^{+1.79}_{-1.77}$	5.07 ± 1.82
0.0014	P_2	< 3.22	< 3.49
0.0019	P_3	< 3.04	< 3.03
0.0025	P_4	< 4.34	< 4.15
0.0034	P_5	3.32 ± 0.99	3.52 ± 1.05
0.0047	P_6	$2.31^{+0.60}_{-0.58}$	2.29 ± 0.64
0.0064	P_7	2.21 ± 0.33	2.27 ± 0.31
0.0087	P_8	2.43 ± 0.19	2.48 ± 0.20
0.0118	P_9	2.29 ± 0.15	2.35 ± 0.15
0.0160	P_{10}	2.31 ± 0.13	2.37 ± 0.12
0.0218	P_{11}	2.20 ± 0.11	2.28 ± 0.11
0.0297	P_{12}	2.38 ± 0.14	2.40 ± 0.13
0.0404	P_{13}	2.28 ± 0.23	2.39 ± 0.23
0.0550	P_{14}	1.98 ± 0.20	2.14 ± 0.14
0.0749	P_{15}	2.37 ± 0.53	$2.41^{+0.20}_{-0.28}$
0.1020	P_{16}	< 4.01	2.20 ± 0.17
0.1388	P_{17}	–	$2.19^{\pm}0.18$
0.1889	P_{18}	–	< 2.37
0.2571	P_{19}	–	< 2.40
0.3500	P_{20}	–	–

---

[a] For one-tailed distributions, the upper 95% confidence limit is given, whereas the 68% limits are shown for two-tailed distributions.

[b] The primordial power spectrum is normalised by a fixed overall amplitude $A_s(k_0) = 2.36 \times 10^{-9}$ [115].

4.3 RESULTS

4.3.1 Primordial Power

Figure 4.2 shows the constraints on the primordial power spectrum from measurements of the cosmic microwave background. The shaded bands are the constraints on the power spectrum from WMAP measurements alone. Over this range of scales there is no indication of deviation from power-law fluctuations. As was shown in Spergel et al. [57], the lack of data at multipole moments larger than $\ell = 1000$ restricts any constraints on the primordial power spectrum at $k > 0.1$ Mpc^{-1}. In contrast, the combined ACT/WMAP constraints are significantly improved, particularly for the power at scales $0.1 < k < 0.19$ Mpc^{-1}. The resulting power spectrum is still consistent with a power-law shape, with $n_s = 0.963$ (the best-fit value found in Chapter 3. Despite the fact that we have added 18 extra degrees of freedom to the fit, a scale-invariant spectrum ($n_s = 1$, shown by the horizontal line on Fig. 4.2) is disfavoured at 2σ. In addition, we find no evidence for a significant feature in the small-scale power. The bands at $k > 0.19$ Mpc^{-1} in the ACT+WMAP case are largely unconstrained by the data. Including 218 GHz ACT data will improve the measurements of the primordial power, since it will relieve the degeneracies between the binned primordial power, the clustered IR source power, and the Poisson source power, all of which provide power at $\ell > 2000$.

The estimated primordial power spectrum values are summarised in Table 4.1. The CMB angular power spectra corresponding to the allowed range in the primordial power spectrum (at 1σ) are shown in Figure 4.3 for WMAP-alone compared to WMAP and ACT combined. The temperature-polarisation cross spectra corresponding to these allowed models are also shown in Figure 4.3, indicating how little freedom remains in the small-scale TE spectrum. This allowed range in C_ℓ^{TE} at multipoles $\ell > 1000$ will be probed by future CMB polarisation experiments such as Planck [270], ACTPol [271] and SPTPol [272].

In this analysis, we use a prior on the Hubble constant. Removing this prior reveals a degeneracy between the primordial power on scales $0.01 < k < 0.02$ Mpc^{-1} (bands P_{8-11} in Figure 4.4), and the set of parameters describing the contents and expansion rate of the universe. Both affect the first acoustic peak. This degeneracy was previously noted in, e.g., Blanchard et al. [256], Hunt and Sarkar [258], Nadathur and Sarkar [261], where a power spectrum model "bump" at $k = 0.015$ Mpc^{-1} was found to be consistent with observations in the context of a low H_0, and without any dark energy. Along this degeneracy, the primordial spectrum can be modified to move the position of the first peak to larger scales (relative to power-law), also increasing its relative amplitude. Since the first peak position is well measured by WMAP, this increase in angular scale is compensated by decreasing θ_A. In a flat universe, this corresponds to a decrease in the Hubble constant and the cosmological constant. The matter density increases to maintain the first peak amplitude. The baryon density then decreases

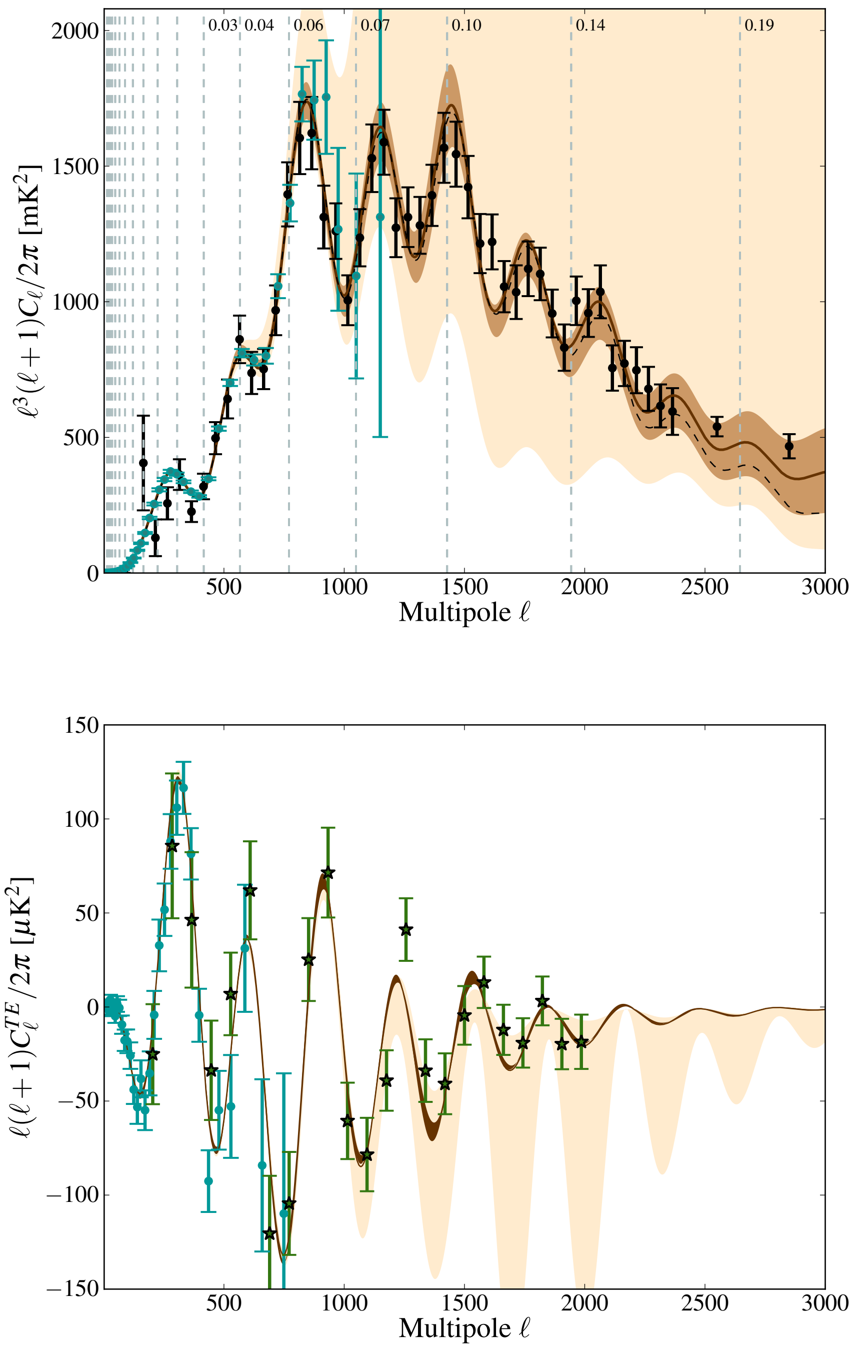

Figure 4.3 Mapping primordial power to the angular power spectrum: the constraints on the primordial power spectrum from Figure 4.2 translate into the angular power spectrum of the temperature CMB fluctuations, shown as $\ell^3(\ell+1)C_\ell^{TT}/2\pi$ mK^2 (upper panel) to highlight the higher order peaks. The dashed vertical lines show the multipoles corresponding to the wavenumbers under consideration, using $\ell = kd$; these wavenumbers as shown for the high$-k$ bands. The dark (light) band shows the 1σ region for the C_ℓ^{TT} spectra for the ACT+WMAP (WMAP only) data. The best-fit curve using the combination of ACT and WMAP data is shown as the dark solid curve and the dashed black curve shows the best-fit power-law spectrum obtained from fitting the data in Chapter 3. The lower panel shows the corresponding C_ℓ^{TE} power spectrum, plotted here as $\ell(\ell+1)C_\ell^{TE}/2\pi$ μK^2, together with WMAP data and data from the QUaD experiment [273]. Note that the fact that the 1σ band from the WMAP only analysis extends only to negative values of the power spectrum is an artefact and not physical.

Table 4.2 Estimated model parameters and 68% confidence limits for the ACT 2008 Southern Survey data combined with WMAP.

	Parameter [a]	ACT+WMAP Power-law[b]	ACT + WMAP binned $P(k)$ with H_0 prior
Primary	$100\Omega_b h^2$	2.222 ± 0.055	2.307 ± 0.124
	$\Omega_c h^2$	0.1125 ± 0.0053	0.1166 ± 0.0085
	θ_A	1.0394 ± 0.0024	1.0419 ± 0.0034
	τ	0.086 ± 0.014	0.100 ± 0.017
Secondary	A_p	15.81 ± 2.01	14.19 ± 2.45
	A_c	< 10.44	< 17.08
	$A_{\rm SZ}$	< 0.92	< 1.55

---

[a] For one-tailed distributions, the upper 95% confidence limit is given, whereas the 68% limits are shown for two-tailed distributions.

[b] The power-law model for the primordial spectrum is $\mathcal{P}(k) = A_s(k_0)\left(\frac{k}{k_0}\right)^{n_s-1}$.

to maintain the relative peak heights. Imposing a prior on the Hubble constant has the effect of breaking this degeneracy. Alternatively, one could impose a prior on the baryon density from Big Bang Nucleosynthesis ($\Omega_b h^2 = 0.022 \pm 0.002$, [274]) which would disfavour the low-H_0 models, as indicated in the top left panel of the bottom rows in Figure 4.4.

It is worth noting that the increase in the matter density along this degeneracy also increases the gravitational lensing deflection power, as a universe with a larger matter content exhibits stronger clustering at a given redshift. ACT maps have sufficient angular resolution to measure this deflection of the CMB [275]. Even without a strong prior on the Hubble constant, models with a bump in the primordial spectrum and $H_0 < 50$ (with $< 10\%$ Dark Energy density) are disfavoured at $> 4\sigma$ from the lensing measurement alone, a result similar to that discussed in Sherwin et al. [276]. Although parameterised differently, the same argument applies to the primordial spectrum considered by Hunt and Sarkar [258], motivated by phase transitions during inflation, that eliminates dark energy but which is also disfavoured at $\simeq 3\sigma$ by the lensing for a standard cold dark matter model. If massive neutrinos are included, this constraint is weakened however, as the amplitude of the deflection power is reduced at multipoles $\ell \simeq 100$ and the current ACT observations do not rule out the model.

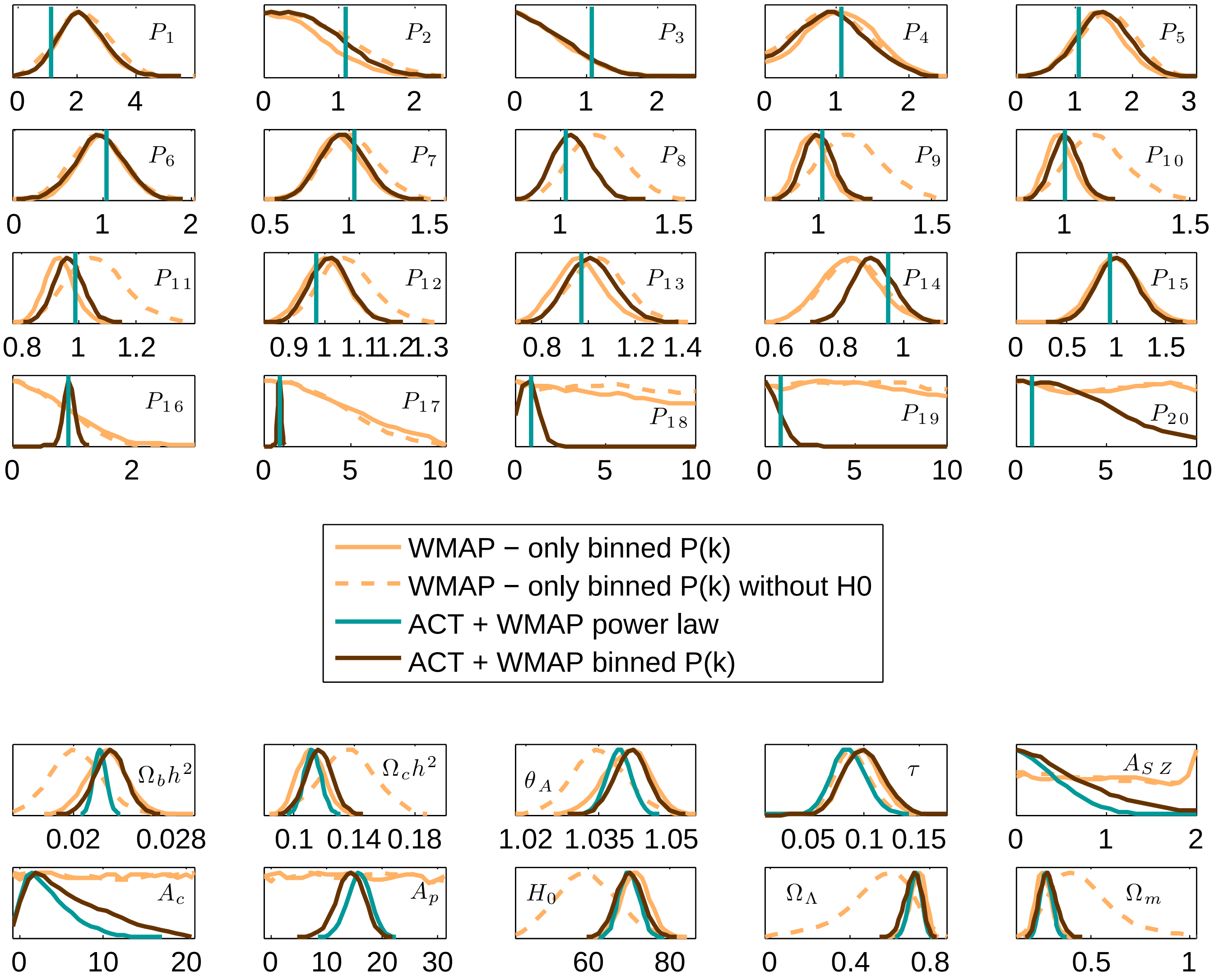

Figure 4.4 Parameter constraints: marginalised one dimensional distributions for the parameters determined from the ACT and WMAP data. The top 20 panels in the figure show the likelihoods for the power spectrum parameters directly determined using MCMC methods, while the lower 10 panels show the primary and secondary cosmological parameters and 3 derived quantities: the Hubble parameter H_0, the dark energy density Ω_Λ, and the matter density Ω_m. The light solid curves show the constraints on the parameters from ACT in combination with WMAP data for the ΛCDM case — the vertical lines in the power spectrum panels show the values the power spectrum would take assuming the best-fit $n_s = 0.963$ power-law from the results in Chapter 3. The parameter constraints for this power-law ΛCDM model are shown as the light curves. The solid dark lines show the distributions from ACT and WMAP data, assuming a prior on the Hubble constant. The best-fit value of the power-law spectral index obtained from fitting the well-constrained bands ($P_5 - P_{17}$) is $n_s = 0.965$. The dashed curves indicate the degeneracy between low values of θ_A and primordial power in modes around the position of the first peak.

The estimated cosmological parameters are given in Table 4.2 and the marginalised one-dimensional likelihoods are shown in Figure 4.4. While the binned $P(k)$ model adds 18 additional parameters to the parameter set, only 13 of those parameters are well constrained. All cosmological parameters in the binned power spectrum model are consistent with those derived using the concordance 6-parameter model with a power-law primordial spectrum. The addition of 13 new parameters which are substantially constrained by the data increases the likelihood of the model such that $-2\ln\mathscr{L} = 9.3$. Using a simple model comparison criterion like the Akaike Information Criterion (e.g. Liddle [277], Takeuchi [278]), the binned power spectrum model is disfavoured over the standard concordance model. Further, we find a power-law slope fit to the 13 constrained bands in power spectrum space (bands labeled from P_5 to P_{17} in Figure 4.4) of $n_s = 0.965$, which is, as expected, consistent with the constraints on the spectral index presented in Chapter 3.

4.3.2 Reconstructed $P(k)$

The primordial power spectrum translates to the angular power spectrum of the CMB, but can in addition be mapped to the late-time matter power spectrum through the growth of perturbations:

$$P(k, z=0) = 2\pi^2 k \mathcal{P}(k) G^2(z) T^2(k) \tag{4.4}$$

where $G(z)$ gives the growth of matter perturbations, $T(k)$ is the matter transfer function, and the $\mathcal{P}(k)$ are the fitted values as in Eq. (4.1). This mapping enables the constraints on the power spectrum from the CMB to be related to power spectrum constraints from other probes at $z \simeq 0$ [240, 279]. We illustrate the power spectrum constraints from the ACT and WMAP data in Figure 4.5. We take $G(z)$ and $T(k)$ from a ΛCDM model, but neither varies significantly as the cosmological parameters are varied within their errors in the flat cosmology we consider in this work. The $P(k)$ constraints from the CMB alone overlap well with the power spectrum measurements from the SDSS DR7 LRG sample [236], which have been deconvolved from their window functions. The ACT data allow us to probe the power spectrum today at scales $0.001 < k < 0.19$ Mpc^{-1} using only the CMB, improving on previous constraints using microwave data. In addition, the lensing deflection power spectrum also provides a constraint on the amplitude of matter fluctuations at a comoving wavenumber of $k \simeq 0.015$ Mpc^{-1} at a redshift $z \simeq 2$. The recent measurement of CMB lensing by ACT [275] is shown as $P(k = 0.015$ Mpc$^{-1}) = 1.16 \pm 0.29$ Mpc^3 in Figure 4.5. These two measurements are consistent with each other and come from two independent approaches: the lensing deflection power is a direct probe of the matter content at this scale (with only a minor projection from $z = 2$ to $z = 0$), while the primordial power is projected from the scales at the surface of last scattering at $z \simeq 1040$ to the power spectrum today.

Finally, cluster measurements provide an additional measurement of the matter power spectrum on a characteristic scale k_c, corresponding to the mass of the cluster, $M_c = (4\pi/3)\rho_m(\pi/k_c)^3$, where ρ_m is the matter density of the universe today. We compute the amplitude of the power spectrum at the scale k_c from reported σ_8 values as

$$P_c(k_c, z = 0) = (\sigma_8/\sigma_{8,\Lambda\mathrm{CDM}})P(k_c, z = 0)_{\Lambda\mathrm{CDM}}\,, \tag{4.5}$$

where $\sigma_{8,\Lambda\mathrm{CDM}} = 0.809$ is the concordance ΛCDM value [115]. We use the measurement of $\sigma_8 = 0.851 \pm 0.115$ from clusters detected by ACT, at a characteristic mass of $M = 10^{15} M_\odot$ [193], as well as measurements from the Chandra Cosmology Cluster Project (CCCP) [186], measured from the 400 square degree ROSAT cluster survey [280]. The quoted value of $\sigma_8 = 0.813 \pm 0.013$ is given at a characteristic mass of $2.5 \times 10^{14}\ h^{-1} M_\odot$. In addition, we illustrate constraints from galaxy clustering calibrated with weak lensing mass estimates of brightest cluster galaxies (BCG) [281], quoted as $\sigma_8 = 0.826 \pm 0.02$. In this case, we compute the characteristic mass M_c (and hence k_c) from the inverse variance weighted average mass of the halos (from Table 2 in Tinker et al. [281]) as $M_c = 4.7 \times 10^{13}\ h^{-1} M_\odot$. To remove the dependence on cosmology, the CCCP and BCG mass measurements are multiplied by a factor of h^{-1} (where $h = 0.738$ is taken from the recent Riess et al. [58] result). The ACT cluster measurement, however, is already expressed in solar mass units, and hence this operation is not required.

Power spectrum constraints from measurements of the Lyman–α forest are shown at the smallest scales probed. The slanted errorbars for the SDSS and Lyman–α data reflect the uncertainty in the power spectrum measurement from the Hubble constant uncertainty alone. Again, these data are normally plotted as a function of h^{-1} Mpc, hence we propagate the 1σ error on the Hubble parameter from Riess et al. [58] through to the plotted error region in both wavenumber and power spectrum. Transforming from units of power spectrum to mass variance $\Delta_M/M = \sqrt{P(k)k^3/(2\pi^2)}$ (indicated in the bottom panel of Figure 4.5), allows one to visualise directly the relationship between mass scale and variance. While $\Delta_M/M \simeq 1$ for $10^{16} M_\odot$ galaxy clusters, the variance decreases as the mass increases and we probe the largest scales, covering ten orders of magnitude in the range of masses of the corresponding probes.

4.4 DISCUSSION

We constrained the primordial power spectrum as a function of scale in 20 bands using a combination of data from the 2008 Southern Survey of the Atacama Cosmology Telescope and WMAP data. We make no assumptions about the smoothness of the power spectrum, beyond a spline interpolation between power spectrum bands. The arcminute resolution of ACT constrains the power spectrum at scales $0.1 < k < 0.19$ Mpc^{-1} which had not yet been well constrained by microwave background experiments. This allows us to test for deviations from scale invariance in a model-independent framework. We find no significant evidence for deviation from a power-law slope. When a power-law spectrum is fit to our well-constrained bands, our best-fit slope of $n_s = 0.965$ is consistent with that determined directly from a standard parameter space of ΛCDM models with a power-law spectrum, using the same data. Mapping the primordial power to the late-time power spectrum using the fluctuations in the matter density, we obtain measurements of the power spectrum today from the cosmic microwave background which are consistent with results from galaxy redshift surveys, but which also probe the power spectrum to much larger scales, $k \simeq 0.001$ Mpc^{-1}, over mass ranges $10^{15} - 10^{22}\ M_\odot$. Finally, the allowed range in the primordial power from the high-ℓ ACT temperature power spectrum measurements

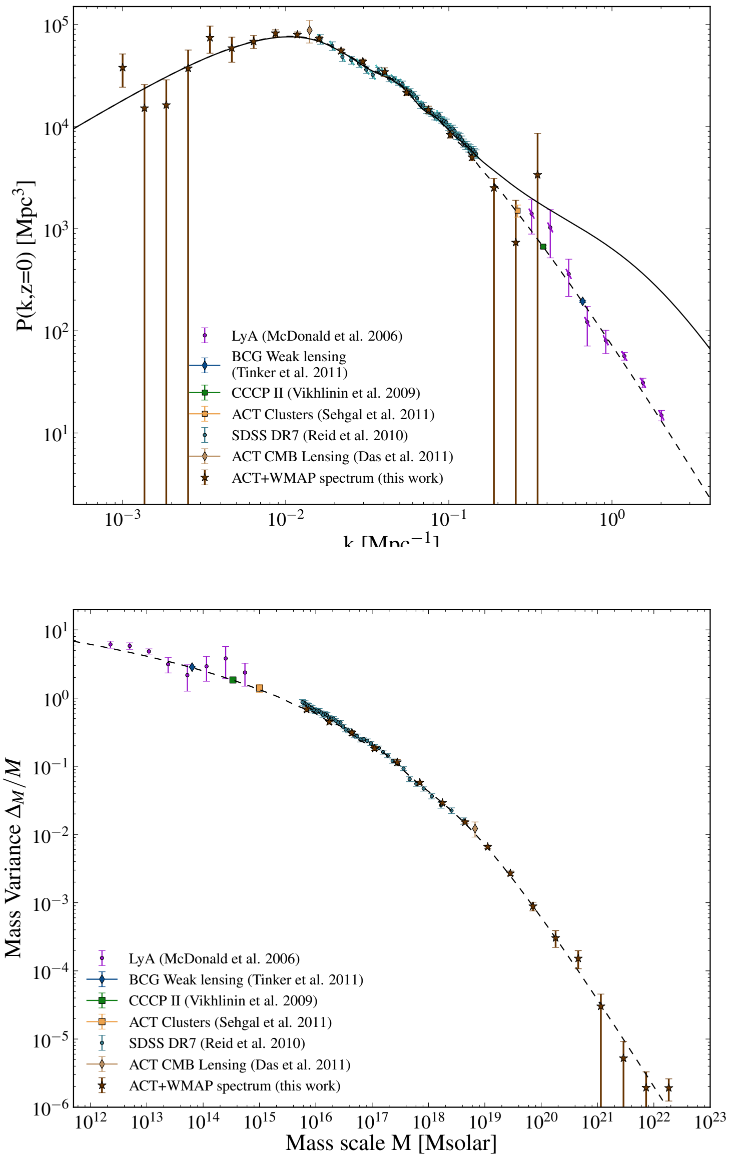

Figure 4.5 The reconstructed matter power spectrum: the stars show the power spectrum from combining ACT and WMAP data (top panel). The solid and dashed lines show the nonlinear and linear power spectra respectively from the best-fit ACT ΛCDM model with spectral index of $n_s = 0.96$ computed using CAMB and HALOFIT [282]. The data points between $0.02 < k < 0.19$ Mpc^{-1} show the SDSS DR7 LRG sample, and have been deconvolved from their window functions, with a bias factor of 1.18 applied to the data. This has been rescaled from the Reid et al. [236] value of 1.3, as we are explicitly using the Hubble constant measurement from Riess et al. [58] to make a change of units from h^{-1} Mpc to Mpc. The constraints from CMB lensing [275], from cluster measurements from ACT [193], CCCP [186] and BCG halos [281], and the power spectrum constraints from measurements of the Lyman–α forest [283] are indicated. The CCCP and BCG masses are converted to solar mass units by multiplying them by the best-fit value of the Hubble constant, $h = 0.738$ from Riess et al. [58]. The bottom panel shows the same data plotted on axes where we relate the power spectrum to a mass variance, Δ_M/M, and illustrates how the range in wavenumber k (measured in Mpc^{-1}) corresponds to range in mass scale of over 10 orders of magnitude. Note that large masses correspond to large scales and hence small values of k. This highlights the consistency of power spectrum measurements by an array of cosmological probes over a large range of scales.

constrains the allowed range in the polarisation-temperature cross spectrum, which will be probed with future polarisation experiments.

5

PHOTOMETRIC SUPERNOVA COSMOLOGY WITH BEAMS AND SDSS-II

5.1 INTRODUCTION

The unexpected faintness of distant Type Ia Supernovae (SN Ia) was the key to the discovery of late-time cosmic acceleration [284, 285]. A decade later, the discovery and analysis of large numbers of high-quality SN Ia data remains a cornerstone of modern cosmology, with various surveys probing SN Ia over a huge range of distances, with a particular focus on understanding and removing potential unaccounted for systematic errors and sharpening them as standard candles [43, 125–127, 131, 133, 137, 138, 286–297]. The current state of the art is a heterogenous sample of hundreds of SNe, predominantly at intermediate redshifts, $z < 1$ [125–130], with a high-z sample from the Hubble Space Telescope [131], and anchored with a low redshift sample [132–138]. The SDSS-II SN survey data [289, 291] fill in the 'redshift gap' between $0.02 < z < 0.4$. In these surveys, multi-band photometric light-curves are very successfully used to estimate the probability that a candidate is a SN Ia as opposed to a core collapse supernova (Ibc or II) or other object, providing vital intelligence for the selection of likely SN Ia for spectroscopic follow-up [298–307].

Future surveys such as the Dark Energy Survey (DES, [308]), Pan-STARRS [309] and the Large Synoptic Survey Telescope (LSST, [310]) will vastly increase the numbers of detected SNe, perhaps by a factor of a thousand in the case of LSST. However, the dilemma facing these surveys is how to make appropriate use of this surfeit of data given that without a very expensive follow-up program, spectroscopic confirmation will be only be possible for a small fraction of the promising SN Ia candidates, varying somewhere between $0.5 - 20\%$. The wealth of current and future data is therefore driving us inexorably towards an era of purely photometric supernova cosmology in which most of the cosmological constraints from the survey come from supernovae with no spectroscopic information, although there may be a host redshift for example.

This is not a task to be undertaken lightly. While multi-band photometry methods strive to reduce the amount of contamination of the Ia sample from interlopers to a minimum, there will always be some level of contamination - currently around the 5% level [304, 305] - and this biases the inferred cosmological constraints at an unacceptable level if one simply uses standard inference techniques. Fortunately one can rigorously incorporate contamination effects into a Bayesian inference framework to yield unbiased cosmological results. In this paper we apply the resulting framework: Bayesian Estimation Applied to Multiple Species (BEAMS, Kunz et al. [311]) to the purely photometric SN data. We test the algorithm against various simulations, and describe potential challenges in future photometric analyses. In addition, we apply the algorithm to the SDSS-II SN data sample. While still in its developing stages, photometric supernova cosmology is a very promising approach to exploit the deluge of supernova data of the coming decade, and we show how BEAMS is one approach that is robust to general assumptions about the SN population.

5.2 THE BEAMS FRAMEWORK FOR PHOTOMETRIC SN COSMOLOGY

5.2.1 *Basic Formalism*

The current state-of-the-art is to restrict any contamination from non-SN Ia interlopers by only doing cosmology on those candidates that have been spectroscopically confirmed as being Type Ia through the identification of characteristic absorption lines such as the Si-II 6150 feature [312, 313]. While this is currently feasible, demanding spectroscopic follow-up of all candidates from future large surveys such as the Dark

Energy Survey [308] and LSST [310] will entail throwing away the great majority of interesting candidates.

BEAMS [311] was developed to address this waste. It is a general Bayesian framework that allows use of all available candidates as long as their probability of being a SN Ia is known in an unbiased way. While it is a general method for estimating parameters from contaminated data, it is readily applied to the SN problem, where we wish to evaluate the posterior distribution $P(\boldsymbol{\theta}|\boldsymbol{d})$, the probability of cosmological parameters, which we denote by $\boldsymbol{\theta} = (\theta_1, \theta_2, ..., \theta_j, \theta_m)$, *given* the SN data, expressed as a vector $\boldsymbol{d} = (d_1, d_2, ..., d_i, ...d_N)$ of N measurements (of, for example, the distance modulus μ for SN).

To apply BEAMS we invoke a binary vector $\boldsymbol{\tau} = (\tau_1, \tau_2, ..., \tau_i, ...\tau_N)$ of length N, equal to the number of data points. The entries of this vector are 1 if the corresponding data point is a Type Ia supernova (SN Ia) and 0 if the point is not (i.e. Type Ibc, II or non-SN), i.e. $\tau_i = 1\ (0)$ if the i-th data point is (or is not) a SN Ia. In general the class of 'non-SN Ia' supernovae can be subdivided into many subclasses; in which case τ would not be a binary vector but would index the possible sub-classes. Here we consider only the simple binomial case.

Applying Bayes' Theorem and marginalising over all possible values of the vector $\boldsymbol{\tau} = \tau_1, \tau_2, ..., \tau_N$, the general posterior becomes [311]:

$$P(\boldsymbol{\theta}|\boldsymbol{d}) = \sum_{\tau} P(\boldsymbol{\theta}, \boldsymbol{\tau}|\boldsymbol{d}) = \sum_{\tau} P(\boldsymbol{d}|\boldsymbol{\theta}, \boldsymbol{\tau}) \frac{P(\boldsymbol{\theta}, \boldsymbol{\tau})}{P(\boldsymbol{d})}, \tag{5.1}$$

where $P(\boldsymbol{\theta}, \boldsymbol{\tau})$ is the prior for the parameters and $P(\boldsymbol{d})$ is the usual evidence factor which does not depend on the cosmic parameters.

Assuming that the data are uncorrelated we then split the effective posterior into two parts for each i-th data point:

$$P(\boldsymbol{d}|\boldsymbol{\theta}, \boldsymbol{\tau}) P(\boldsymbol{\tau})|_i = \left[P(d_i|\boldsymbol{\theta}, \tau_i = 1) P_i + P(d_i|\boldsymbol{\theta}, \tau_i = 0)(1 - P_i) \right], \tag{5.2}$$

where $P_i = P(\tau_i = 1)$, is the probability that a given point is in fact a SN Ia, $P(d_i|\boldsymbol{\theta}, \tau_i = 1)$ is the likelihood of the Ia distribution, and $P(d_i|\boldsymbol{\theta}, \tau_i = 0)$ is the non-SN Ia likelihood.

The probabilities P_i are determined through standard light-curve fitters such as those mentioned above, which typically assume that the data are from a SN Ia population and hence fit SN Ia light-curve templates to the data points, although other approaches fit multiple templates to the data and obtain probabilities from the relative χ^2 [304, 305]. In general the conversion from a normalised χ^2, describing a goodness of fit, to the probability that a given supernova is of Type Ia or not is difficult and so the probabilities can be skewed (see Newling et al. [314] for a detailed investigation of potential bias from incorrect assumptions about the probabilities). In addition, a data set may contain very different numbers of Type Ia and core-collapse supernovae. For this reason we add a global parameter A that re-normalises the relative probability (the Bayes factor) of being of Type Ia or not through $P_{\mathrm{Ia},i}/(1 - P_{\mathrm{Ia},i}) \to AP_{\mathrm{Ia},i}/(1 - P_{\mathrm{Ia},i})$. In general one might consider A to vary with redshift, or indeed with the light-curve fitter used, given the variety of assumptions made by the fitters. We leave these tests to future work and in this analysis we consider only one global parameter A. The final probability that enters the BEAMS likelihood is then

$$P^{(A)}_{\mathrm{Ia},i} = \frac{AP_{\mathrm{Ia},i}}{1 - P_{\mathrm{Ia},i} + AP_{\mathrm{Ia},i}} \tag{5.3}$$

where we estimate A simultaneously with the other parameters (subject to a Jeffreys' prior, i.e. we sample uniformly in $\ln A$, with a bound that $A < 100$). This mapping provides an indication of whether or not the input probabilities (from the light curve fitter for example) are biased, as we expect the distribution to be peaked around one. The total BEAMS posterior is then

$$P(\boldsymbol{\theta}|\boldsymbol{d}) \propto P(\boldsymbol{\theta}) \times \prod_{i=1}^{N} \left\{ P(d_i|\boldsymbol{\theta}, \tau_i = 1) P^{(A)}_{\mathrm{Ia},i} + P(d_i|\boldsymbol{\theta}, \tau_i = 0) \left(1 - P^{(A)}_{\mathrm{Ia},i}\right) \right\}$$

where the parameter vector $\boldsymbol{\theta}$ now contains the cosmological parameters $\{H_0, \Omega_m, \Omega_\Lambda\}$, and the probability parameter A and extra parameters necessary to model the supernova likelihoods discussed below. $P(\boldsymbol{\theta})$ represents the prior probabilities of the parameters. If we are interested only in the cosmological parameters then we marginalise over all the others. We will now discuss in detail our choice of the Type Ia and non-SN Ia likelihoods.

5.2.2 The Likelihood Distribution for SN Ia

The Ia likelihood is modelled as usual as a Gaussian probability distribution function (pdf) for the observed distance modulus μ_i centered around the theoretical value $\mu(z, \boldsymbol{\theta})$ with a variance $\sigma^2_{\mathrm{tot},i}$:

$$P(\mu_i|\boldsymbol{\theta}, \tau_i = 1) = \frac{1}{\sqrt{2\pi}\sigma_{\mathrm{tot},i}} \exp\left(-\frac{(\mu_i - \mu(z_i, \boldsymbol{\theta}))^2}{2\sigma^2_{\mathrm{tot},i}}\right). \tag{5.4}$$

The distance modulus is defined as the difference between the absolute and apparent magnitudes, $\mu = M - m$. The distance modulus is related to the cosmological model via:

$$\mu(z, \boldsymbol{\theta}) \equiv 5 \log d_L(z, \boldsymbol{\theta}) + 25\,, \tag{5.5}$$

where

$$d_L(z, \boldsymbol{\theta}) = \frac{c(1+z)}{\sqrt{\Omega_k} H_0} \times \sinh\left(\sqrt{\Omega_k} \int_0^z \frac{dz}{\sqrt{\Omega_m(1+z)^3 + \Omega_k(1+z)^2 + \Omega_{\mathrm{DE}} f(z)}}\right)$$

is the luminosity distance measured in Mpc; $\Omega_m, \Omega_k, \Omega_{\mathrm{DE}}$ are the energy densities of matter, curvature and dark energy respectively relative to flatness, obeying $\Omega_m + \Omega_k + \Omega_{\mathrm{DE}} = 1$, H_0 is the Hubble constant, and the function $f(z) = \rho_{\mathrm{DE}}(z)/\rho_{\mathrm{DE}}(0)$ describes the evolution of the dark energy density. While one of the ultimate goals in SN cosmology is to test for dynamics with redshift of the equation of state w, this relies on a sample at both high and low redshift to anchor the Hubble diagram and provide a long lever arm. In this work, we discuss how BEAMS improves constraints on parameters when including a photometric sample, and hence do not include the low or high redshift samples in this case. For this reason we focus on the $\Omega_m - \Omega_\Lambda$ combination of cosmological parameters, and so will only consider ΛCDM models for which $f(z) = 1$. In principle we should also consider radiation, but its energy density is negligible at late times when we observe supernovae.

One might assume that since both the distance modulus μ_i and the probability $P_{\mathrm{Ia},i}$ are obtained through fitting light-curve data to model templates, correlations between the probabilities and the distances would be generated. We test for such correlations in the SDSS-II SN data, which is discussed in Section 5.6.

We model the error on the distance modulus of each supernova as a sum in quadrature of several independent contributions,

$$\sigma^2_{\text{tot},i} = \sigma^2_{\mu,i} + \sigma^2_{\tau} + \sigma^2_{\mu,z}, \tag{5.6}$$

where $\sigma_{\mu,i}$ is the error obtained from fits to the SN light-curve, σ_τ is the characteristic intrinsic dispersion of the supernova population, which we add as an additional global parameter with Jeffreys' prior, and where $\sigma_{\mu,z}$ converts the uncertainty in redshift due to measurement errors and peculiar velocities into an error in the distance of the supernova as [289, 290]:

$$\sigma_{\mu,z} = \frac{5}{\ln(10)} \frac{1+z}{z(1+z/2)} \sqrt{\sigma_z^2 + (v_{pec}/c)^2}, \tag{5.7}$$

with σ_z as redshift error, and v_{pec} as the typical amplitude of the peculiar velocity of the supernova, which we take as 300 km s^{-1}.

In general, light-curve fitters such as SALT2 [315] or MLCS2k2 [316] fit magnitudes in various bands and time epochs to obtain a distance modulus. The two fitters are based on different approaches and hence make different assumptions about the model. In general one mights also include a systematic error due to differences in distance modulus from using different light-curve fitters as discussed in Kessler et al. [289]. However, given that we are using only one light-curve fitter in this analysis, and as we are interested in the relative improvement of constraints when applying BEAMS, we ignore this constant systematic error without loss of generality.

5.2.3 *Forms of the non-SN Ia Likelihood*

The simplest choice, adopted here, is to model the likelihood of the non-SN Ia through a mean and a dispersion. The least-informative choice of pdf in this case is also a Gaussian [317],

$$P(\mu_i|\boldsymbol{\theta}, \tau_i = 0) = \frac{1}{\sqrt{2\pi} s_{\text{tot},i}} \exp\left(-\frac{(\mu_i - \eta(z_i, \boldsymbol{\theta}))^2}{2 s^2_{\text{tot},i}} \right). \tag{5.8}$$

As we do not know the mean η and variance $s^2_{\text{tot},i}$ of the non-SN Ia population, we describe them with additional parameters. For the variance we use the same form as for the Type Ia supernovae, Eq. (5.6), but with a potentially different intrinsic dispersion s_τ^2 described by an independent parameter (again with a Jeffreys' prior). We assume that the measurement errors and the contribution from the peculiar velocities enter in the same way for Type Ia and other supernovae and so keep these terms identical.

We do not know what to expect for the mean of the non-SN Ia pdf and so we allow for a range of possibilities. As the brightness is probably also linked to the luminosity distance, we describe the expected non-SN Ia distance modulus (as provided by the light-curve fitter) as a deviation from the theoretical value, $\eta(z,\boldsymbol{\theta}) = \mu(z,\boldsymbol{\theta}) + \Upsilon(z)$, where we consider the following cases:

$$\begin{aligned} \Upsilon(z) \quad \propto: \quad & az + b \\ & az + bz^2 + c \\ & az + bz^2 + cz^3 + d \\ & (az + bz^2 + c)/(1 + dz). \end{aligned} \tag{5.9}$$

We then employ a criterion based on model probability to decide which of these functions to use. We note that the explicit link of $\eta(z,\boldsymbol{\theta})$ to $\mu(z,\boldsymbol{\theta})$ carries a risk that the non-SN Ia likelihood can bias the posterior estimation of the cosmological parameters. For this reason we verify that the contours do not shift when we set directly $\eta(z,\theta) = \Upsilon(z)$, although we will need a higher-order expansion in general (and of course the recovered parameters of the function $\Upsilon(z)$ will change).

For a cosmological analysis we just marginalise over the values of the parameters in $\Upsilon(z)$, but these parameters contain information on the distribution of non-SN Ia supernovae and thus their posterior is of interest as well, allowing us to gain insight into the distribution characteristics on the non-SN Ia population at no additional 'cost'. However, the simple binomial case considered here, where the non-SN Ia population consists of all types of core collapse SNe, is probably too simplistic to accurately describe the distribution of non-SN Ia supernovae. This could be improved by investigating the major contributions to the distance modulus residuals from simulations (see Falck et al. [144] for one such investigation). Alternatively, if the data set is large enough, then it is also possible to use a more general non-SN Ia model (e.g. a mixture of Gaussians) and to use model selection methods to choose the appropriate amount of freedom. We leave such improvements to future work.

5.2.4 *Comparison to Standard χ^2 Methods*

The primary difference between BEAMS and current methods is that the latter either require that all data are spectroscopically confirmed, or apply a range of quality cuts. In this paper we will compare the performance BEAMS to these two approaches, by processing the data that pass the required selection criteria using the Ia likelihood, Eq. (5.4). We will hereafter refer to this as the χ^2 approach.

The sample containing only spectroscopically confirmed supernovae will be called the *spectro sample*. In addition to spectroscopic confirmation we will also apply a cut on the goodness-of-fit probability from the light-curve templates within the MLCS2k2 fitter, $P_{\text{fit}} > 0.01$, and a cut on the light-curve fitter parameter $\Delta > -0.4$, where Δ is the shape-luminosity parameter in MLCS2K2 mode and describes the intrinsic SN colour dependence on brightness. More intrinsically brighter supernovae would have a more negative value of Δ, however this parameter is only defined for Type Ia light-curves. The larger *cut sample* is selected both by removing 5σ outliers from any data set and by imposing various cosmology cuts typical of what has been previously suggested for future photometric cosmological analyses. These cuts vary according to the type of data used (the various datasets are summarised in the sections that follow), but generally include a probability cut on P_{typer} (where the probability comes from a general supernova typing procedure as in Sako et al. [304, 305])[1] and a cut on the goodness-of-fit of the light-curve data to the Type Ia typer, χ^2_{lc}. Finally, the *photo sample* will be the sample to which BEAMS will be applied, and will include all the data. While the spectro and cut samples have by definition $P_{\text{Ia}} = 1$ (as they are analysed in the χ^2 approach), we do not set the probabilities to unity when applying BEAMS to the full sample.

---

[1] If the MLCS2k2 fitter probabilities were themselves used to make a cut sample, then objects would only be included if they had probabilities greater than some threshold, for example $P_{\text{fit}} > 0.9$.

5.3 DATASETS

We apply BEAMS to three datasets. Firstly we generate an idealistic simulated dataset where the input Ia and non-SN Ia model for distance modulus are known, and all data are simulated as Gaussian distributions around this model. The second level of simulations are generated from SNANA [318] as light-curves and then fit using MLCS2k2 [316], based on an SDSS-II-like dataset. Finally we apply BEAMS to the SDSS-II SN Photometric data from 2005 to 2008. The various datasets are described below.

5.3.1 *Level I: Gaussian Simulations*

We simulate simulations of 50 000 SNe, with redshifts drawn from a Gaussian distribution, $z \sim \mathcal{N}(0.3, 0.15)$, and distance moduli drawn from a flat ΛCDM universe with $(\Omega_m, \Omega_\Lambda, H_0, w_0, w_a) = (0.3, 0.7, 70, -1, 0)$. The non-SN Ia population has an additional contribution to the distance modulus, $\eta(z) = \mu(z) + az + bz^2 + c$, where we choose $(a, b, c) = (1, -3, 1.5)$. We assign probabilities by transforming uniformly distributed random numbers between zero and one into random numbers from a given distribution (here we assume a linear distribution). For each data point d_i, one starts by throwing two uniform random numbers, r_i and q. We then apply the operation $f(q)$ to the random number q (in our case $f(q) = q$ but f can in general be any function of a uniform random number q such that $0 < f(q) < 1$). The number $0 < r_i < 1$ is then repeatedly drawn from a uniform distribution until $r_i > f(q)$. Note that while we repeatedly draw r_i until this condition is satisfied, q is only drawn once per SN. This ensures that the final set of probabilities $\boldsymbol{P}_{\text{Ia}} = \{r_1, r_i, ..r_N\}$ follows a linear distribution. We then assign the *types* from the two samples (of Ias and non-SNe Ia), i.e. we choose a random number t and if $t < r_i$ (i.e. also follows the same linear relationship) we take the data point to be a Ia, and if $t > r_i$ we assign it as a non-SN Ia, until we run out of data points from either sample. This procedure reduces the sample size from 50 000 to 37529. We assign a 'measurement error' to each point of $\sigma_\mu = 0.1$; add an intrinsic error $\sigma_\tau = 0.16$ and a peculiar velocity error based on Eq. (5.6), with $v_{pec} = 300\text{km s}^{-1}$. We then randomly scatter to the data

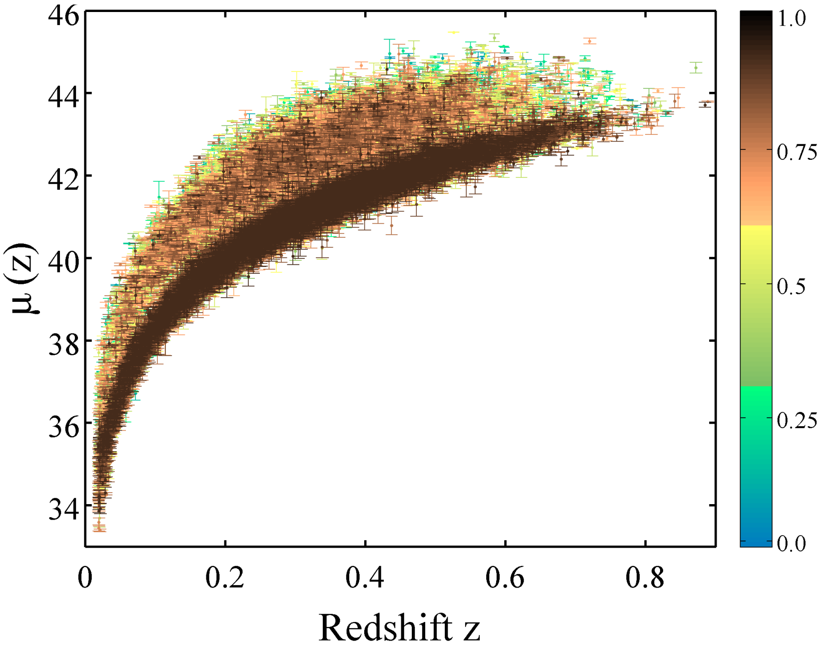

Figure 5.1 Level I data: 37529 points simulated according to a Gaussian distributions around a distance modulus in a flat ΛCDM model for the Ia population (25000 points) and with extra terms up to quadratic order in redshift for the non-Ia population. The points are coloured according to their probabilities from blue (low probability) to dark brown (high probability).

points based on the total errorbar. To mimic what happens in a light-curve fitter, only the measurement error is recorded, however. When performing parameter estimation on the points we either add this measurement error in quadrature to the other terms whose amplitudes are fixed (in the case of the χ^2 approach), or we estimate the magnitudes of the intrinsic dispersion when we apply the BEAMS algorithm. We randomly choose 10% of the Ia data and assign spectro status; this represents the data that are followed up by large telescopes on the ground. This 'spectro sample' is drawn so that we can compare the BEAMS estimated result to the χ^2 approach on a smaller sample. The data are shown in Figure 5.1. In the BEAMS analysis we checked on a small number of simulated samples that the results obtained were unbiased, however in general one would compute large numbers of simulations and check that the inferred cosmology was unbiased to a high level of precision.

5.3.2 *Level II: SNANA Simulations*

The Supernova Analysis package SNANA [318] contains both a simulation module to generate light-curve data, and an in-built light-curve fitter (for this work we used the MLCS2k2 fitter, however both SALT2 and MLCS2k2 are contained within the SNANA package), which allows one to process the data end-to-end within the program. This provided a robust procedure to test the BEAMS algorithm, where the final distribution of distance moduli are not explicitly given, but rather arise from the generation of SN data from light-curve templates, and the fitting of those templates with standard light-curve fitters.

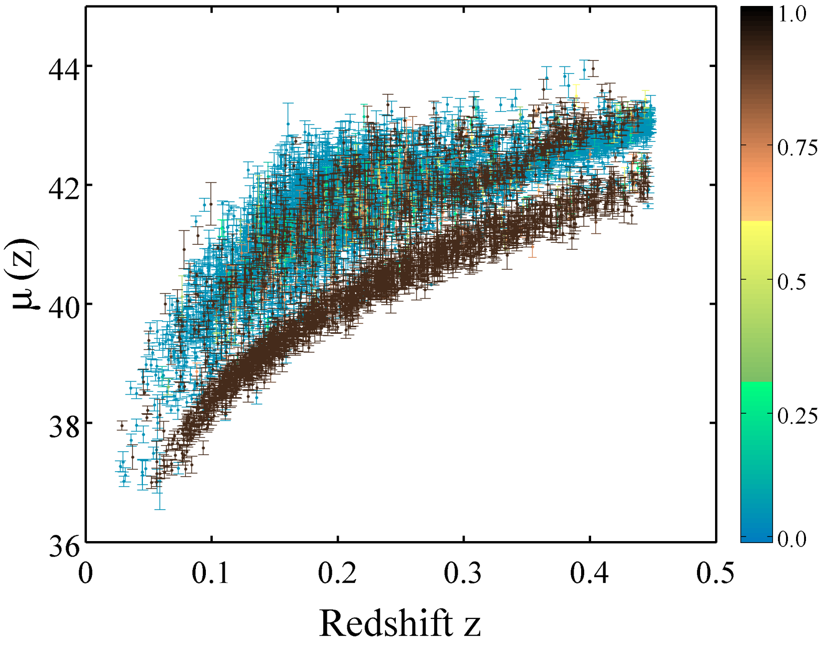

Figure 5.2 Level II data: 5391 SNANA simulated data points generated from a ΛCDM concordance cosmology and fitted with efficiency corrections as discussed in the text. The data contain 1290 SN Ia, and we define a smaller subset (264 SNe Ia) as a spectroscopic subsample, to mimic current data. As in Figure 5.1, the points are coloured by probability from low (blue points) to high (dark brown points). Note that the form of the non-Ia population is similar to the data simulated in Level I, which was simulated using a quadratic form to model the deviation of the non-Ia population from the standard form of the distance modulus.

The simulation specifications were chosen to match the SDSS-II SN survey characteristics as faithfully as possible, and resemble the BOSS sample, which contains spectroscopic redshifts for all SN observed in the SDSS-II SN search. Over 200000 SNe were simulated to match the SDSS-II SN Survey characteristics as faithfully as possible, between redshifts $0.02 < z < 0.5$, assuming a ΛCDM $(\Omega_m, \Omega_\Lambda) = (0.3, 0.7)$ cosmology. Type Ia SNe were simulated with a value of $R_V = 2.18$, while non-SNe Ia were simulated from a sample of Type II templates. The g, r and i light-curves of each simulated SNe were then fitted to Type Ia SNe templates assuming that the redshift of the SN was known. We impose various selection cuts on the sample, namely that each candidate should at least 5 epochs of observation, with at least one high signal-to-noise $(S/N > 5)$ epoch each in the g, r, i bands. Each candidate must have one epoch at least 10 days past the maximum light, and one observation pre-peak magnitude. These criteria restrict our sample to a total of 5391 simulated SNe. We apply the cuts discussed in Section 5.2.4 to generate a cut and a spectro sample. The spectroscopic sample of 264 SNe was chosen from 10% of the Type Ias in the sample (some of which did not survive the light-curve goodness-of-fit cuts) to roughly match the number in the spectro subsample of the Level III dataset.

5.3.3 *Level III: SDSS-II SN Photometric Data*

The Sloan Digital Sky Survey Supernova Search operated for three, three-month seasons during 2005 to 2008. The analysis and cosmological interpretation of the first season of data (hereafter Fall 2005) are described in Kessler et al. [289], while Lampeitl et al. [290] compare the SDSS-II SN data with other probes to constrain dark energy using low-redshift probes alone. Sollerman et al. [319] use the SDSS-II SN data to constrain non-standard cosmological models. The photometry and light-curves from the Fall 2005 season are described in detail in Holtzman et al. [291]. In addition to the spectroscopically confirmed SNe Ia discovered in the SDSS-II SN, many high-quality candidates without spectroscopic confirmation (i.e. only photometric observations have been made of the SNe) but with a spectroscopic redshift of the host galaxy were obtained. We include these SNe in both the cut sample and the spectro samples in the full photo sample, but do not set the probabilities of these points to unity. These supernovae are fit with MLCS2k2 [316] to obtain a distance modulus for each supernova, *assuming* the supernova is a Type Ia, in the same way as the Level II SNANA simulations. As outlined in Section 5.2.4, we impose the standard selection

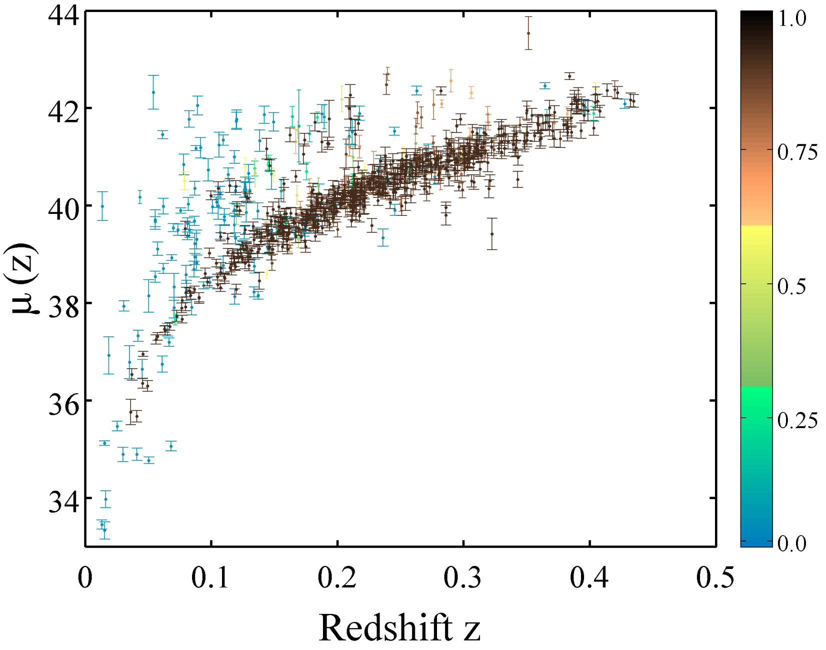

Figure 5.3 Level III data: the photometric sample of the full three seasons of SDSS-II SN survey. The 792 points are only included in the dataset given that accurate host galaxy redshifts are available for the sample. The sample includes 297 spectroscopically confirmed SNe, and are colour coded using probabilities from the Sako et al. [304, 305] typer from low (blue) to high (dark brown).

cuts on the probability of the fit to the MLCS2k2 light-curve template $P_{\text{fit}} > 0.01$ and $\Delta > -0.4$ to all data, and require that the data used have spectroscopic host galaxy redshift information. Applying these cuts to the full three year data yields a photometric sample of 792 SNe, with a spectroscopic subsample of 297 SNe. The spectro sample consists of the data points which have been spectroscopically confirmed by other ground-based telescopes, while the cut sample consists of the data points which have a typer probability of $P_{\text{typer}} > 0.9$ and a goodness-of-fit to the light-curve templates within the [304, 305] typer, $\chi^2_{lc} < 1.8$.

5.4 APPLICATION OF BEAMS

5.4.1 *Markov Chain Monte Carlo Methods*

In this work, the BEAMS algorithm is implemented within a Markov Chain Monte Carlo (MCMC) framework, and the Metropolis-Hastings [145] acceptance criterion was used. We use the cosmological parameters

$$\{\Omega_m, \Omega_\Lambda, H_0\} \tag{5.10}$$

in the case of the χ^2 approach on the spectro and cut samples, and add additional parameters

$$\{A, \sigma_\tau, s_\tau, a, b, c\} \tag{5.11}$$

in the case of the BEAMS application (and the quadratic model, in the other models for $Y(z)$ we adjust the parameters accordingly). The chains were in general run for around 100 000 steps per model, this was sufficient to ensure convergence. We test for convergence using the techniques described in Dunkley et al. [146]. We impose positivity priors on the energy densities of matter and dark energy, and impose a flat prior on the Hubble parameter between $20 < H_0 < 100$ km $\mathrm{s}^{-1}\mathrm{Mpc}^{-1}$. We impose broad Gaussian priors on the parameters of the non-SN Ia likelihood function, and step logarithmically in the probability normalisation parameter A, the intrinsic dispersion parameters of both the Ia and non-SN Ia distributions.

5.4.2 *BEAMS Comparisons across Levels I, II, III*

The BEAMS approach can be compared to standard χ^2 techniques, namely the χ^2 approach applied to subsets of the dataset resulting from cuts. For the Level I simulation we define the spectro sample as a randomly selected sample of 10% of the points we know to be of Type Ia. We compare the constraints using the three level datasets and various approaches in Figure 5.4. In each case, the BEAMS algorithm applied to the data gives the tightest constraints that are also consistent with the input

Table 5.1 Summary of datasets - the redshift distribution and sample sizes of the datasets compared in Figure 5.4. In the case of the Level III (real) data, the true numbers of Ia SNe in the sample are unknown.

Dataset	Level I	Level II	Level III
Redshift range	(0.02, 0.9)	(0.02, 0.45)	(0.02, 0.45)
Total Sample Size	37529	5391	792
No of Ia points	25000	1290	unknown
No of spectro points	2500	264	297

cosmology (in the case of simulations) and the spectroscopic sample (in the case of the data). In the case of the Level I simulation (since there is no light-curve fitting procedure in this simulation) the 'cut sample' is taken to be all points with probability $P_{\mathrm{Ia}} > 0.9$, while for the Level II simulations this is taken as all points that satisfy the basic cuts (such as the cut on the Δ parameter), and which also satisfy $P_{\mathrm{Ia}} > 0.9$ and the goodness-of-fit $\chi^2_{lc} < 1.8$. Note that the cut on the goodness-of-fit is not particularly conservative. In general, the more conservative the cut, the less biased the contours become. However, this is at the cost of the size of the contours, which increase, thereby losing the statistical power of the large sample. The curve corresponding to the spectroscopic subset we define as 'unbiased' since they by definition are the contours that would result in a contemporary analysis.

As is shown in Figure 5.4, BEAMS recovers the input cosmology of the simulations and estimates parameters consistent with the spectroscopic sample in the case of the Level III data. Moreover, the contours are three times smaller than when using the spectroscopic sample alone. In the Level II SNANA simulation the contours are $\simeq 40\%$ of the area of the spectroscopic sample, while in the case of ideal Level I Gaussian simulations, the BEAMS contours using all the points are $\simeq 16\%$ of the area of the spectroscopic sample. This highlights the potential of photometric supernova cosmology to drastically reduce the size of error contours with larger samples while remaining unbiased relative to the 'known' spectroscopic case.

5.4.3 *Scaling of Errorbars*

As discussed in Kunz et al. [311] for the one-dimensional case, the effective number of SNe that result when applying BEAMS scales as the number of spectroscopic SNe and the average probability of the dataset multiplied by the remainder of the photometric sample.

In our applications we have, however, not used the fact that we know that some points are confirmed as Type Ia. In other words, the probability of each data point was taken from the light-curve fitter and was not adjusted to one or zero depending on the

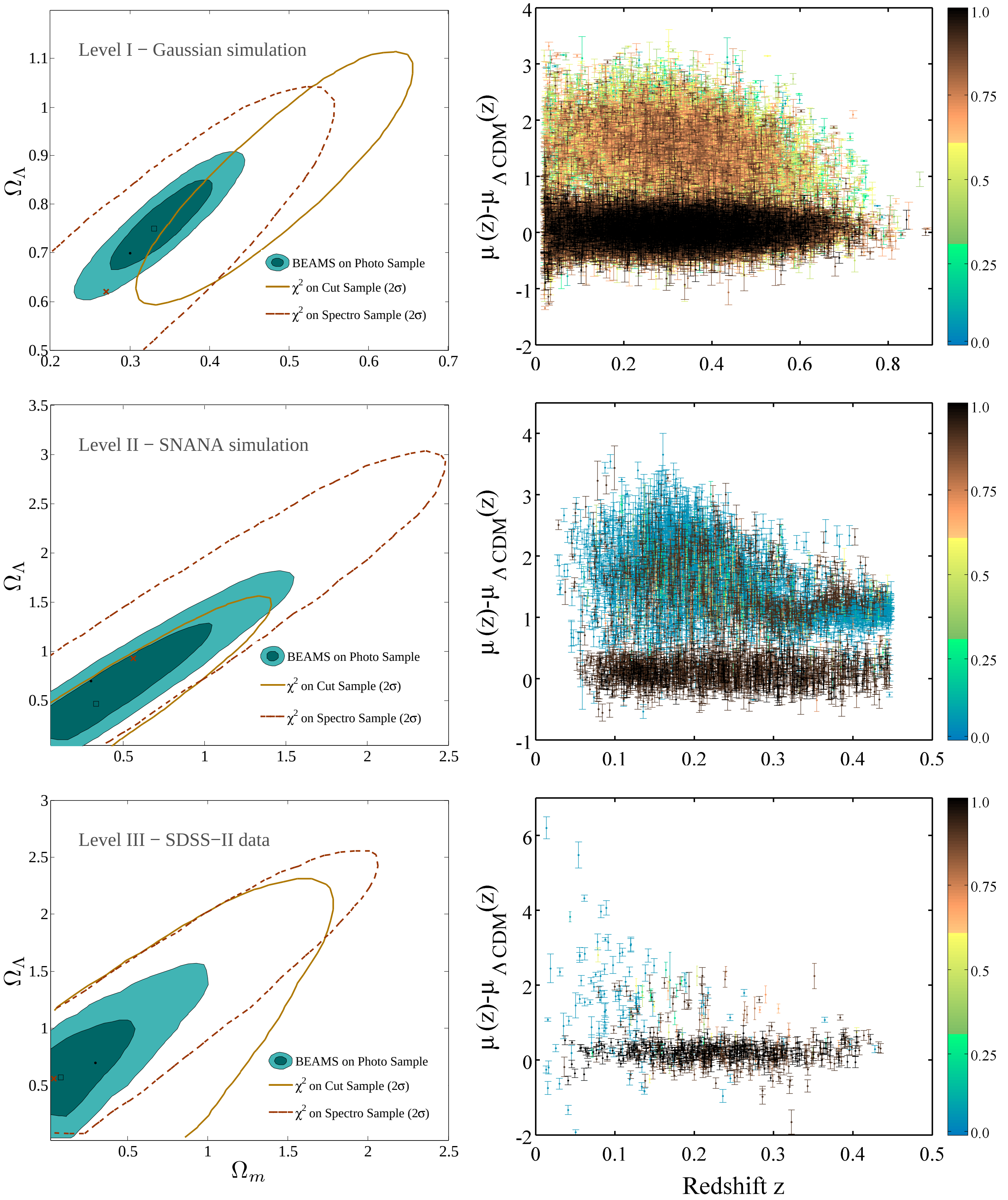

Figure 5.4 Comparing analysis techniques on various datasets: The left panel shows the 2σ contours in the $\Omega_m - \Omega_\Lambda$ plane for Levels I-III (top to bottom), while the right panel shows the $\Delta\mu(z)$ for the sample, where the data are coloured by probability from low (blue) to high (dark brown). In addition, the points which are 'spectroscopic' coloured in black. The levels are characterised in Table 5.1. In each case the BEAMS constraints recover concordance cosmology (which is what was input for the simulated data, and which one might hope to recover in the real-world data). The best-fit BEAMS point is given by the black square, while the best-fit cosmology from the spectroscopic data is indicated by the brown cross. While the cut approach based on probability of fit (and the parameter Δ in the case of the Level II and Level III data)) of light curve templates recovers the sample cosmology as the spectroscopic sample for stringent enough cuts, these cuts reduce the sample size significantly. The top left hand panel shows how even a relatively stringent cut on probability of $P_{\rm cut} = 0.9$ biases the inferred cosmology; stronger cuts will recover the true cosmology at the cost of sample size.

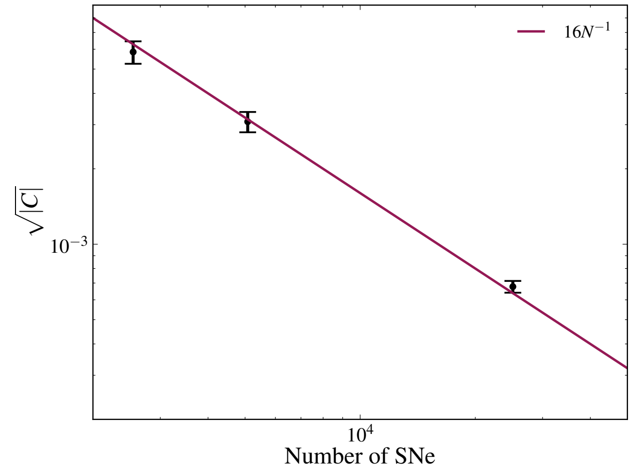

Figure 5.5 Errors scale with number of SNe: the size of the error ellipse, approximated by the square root of the determinant of the two-dimensional chain of Ω_m, Ω_Λ shows the reduction in size with increasing the number of SNe in the simulation.

known type. Hence we expect the size of the contours in the $i - j$ plane to scale as

$$C_{ij}^{1/2} \rightarrow \frac{C_{ij}^{1/2}}{\sqrt{\langle P_{\rm Ia}\rangle N_{photo}}}. \tag{5.12}$$

We compute the size of the error ellipse for various Level I simulations as a function of the size of the simulation, shown in Figure 5.5. We impose a prior on the densities, and hence the ellipses are not closed for smaller samples. For large enough sample sizes the ellipse is closed and we observe that the error ellipses scale in area as $\propto 1/\langle P_{\rm Ia}\rangle N$, which is consistent with earlier results [311].

Large supernova surveys will not only increase the total number of Type Ia SNe candidates, but will allow one to investigate systematics about the SNe populations directly. The BEAMS algorithm is designed to include and adapt to information about the non-SN Ia population easily. By adapting the form of the non-SN Ia population, and including more than one population group, one could use BEAMS to gain insight into the contaminant distribution itself.

Table 5.2 Comparison of non-SN Ia likelihood models for Level I data: χ^2 values for the fits using various forms of the non-SN Ia likelihood for the Level I simulations, where the true underlying model is a quadratic. The constraints on $\Omega_m - \Omega_\Lambda$ are shown in Figure 5.6.

Model	$\Delta\chi^2_{eff}$ [a]	Parameters
$Y(z) = az + c$	0	2
$Y(z) = az + bz^2 + c$	-192.9	3
$Y(z) = az + bz^2 + cz^3 + d$	-193.3	4
$Y(z)^b = (az + bz^2 + c)/(1 + dz)$	-193.4	4

[a] Difference in the effective χ^2 between a given model and the linear case.
[b] Padé approximant of the first order.

5.4.4 *Constraining $\eta(z)$ Forms for the non-SN Ia Population*

5.4.4.1 *Level I: Gaussian Simulations*

While we simulate data according to the prescription described in Section 5.2.3 using a quadratic model for the differences between the standard ΛCDM $\mu(z)$ and the non-SN Ia distance modulus, we test that assuming a different functional form within the parameter estimation does not significantly bias the inferred cosmology. We define the effective $\chi^2_{eff} = -2\ln\mathscr{L}$, where the posterior $\mathscr{L}$ is a linear sum of the terms in Equation (5.4), and provide values relative to the simplest linear model for $Y(z)$.

In other words, in Figure 5.6 we show that BEAMS is reasonably insensitive to the assumed form of the non-SN Ia likelihood, provided it is allowed enough freedom to capture the underlying model. A linear model fails to recover the correct cosmology, as it does not have enough freedom to recover the difference between the Ia and non-SN Ia distribution. It correspondingly has a very high χ^2 relative to the other approaches. The higher-order functions recover consistent cosmologies, and the χ^2 of these models improves by $\Delta\chi^2 < 0.5$, even though the models have increased the number of parameters by one.

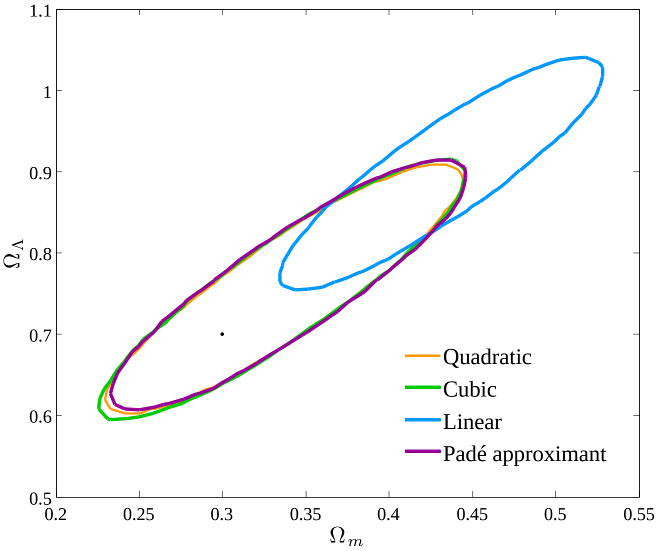

Figure 5.6 Different $\eta(z)$ distributions for the non-Ia likelihood using Level I data: 2σ constraints in the $\Omega_m - \Omega_\Lambda$ plane for different versions of the non-Ia distance modulus function. Here we have simulated a quadratic model, and run BEAMS assuming a linear, quadratic, cubic and Padé form $\Upsilon(z)$, as described in Section 5.2.3 and summarised in Table 5.2.

5.4.4.2 *Level II: SNANA Simulations*

In the case of the Level I Gaussian simulated data, the explicit form of the $\Upsilon(z)$ was specified as quadratic and then various other forms for $\Upsilon(z)$ were fit for within the BEAMS approach. In general, any model with enough freedom (of equal or higher order to the input model) managed to recover the input cosmology. We apply this test to the Level II SNANA simulations, where the data are generated from fitting generated light-curve data to templates. Naïvely one might not expect a simple model to fit the data. In general we find that while a cubic model performed the best at fitting the data (it had the lowest χ^2_{eff} relative to the linear model), the inferred cosmology in the quadratic case is consistent with the input cosmology. Fitting the Level II SNANA simulated data with a linear model led to a large bias in the inferred cosmology, in a similar way to what is seen Figure 5.6 for the Level I case. In general one might consider adding more degrees of freedom to the model until no further improvement is seen in the $\Delta\chi^2$. While this will become relevant in the data-driven future, current data (see the Level III data model comparison) do not motivate for such an investigation at present.

Table 5.3 Comparison of non-SN Ia likelihood models for Level II data: χ^2 values for the fits using various forms of the non-SN Ia likelihood for the Level II simulations, where the true underlying model is unknown. The constraints on $\Omega_m - \Omega_\Lambda$ are consistent for all models of second order or higher.

Model	$\Delta\chi^2_{eff}$[a]	Parameters
$Y(z) = az + c$	0	2
$Y(z) = az + bz^2 + c$	-29.6	3
$Y(z) = az + bz^2 + cz^3 + d$	-159.7	4
$Y(z)^b = (az + bz^2 + c)/(1 + dz)$	-66.1	4

[a] Difference in the effective χ^2 between a given model and the linear case.
[b] Padé approximant of the first order.

5.4.4.3 *Level III: SDSS-II Photometric SN Data*

In general the theoretical distance modulus for the non-SN Ia population is arbitrary. In the large supernova sample limit we will learn about the distribution of those SNe that are not from the Ia distribution, however we treat them here as nuisance parameters that we marginalise over. We shall let the data inform us of the best choice of model for the non-SN Ia distribution. Table 5.4 shows the various forms of the non-SN Ia distribution considered, and the χ^2 of the fit. The data seem consistent with a quadratic model, and the constraints do not change significantly for any assumed form, as shown in Figure 5.7.

5.4.5 *BEAMS Posterior Probabilities*

5.4.5.1 *Methodology*

The probability P_i is a prior probability from the earlier fitting and mapping process on whether or not the specific data belongs to the Type Ia population of supernovae. As described in Kunz et al. [311], however, one can promote P_i to a free variable, and its posterior distribution then contains information on how well it fits the Ia or

Table 5.4 Comparison of non-SN Ia likelihood models for Level III data: χ^2 values for the fits using various forms of the non-SN Ia likelihood for the SDSS-III data. While the χ^2 decreases as the number of parameters increases, not significantly given the amount of freedom in the higher order models. The constraints on $\Omega_m - \Omega_\Lambda$ from these fits are shown in Figure 5.7. The parameter values are the mean of the one-dimensional likelihood for the model parameters. This form also appears to be consistent with the SNANA simulated data (see Figure 5.3).

Model	$\Delta\chi^2_{eff}{}^a$	Parameters
$Y(z) = az + c$	0	2
Parameters (a, c)	$(-5.3, 1.7)$	
$Y(z) = az + bz^2 + c$	-1.3	3
Parameters (a, b, c)	$(-9.69, 10.73, 2.1)$	
$Y(z) = az + bz^2 + cz^3 + d$	-2.9	4
Parameters(a, b, c, d)	$(0.59, -4.97, 9.98, 1.64)$	
$Y(z)^b = (az + bz^2 + c)/(1 + dz)$	-0.2	4
Parameters (a, b, c, d)	$(-33.3, 83.4, 1.43, -19)$	

[a] Difference in the effective χ^2 between a given model and the linear case.

[b] Padé approximant of the first order.

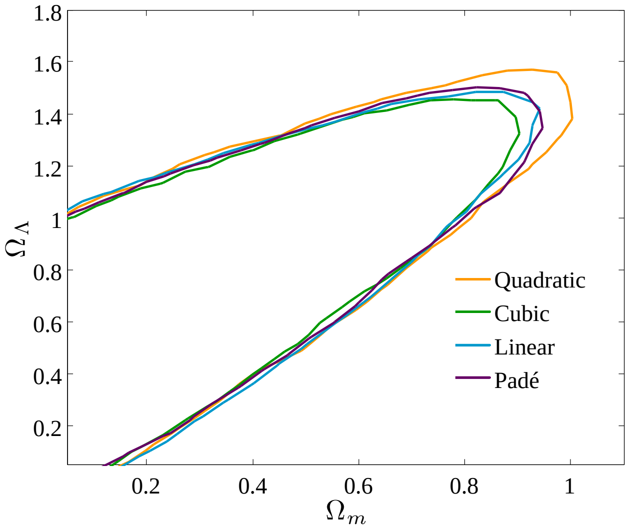

Figure 5.7 Different $\eta(z)$ distributions for the non-Ia likelihood using Level III data: 2σ constraints in the $\Omega_m - \Omega_\Lambda$ plane for different versions of the non-Ia distance modulus function. The contours remain consistent regardless of the choice of the form of $Y(z)$. The χ^2 values for these models are summarised in Table 5.4.

then non-Ia class of supernovae. If we leave just P_i for one i free, and fix all other parameters, then the posterior becomes

$$P(\boldsymbol{\theta}|\boldsymbol{\mu}) \propto \left(\prod_{j\neq i}^{N} P(\boldsymbol{\theta}|\mu_j)\right)\{P(\mu_i|\boldsymbol{\theta},\tau_i=1)P_i \\ +P(\mu_i|\boldsymbol{\theta},\tau_i=0)(1-P_i)\} \tag{5.13}$$

where $P(\boldsymbol{\theta}|\mu_j)$ is the posterior at the fixed parameter vector $\boldsymbol{\theta}$ for all supernovae except i. The above expression is just a straight line going from $\prod_{j\neq i}^{N} P(\boldsymbol{\theta}|\mu_j)P(\mu_i|\boldsymbol{\theta},\tau_i=0)$ at $P_i=0$ to $\prod_{j\neq i}^{N} P(\boldsymbol{\theta}|\mu_j)P(\mu_i|\boldsymbol{\theta},\tau_i=1)$ at $P_i=1$. In general, we do not fix the parameters but sample from the full posterior, and then marginalise over everything except P_i. This results again in the posterior for P_i being a straight line.

To extract the *model probabilities* corresponding to supernova i being of Type Ia or not, as opposed to the posterior distribution of the parameter P_i, we take recourse to the Savage-Dickey density ratio [320, 321]: In nested models the relative model probability (in favour of the more simple model) is the ratio of the posterior divided by the prior at the nested point. The two models $\mathcal{M}_1$="Ia" and $\mathcal{M}_2$="not Ia" are not nested, but we can use a trick by extending our model space with a third model $\mathcal{M}_3$="P_i free". Then the two models are nested in that third model at the points $P_i=1$ and $P_i=0$ respectively. Therefore the relative probabilities $B_{31}^{(i)}=P(\mathcal{M}_3)/P(\mathcal{M}_1)$ and $B_{32}^{(i)}=P(\mathcal{M}_3)/P(\mathcal{M}_2)$ for supernova i can be extracted from a the MCMC chain with free probability P_i, by looking at the end-points of the normalised posterior for P_i, marginalised over all other parameters. Given the discussion above on the shape of the posterior of P_i, what we do in practice is to fit a straight line to the distribution of P_i values of a MCMC chain in which we left P_i free. The values at the end points give directly B_{31} and B_{32}. The relative probability between models $\mathcal{M}_1$ and $\mathcal{M}_2$ is now simply $B_{12}^{(i)}=B_{32}^{(i)}/B_{31}^{(i)}$.

To which value should we set the probabilities that we keep fixed? A natural possibility would be to use the output of a prior typing stage, but this choice involves the risk that the prior probabilities could be biased. Instead we could use $P=1/2$ to convey the minimal amount of extra information. In this case we should also use the A parameter to allow for an automatic correction of different total numbers of supernovae of different types. This choice has another advantage: as shown in Section IVA of [311] we get effectively $P = 1/2$ if we marginalise over a fully free P, so this is also the choice where we let all P_j's float freely and marginalise over all but P_i. For this reason we will use $P = 1/2$ together with a free global A in the remainder of this section.

5.4.5.2 *Toy-model Illustration of Posterior Probabilities*

Let us illustrate the meaning of the posterior probabilities that we expect to find if BEAMS works with a simple toy model: We assume that we are dealing with two populations (let us call them 'red' and 'blue') drawn from two normal distributions with means at $\pm\theta$ and equal variances of $\sigma^2 = 1$, see the top panel of Fig. 5.8.

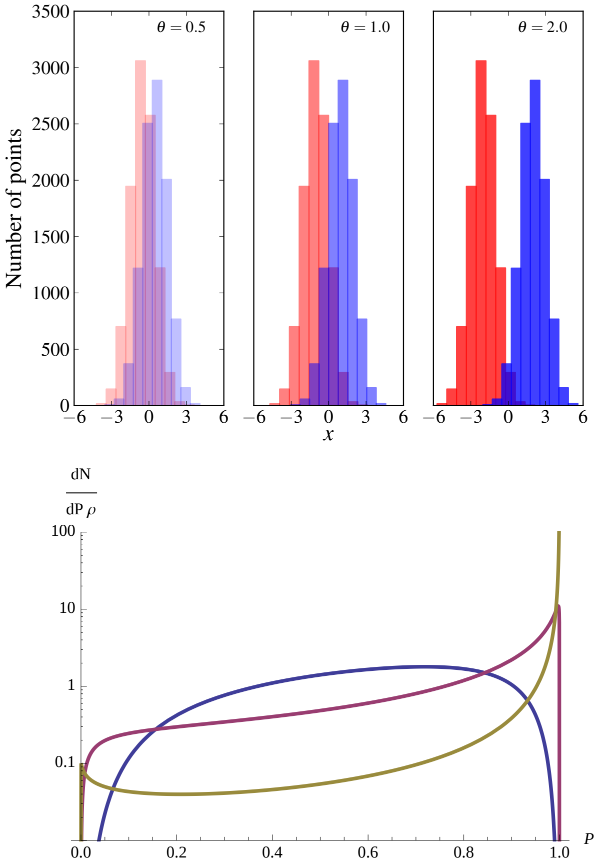

Figure 5.8 Top panel: illustration of the two toy distributions, in the case of $\theta = 0.5, 1.0, 2.0$ (left to right). Bottom panel: probability histogram density plots, or number of red points with a given probability, where $dN^{(r)}(P)$ is given in Eq. (5.18) are shown for $\theta = 0.5$ (blue), 1 (red) and 2 (yellow).

Effectively this means that we are measuring the distance $\Delta = 2\theta$ between the two mean values in units of the standard deviation. We also allow for different numbers of points drawn from the red and blue Gaussians through a 'rate parameter' $\rho \in [0, 1]$ that gives the probability to draw a red point. If we draw N points in total, we will then have on average ρN red points and $(1-\rho)N$ blue points. The likelihood for a set of points $\{x_j\}$, with j running from 1 to N, is then

$$P(\{x_j\}|\theta) = \prod_{j=1}^{N} \frac{1}{\sqrt{2\pi}} \left(P e^{-\frac{1}{2}(\theta - x_j)^2} + (1-P) e^{-\frac{1}{2}(\theta + x_j)^2} \right). \tag{5.14}$$

for $P = \rho$.

To simplify the analysis we assume that we are dealing with large samples so that θ is determined to high precision, with an error much smaller than σ. In this case (and since this is a toy model) we can take the parameter θ fixed. We also note that if we are running this in BEAMS with a true prior probability $P = \rho$ then we would find a normalisation parameter $A = 1$, while for $P = 1/2$ we would obtain $A = \rho/(1-\rho)$, and we again assume that this parameter can be fixed to its true value. Then it is easy to see that if we leave the probability for point i, P_i, free, we find a Bayes factor

$$B = \frac{P(\{x_j\}|\theta, P_i = 1)}{P(\{x_j\}|\theta, P_i = 0)} = \frac{e^{-\frac{1}{2}(\theta - x_i)^2}}{e^{-\frac{1}{2}(\theta + x_i)^2}} = e^{2\theta x_i}. \tag{5.15}$$

In other words, $\ln(B) = x_i \Delta$, just the value of the data point times the separation of the means. If the point is exactly in between the two distributions $x_i = 0$ then $B = 1$, i.e. its BEAMS posterior probability to be red or blue is equal. Notice that this the answer irrespective of the value of ρ and happens because we have removed any influence of the rate parameter A on the free P_i. This means that if we want to think of the BEAMS posterior probability as the probability to be red or blue, we should update the Bayes factor with A, i.e. use $\tilde{B} = BA$, with an associated probability $P = \tilde{B}/(1+\tilde{B})$. We also see that the probability to be red increases exponentially as x_i increases. As we will see below, this reflects the fact that the number of red points relative to the blue points increases in the same way. The rapidity of this increase is governed by the separation, Δ, of the two distributions.

What is the distribution of the posterior probabilities, i.e. the histogram of probability values, and what determines how well BEAMS does as a typer in this example? The number of red points in an interval $[x, x+dx]$ is just given by the 'red' probability distribution function at this value, times dx. To plot this function in terms of P we also need

$$
\begin{aligned}
x(P) &= \frac{\ln(B)}{\Delta} = \frac{\ln(P/(1-P))}{\Delta} &(5.16)\\
\frac{dP}{dx} &= \Delta P(1-P). &(5.17)
\end{aligned}
$$

The probability histograms for the red (r) and blue (b) points, normalised to ρ and $1-\rho$ respectively, then are:

$$
\begin{aligned}
dN^{(r)}(P) &= \frac{\rho}{\sqrt{2\pi}\Delta}\frac{dP}{P(1-P)} &(5.18)\\
&\quad \times \exp\left\{-\frac{1}{2}\left(\frac{\ln[P/(1-P)]}{\Delta} - \theta\right)^2\right\}\\
dN^{(b)}(P) &= \frac{1-\rho}{\sqrt{2\pi}\Delta}\frac{dP}{P(1-P)} &(5.19)\\
&\quad \times \exp\left\{-\frac{1}{2}\left(\frac{\ln[P/(1-P)]}{\Delta} + \theta\right)^2\right\}
\end{aligned}
$$

We plot $(1/\rho)dN^{(r)}/dP$ for $\theta = 1/2$, 1 and 2 in the lower panel of Fig. 5.8. We see how the values become more concentrated around $P = 1$ for larger separation of the distributions, i.e. BEAMS becomes a "better" typer. But for very large separations there are also suddenly more supernovae at low P (yellow curve). The reason is that BEAMS does not try to be the best possible typer, instead it respects the condition that the probabilities have to be unbiased, in the sense that

$$
\frac{dN^{(r)}}{dN^{(b)}} = \left(\frac{P}{1-P}\right)\left(\frac{\rho}{1-\rho}\right) = BA = \tilde{B}. \tag{5.20}
$$

Since BEAMS only uses the information coming from the distribution of the values, its power (as reflected in the distribution of probability values $dN(P)$) is given by how strongly the distributions are separated. If they are identical ($\theta = 0$) then BEAMS can only return $P = 1/2$ while for larger θ there is a stronger preference for one type over another. But given the two populations, we can in principle derive the probability histogram by just looking at the ratio of data points of either type at each point in data space, there is nothing else BEAMS can do. Also, in order for the probabilities to be unbiased (up to the rates which are taken into account by A) if there are, say, 200 red points in the $P = 0.9$ bin and only 10 in the $P = 0.8$ bin, then we need to find about two blue points in the $P = 0.8$ bin but 20 in the $P = 0.9$ bin. Although this looks like a significant misclassification problem, it is just a reflection of Eq. (5.20) and is actually the desired behaviour.

5.4.5.3 *Application to Level II*

In order to check whether BEAMS is able to produce posterior probabilities with the expected properties, we ran it on the level II simulated data for constant $P = 1/2$ prior probabilities, allowing for a free A. We plot the two probability histograms in the upper panel of Figure 5.9, for probabilities that were updated with the posterior value of the rate parameter, $A = 0.33$, together with the ratio of the two histograms in the lower panel to test whether we recover Eq. (5.20). Given that B is the ratio of the number of Ia to non-SN Ia points, we have that $P = \ln(B) = \ln(N_{\rm Ia}) - \ln(N_{\rm nonIa})$. Hence, the error bars on $\ln(B)$ are taken to be

$$\sigma(P)^2 = \frac{1}{(PN_{\rm tot}^{(P)})} + \frac{1}{((1-P)N_{\rm tot}^{(P)})} \tag{5.21}$$

where $N_{\rm tot}^{(P)}$ are the total actual number of supernovae in the probability bin. The number of non-Ia in the final $P = 0.95$ is slightly increased relative to the adjacent bins, but the ratio is consistent with expectations. There are however very few Ia with very low probabilities, which is the only region where there is a significant bias. We bin the probabilities obtained from the Sako et al. [304, 305] typer and those from the MLCS2k2 χ^2 fit to the Ia light-curve template in Figure 5.10, and show how the normalisation parameter A goes a way to reducing the bias in the probabilities.

5.4.5.4 *Approximate Methods*

The procedure to extract the posterior probabilities as outlined above is rather slow, as we need to run a full MCMC analysis for each supernova. This is only so because we evaluate the posterior for P_i *given* all other probabilities fixed to their mapped values. Leaving all the probabilities free would lead to a very high dimensional and complex

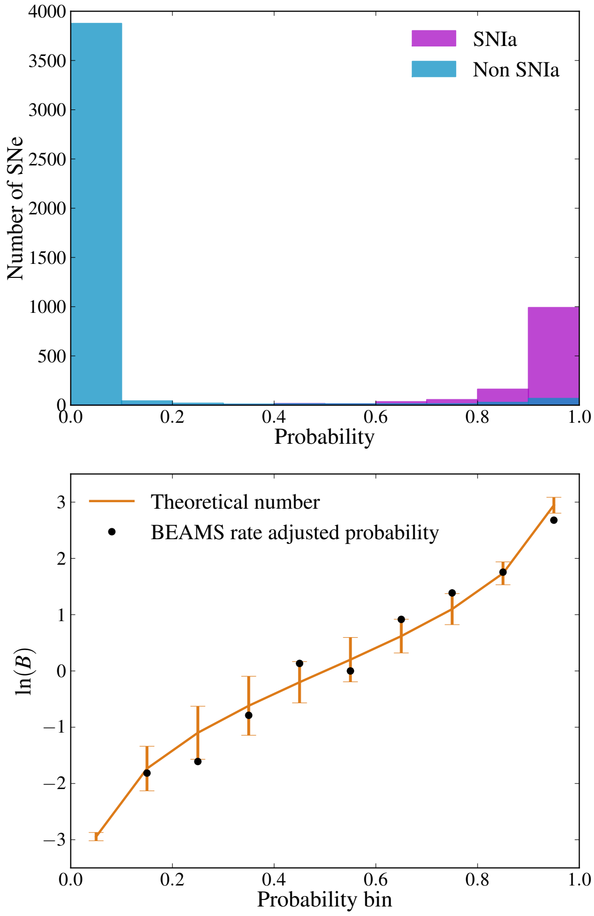

Figure 5.9 BEAMS posterior probabilities: the histogram of rate-adjusted BEAMS posterior probabilities for the Type Ia supernovae (purple) and the non-Ia supernovae (blue) – upper panel. Lower panel: ratio of SN Ia to non-SN Ia supernovae in probability bins (black dots) compared to the theoretical expectation $P/(1-P)$ (orange curve and error bars). The first bin at $P = 0.05$ has very few SNe Ia so that the data point is not visible.

posterior that would be very hard to sample from. However, since we are working at any rate in the limit of at most weak correlations between supernovae, we can leave free a subset n of the P_i simultaneously. It is better if n is much smaller than the total number of supernovae, and not too large in any case, for example $n = 10$. In addition, the more uncorrelated the P_i, the easier it is to sample from the total posterior. But in this way we speed the process up by a factor of n, making it more tractable for large sets. Additionally, since the runs are independent, they can be performed on a large computer in parallel, so that even large supernova samples can be analysed with the computational resources available to the typical astrophysics department (for example,

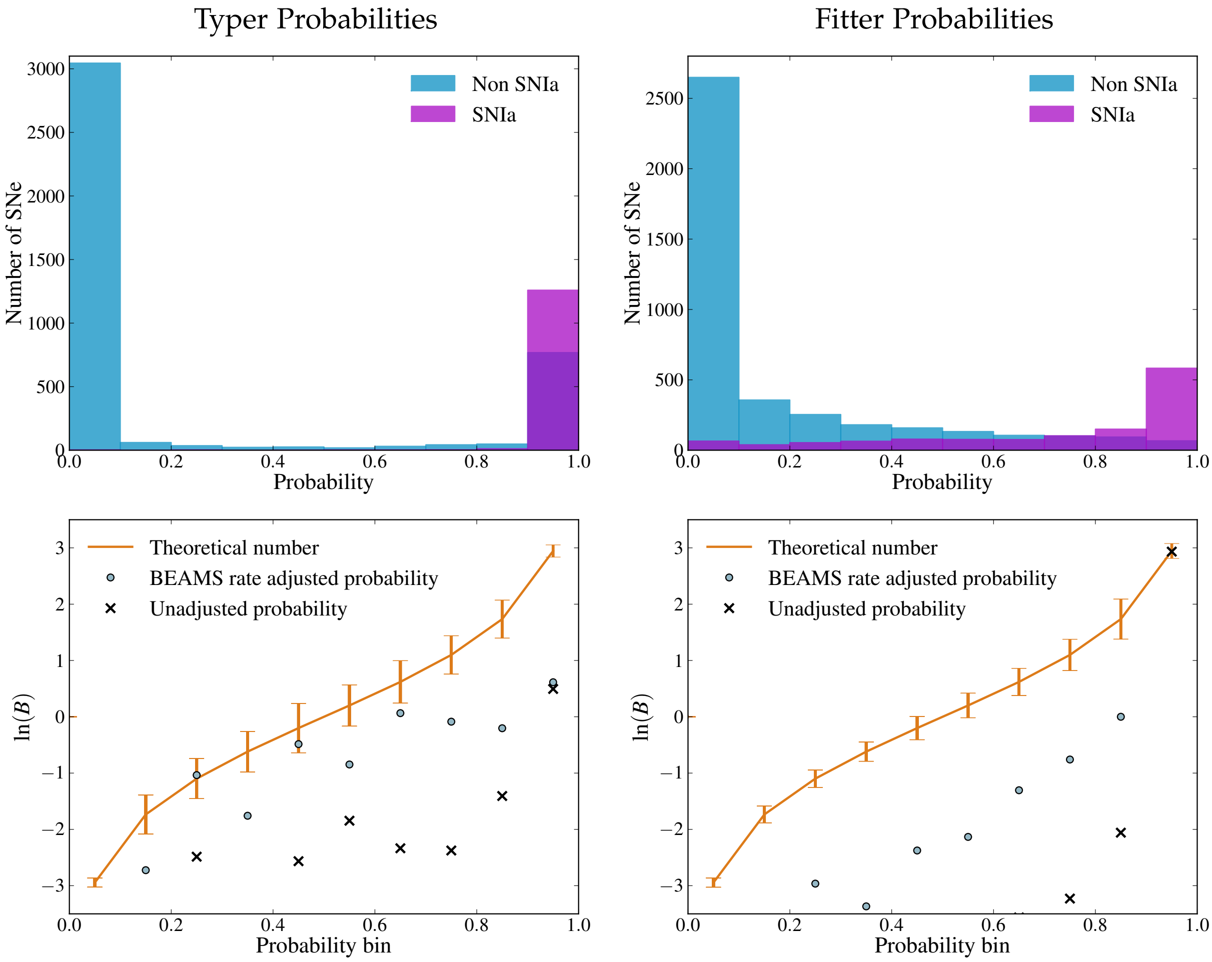

Figure 5.10 Comparing probabilities: for comparison, we plot the probability histograms and the bias test for the Sako et al. [304, 305] probabilities, P_{typer} (left column) and the MLCS2k2 fitter probabilities P_{fit} (right column) for the SNANA simulations. The Sako et al. [304, 305] typer manages to put more Ia into the highest probability bin, but also gives some non-SN Ia points very high probability, and is more biased. The P_{fit} probabilities are less strong, but are also less biased. In each case, normalising the probabilities using the A parameter reduces the level of probability bias.

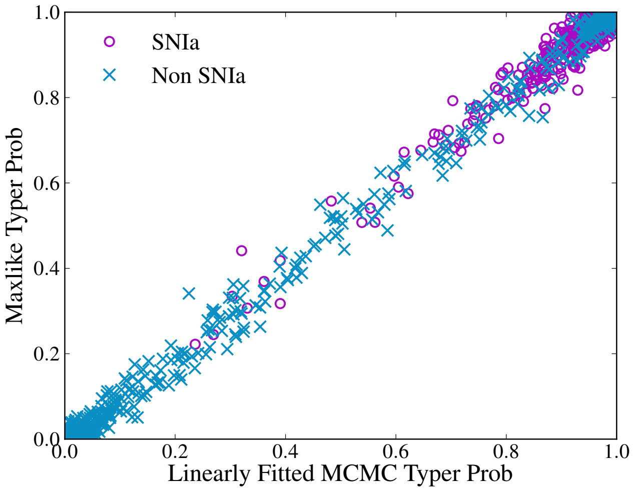

Figure 5.11 Approximate and direct methods for obtaining the posterior probabilities. There is a tight agreement between the probabilities obtained through full MCMC runs and the approximate approach taking the ratio of the Ia to the non-SN Ia likelihoods at the maximum likelihood point (for the cosmological parameters).

we ran the Level II analysis above without this trick in just a day on the local cluster).

A quicker method of determining the posterior probabilities is obtained by taking the ratio of the probability that a data point, i is from the Ia type relative to the probability that is is a non-SN Ia. If instead of marginalising over all other parameters, we evaluate the posterior at the maximum likelihood point for the *cosmological parameters*, where $\boldsymbol{\theta} = \boldsymbol{\theta}^*$, the ratio is simply given by

$$\frac{P(\mu_i|\boldsymbol{\theta}^*, \tau_i = 1)}{P(\mu_i|\boldsymbol{\theta}^*, \tau_i = 0)}. \tag{5.22}$$

We compare the approach to the computationally intensive one discussed above in Figure 5.11 as a function of true SN type for the Level II data. In general the probabilities are consistent, especially in the case of the Ia SNe, with no SN Ia being given a high probability in the full approach and being given a low probability using the ratio of maximum likelihoods. The mean and standard deviation of the distribution of residuals between the two approaches are $\delta P_{\mathrm{Ia}} = 0.005 \pm 0.015$. As such, the approximate method provides a robust check of the full approach, as differences in the probabilities are mostly related to convergence properties of the full estimation. As might be expected, non-SNe Ia that are given a high probability using the full method are also given a high P_{Ia} using the approximate method.

5.5 TESTS AND CHECKS FOR BIAS

5.5.1 *Level I Tests*

5.5.1.1 *Dependence on Probability*

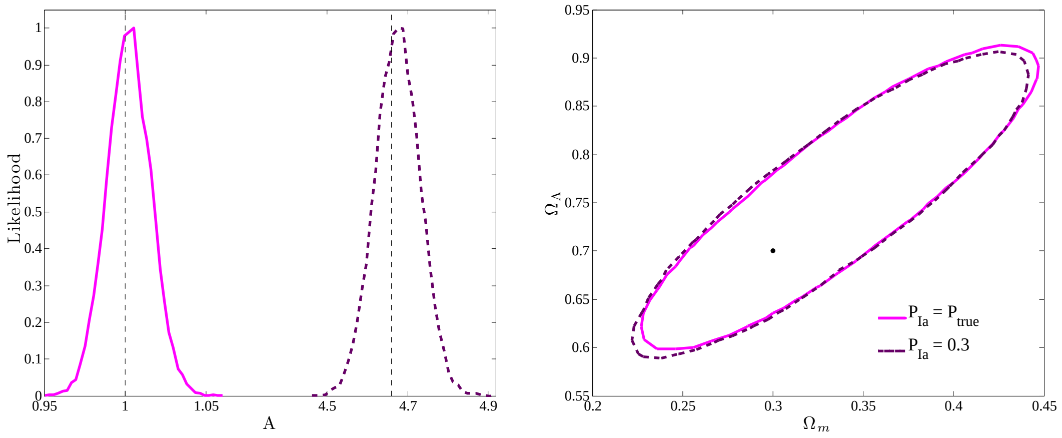

Figure 5.12 BEAMS corrects for biased input probability: the marginalised one-dimensional likelihood for the normalisation parameter A (left panel) and estimated contours (right panel) for simulated Level I data under two forms of the probability distribution. The pink curve and contours correspond to the linear unbiased case, where the probabilities are generated in a linear model, and the types are assigned according to the probabilities. The purple dashed contours correspond to assigning a probability of $P_{\rm Ia} = 0.3$ to all points. The dashed vertical lines show the expected value of the parameter A such that the true input mean probability of $P_{\rm Ia} = 0.667$ is recovered. Note that the x-axis in the top panel has been shortened to allow for comparison of the two distributions.

The BEAMS algorithm naturally uses some indication of the probability of a data point to belong to the Ia population, whether it is some measure of the goodness-of-fit of the data to a Type Ia light-curve template, or something more robust such as the relative probability that the point is a Ia compared to being of a different type. By including a normalisation factor, we can correct for general biases in the probabilities of the Ia points. One might still question, however, how sensitive BEAMS is to the input probability of the objects. We test this using the level I simulations as follows: the data are generated from a model as described above, with unbiased linear probabilities that follow the true distribution of Ia type. This is the standard case. We then compare this to the case where we assign a probability of $P_{\rm Ia} = 0.3$ to all points (which we know will be biased since the mean probability of the sample is 0.667). We illustrate the changes in constraints in Figure 5.12. If we ignore all probability information and set it to a (biased) value of $P_{\mathrm{Ia}} = 0.3$, the probability information is essentially controlled by the normalisation parameter. A tends to a value of 4.7, which, when inserted into Equation (5.3) yields a 'normalised' probability of $P_{\mathrm{Ia}} = 0.668$. Hence BEAMS uses the normalisation parameter to remap the mean of the *given* probabilities to ones that have a mean that fits the true *unbiased* probabilities. In correcting for this effect, BEAMS manages to recover cosmological parameters consistent with the unbiased case.

5.5.1.2 *Dependence on Rates*

An additional complication to the probabilities could be a dependence of the probabilities with redshift, which would occur if the probabilities depend on redshift. The relative numbers of SNe at a given redshift depend on the various SN rates (or number of explosions per year per unit volume). In general, non-SN Ia rates are less certain than Type Ia rates, since SNe are mainly followed up in a cosmological survey if they already appear to be good Ia candidates. As a test of this dependence, we modify the probabilities in two ways: firstly, we scale the true probabilities as a function of redshift as

$$P_{Ia,z} = \min\left(P_{\mathrm{Ia}}\frac{1+z}{1+z_{max}}, 1\right), \tag{5.23}$$

which increases the probability of being Ia of data at higher redshift. In this case the fact that there is no redshift dependence in A itself introduces a slight bias in the inferred cosmology, as is shown in Figure 5.13, with the input cosmology only recovered at 2σ (the filled 1 and 2σ contours from the linear unbiased case are shown for comparison). An alternative way of probing this dependence is by artificially changing the relative numbers of Ia to non-SN Ia SNe in a given Level I simulation. We do this by simply removing a subset of the Ia data (where the data are binned in ten redshift bins) after assigning probabilities to ensure that we are effectively biasing the probabilities - or rather, that the probability of being a Type Ia at a given redshift will not reflect how many Ia actually exist at that redshift. This case is also shown in

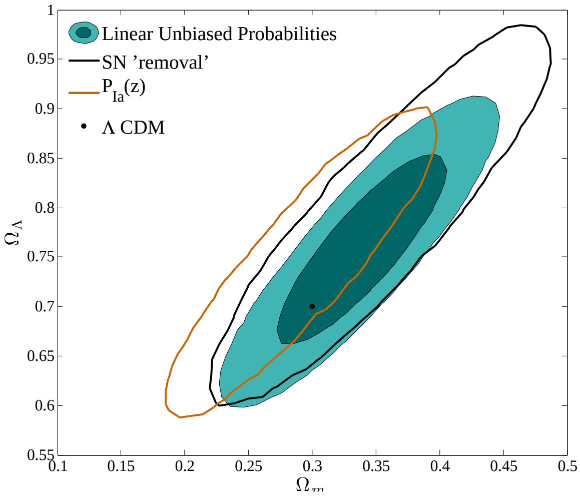

Figure 5.13 The dependence of the probabilities on SN rate: the 2σ contours in the $\Omega_m - \Omega_\Lambda$ plane when considering two different methods of introducing a redshift dependence on the probabilities. The brown contours show the case where the P_{Ia} probabilities were explicitly changed to depend on redshift through Eq. (5.23). The black curves illustrate the case where the overall probabilities are left unchanged, but the number of Ia SNe relative to the non-SNe Ia is changed as a function of redshift. Ignoring all probability information (by setting the probability of each point to $P = 0.5$) would make one less sensitive to bias of this type, as the 'contribution' of each data point is then decided through the global A parameter.

Figure 5.13, where the contours are slightly larger than the standard case (given that data are removed), but are consistent with the input cosmology at 1σ.

5.5.1.3 *Dependence on Error Accuracy*

The full error on the distance modulus is given in Eq. (5.7) - where the error combines measurement error (from light-curve fitting), intrinsic dispersion (from the absolute magnitude distribution of the SNe) and peculiar velocity error. In general the peculiar velocity error is degenerate with the non-SN Ia distribution characteristics in that the velocity error tends to increase the errors at low redshift. However, the intrinsic dispersion of the non-SN Ia effectively controls the spread in the distribution, which we know to increase at low redshift. Hence, fitting for the two parameters together can lead to one being unconstrained. In the cosmological analysis we set the velocity term to be set by $v_{pec} = 300$ km s^{-1}, however we test that setting it to double this value does not change the inferred cosmology. When we allow v_{pec} to be free, we find it unconstrained by the data, with the minimum value saturating the lower bound of the prior of $\log(v_{pec}/c) = -20$, and the maximum given by $v_{pec} < 1922$ km s^{-1}.

5.5.2 *Level II Tests*

The SNANA simulation mimics real-life observations in that it treats the simulated light-curves as 'real' data and fits them in the same way one would fit and analyse current data. The main bias from this dataset will be any bias introduced in the probabilities of the data to be of Type Ia, since we have no guarantee *a priori* that the probabilities will be unbiased. We thus fit for the cosmology assuming different proxies for the probability, either taking the probability from the light-curve fitter alone, P_{fit}, setting the probabilities to an arbitrary value of $P = 1/2$, or using a typer probability P_{typer} [304, 305] which computes the *relative* goodness-of-fit of different Ia and non-SN Ia templates to the data. Typing SNe effectively is an active area of research

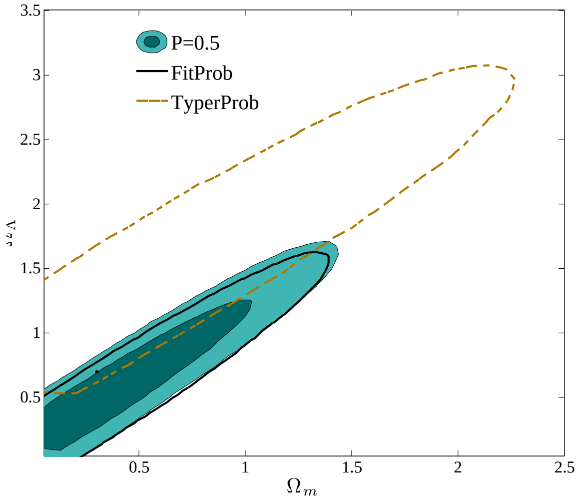

Figure 5.14 Using different probabilities for the Level II data: the blue filled $1, 2\sigma$ contours show the constraints when setting the probabilities of all points to $P = 0.5$, while the black curve show the 2σ contours when using the goodness-of-fit probabilities from the MLCS2k2 fitter, and the light brown curves show the constraints when using the Sako et al. [304, 305] typer probabilities.

[298–306, 322], indeed, a recent community wide challenge provided a way of testing the ability of various approaches to type SN efficiently (see Kessler et al. [323] and references therein). With more data and improved algorithms, the probabilities used in photometric SN analysis will greatly improve. As Figure 5.14 illustrates, however, BEAMS can use the minimal amount of probability information, and recover consistent results. A more detailed investigation into comparing probabilities from different typers and fitting algorithms and correcting for them using multiple normalisation parameters ($\boldsymbol{A} = \{A_1, A_2, ...\}$) is left to future work.

5.5.3 *Level III Tests*

In Figure 5.15 we compute the cosmological parameters using different prescriptions for the probabilities, in the same manner as the previous section. In the case of the Sako et al. [304, 305] typer, the average probability is $\langle P_{\mathrm{typer}} \rangle = 0.79$. In this case the normalisation parameter A peaked around 0.3, resulting in a normalised average probability of $\langle P^{(A)}_{\mathrm{Ia},i} \rangle = 0.525$. In the case where the MLCS2k2 goodness-of-fit probabilities are used, the average probability of being a Ia is lower, $\langle P_{\mathrm{fit}} \rangle = 0.41$. In this case the A parameter is distributed around $A = 25$, leading to $\langle P^{(A)}_{\mathrm{Ia},i} \rangle = 0.95$ - BEAMS tries to increase the average probability of all points to be close to unity. Finally when setting the probability to 0.5, A is centered around 2.5, leading to $\langle P^{(A)}_{\mathrm{Ia},i} \rangle = 0.71$. We use the final (conservative) case in the cosmological analysis. The differences in the value of the normalisation parameter reflect not only that the distributions have different means, but that the distributions have different shapes. In the case of the goodness of fit probabilities, P_{fit} has a large peak at low probabilities, while the opposite is true when using the typer probabilities.

5.6 PROBABILITY CORRELATIONS

As we highlighted in Section 5.4.5, the normalization parameter A is crucial to normalize the probabilities in order to avoid biases introduced by the fitting or typing procedure. Moreover, it provides a mechanism for removing the strong dependence on probability directly, by allowing BEAMS to adjust the probabilities according to the global fit to a distance modulus function. In Figure 5.16 we show that there are no strong correlations between the Ia probability determined from the SNANA fits to the light curve models and the difference between the input cosmology and the inferred cosmological model. In general there is more spread in the non-SN Ia population, however there are some non-SN Ia points with high probability, and there are low-

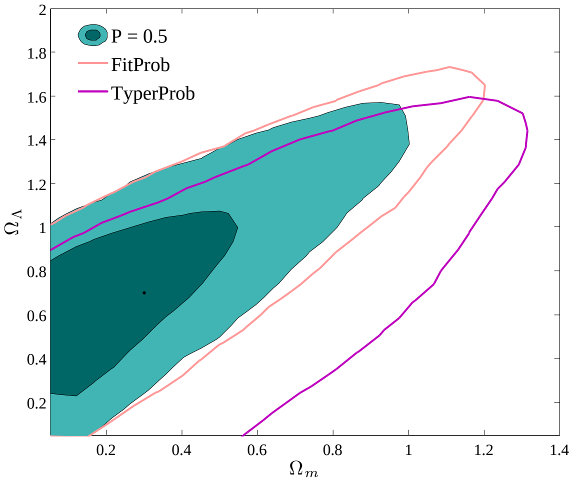

Figure 5.15 Probability checks on Level III data: the resulting contours when using the photometric dataset of the SDSS-II SN sample, with various probabilities. The solid $1, 2\sigma$ blue contours are from ignoring probability information, and setting all the probabilities of the points to $P_{\mathrm{Ia}} = 0.5$. The light curves (2σ constraints) result when using the MLCS2k2 goodness-of-fit probability, which is un-normalised relative to the other types, and is typically low for the sample. The dark contours are from using the probabilities for each point from the Sako et al. [304, 305] prescription, also at 2σ. In the case of the Level III data, using different prescriptions for the probabilities does not affect the inferred cosmology.

probability Ia data. We leave the investigation of different forms for A to future work.

5.7 NOTES ON BEAMS TROUBLESHOOTING

Analysis of purely photometric data brings its own challenges to the fore. We briefly highlight some considerations when applying the algorithm to such data. In order for BEAMS to recover the correct cosmology, it requires the freedom to capture the characteristics of the non-SN Ia (and indeed the SN Ia) distributions. In particular, we found that the error analysis has a significant impact on the inferred cosmology, both within BEAMS but equally for a basic χ^2 approach. Our addition of two different intrinsic dispersion terms for the Ia and non-SN Ia populations effectively change the relative weighting of the populations in a consistent manner, while still taking into account the measurement error on each point, which may or may not be a function of

MuP.png

Figure 5.16 **Distance modulus-probability correlations in the Level II SNANA simulations:** while a correlation exists between the Type Ia probability (determined from the χ^2 fit to the light curve models within SNANA) and supernova type - ‘true’ Ias have a higher probability of being Ia - there is no significant correlation between the residual distance modulus of the SNANA simulation and the P_{Ia} probability.

type.

As we highlighted in Section 5.4.5, the normalisation parameter A is crucial to normalise the probabilities in order to avoid biases introduced by the fitting or typing procedure. Moreover, it provides a mechanism for removing the strong dependence on probability directly, by allowing BEAMS to adjust the probabilities according to the global fit to a distance modulus function. We leave the investigation of different forms for A to future work.

When applying fitting procedures such as MLCS2k2 to the dataset, efficiency maps (to account for Malmquist bias, for example) should be carefully calibrated not to introduce redshift dependent biases to the dataset. Alternatively, the BEAMS likelihood can be adjusted from a standard Gaussian to a truncated or deformed Gaussian distribution to account for the selection bias in the survey. We leave this investigation for future work. As the amount of observations of the contaminants increases, new forms of the non-SN Ia distance modulus function may be more strongly motivated by the data. While we have tested various forms for simulated SNANA data and for the SDSS-II survey data, these functions should be varied to allow the model enough freedom to capture the deviations from the standard Ia distance modulus relation. In addition, future data may motivate for multiple populations, a feature which is easily included in BEAMS.

5.8 DISCUSSION

Bayesian Estimation Applied to Multiple Species (BEAMS) is a statistically robust method of parameter estimation in the presence of contamination. The power of BEAMS is in the fact that it makes use of all available data, hence reducing the statistical error of the measurement, whether or not the purity of the sample can be guaranteed. Rather than discarding data, the probability that the data are “pure” is used as a weight in the full Bayesian posterior, reducing potential bias from the interloper distribution.

We tested the BEAMS algorithm on ideal Gaussian simulations, and on realistic simulated data obtained from light-curve fitting [318], and showed that BEAMS obtains contours that are reduced in size to the case where only a small spectroscopically confirmed subset of data is available, while in addition the constraints are unbiased relative to the spectroscopic set. We tested the BEAMS approach by considering various distributions for the non-SN Ia population, and checked for potential bias introduced through the probability information or error accuracy. In addition, we discuss the ability of BEAMS to determine the posterior probability of a point based on its fit to the best-fit model. In this Chapter we have restricted ourselves to the binomial case of a SN Ia population and a general core collapse, or non-SN Ia, population. This method can easily be extended to the multi-nomial case, as we learn more about the distributions of the contaminant populations. We have also focused attention on the case where host galaxy redshifts are known for all supernova candidates. One can include photometric redshift error by looping N times, once per supernova and marginalising over the redshift of the i-th SN in each case (in a similar fashion as the method of obtaining the *post facto* estimation of the Ia probability of each SN in Section 5.4.5. The sensitivity to redshift error can also be included directly through fitting for cosmology directly in 'light-curve' space (see for example March et al. [324]). However, we leave this general treatment of redshift uncertainty in BEAMS to future work. In the specific case of the SDSS-II Supernova Survey, we will apply BEAMS to the larger SN sample with spectroscopic host galaxy redshifts from the BOSS survey. Not only will the sample size of data points with accurate host redshifts increase (thereby further reducing the cosmological contours from photometric data) but will allow one to easily calibrate the constraints obtained with the current application of BEAMS against the case where one only has photometric redshifts, which will be the case for LSST [307]. Finally, as we learn more about the functional form of the contaminant population [144], BEAMS allows one to easily marginalise over the parameters of the model, and in so doing learn about the specific distribution characteristics. With the wealth of new data awaiting SN cosmology, BEAMS provides a platform to learn more about the SN populations while at the same time tackling the fundamental questions about the constituents of the universe.

6

CONCLUSIONS

We are firmly in the epoch of 'precision cosmology', with data from many independent observations coupled with advanced statistical tools providing the opportunity to constrain viable theoretical models of the universe. In this thesis, we presented new data from the Atacama Cosmology Telescope, which measure the temperature anisotropies in the Cosmic Microwave Background to unprecedented levels of angular precision. These measurements of small-scale temperature fluctuations yield a large quantity of raw data, which is processed to form temperature maps of the microwave sky, and ultimately temperature power spectra from these maps. Such new data require systematic processing and checks for possible bias introduced by the analysis and data-reduction pipeline. We presented the checks performed on the ACT data to test for any such effects, which were carried out on multiple seasons of ACT data.

Once the data have been processed and all sources of error are accounted for, the power spectrum is used to constrain cosmological parameters, both primary cosmological parameters and contributions to the small-scale power from secondary sources such as the Sunyaev-Zel'dovich effect from galaxy clusters, in addition to power from unresolved radio sources and dusty galaxies. In our analysis of the ACT data, the concordance cosmological model is still favoured and we improve constraints on possible deviations from the concordance ΛCDM model. While the amplitude of the power from unresolved SZ sources is lower than expected in a ΛCDM universe, it is consistent with an amplitude corresponding to a clustering signal of $\sigma_8 = 0.8$ at the

95% confidence limit. In addition we place new constraints on the amplitude of power from unresolved Poisson sources (both radio and infrared) and correlated infrared sources.

The peaks in the Silk damping regime $1000 < \ell < 3000$ provide a powerful tool with which to constrain deviations from concordance. We detect the presence of lensing through its effect on the temperature power spectrum at 2.8σ, and have detected relativistic species at 4σ using CMB data alone. The best-fit model to the ACT data in combination with WMAP favours an excess of damping on small scales, however this is at less than 95% confidence. We find that a scale invariant power spectrum is disfavoured by the ACT data at 3σ while the amount of running in the spectral index preferred is consistent with ΛCDM.

In addition to this general cosmological analysis, we focused on using the ACT data in combination with WMAP data to test for possible deviations from a power-law primordial spectrum using a minimally parametric form, where the primordial power is separated into bins logarithmically in k-space, and the amplitude of power is estimated in each bin. The ACT data add points at small scales which increase the lever arm with which to test for such deviation. We find no evidence for deviation from power-law, and hence present constraints on the primordial power at scales between $0.001 < k < 0.19$ Mpc^{-1}. We translated the constraints on primordial power into late-time power spectrum measurements from the CMB using the transfer function, and hence illustrate the measurements of the matter power in the fully linear regime using the CMB only. These measurements are consistent with complementary measurements from galaxy clustering and weak lensing, and add to the arsenal of cosmological observations which probe a range in masses from $10^{15}M_{\odot}$ to $10^{22}M_{\odot}$.

We have made use of new data to place tighter constraints on the cosmological model, and deviations from the standard picture. In the future, small-scale *polarisation* measurements will increase our constraining power even further. The upcoming ACTPol experiment will increase the data available and will be less sensitive to emission from secondary sources, yielding a cleaner window on the primordial power right down the Silk damping tail of the CMB; allowing for lensing reconstruction of the deflection field and measurement of the polarisation signal induced from gravitational lensing. This will provide the natural extension for this work, as we use the techniques learned to take advantage of the dataset. In addition to measurements of the small-scale microwave sky, future observations of Type Ia Supernovae will vastly increase the statistical power of these objects to constrain late-time cosmological parameters. The increase in numbers comes at the cost of including data from contaminated populations of core collapse supernovae, and robust statistical techniques are required to remove this contamination. In the case of photometric data, light-curve fitting provides one with a *probability* that any given point belongs to the population of interest, as the lack of spectroscopic information does not allow one to have 100% confidence that the point is in fact a Type Ia SN.

We presented one such approach of dealing with contaminated data, Bayesian Estimation Applied to Multiple Species and applied it to photometric supernova data, including in our weighted Bayesian posterior the probability of each data point to belong to the Ia class of objects. We tested against possible sources of bias inherent in photometric supernova analysis, and applied BEAMS to both simulations and real data from the Sloan Digital Sky Survey II Supernova Search. We showed how BEAMS improves the constraints on cosmological parameters when including the photometric dataset with galaxy redshift information. We discussed the sensitivity of the algorithm to assumptions about the specifics of the SN Ia properties such as the supernova rate, and presented a method for testing whether or not the probabilities assigned to the Ia data are themselves biased. Finally, we showed that using the BEAMS data increases statistical estimation by a factor of three, and presented a discussion on the pitfalls in photometric supernova cosmology and the issues which need to be addressed for future large SN surveys such as LSST. A natural extension of this work is on the large datasets of LSST and other telescopes which will be operational in the next few years, making this field a developing and interesting one. We will continue to refine our algorithm in future work, including more freedom in the model and allowing for more complexity in the underlying distributions.

Through new datasets such as ACT and new statistical techniques such as BEAMS, we can make strides in refining and confronting our theoretical models and gaining an understanding of the complex cosmos around us.

REFERENCES

[1] A. Friedmann, Zeitschrift fur Physik **21**, 326 (1924).

[2] G. Lemaître, Annales de la Societe Scietifique de Bruxelles **53**, 51 (1933).

[3] H. P. Robertson, ApJ **82**, 284 (1935).

[4] A. G. Walker, Proceedings of the London Mathematical Society **s2-42**, 90 (1937), , .

[5] T. Clifton, P. G. Ferreira, A. Padilla, et al. (2011), .

[6] A. Einstein, Sitzungsberichte der Königlich Preußischen Akademie der Wissenschaften (Berlin), Seite 1030-1085. pp. 1030–1085 (1914).

[7] E. Komatsu, K. M. Smith, J. Dunkley, et al., ApJS **192**, 18 (2011), .

[8] The ALEPH Collaboration, The DELPHI Collaboration, The L3 Collaboration, et al., Phys. Rep. **427**, 257 (2006), .

[9] M. Tegmark, Phys. Scripta **T121**, 153 (2005), .

[10] J. Lesgourgues and S. Pastor, Phys. Rept. **429**, 307 (2006), .

[11] S. Hannestad, Progress in Particle and Nuclear Physics **65**, 185 (2010), .

[12] S. Bashinsky and U. Seljak, Phys. Rev. D **69**, 083002 (2004).

[13] Z. Hou, R. Keisler, L. Knox, et al., ArXiv e-prints (2011), .

[14] W. Hu and S. Dodelson, ARA&A **40**, 171 (2002),

[15] W. Hu, M. Fukugita, M. Zaldarriaga, et al., ApJ **549**, 669 (2001), .

[16] M. S. Turner, in *The Third Stromlo Symposium: The Galactic Halo*, edited by B. K. Gibson, R. S. Axelrod, & M. E. Putman (1999), vol. 165 of *Astronomical Society of the Pacific Conference Series*, pp. 431–+, .

[17] D. A. Dicus et al., Phys. Rev. **D26**, 2694 (1982).

[18] N. C. Rana and B. M. Seifert, Phys. Rev. **D44**, 393 (1991).

[19] S. Dodelson and M. S. Turner, Phys. Rev. **D46**, 3372 (1992).

[20] A. D. Dolgov and M. Fukugita, Phys. Rev. **D46**, 5378 (1992).

[21] S. Hannestad and J. Madsen, Phys. Rev. D **52**, 1764 (1995), .

[22] A. D. Dolgov, S. H. Hansen, and D. V. Semikoz, Nuclear Physics B **503**, 426 (1997), .

[23] N. Y. Gnedin and O. Y. Gnedin, ApJ **509**, 11 (1998), .

[24] R. E. Lopez, S. Dodelson, A. Heckler, et al., Physical Review Letters **82**, 3952 (1999), .

[25] V. Simha and G. Steigman, Journal of Cosmology and Astro-Particle Physics **6**, 16 (2008), .

[26] J. P. Kneller and G. Steigman, New Journal of Physics **6**, 117 (2004), .

[27] D. J. Fixsen, ApJ **707**, 916 (2009), .

[28] R. H. Dicke and P. J. E. Peebles, in *General Relativity: An Einstein centenary survey*, edited by S. W. Hawking & W. Israel (1979), pp. 504–517.

[29] A. H. Guth, Phys. Rev. **D23**, 347 (1981).

[30] A. A. Starobinsky, ZhETF Pis ma Redaktsiiu **30**, 719 (1979).

[31] A. R. Liddle, Astrophys.Space Sci. **261**, 281 (1999).

[32] D. Baumann, ArXiv e-prints (2009), .

[33] J. Dunkley, R. Hlozek, J. Sievers, et al., ApJ **539**, 52 (2011), .

[34] P. A. M. Dirac, Proc. Roy. Soc. Lond. **A133**, 60 (1931).

[35] J. A. Wheeler and R. P. Feynman, Rev. Mod. Phys. **17**, 157 (1945).

[36] H. B. G. Casimir, Indag. Math. **10**, 261 (1948), [Kon.Ned.Akad.Wetensch.Proc.51:793-795,1948].

[37] S. Coleman and F. De Luccia, Phys. Rev. D **21**, 3305 (1980), .

[38] M. Ishak, Foundations of Physics **37**, 1470 (2007), .

[39] J. A. Frieman, in *American Institute of Physics Conference Series*, edited by P. Pellegrini, S. Daflon, J. S. Alcaniz, & E. Telles (2008), vol. 1057 of *American Institute of Physics Conference Series*, pp. 87–124, .

[40] S. M. Carroll, in *The New Cosmology: Conference on Strings and Cosmology*, edited by R. E. Allen, D. V. Nanopoulos, & C. N. Pope (2004), vol. 743 of *American Institute of Physics Conference Series*, pp. 16–32, .

[41] S. Perlmutter, G. Aldering, G. Goldhaber, et al., ApJ **517**, 565 (1999), .

[42] A. G. Riess, A. V. Filippenko, P. Challis, et al., AJ **116**, 1009 (1998), .

[43] J. L. Tonry, B. P. Schmidt, B. Barris, et al., ApJ **594**, 1 (2003), .

[44] R. A. Knop, G. Aldering, R. Amanullah, et al., ApJ **598**, 102 (2003).

[45] L. Verde, A. F. Heavens, W. J. Percival, et al., MNRAS **335**, 432 (2002), .

[46] M. Chevallier and D. Polarski, Int. J. Mod. Phys. D **10**, 213 (2001), E. Linder, Phys. Rev. Lett. 20, 9 (2003).

[47] E. V. Linder, Phys. Rev. Lett. **90**, 091301 (2003), .

[48] J. Weller and A. Albrecht, Phys. Rev. D **65**, 103512 (2002), .

[49] B. A. Bassett, M. Kunz, J. Silk, et al., Mon. Not. Roy. Astron. Soc. **336**, 1217 (2002), .

[50] P. S. Corasaniti, M. Kunz, D. Parkinson, et al., Phys. Rev. D **70**, 083006 (2004), .

[51] W. Hu, ArXiv Astrophysics e-prints (1995), .

[52] H. Kodama and M. Sasaki, Prog. Theor. Phys. Suppl. **78**, 1 (1984).

[53] U. Seljak, ApJ **435**, L87 (1994), .

[54] C.-P. Ma and E. Bertschinger, ApJ **455**, 7 (1995), .

[55] J. Silk, ApJ **151**, 459 (1968), .

[56] D. N. Spergel, L. Verde, H. V. Peiris, et al., ApJS **148**, 175 (2003).

[57] D. N. Spergel, R. Bean, O. Doré, et al., ApJS **170**, 377 (2007), .

[58] A. G. Riess, L. Macri, S. Casertano, et al., ApJ **730**, 119 (2011), .

[59] R. A. Sunyaev and Y. B. Zel'dovich, Astrophys. Space Sci. **7**, 3 (1970),

[60] J. E. Carlstrom, G. P. Holder, and E. D. Reese, ARA&A **40**, 643 (2002),

[61] T. A. Marriage, V. Acquaviva, P. A. R. Ade, et al., ApJ **737**, 61 (2011), .

[62] R. Williamson, B. A. Benson, F. W. High, et al., ArXiv e-prints (2011), .

[63] N. Sehgal, P. Bode, S. Das, et al., ApJ **709**, 920 (2010), , .

[64] A. Lewis and A. Challinor, Phys. Rep. **429**, 1 (2006), .

[65] W. Hu and T. Okamoto, ApJ **574**, 566 (2002), .

[66] D. Hanson, A. Challinor, and A. Lewis, General Relativity and Gravitation **42**, 2197 (2010), .

[67] M. Zaldarriaga and U. Seljak, Phys. Rev. D **55**, 1830 (1997), .

[68] W. Hu, Phys. Rev. D **62**, 43007 (2000).

[69] S. Das, B. D. Sherwin, P. Aguirre, et al., Physical Review Letters **107**, 021301 (2011), .

[70] K. M. Smith, O. Zahn, and O. Doré, Phys. Rev. D **76**, 043510 (2007), .

[71] C. M. Hirata, S. Ho, N. Padmanabhan, et al., Phys. Rev. D **78**, 043520 (2008), .

[72] G. Smoot, C. Bennett, R. Weber, et al., ApJ **360**, 685 (1990).

[73] G. S. Tucker, G. S. Griffin, H. T. Nguyen, et al., ApJ **419**, L45+ (1993), .

[74] K. Ganga, E. Cheng, S. Meyer, et al., ApJ **410**, L57 (1993), .

[75] E. L. Wright, G. F. Smoot, C. L. Bennett, et al., ApJ **436**, 443 (1994), .

[76] C. L. Bennett, A. J. Banday, K. M. Górski, et al., ApJ **464**, L1 (1996), .

[77] G. Hinshaw, A. J. Banday, C. L. Bennett, et al., ApJ **464**, L17 (1996), .

[78] G. Hinshaw, A. J. Branday, C. L. Bennett, et al., ApJ **464**, L25 (1996), .

[79] A. Kogut, A. J. Banday, C. L. Bennett, et al., ApJ **460**, 1 (1996), .

[80] A. Kogut, A. J. Banday, C. L. Bennett, et al., ApJ **464**, L5 (1996), .

[81] A. Kogut, A. J. Banday, C. L. Bennett, et al., ApJ **464**, L29 (1996), .

[82] E. L. Wright, C. L. Bennett, K. Górski, et al., ApJ **464**, L21 (1996), .

[83] K. M. Górski, A. J. Banday, C. L. Bennett, et al., ApJ **464**, L11 (1996), .

[84] L. Knox and L. Page, Phys. Rev. Lett. **85**, 1366 (2000), .

[85] A. D. Miller et al., ApJ **524**, L1 (1999), .

[86] E. Torbet et al., ApJ **521**, L79 (1999), .

[87] S. T. Myers, A. C. S. Readhead, and C. R. Lawrence, ApJ **405**, 8 (1993), .

[88] J. O. Gundersen, M. Lim, J. Staren, et al., ApJ **443**, L57 (1995), .

[89] J. B. Peterson, G. S. Griffin, M. G. Newcomb, et al., ApJ **532**, L83 (2000), .

[90] N. W. Halverson, E. M. Leitch, C. Pryke, et al., ApJ **568**, 38 (2002), .

[91] J. M. Kovac, E. M. Leitch, C. Pryke, et al., Nature **420**, 772 (2002).

[92] G. Romeo, S. Ali, B. Femenía, et al., ApJ **548**, L1 (2001), .

[93] D. L. Harrison, J. A. Rubiño-Martin, S. J. Melhuish, et al., MNRAS **316**, L24 (2000), .

[94] L. Piccirillo, B. Femenía, N. Kachwala, et al., ApJ **475**, L77 (1997), .

[95] S. Hancock, C. M. Gutiérrez, R. D. Davies, et al., MNRAS **289**, 505 (1997), .

[96] J. C. Baker, K. Grainge, M. P. Hobson, et al., MNRAS **308**, 1173 (1999), .

[97] S. R. Dicker, S. J. Melhuish, R. D. Davies, et al., MNRAS **309**, 750 (1999), .

[98] E. M. Leitch, A. C. S. Readhead, T. J. Pearson, et al., ApJ **532**, 37 (2000), .

[99] K. S. Dawson, W. L. Holzapfel, J. E. Carlstrom, et al., ApJ **553**, L1 (2001), .

[100] A. de Oliveira-Costa, A. Kogut, M. J. Devlin, et al., ApJ **482**, L17+ (1997).

[101] E. S. Cheng, D. A. Cottingham, D. J. Fixsen, et al., ApJ **488**, L59 (1997), .

[102] G. S. Tucker, H. P. Gush, M. Halpern, et al., ApJ **475**, L73 (1997), .

[103] P. D. Mauskopf, P. A. R. Ade, P. de Bernardis, et al., ApJ **536**, L59 (2000), .

[104] S. Hanany, P. Ade, A. Balbi, et al., ApJ **545**, L5 (2000), .

[105] G. W. Wilson, L. Knox, S. Dodelson, et al., ApJ **532**, 57 (2000), .

[106] J. E. Ruhl, P. A. R. Ade, J. J. Bock, et al., ApJ **599**, 786 (2003).

[107] J. L. Sievers, B. S. Mason, L. Weintraub, et al., ArXiv e-prints (2009), .

[108] C. L. Reichardt, P. A. R. Ade, J. J. Bock, et al., ApJ **694**, 1200 (2009), .

[109] C. L. Kuo, P. A. R. Ade, J. J. Bock, et al., ApJ **664**, 687 (2007), .

[110] K. Grainge, P. Carreira, K. Cleary, et al., MNRAS **341**, L23 (2003), .

[111] A. Benoît, P. Ade, A. Amblard, et al., A&A **399**, L19 (2003), .

[112] J. Ruhl, P. A. R. Ade, J. E. Carlstrom, et al., in *Proc. SPIE*, edited by J. Zmuidzinas, W. S. Holland, and S. Withington (SPIE, 2004), vol. 5498, pp. 11–29, .

[113] N. R. Hall, R. Keisler, L. Knox, et al., ApJ **718**, 632 (2010), .

[114] R. Keisler, C. L. Reichardt, K. A. Aird, et al., ArXiv e-prints (2011), .

[115] D. Larson, J. Dunkley, G. Hinshaw, et al., ApJS **192**, 16 (2011), .

[116] M. Tegmark, ApJ **480**, L87 (1997), .

[117] W. H. Press, S. A. Teukolsky, W. T. Vetterling, et al., *Numerical Recipes: The Art of Scientific Computing* (Cambridge University Press, 2007), 3nd ed.

[118] G. Hinshaw, M. R. Nolta, C. L. Bennett, et al., ApJS **170**, 288 (2007), .

[119] S. Das, A. Hajian, and D. N. Spergel, Phys. Rev. D **79**, 083008 (2009), .

[120] S. P. Oh, D. N. Spergel, and G. Hinshaw, ApJ **510**, 551 (1999).

[121] W. Hillebrandt and J. C. Niemeyer, ARA&A **38**, 191 (2000), .

[122] M. M. Phillips, ApJ **413**, L105 (1993), .

[123] S. Perlmutter, G. Aldering, S. Deustua, et al., in *American Astronomical Society Meeting Abstracts* (1997), vol. 29 of *Bulletin of the American Astronomical Society*, pp. 1351–+, .

[124] W. D. Arnett, ApJ **263**, L55 (1982).

[125] G. Aldering, G. Adam, P. Antilogus, et al., in *Survey and Other Telescope Technologies and Discoveries. Edited by Tyson, J. Anthony; Wolff, Sidney. Proceedings of the SPIE, Volume 4836, pp. 61-72 (2002).*, edited by J. A. Tyson and S. Wolff (2002), pp. 61–72.

[126] K. Krisciunas, ArXiv e-prints (2008), .

[127] M. Kowalski, D. Rubin, G. Aldering, et al., ApJ **686**, 749 (2008), .

[128] M. Hicken, P. Challis, S. Jha, et al., ApJ **700**, 331 (2009), .

[129] R. Amanullah, C. Lidman, D. Rubin, et al., ApJ **716**, 712 (2010), .

[130] M. Sullivan, J. Guy, A. Conley, et al., ArXiv e-prints (2011), .

[131] A. G. Riess, L.-G. Strolger, J. Tonry, et al., ApJ **607**, 665 (2004), .

[132] M. Hamuy, M. M. Phillips, N. B. Suntzeff, et al., AJ **112**, 2391 (1996).

[133] A. G. Riess, R. P. Kirshner, B. P. Schmidt, et al., AJ **117**, 707 (1999), .

[134] K. Krisciunas, M. M. Phillips, C. Stubbs, et al., AJ **122**, 1616 (2001), .

[135] K. Krisciunas, M. M. Phillips, N. B. Suntzeff, et al., AJ **127**, 1664 (2004), .

[136] K. Krisciunas, N. B. Suntzeff, M. M. Phillips, et al., AJ **128**, 3034 (2004), .

[137] S. Jha, R. P. Kirshner, P. Challis, et al., AJ **131**, 527 (2006), .

[138] C. Contreras, M. Hamuy, M. M. Phillips, et al., AJ **139**, 519 (2010), .

[139] R. Amanullah, C. Lidman, D. Rubin, et al., ApJ **716**, 712 (2010), .

[140] LSST Science Collaborations, P. A. Abell, J. Allison, et al., ArXiv e-prints (2009), .

[141] The Dark Energy Survey Collaboration, ArXiv Astrophysics e-prints (2005), .

[142] L. Wang, P. A. Pinto, and H. Zhan, Bulletin of the American Astronomical Society **37**, 1202 (2005).

[143] D. Richardson, D. Branch, and E. Baron, AJ **131**, 2233 (2006), .

[144] B. Falck, A. Riess, and R. Hlozek, in *Bulletin of the American Astronomical Society* (2010), vol. 41 of *Bulletin of the American Astronomical Society*, pp. 390–+.

[145] N. Metropolis, A. W. Rosenbluth, M. N. Rosenbluth, et al., Journal of Chemical Physics **6**, 1087 (1953).

[146] J. Dunkley, M. Bucher, P. G. Ferreira, et al., MNRAS **356**, 925 (2005), .

[147] M. R. Nolta, J. Dunkley, R. S. Hill, et al., ApJS **180**, 296 (2009), .

[148] J. Sayers, S. R. Golwala, P. Rossinot, et al., ApJ **690**, 1597 (2009), .

[149] M. L. Brown, P. Ade, J. Bock, et al., ApJ **705**, 978 (2009), .

[150] R. B. Friedman, P. Ade, J. Bock, et al., ApJ **700**, L187 (2009), .

[151] C. L. Reichardt, O. Zahn, P. A. R. Ade, et al., ApJ **701**, 1958 (2009), .

[152] M. K. Sharp, D. P. Marrone, J. E. Carlstrom, et al., arXiv:0901.4342 (2009), .

[153] K. S. Dawson, W. L. Holzapfel, J. E. Carlstrom, et al., ApJ **647**, 13 (2006), .

[154] M. Lueker, C. L. Reichardt, K. K. Schaffer, et al., arXiv:0912.4317 (2009), .

[155] J. W. Fowler, V. Acquaviva, P. A. R. Ade, et al., ApJ **722**, 1148 (2010), .

[156] J. Dunkley, E. Komatsu, M. R. Nolta, et al., ApJS **180**, 306 (2009), .

[157] U. Seljak, J. Burwell, and U.-L. Pen, Phys. Rev. D **63**, 063001 (2001).

[158] E. Komatsu and U. Seljak, MNRAS **336**, 1256 (2002), .

[159] B. S. Mason, L. Weintraub, J. Sievers, et al., ApJ **704**, 1433 (2009), .

[160] J. W. Fowler, M. D. Niemack, S. R. Dicker, et al., Appl. Opt. **46**, 3444 (2007).

[161] A. D. Hincks, V. Acquaviva, P. Ade, et al., arXiv:0907:0461 (2009), .

[162] P. A. R. Ade, G. Pisano, C. Tucker, et al., in *Proc. SPIE*, edited by J. Zmuidzinas, W. S. Holland, S. Withington, et al. (2006), vol. 6275, p. 62750T.

[163] D. S. Swetz, P. A. R. Ade, C. Allen, et al., in *Proc. SPIE*, edited by W. D. Duncan, W. S. Holland, S. Withington, et al. (SPIE, 2008), vol. 7020, p. 702008, .

[164] E. Hivon, K. M. Górski, C. B. Netterfield, et al., ApJ **567**, 2 (2002), , .

[165] E. Komatsu, J. Dunkley, M. R. Nolta, et al., ApJS **180**, 330 (2009), .

[166] P. J. E. Peebles, *The large-scale structure of the universe* (Research supported by the National Science Foundation. Princeton, N.J., Princeton University Press, 1980. 435 p., 1980).

[167] D. Scott and M. White, A&A **346**, 1 (1999), .

[168] M. Negrello, F. Perrotta, J. González-Nuevo, et al., MNRAS **377**, 1557 (2007), .

[169] M. Righi, C. Hernández-Monteagudo, and R. A. Sunyaev, A&A **478**, 685 (2008).

[170] M. J. Devlin, P. A. R. Ade, I. Aretxaga, et al., Nature **458**, 737 (2009), .

[171] M. P. Viero, P. A. R. Ade, J. J. Bock, et al., ArXiv e-prints (2009), .

[172] K. Ganga, B. Ratra, and N. Sugiyama, ApJ **461**, L61 (1996), .

[173] S. L. Bridle, R. Crittenden, A. Melchiorri, et al., MNRAS **335**, 1193 (2002), .

[174] J. R. Bond, C. R. Contaldi, U.-L. Pen, et al., ApJ **626**, 12 (2005).

[175] A. V. Kravtsov, D. Nagai, and A. A. Vikhlinin, ApJ **625**, 588 (2005), .

[176] L. Toffolatti, F. Argueso Gomez, G. de Zotti, et al., MNRAS **297**, 117 (1998), .

[177] G. de Zotti, R. Ricci, D. Mesa, et al., A&A **431**, 893 (2005).

[178] G. Lagache, H. Dole, J. Puget, et al., ApJS **154**, 112 (2004), .

[179] T. R. Greve, R. J. Ivison, F. Bertoldi, et al., MNRAS **354**, 779 (2004), .

[180] T. R. Greve, A. Pope, D. Scott, et al., MNRAS **389**, 1489 (2008), .

[181] M. J. White and S. Majumdar, Astrophys. J. **602**, 565 (2004), .

[182] E. L. Chapin, A. Pope, D. Scott, et al., ArXiv e-prints (2009), .

[183] M. Veneziani, A. Amblard, A. Cooray, et al., ApJ **702**, L61 (2009), .

[184] M. Lueker, C. L. Reichardt, K. K. Schaffer, et al., ApJ **719**, 1045 (2010), .

[185] J. P. Henry, A. E. Evrard, H. Hoekstra, et al., ApJ **691**, 1307 (2009), .

[186] A. Vikhlinin, A. V. Kravtsov, R. A. Burenin, et al., ApJ **692**, 1060 (2009), .

[187] A. Mantz, S. W. Allen, D. Rapetti, et al., MNRAS pp. 1029–+ (2010), .

[188] D. S. Swetz, P. A. R. Ade, M. Amiri, et al., arXiv:1007.0290 (2010), .

[189] R. Dünner, et al. In preparation. (2012).

[190] A. Hajian, V. Acquaviva, P. A. R. Ade, et al., arXiv:1009.0777 (2010), .

[191] T. A. Marriage, V. Acquaviva, P. A. R. Ade, et al., ArXiv e-prints (2010), .

[192] F. Menanteau, J. Gonzalez, J. Juin, et al., ArXiv e-prints (2010), .

[193] N. Sehgal, H. Trac, V. Acquaviva, et al., ApJ **732**, 44 (2011), .

[194] T. A. Marriage, J. B. Juin, Y. Lin, et al., ArXiv e-prints (2010), .

[195] C. L. Bennett, M. Bay, M. Halpern, et al., ApJ **583**, 1 (2003).

[196] M. K. Sharp, D. P. Marrone, J. E. Carlstrom, et al., ApJ **713**, 82 (2010), .

[197] D. P. Finkbeiner, M. Davis, and D. J. Schlegel, ApJ **524**, 867 (1999), .

[198] E. Komatsu and U. Seljak, MNRAS **327**, 1353 (2001), .

[199] L. D. Shaw, O. Zahn, G. P. Holder, et al., ApJ **702**, 368 (2009), .

[200] H. Trac, P. Bode, and J. P. Ostriker, ArXiv e-prints (2010), .

[201] P. Bode, J. P. Ostriker, and A. Vikhlinin, ApJ **700**, 989 (2009), .

[202] C. Hernández-Monteagudo and S. Ho, MNRAS **398**, 790 (2009), .

[203] Y. Lin, B. Partridge, J. C. Pober, et al., ApJ **694**, 992 (2009), .

[204] L. Knox, A. Cooray, D. Eisenstein, et al., ApJ **550**, 7 (2001), .

[205] N. Fernandez-Conde, G. Lagache, J. Puget, et al., A&A **481**, 885 (2008), .

[206] M. P. Viero, P. A. R. Ade, J. J. Bock, et al., ApJ **707**, 1766 (2009), .

[207] A. Lewis, A. Challinor, and A. Lasenby, ApJ **538**, 473 (2000).

[208] N. Metropolis, A. W. Rosenbluth, and A. H. Rosenbluth, M. N. and Teller, J. Chem. Phys. **21**, 1087 (1953).

[209] N. Y. Gnedin, ApJ **535**, 530 (2000), .

[210] H. Trac, R. Cen, and A. Loeb, ApJ **689**, L81 (2008), .

[211] W. J. Percival, B. A. Reid, D. J. Eisenstein, et al., MNRAS **401**, 2148 (2010), .

[212] A. G. Riess, L. Macri, S. Casertano, et al., ApJ **699**, 539 (2009), .

[213] E. Komatsu and T. Kitayama, ApJ **526**, L1 (1999), .

[214] N. Battaglia, J. R. Bond, C. Pfrommer, et al., ArXiv e-prints (2010), .

[215] B. T. Draine, ARA&A **41**, 241 (2003), .

[216] V. F. Mukhanov and G. V. Chibisov, JETP Letters **33**, 532 (1981), .

[217] S. W. Hawking, Phys. Lett. **B115**, 295 (1982).

[218] A. A. Starobinsky, Phys. Lett. **B117**, 175 (1982).

[219] A. H. Guth and S. Y. Pi, Phys. Rev. Lett. **49**, 1110 (1982).

[220] J. M. Bardeen, P. J. Steinhardt, and M. S. Turner, Phys. Rev. D **28**, 679 (1983).

[221] V. F. Mukhanov, H. A. Feldman, and R. H. Brandenberger, Phys. Rept. **215**, 203 (1992).

[222] E. Calabrese, A. Slosar, A. Melchiorri, et al., Phys. Rev. D **77**, 123531 (2008), .

[223] A. Kosowsky and M. S. Turner, Phys. Rev. D **52**, 1739 (1995), .

[224] D. Baumann, M. G. Jackson, P. Adshead, et al., in *American Institute of Physics Conference Series*, edited by S. Dodelson, D. Baumann, A. Cooray, J. Dunkley, A. Fraisse, M. G. Jackson, A. Kogut, L. Krauss, M. Zaldarriaga, & K. Smith (2009), vol. 1141 of *American Institute of Physics Conference Series*, pp. 10–120, .

[225] R. Easther and H. Peiris, JCAP **0609**, 010 (2006), .

[226] W. H. Kinney, E. W. Kolb, A. Melchiorri, et al., Phys. Rev. **D74**, 023502 (2006), .

[227] A. Shafieloo and T. Souradeep, Phys. Rev. D **78**, 023511 (2008), .

[228] L. Verde and H. Peiris, JCAP **7**, 9 (2008), .

[229] M. Cortês, A. R. Liddle, and P. Mukherjee, Phys. Rev. D **75**, 083520 (2007), .

[230] M. Kamionkowski, A. Kosowsky, and A. Stebbins, Phys. Rev. D **55**, 7368 (1997).

[231] A. R. Liddle and D. H. Lyth, Phys. Lett. **B291**, 391 (1992).

[232] H. C. Chiang, P. A. R. Ade, D. Barkats, et al., ApJ **711**, 1123 (2010), .

[233] K. Ichikawa, M. Kawasaki, and F. Takahashi, JCAP **0705**, 007 (2007), .

[234] G. Mangano, A. Melchiorri, O. Mena, et al., JCAP **0703**, 006 (2007), .

[235] J. Hamann, S. Hannestad, G. G. Raffelt, et al., JCAP **0708**, 021 (2007), .

[236] B. A. Reid, W. J. Percival, D. J. Eisenstein, et al., MNRAS **404**, 60 (2010), .

[237] A. Mantz, S. W. Allen, and D. Rapetti, MNRAS **406**, 1805 (2010), .

[238] R. H. Cyburt, B. D. Fields, K. A. Olive, et al., Astroparticle Physics **23**, 313 (2005), .

[239] Y. Wang, D. N. Spergel, and M. A. Strauss, ApJ **510**, 20 (1999), .

[240] M. Tegmark and M. Zaldarriaga, Phys. Rev. D **66**, 103508 (2002), .

[241] S. L. Bridle, A. M. Lewis, J. Weller, et al., MNRAS **342**, L72 (2003).

[242] P. Mukherjee and Y. Wang, ApJ **599**, 1 (2003).

[243] M. Bridges, A. N. Lasenby, and M. P. Hobson, MNRAS **381**, 68 (2007), .

[244] J. Martin and C. Ringeval, JCAP **0608**, 009 (2006), .

[245] T. Chantavat, C. Gordon, and J. Silk, ArXiv e-prints (2010), .

[246] M. Bridges, F. Feroz, M. P. Hobson, et al., MNRAS **400**, 1075 (2009), .

[247] H. V. Peiris and L. Verde, Phys. Rev. D **81**, 021302 (2010), .

[248] J. A. Vazquez, A. N. Lasenby, M. Bridges, et al., ArXiv e-prints (2011), .

[249] L. Amendola, S. Gottloeber, J. P. Muecket, et al., ApJ **451**, 444 (1995), .

[250] R. Kates, V. Muller, S. Gottlober, et al., MNRAS **277**, 1254 (1995), .

[251] F. Atrio-Barandela, J. Einasto, S. Gottlöber, et al., Soviet Journal of Experimental and Theoretical Physics Letters **66**, 397 (1997), .

[252] J. Einasto, M. Einasto, E. Tago, et al., ApJ **519**, 469 (1999), .

[253] W. H. Kinney, Phys. Rev. D **63**, 043001 (2001), .

[254] J. Adams, B. Cresswell, and R. Easther, Phys. Rev. D **64**, 123514 (2001), .

[255] M. Matsumiya, M. Sasaki, and J. Yokoyama, Phys. Rev. D **65**, 083007 (2002), .

[256] A. Blanchard, M. Douspis, M. Rowan-Robinson, et al., Astron. Astrophys. **412**, 35 (2003), .

[257] A. Lasenby and C. Doran (2003), .

[258] P. Hunt and S. Sarkar, Phys. Rev. D **76**, 123504 (2007), .

[259] N. Barnaby and Z. Huang, Phys. Rev. D **80**, 126018 (2009), .

[260] A. Achúcarro, J. Gong, S. Hardeman, et al., JCAP **1**, 30 (2011), .

[261] S. Nadathur and S. Sarkar, ArXiv e-prints (2010), .

[262] S. Hannestad, JCAP **0305**, 004 (2003), .

[263] J. Martin and C. Ringeval, Phys. Rev. **D69**, 127303 (2004), .

[264] J. Martin and C. Ringeval (2004), .

[265] C. Sealfon, L. Verde, and R. Jimenez, Phys. Rev. D **72**, 103520 (2005), .

[266] W. H. Press, S. A. Teukolsky, W. T. Vetterling, et al., *Numerical Recipes in C: The Art of Scientific Computing* (Cambridge University Press, 1992), 2nd ed.

[267] E. Komatsu and D. N. Spergel, Phys. Rev. D **63**, 63002 (2001), .

[268] A. Lewis and A. Challinor, Phys. Rev. D **66**, 023531 (2002), .

[269] A. G. Riess, L. Macri, S. Casertano, et al., ApJ **699**, 539 (2009), .

[270] Planck Collaboration, P. A. R. Ade, N. Aghanim, et al., ArXiv e-prints (2011), .

[271] M. D. Niemack, P. A. R. Ade, J. Aguirre, et al., in *Society of Photo-Optical Instrumentation Engineers (SPIE) Conference Series* (2010), vol. 7741 of *Society of Photo-Optical Instrumentation Engineers (SPIE) Conference Series*, .

[272] J. E. Carlstrom, P. A. R. Ade, K. A. Aird, et al., ArXiv e-prints (2009), .

[273] M. L. Brown, P. Ade, J. Bock, et al., ApJ **705**, 978 (2009), .

[274] D. Tytler, J. M. O'Meara, N. Suzuki, et al., Physica Scripta Volume T **85**, 12 (2000), .

[275] S. Das, B. D. Sherwin, P. Aguirre, et al., ArXiv e-prints (2011), .

[276] B. D. Sherwin, J. Dunkley, S. Das, et al., ArXiv e-prints (2011), .

[277] A. R. Liddle, Monthly Notices of the Royal Astronomical Society **351**, L49 (2004), ISSN 1365-2966.

[278] T. Takeuchi, Astrophysics and Space Science **271**, 213 (2000), ISSN 0004-640X.

[279] S. Bird, H. V. Peiris, M. Viel, et al., ArXiv e-prints (2010), .

[280] R. A. Burenin, A. Vikhlinin, A. Hornstrup, et al., ApJS **172**, 561 (2007), .

[281] J. L. Tinker, E. S. Sheldon, R. H. Wechsler, et al., ArXiv e-prints (2011), .

[282] R. E. Smith, J. A. Peacock, A. Jenkins, et al., MNRAS **341**, 1311 (2003), .

[283] P. McDonald, U. Seljak, S. Burles, et al., ApJS **163**, 80 (2006), .

[284] A. G. Riess, A. V. Filippenko, P. Challis, et al., AJ **116**, 1009 (1998), .

[285] S. Perlmutter, G. Aldering, G. Goldhaber, et al., ApJ **517**, 565 (1999), .

[286] M. Hamuy, M. M. Phillips, N. B. Suntzeff, et al., AJ **112**, 2398 (1996), .

[287] M. Hamuy, M. M. Phillips, N. B. Suntzeff, et al., AJ **112**, 2391 (1996), .

[288] J. Sollerman, C. Aguilera, A. Becker, et al., ArXiv Astrophysics e-prints (2005), .

[289] R. Kessler, A. C. Becker, D. Cinabro, et al., ApJS **185**, 32 (2009), .

[290] H. Lampeitl, R. C. Nichol, H. Seo, et al., ArXiv e-prints (2009), .

[291] J. A. Holtzman, J. Marriner, R. Kessler, et al., AJ **136**, 2306 (2008), .

[292] M. Hamuy, G. Folatelli, N. I. Morrell, et al., PASP **118**, 2 (2006), .

[293] W. L. Freedman, C. R. Burns, M. M. Phillips, et al., ApJ **704**, 1036 (2009), .

[294] M. Hamuy, G. Folatelli, N. I. Morrell, et al., PASP **118**, 2 (2006), .

[295] W. D. Li, A. V. Filippenko, R. R. Treffers, et al., in *American Institute of Physics Conference Series*, edited by S. S. Holt and W. W. Zhang (2000), pp. 103–106.

[296] M. Hicken, P. Challis, R. P. Kirshner, et al., in *American Astronomical Society Meeting Abstracts* (2006), p. 72.04.

[297] M. Hamuy, J. Maza, M. M. Phillips, et al., AJ **106**, 2392 (1993).

[298] B. D. Johnson and A. P. S. Crotts, AJ **132**, 756 (2006), .

[299] N. V. Kuznetsova and B. M. Connolly, ArXiv Astrophysics e-prints (2006), .

[300] N. Connolly and B. Connolly, ArXiv e-prints (2009), .

[301] D. Poznanski, D. Maoz, and A. Gal-Yam, ArXiv Astrophysics e-prints (2006), .

[302] S. A. Rodney and J. L. Tonry, ApJ **707**, 1064 (2009), .

[303] S. A. Rodney and J. L. Tonry, ArXiv e-prints (2010), .

[304] M. Sako, B. Bassett, A. Becker, et al., AJ **135**, 348 (2008), .

[305] M. Sako, B. Bassett, B. Connolly, et al., ArXiv e-prints (2011), .

[306] D. M. Scolnic, A. G. Riess, M. E. Huber, et al., ApJ **706**, 94 (2009), .

[307] Y. Gong, A. Cooray, and X. Chen, ApJ **709**, 1420 (2010), .

[308] J. P. Bernstein, R. Kessler, S. Kuhlmann, et al., ArXiv e-prints (2009), .

[309] N. Kaiser and Pan-STARRS Team, in *Bulletin of the American Astronomical Society* (2005), p. 1409.

[310] LSST Science Collaborations: Paul A. Abell, J. Allison, S. F. Anderson, et al., ArXiv e-prints (2009), .

[311] M. Kunz, B. A. Bassett, and R. A. Hlozek, Phys. Rev. D **75**, 103508 (2007), .

[312] J. B. Oke and L. Searle, ARA&A **12**, 315 (1974).

[313] R. P. Kirshner, J. B. Oke, M. V. Penston, et al., ApJ **185**, 303 (1973).

[314] J. Newling, B. Bassett, M. Varughese, et al., In preparation (2011).

[315] J. Guy, P. Astier, S. Baumont, et al., A&A **466**, 11 (2007), .

[316] S. Jha, A. G. Riess, and R. P. Kirshner, ApJ **659**, 122 (2007), .

[317] E. T. Jaynes and G. L. Bretthorst, *Probability Theory* (2003).

[318] R. Kessler, J. P. Bernstein, D. Cinabro, et al., PASP **121**, 1028 (2009), .

[319] J. Sollerman, E. Mörtsell, T. M. Davis, et al., ApJ **703**, 1374 (2009), .

[320] J. Dickey, The Annals of Statistics **42**, 204 (1971).

[321] E. Gûnel and J. Dickey, Biometrika **61**, 545 (1974).

[322] J. Newling, M. Varughese, B. Bassett, et al., MNRAS **414**, 1987 (2011), .

[323] R. Kessler, B. Bassett, P. Belov, et al., PASP **122**, 1415 (2010), .

[324] M. C. March, R. Trotta, P. Berkes, et al., ArXiv e-prints (2011), .